NOTE TO USERS

Page(s) not included in the original manuscript and are unavailable from the author or university. The manuscript was scanned as received.

96

This reproduction is the best copy available.

UMI®

Experimental and Computational Studies of Loop Heat Pipes

by

Nima Atabaki

Department of Mechanical Engineering

McGill University
Montréal, Québec, Canada

January 2006

A thesis submitted to McGill University
in partial fulfillment of the requirements for the degree of
Doctor of Philosophy

Your file Votre référence
ISBN: 978-0-494-25091-4
Our file Notre référence
ISBN: 978-0-494-25091-4

Abstract

Computational and experimental investigations of fluid flow and heat transfer aspects of loop heat pipes (LHPs) are presented in this thesis. The overall goal is to formulate and develop cost-effective mathematical models and numerical solution methods for computer simulations of LHPs. This work has five distinct parts.

First, a basic network thermofluid model of conventional LHPs operating under steady-state conditions is proposed, implemented, tested, and applied. It illustrates the main steps in the formulation of such models. The capabilities of this basic model are assessed by applying it to an LHP for which experimental results are available in the literature. The results show that this model is capable of at least qualitatively accurate predictions and could serve as a tool in preliminary designs of LHPs.

Second, experimental apparatus and procedures are designed and implemented for measurements of the following properties of sintered powder-metal porous plates that are used as wicks in LHPs: Porosity; maximum effective pore size; effective permeability; and effective thermal conductivity when saturated with a liquid (distilled water in this work). The aforementioned experimental apparatus and procedures are applied to two sintered powder-metal porous plates, one made of nickel 200 and the other of stainless steel 316, and the results are presented and discussed.

Third, an LHP with a flat (plate-type) evaporator and a fixed active mass of the working fluid (distilled water) is designed and constructed, and an experimental investigation of its steady-state operation is conducted. Full details of this LHP and the experimental setup and procedures are presented. The experimental results augment the available repertoire of experimental data on LHPs. They are used to test the predictions of the proposed network thermofluid model.

Fourth, an enhanced version of the aforementioned basic network thermofluid model is proposed and adapted for computer simulations of the above-mentioned LHP operating under steady-state conditions.

Fifth, results of experimental and computational investigations of the above-mentioned LHP, operating with a stainless steel 316 wick and distilled water as the working fluid, are presented, compared, and discussed. The proposed network thermofluid model provides predictions that are within ±10% of the experimental results.

Résumé

Des études numériques et expérimentales des aspects de l'écoulement et du transfert de chaleur des boucles fluides diphasiques [Loop Heat Pipes (LHPs) en anglais] sont présentées. L'objectif principal de cette thèse est de formuler et développer des modèles mathématiques et des méthodes de solutions numériques pour simuler les LHPs.

Un modèle de réseau thermofluide de base pour le fonctionnement des LHPs conventionnels en régime permanent est proposé, testé et appliqué. La performance de ce modèle de base a été évaluée en l'appliquant à un LHP pour lequel les données expérimentales sont disponibles dans la littérature. Ces résultats montrent que le modèle est capable de fournir des prédictions qualitative et qu'il peut être utilisé comme un outil pour les designs préliminaires des LHPs.

Des dispositifs et des procédures expérimentaux ont été conçus et utilisés pour mesurer les propriétés suivantes des plaques poreuses de poudre de métaux sintérisées qui ont été utilisé comme mèches dans les LHPs: La porosité, la taille effective maximum du pore, le perméabilité effective, et la conductivité thermique effective lorsque la mèche est saturée par un fluide (eau distillée). Les susnommés dispositifs expérimentaux et procédures ont été appliqués aux deux plaques poreuses construites de nickel 200 et de l'acier inoxydable 316 et les résultats sont présentés et discutés.

Un LHP avec un évaporateur rectangulaire (type de plaque) et une masse fixée active du fluide caloporteur (eau distillée) est conçue et construite, et son fonctionnement en régime permanent a été étudié. Les détails de ce LHP et du prototype expérimental et les procédures utilisées sont présentés. Les résultats obtenus sont utilisés pour tester les prédictions du modèle de réseau thermofluide proposé.

Une version améliorée du modèle de réseau thermofluide de base susnommée est proposée et adaptée pour simuler numériquement le fonctionnement du LHP mentionné ci haut en régime permanent.

Les résultats expérimentaux et numériques du LHP mentionné ci-dessus, avec la mèche fabriquée en acier inoxydable 316 sont présentés, comparés, et discutés. Le modèle de réseau thermofluide proposé fourni des prédictions qui sont à ±10% des résultats expérimentaux.

Acknowledgements

I am deeply indebted to my supervisor, Professor B. Rabi Baliga, whose teachings, guidance, support, suggestions, and encouragements helped me throughout this research and during the writing of this thesis. His constructive criticisms and his mission of insisting on only high-quality work have been of great value for my research and me. I owe him lots of gratitude for having shown me this way of research.

I am grateful to the Department of Mechanical Engineering and the Graduate and Postdoctoral Studies Office (GPSO) for awarding me two McGill Graduate Student Fellowships (MGSF). My sincere thanks also go to the Natural Sciences and Engineering Research Council Canada (NSERC) and Fonds québécois de la recherche sur la nature et les technologies (NATEQ) for providing me postgraduate scholarships. I would also like to acknowledge with thanks the financial support provided for this work by NSERC through research grants to Professor B. Rabi Baliga.

I would like to thank all professors who have accepted the task of examining this thesis and also staff members of the McGill GPSO for their help with all the related administrative details.

Special thanks to the crew of the Machine Tool Laboratory in the Department of Mechanical Engineering, Antonio Micozzi, Nicola DePalma, J. Roy Westgate, and Benoit Demers, for their professionalism, help, and superb craftsmanship in the making of the fixtures for the experimental apparatus.

I would like to thank the following technical staff members of the Department of Mechanical Engineering for all their help and support: George Tewfik, Mario Iacobaccio, John Boisvert, Raymond Lemay, and Gary Savard. Many thanks also go to Joyce Nault, Della Maharajh, Jean Milliken, Barbara Lapointe, Marie-Anne Wong Lun Cheong, Mary Fiorilli, and Lisa B. Lapka, and to Professor Meyer Nahon, for their help with all the paperwork and administrative details.

I would like to thank Professor Srikar T. Vengallatore and Line Mongeon (a technician in the Facility for Electron Microscopy Research at McGill University) for providing guidance and assistance with the scanning electron microscopy of the sintered powder-metal plates used in this work. Many thanks also go to Mr. Robert Monet, President of Superior Alloy Technology Company in St-Bruno, Quebec, for his assistance in the laser cutting of these sintered powder-metal plates.

Many thanks go to my colleagues and friends from the Heat Transfer Laboratory, David Scott, José Canadedo Ibarra, Nirma Jesusathan, Alexandre Lamoureux, Lorena Camargo, and Eric Duplain for their help and camaraderie that created a wonderful work environment. I am also grateful to my officemates and friends in room 368 of the Macdonald Engineering Building, Neil Bulman-Fleming, Nasi Monshi, Lokesh Thakur, and Dr. Gilbert Bandé, for their friendship, help, and the fun times we enjoyed together.

Finally, I would like to thank my dear wife, Shahrzad, and my parents for their continuous love, support, and encouragements.

Table of Contents

List of Figures

List of Tables

Nomenclature

$A_{ef-wick}$	Effective open flow area of the wick
A_G	Cross-sectional area of the groove
A_{lp}	Total heat transfer surface area of the lower piece of the evaporator
A_{vl}	Cross section of vapor-transport line
C_f	Dimensionless friction pressure drop; Eq.(5.16) and Eq.(5.17)
$c_{p,v}$	Specific heat at constant pressure for the vapor-phase
$c_{p,l}$	Specific heat at constant pressure for the liquid-phase
C_{wick}	Constant in correlation for wick pressure drop; Eq. (5.8)
d_p (=2 r_p)	Effective capillary pore size
$(dP/dz)_g^s$	Axial gradient of the static pressure for the gas-phase flowing alone inside the pipe with its own mass flow rate
$(dP/dz)_l^s$	Axial gradient of the static pressure for the liquid-phase flowing alone inside the pipe with its own mass flow rate
D_{vl}	Internal diameter of vapor-transport line
$D_{vl\text{-}out}$	Outside diameter of vapor-transport line
$\Delta P_{2\varphi}$	Two-phase pressure drop
ΔP_{cap}	Capillary pressure
$\Delta P_{cap,\max}$	Maximum capillary pressure
ΔP_{cc}	Liquid-vapor mixture pressure drop thorough the compensation chamber
$\Delta P_{cd}^{2\varphi}$, $\Delta P_{cd-2\varphi}$	Overall pressure drop in the two-phase region of the condenser
ΔP_{cd-sc} , $\Delta P_{sc,cd}$	Overall pressure drop in the subcooled region of the condenser
$\Delta P_{channel}$	Pressure drop in the grooved channel
$\Delta P_{ev,ent}$	Liquid pressure drop from the exit of the compensation chamber to the annular wick entrance in the evaporator
$\Delta P_{fittings}$	Pressure drop through fittings
ΔP_{ll}	Overall pressure drop in the liquid-transport line
ΔP_{tot}	Total pressure drop across the LHP
ΔP_{vl}	Overall pressure drop in the vapor-transport line
ΔP_{vl-ent}	Pressure drop of the vapor flow inside the evaporator (vapor grooves, vapor collector and evaporator exit pipe)
ΔP_{wick}	Friction pressure drop for the liquid phase of the working fluid flowing through the wick inside the evaporator
$(\Delta P)_{fric}^{2\varphi}$	Two-phase friction pressure drop
$(\Delta P)_{f,ev}^{2\varphi}$	Two-phase pressure drop (vapor grooves, vapor collector and evaporator exit pipe)

$(\Delta P)_{grav}$	Gravity pressure drop
$(\Delta P)_{mom}$	Momentum pressure drop
e	Roughness (rms) of the internal surface of the pipe
f	Darcy friction factor
F	Modified Froude number [Taitel and Dukler (1976)]; Eq. (5.21)
$Fr_{l,aw}$	Modified Froude number [Awwad et al. (1995)]; Eq. (5.45)
Fr_l	Liquid Froude number; $Fr_l = G^2/(\rho_l^2 g D_{vl})$
F_{so}	Modified Froude number [Soliman (1982)]; Eq. (5.23)
g	Gravitational acceleration
G	Mass flux
Ga	Galileo number; Eq. (5.24)
h	Heat transfer coefficient
$h_m^{2\varphi}$	Average heat transfer coefficient in two-phase region of the condenser
h_{cap}	Capillary height
h_{ll-in}	Heat transfer coefficient for the internal convection in the liquid-transport line (based on the inside surface area)
h_{ll-out}	Effective heat transfer coefficient from the pipe inside surface to the ambient in the liquid-transport line (based on the inside surface area)
h_{vl-in}	Heat transfer coefficient for the internal convection in the vapor-transport line (based on the inside surface area)
h_{vl-out}	Effective heat transfer coefficient from the pipe inside surface to the ambient in the vapor-transport line (based on the inside surface area)
i	Specific enthalpy
$i_{exit,c}$	Fluid specific enthalpy at the exit of the condenser
i_f	Specific enthalpy of the saturated liquid phase
i_g	Specific enthalpy of the saturated vapor phase
i_{fg}	Enthalpy of evaporation
i_l	Specific enthalpy of the liquid phase
i_v	Specific enthalpy of the vapor phase
Ja_l	Liquid Jakob number; Eq. (5.26)
K	Modified Froude number [Taitel and Dukler (1976)]; Eq. (5.22)
$k_{c,pipe}$	Thermal conductivity of the condenser pipe wall
$k_{c,sleeve}$	Thermal conductivity of the condenser sleeve-material (cover-plate)
k_e	Effective thermal conductivity
k_f	Thermal conductivity of the fluid inside the pores
k_g	Thermal conductivity of the gas-phase
k_l	Thermal conductivity of the liquid-phase
k_o	Thermal conductivity of the continuous media
k_p	Thermal conductivity of the material inside the pores

k_s	Thermal conductivity of the solid-phase
K_{wick}, K	Effective permeability of the wick
L	Length
L_c	Length of the straight pipe that connects any two consecutive U-bends
l_{ox}, l_{oy}	Half-length of the opening for square porous samples
l_{wick}	Thickness of the wick
l_x, l_y	Half-length of the square porous samples
l_z	Thickness of porous samples
$M_{channel}$	Vapor flow Mach number in the grooved channels
$m_{cd-2\varphi}$	Fluid mass in the two-phase region of the condenser
m_{cd-sc}	Liquid mass in the subcooled region of the condenser
$m_{dry\_porous\_matl}$	Total mass of the dry porous material; Eq. (3.1)
m_{lline}	Liquid mass in the liquid-transport line
m_{lpool}	Liquid mass in the evaporator liquid pool
m_{lwick}	Liquid mass in the wick inside the evaporator
m_{total}	Total mass of the working fluid in the LHP
$m_{vgroove}$	Vapor mass in the evaporator grooves and vapor-accumulation region
m_{vline}	Fluid mass in the vapor-transport line
$\dot{m}$	Mass flow rate
$\dot{m}_g$	Gas-phase superficial mass flux
$\dot{m}_l$	Liquid-phase superficial mass flux
$\dot{m}''$	Mass flux
Nu	Nusselt number
$Nu_{vl\text{-}in}$	Nusselt number: Vapor flow in the vapor-transport line
$Peri$	Perimeter
Pr	Prandtl number
q_{app}	Net rate of heat input to the evaporator
q_{cc-amb}	Rate of heat transfer from the fluid stocked in the compensation chamber to the ambient environment
$q_{cd-reject}$	Rate of heat rejected in the condenser to the heat sink (constant-temperature oil bath)
q_{fg}	Part of q_{app} that goes into the evaporation of the working fluid in the evaporator
q_{fgc}	Rate of heat transfer needed to condense the working fluid in the condenser
q_{hl}	Rate of heat leak from the evaporator to the liquid pool
$q_{loss-eb}$	Rate of heat loss from the evaporator body
$q_{loss-ll}$	Rate of heat loss from the liquid in the liquid-transport line

$q_{loss-vl}$	Rate of heat loss from the fluid in the vapor-transport line
q_{sc}	Rate of heat rejection from the liquid in the subcooled part of the condenser
q_{vsh}	Rate of heat transfer that is used up in the superheating of the vapor during its passage through the grooved channels
q''	Heat flux
R	Radius of curvature of bends
r	Radius
r_c	Mean radius of curvature
r_p	Effective capillary pore radius
R_v	Specific gas constant
Re_{vl}	Reynolds number: Vapor flow in the vapor-transport line
Re_{vo}	Vapor-only Reynolds number
$R_{th-ll-in}$	Thermal resistance for the internal convection in the liquid-transport line
$R_{th-ll-out}$	Liquid transport line external thermal resistance (sum of the thermal resistances associated with the pipe wall, insulating material, and the external heat transfer)
$R_{th-vl-in}$	Thermal resistance for the internal convection in the vapor-transport line
$R_{th-vl-out}$	Vapor-transport line external thermal resistance (sum of the thermal resistances associated with the pipe wall, insulating material, and the external heat transfer)
R_{op}	Radius of the flow opening for cylindrical porous samples
$R'_{2\varphi}$	Thermal resistances (per unit length of the pipe) for the internal two-phase flow
$R'_{pipewall}$	Thermal resistances (per unit length of the pipe) for radial heat conduction through the pipe wall
R'_{oil}	Thermal resistances (per unit length of the pipe) for external convection over the condenser pipe immersed in the oil bath
R''	Thermal resistance in m²-°C/W
$T_{2\varphi-exit}$	Saturation temperature at the beginning of the subcool region of the condenser
T_{amb}	Ambient temperature
$T_{cd-exit}$	Liquid temperature at the exit of the condenser
$T_{cd\text{-}in}$	Vapor temperature at the exit of the vapor-transport line
T_{ev-bot}	Average temperature at the bottom surface of the lower piece of the evaporator
$T_{ev\text{-}in}$	Temperature of the subcooled liquid at the inlet of the evaporator
T_{sat}	Saturation temperature at the liquid-vapor interface in the evaporator
T_{sat-cc}	Saturation temperature of the fluid inside the compensation chamber
T_{sat-cd}	Saturation temperature of the fluid inside the condenser
T_{wall}	Temperature of the inside surface of the pipe wall

$T_{w,ent}$ Temperature of the liquid entering the wick

U_{ev} Overall heat transfer coefficient from the evaporator bottom surface to the ambient environment

UA Overall thermal conductance

$(UA'_{vl})_k$ Thermal conductance per unit length for segment k

v_v Vapor absolute velocities averaged across the interface

v_l Liquid absolute velocities averaged across the interface

x Local quality

x_{cd-in} Quality at the exit of the vapor-transport line

X Lockhart and Martinelli (1949) parameter; Eq. (5.20)

Greek Symbols

α Vapor void fraction;

α_{con} Porous material consolidation parameter

β Shape factor in Eq. (3.24)

δ Empirical constant in the correlation of Alexander (1972)

ε Porosity

φ_g Two-phase pressure drop multiplier based on the gas-phase

φ_l Two-phase pressure drop multiplier based on the liquid-phase

γ Ratio of the radius to the thickness of cylindrical porous samples $(\gamma = R/l_z)$

γ_v Vapor specific heat ratio, $(c_p/c_v)_v$

μ_g Dynamic viscosity of gas-phase

μ_l Dynamic viscosity of liquid-phase

ν Kinematic viscosity

θ Angle subtended at the center of the tube cross-section by the portion of the inner wall that is above the liquid level

θ_c Contact angle at static equilibrium condition

θ_d Dynamic contact angle of the liquid-vapor interface

θ_l Pipe inclination angle (measured from horizon)

ρ_g Mass density of gas-phase

ρ_l Mass density of liquid-phase

ρ_s Mass density of solid-phase

σ_{lv} , σ Liquid-vapor surface tension

τ_w Shear stress at the wall

ω Ratio of the radius of the open area to the radius of porous samples $(\omega = R_{op}/R)$

Superscripts

2φ	Two-Phase
1φ	Single-Phase

Superscripts

b	Bend
cd	Condenser
ev	Evaporator
fric	Friction
grav	Gravity
g	Gas-phase
l	Liquid-phase
ll	Liquid-transport line
mom	Momentum
oil	Oil
sc	Subcooled
st	Straight
v	Vapor-phase
vl	Vapor-transport line

Chapter 1:
Introduction

Computational and experimental studies of fluid flow and heat transfer aspects of loop heat pipes (LHPs) are presented and discussed in this thesis. LHPs are devices that use liquid-vapor phase-change phenomena and capillary forces in a wick to continuously transport heat from an evaporator to a condenser. The phase-change phenomena and the capillary-driven movement of the fluid within LHPs allow them to transfer heat with relatively small temperature drops over long distances. Furthermore, for the same temperature drops and distances between the heat source and the heat sink, the rates of heat transfer achievable with LHPs are usually one to three orders of magnitude larger than those possible with either conventional convection systems (without phase change) or solid thermal conductors.

Currently available LHPs are capable of rates of heat transfer of the order of 1 kW over a length of 10 m and heat flux loads as high as 1.3×10^6 W/m^2, and these capabilities are expected to increase over the next few years [Kaya and Ku (2003); Pastukhov et al. (2003); Maydanik (2005)]. Over the last three decades, LHPs have found numerous applications, for example, in satellites, solar energy systems, electronics cooling arrangements, gas turbines, avionic systems, cryogenic systems, and heating, ventilation, and air-conditioning (HVAC) systems. In these applications, the attractiveness of LHPs pertains to their intrinsically passive nature, in that they do not require any external motive devices (such as pumps), and their aforementioned ability to continuously transport heat with relatively small temperature drops over long distances.

In this chapter, concise discussions of the key components and operational features of heat pipes, loop heat pipes, and capillary pumped loops are presented first as background information. Then the motivation for this work and its overall goal are presented. Following that, the specific objectives of this thesis are put forward. A concise review of the pertinent literature is presented next. Finally, the organization of the thesis is summarized.

1.1 Background Information

Heat pipes (HPs) chronologically precede loop heat pipes (LHPs), and many of the underlying concepts and principles of operation of HPs are similar to those of LHPs. Therefore, this section is started with a discussion of HPs, and then a discussion of LHPs is presented. Following that, capillary pumped loops (CPLs), which are also two-phase capillary-driven heat transfer devices with principles of operation rather similar to those of LHPs, are discussed. At the end of this section, a discussion of some of the advantages of LHPs and CPLs over HPs is presented.

1.1.1 Heat Pipes

The heat pipe (HP) was invented by Grover et al. (1964) at Los Alamos Scientific Laboratory. A basic HP, in its simplest configuration, is presented schematically in Figure 1.1. It consists of a closed pipe of circular cross-section with an annular layer of porous material or wick covering its inside surface. Most of the wick is saturated with the liquid phase of a working fluid and the rest of the volume of the HP is occupied by the vapor phase.

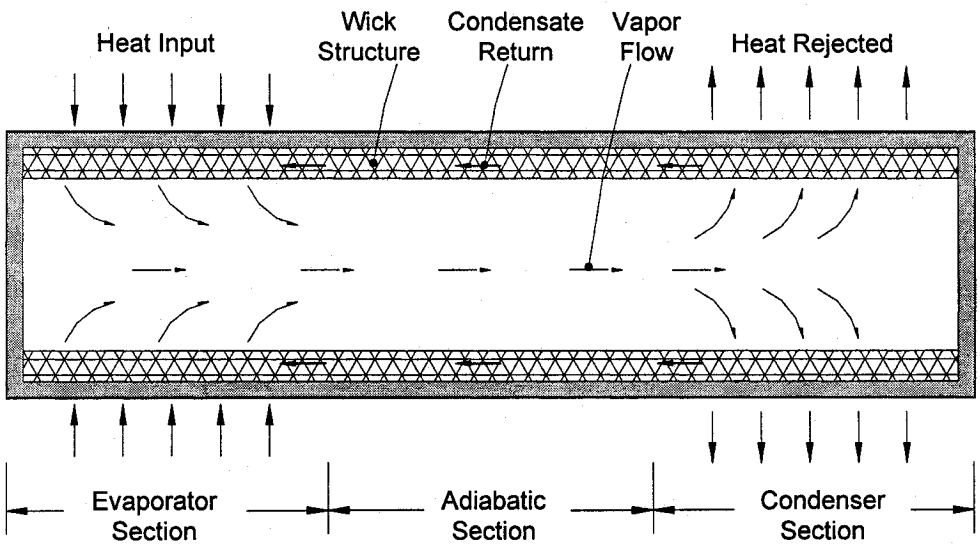

Figure 1.1: Schematic representation of a typical heat pipe.

As shown in Figure 1.1, a typical HP has three distinct sections: An evaporator, an adiabatic section (in practice, a section with negligibly small heat losses or gains), and a condenser. When heat is applied to the evaporator, the liquid in the wick is evaporated,

and the heat input is absorbed primarily as the latent heat of vaporization. The removal of heat from the condenser causes the vapor to condense on the wick and release the latent heat of vaporization to a heat sink (maintained at lower temperature). The pressure gradient resulting from the accumulation of the vapor in the evaporator and its depletion at the other end in the condenser forces the vapor to flow through central core of the HP. As the amount of liquid diminishes by evaporation, the liquid-vapor interface in the evaporator enters the wick, causing a capillary head (pressure increase across the liquid-vapor interface) to develop there. This capillary head sustains the pressure drop needed to transport the vapor from the evaporator to the condenser of the HP through its core space, and also to drive the flow of the liquid from the condenser to the evaporator through the wick. If the rate of heat input to the evaporator and its extraction in the condenser are sustained, the fluid circulates continuously, and steady-state conditions are attained, as long as the operating parameters of the HP stay within some critical ranges.

HPs have been constructed using tubes with hydraulic diameters ranging from about 100 μm (micro heat pipes) up to a few centimeters, and they can be designed to operate over a very wide range of temperature by choosing appropriate working fluids [Chi (1976); Silverstein (1992)]: Cryogenic HPs typically operate at temperatures ranging from 10 K to 122 K, and use hydrogen, nitrogen, oxygen, and methane as the working fluid; in high-temperature HPs, liquid metals such as mercury, cesium, potassium, sodium, and lithium are used as the working fluid, and their approximate operating temperature range is between 600 K to 1900 K; intermediate- or moderate-temperature HPs, with working fluids such as common refrigerants, methanol, ammonia, and water, operate at temperatures that lie in the range 122 K to 600 K.

HPs have several operational limits: They are generally referred to as the capillary limit, the sonic limit, the entrainment limit, and the boiling limit. Detailed discussions of these limits are available in many published works, for example, those of Chi (1976), Ochterbeck and Peterson (1997), and Silverstein (1992). These limits are concisely explained below.

Capillary limit: In steady-state operation of HPs, as mentioned above, the capillary head developed in the wick (at the liquid-vapor interface) sustains the pressure drop needed to transport the vapor from the evaporator to the condenser, and also drive the

flow of the liquid in the reverse direction through the wick. The meniscus inside the wick adjusts naturally to develop a capillary head that overcomes the aforementioned pressure drops in a HP. The total pressure drop in a HP is a function of the fluid mass flowrate, which, in turn, is a function of the rate of heat input to the evaporator. For a given wick and working fluid combination, the capillary head is limited to a maximum value. Therefore, there is a maximum overall pressure drop that can be handled in a HP, which, in turn, dictates the maximum mass flow rate that can be circulated, and, consequently, the rate of heat transfer from the evaporator to the condenser. This limit on the heat transport capability of a HP is known as the capillary limit. If the applied rate of heat input exceeds this limit, the capillary head is unable to supply the required liquid input to the evaporator and the wick dries out: In this situation, the temperature in the evaporator rises suddenly, and, in extreme cases, the HP could be totally damaged.

Sonic limit: The sonic limit is the highest possible heat transport rate that can be sustained in a HP for a specific vapor temperature in the evaporator. This limit is reached when the vapor leaving the evaporator attains the local velocity of sound (Mach number equal to one). In this situation, the flow is said to be choked, and the vapor flow and associated heat transport rate are at a maximum. An increase in the heat input rate beyond what can be transported at the sonic limit for a given vapor temperature would cause this temperature to rise to a value at which the new sonic limit becomes adequate for the task at hand [Silverstein (1992)]. In principle, this increase in the operating temperature of a HP could be accommodated until levels dictated by other limiting criteria, such as material limitations, are reached. However, there is a substantial temperature drop along the length of the evaporator as conditions within a HP approach the sonic limit. Thus, HPs are usually designed to operate well below the sonic limit.

Entrainment limit: Since the vapor and the liquid move in opposite directions in a HP, a shear force exists at the liquid-vapor interface. At a high vapor velocity, liquid droplets can detach from the surface of the wick and get entrained in the vapor flow. When this occurs, it results in a dry-out of the wick in the evaporator. Usually, this condition is assumed to be reached when the Weber number reaches a critical value, of the order of unity: The Weber number is a dimensionless parameter that represents the ratio of the vapor inertia force to the liquid-vapor surface tension force. The entrainment

limit dictates a maximum vapor velocity that can be sustained within a HP, which, in turn, limits the rate of heat transport it can provide.

Boiling limit: When heat is added to the evaporator section of a HP, a temperature gradient is produced across the thickness of the wick. At steady-state operating conditions, the temperature of the liquid in the wick is equal to or higher than the temperature of the adjacent saturated vapor. In addition, at the liquid-vapor interface, due to surface tension effects and the associated capillary pressure jump, the saturation temperature of the vapor is higher than that of the adjacent liquid. In other words, the liquid in contact with the interface is superheated. Furthermore, the temperature of the liquid inside the wick rises with distance from the interface, reaching a maximum value at the outer wick surface (the pipe wall). Therefore, the liquid is superheated over the entire wick thickness during steady-state operation of a HP. However, when the liquid superheat exceeds a critical value, vapor bubbles form at nucleation sites in the liquid-saturated portion of the wick, initiating boiling [Silverstein (1992)]. The rate of heat transfer at which this nucleate boiling starts is called the boiling limit. The onset of boiling can cause the liquid to be driven out of the wick, resulting in dry-out and interruption of the capillary pumping, causing the evaporator section to overheat and possibly leading to permanent damage or even a meltdown of some of its components.

Gravitational effects: HPs are also sensitive to gravitational effects, especially when the condenser is located below the evaporator section. In such situations, the capillary head must overcome the net gravitational head, in addition to of the total friction and minor pressure losses in a HP: This requirement, in turn, leads to a reduction in the maximum mass flow rate and heat transfer capabilities of the HP.

1.1.2 Loop Heat Pipes

As was discussed above, HPs have several intrinsic operational limits that restrict their maximum heat transport capability. Therefore, over the last three decades, there have been increasing research efforts to invent and develop devices based on similar principles, but capable of higher maximum rates of heat transfer than HPs. Loop heat pipes (LHPs) are among the results of such efforts. LHPs were invented in the former Soviet Union in the early 1970s [Maydanik (2005)]. Figure 1.2 schematically illustrates

the major components of a typical LHP, namely, an evaporator, a compensation chamber, a vapor-transport line, a condenser, and a liquid-transport line.

In LHPs, the evaporator and the compensation chamber are integrated, and linked together both hydrodynamically and thermally. Generally, the evaporator is composed of an internally grooved pipe and an annular wick with a liquid core (liquid pool) at its center. A typical LHP is schematically illustrated in Figure 1.2.

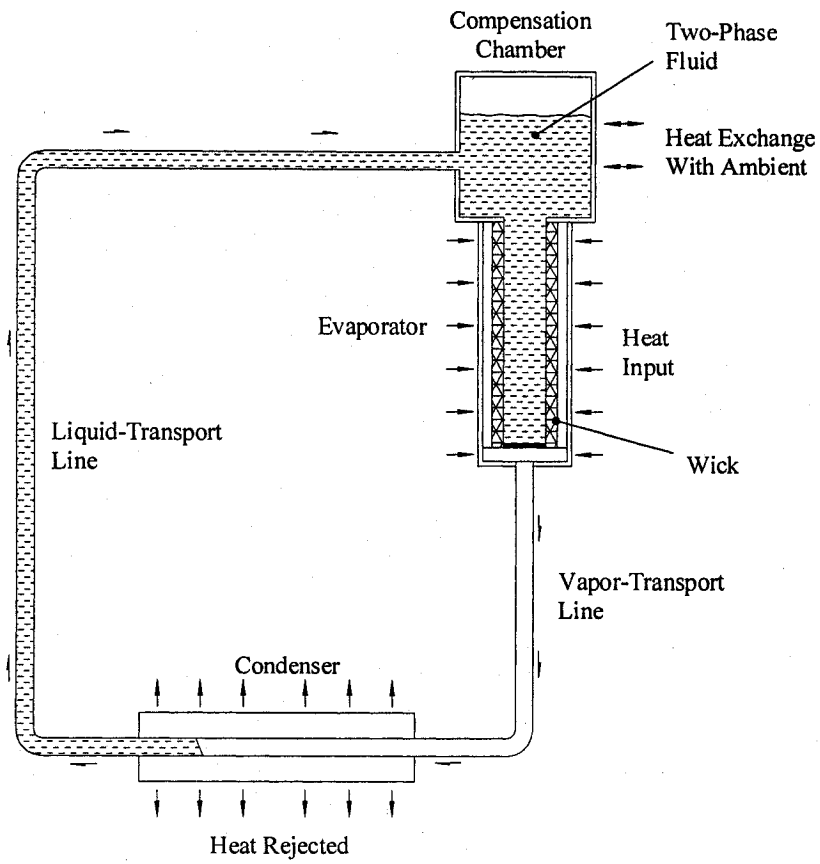

Figure 1.2: Schematic representation of a typical loop heat pipe.

In steady-state operation of LHPs, the heat input to the evaporator is conducted through its metallic grooved wall to the adjoining wick surface. This causes the saturated liquid in the wick to evaporate at its outer surface and the vapor to flow into the grooved channel (see Figure 1.3). As in HPs, the depletion of the liquid in the evaporator causes the liquid-vapor interface to enter the wick and, thereby, creates a capillary pressure head.

The pressure in the vapor phase at the interface is higher than that of the liquid on the other side, by an amount equal to the capillary pressure jump, and the accumulated vapor in the grooved channels is pushed to the end of the evaporator. The vapor collected from all grooves then flows through a smooth pipe (vapor-transport line) and reaches the condenser. In the condenser, the vapor is first condensed, and then, if the condenser is long enough, the condensed liquid is subcooled.

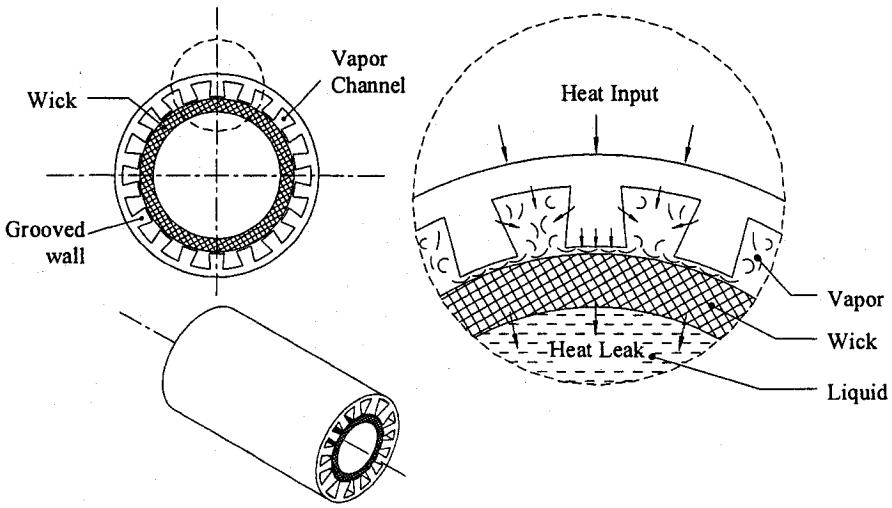

Figure 1.3: Schematic representation of the evaporator of a typical loop heat pipe.

The liquid collected in the condenser flows through the liquid-transport line and reaches the compensation chamber. Upon entering the compensation chamber, this liquid is heated, due to "heat leak" from the evaporator [Kaya and Hoang (1999)], and it also experiences heat exchange with the ambient environment. The liquid then reaches the inner surface of the wick. Upon entering the wick, the liquid pressure drops as it flows through the wick structure, and its temperature rises, due to heat conducted through the grooved walls to the wick. At the liquid-vapor interface, the liquid temperature reaches the temperature of the saturated vapor: As the saturated vapor is at a higher pressure than the adjoining liquid, due to the capillary pressure jump, the liquid at the liquid-vapor interface is superheated.

Figure 1.4 represents a steady-state performance curve of a typical LHP [Bienert and Wolf (1995)]. In this figure, the overall temperature difference (between the evaporator

and the sink to which the condenser rejects heat) is plotted versus the rate of heat input to the evaporator.

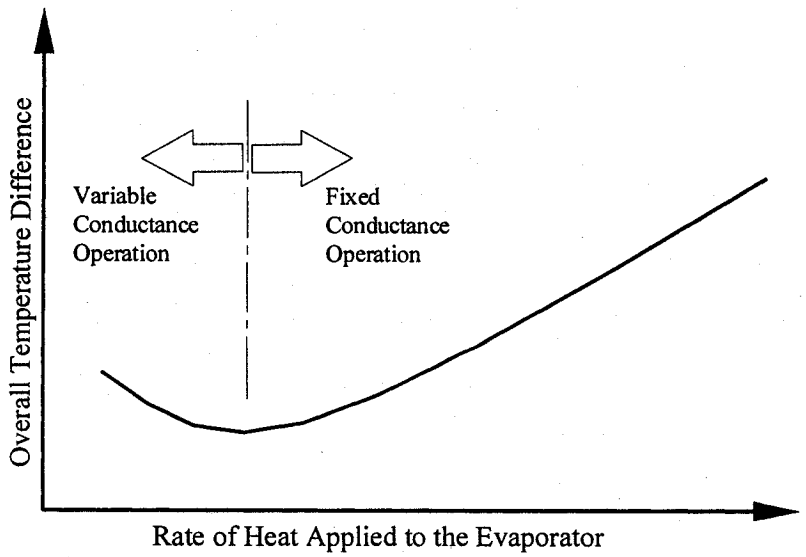

Figure 1.4: Steady-state performance curve of a typical loop heat pipe.

In steady-state operation, at low values of the rate of heat input to the evaporator, LHPs work in a variable-conductance mode, while for higher values of this parameter, they behave as fixed-conductance devices (see Figure 1.4). At low rates of heat input, the rate of heat rejection in the condenser is more than that required for full condensation of the vapor entering it. Therefore, the vapor is first fully condensed, and then the condensed liquid is subcooled during its passage through the remaining length of the condenser section. As a result, the zero-quality point (position where the vapor is fully condensed) is located somewhere within the condenser, as is shown schematically in Figure 1.2. As the rate of heat input is increased, at a constant sink temperature, the condenser is gradually unblocked (increasingly filled with vapor), the zero-quality point interface moves toward the end of the condenser, and the excess liquid is pushed into the compensation chamber where it is stocked: Under these conditions, the rate of heat rejection in the condenser is increased without an increase in the operating saturation temperature, and, consequently, the overall LHP thermal conductance (evaporator plus condenser) is augmented. In this mode of operation of an LHP, depending on its thermal

coupling to the ambient environment, the overall temperature difference ($T_{evap} - T_{sink}$) remains constant or decreases.

At higher rates of heat input, the condenser becomes completely filled with two-phase fluid, and the overall thermal conductance of the LHP remains essentially constant. Under these conditions, additional increases in the rate of heat input require corresponding increases in the driving temperature difference between the condenser and the sink, resulting in an increase in the operating saturation temperature in the evaporator and an augmentation of the overall temperature difference ($T_{evap} - T_{sink}$). The steady-state performance curve of LHPs is discussed in more detail in Chapter 2.

1.1.3 Capillary Pumped Loops

A schematic representation of a capillary pumped loop (CPL) is given in Figure 1.5. This device was invented in the United States of America in the mid-1960s [Ku (1993)]. A typical CPL consists of an evaporator, a two-phase reservoir, a vapor-transport line, a condenser, and a liquid-transport line. The evaporator of a typical CPL is similar to that of a typical LHP (see Figure 1.3), but it is not integrated with a compensation chamber.

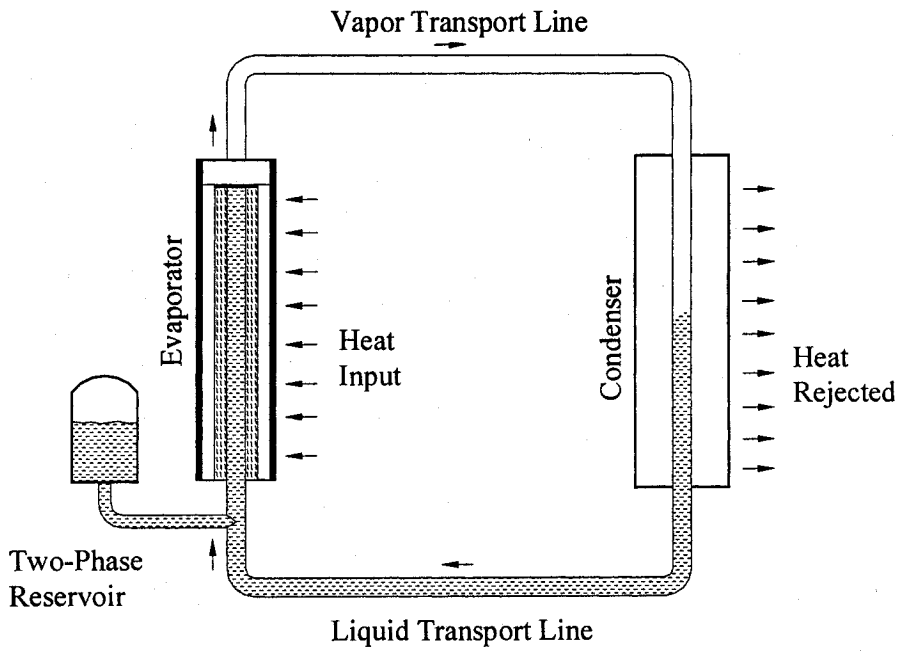

Figure 1.5: Schematic representation of a typical capillary pumped loop.

LHPs and CPLs are conceptually quite similar: A detailed discussion of the similarities and the difference between these devices is available in Nikitkin and Cullimore (1998). The main difference between LHPs and CPLs lies in the location of the two-phase reservoir in the loop. In LHPs, as was discussed previously, the two-phase reservoir (the compensation chamber) is a part of (integrated with) the evaporator (see Figure 1.2). In CPLs, on the other hand, this reservoir is a separate chamber that is connected via a relatively short pipe to the liquid-transport line, at a point that is usually quite close to the evaporator (see Figure 1.5).

In both LHPs and CPLs, the two-phase reservoir has two main roles: 1) ensure the presence of the liquid phase at the liquid-vapor interface in the wick for continuous evaporation and, therefore, continuous operation of the loop; and 2) absorb any excess mass of working fluid that is expelled from the loop during the startup phase or due to changes in the operating conditions. In CPLs, prior to startup, the reservoir is actively controlled (for example, by thermostatically controlled heating) to ensure that the liquid is displaced from the reservoir and is present in the wick for evaporation. However, under normal operation, no such control of the compensation chamber is needed during the startup phase of LHPs. In practical terms, the two-phase reservoir in CPLs is not thermally connected to the loop. Therefore, for operating temperatures above the ambient temperature, even during steady-state operation, the two-phase reservoir in CPLs has be to be heated in order to compensate for heat losses. In LHPs, on the other hand, the two-phase reservoir (compensation chamber) is thermally linked with the evaporator, and it absorbs part of the rate of heat input to the evaporator: Thus the temperature inside the compensation chamber is automatically regulated as the rate of heat transfer to the subcooled liquid entering it and any heat loss to the ambient environment are both balanced by the rate of heat leak (gained) from the evaporator.

As mentioned by Ku (1993), the distribution of the liquid between the two-phase reservoir and the condenser in CPLs is governed by the requirement of a pressure balance between them. Changes in heat loads and/or thermal sink conditions cause the liquid to redistribute until this pressure balance is established. Therefore, the area over which the vapor condenses in the condenser (active heat transfer area) adjusts automatically to the heat load and the thermal sink conditions. Thus, it is possible to control the operating

temperature of a CPL by controlling the saturation temperature (and hence the saturation pressure) in the two-phase reservoir. For a fixed (controlled) saturation temperature in the two-phase reservoir, any increase in the rate of heat input to the evaporator section causes the displacement of the condensate (liquid) from the condenser into the two-phase reservoir, allowing the CPL to operate in the variable-conductance mode. As a result, its operating temperature remains constant, independent of the rate of heat input to the evaporator, and close to the set temperature of the two-phase reservoir.

As discussed in Nikitkin and Cullimore (1998), if the two-phase reservoir is not large enough, at some rate of heat input, it becomes completely filled with the liquid. At this point, the reservoir looses its regulatory role, and any increase of the heat input to the evaporator causes the operating temperature to increase proportionally: In other words, the CPL works in a fixed-conductance mode of operation. On the other hand, if the rate of heat input to a variable-conductance CPL with an oversized two-phase reservoir is increased to too high a level, the vapor could fill up both the condenser and the liquid-transport line, and it may also enter into the wick, resulting in failure. Therefore, sometimes it is useful to design the two-phase reservoir and the charge (total mass of working fluid) such that the CPL works at high powers in the fixed-conductance mode.

1.1.4 Advantages of Loop Heat Pipes and Capillary Pumped Loops over Heat Pipes

In LHPs and CPLs, smooth tubing is used for both the liquid- and the vapor-transport lines, and a wick is necessary only in the evaporator: Thus, the pressure drop associated with the flow of liquid through the wick decreases significantly in comparison with the corresponding value in HPs (where the wick covers the entire length of the pipe) for the same overall mass flow rate of the working fluid. Therefore, LHPs and CPLs are usually capable of higher maximum heat transfer rates than HPs, over longer distances. Furthermore, the pore sizes of the wicks used in LHPs and CPLs can be finer than those of wicks used in HPs: The corresponding increase in capillary head allows LHPs and CPLs to cope better with adverse gravitational effects. In addition, in LHPs and CPLs, the evaporator and the condenser can be installed far from each other, which facilitates applications of these devices (by providing flexibility in the positioning of the heat source and the heat sink).

Another advantage of LHPs and CPLs over HPs is that the vapor- and liquid-flow paths are totally separated. In HPs, the vapor and the returning liquid (condensate) flow in opposite directions, and, as was explained earlier, there is a heat transfer limit associated with this counter-flow phenomena, known as the entrainment limit.

LHPs and CPLs also offer the possibility of cooling multiple heat sources and rejecting the collected heat to a single thermal sink: This can be achieved by deploying multiple evaporators, in a hydrodynamically parallel configuration, and rejecting the total heat input via a single condenser. Multi-evaporator CPLs and LHPs are discussed in papers by Ku (1998), Yun et al. (1999), and Goncharov et al. (2000).

As the wick is usually employed only in the evaporator of LHPs and CPLs, these devices have a diode-like characteristic, in that the heat transfer is possible only in one direction (from the evaporator to the condenser). In contrast, the wick covers the entire length of HPs, and, therefore, the heat transfer direction can be switched. The diode-like characteristic of LHPs and CPLs make them particularly suitable for space applications [Swanson and Birur (2003)] or any other applications where a reversal in the direction of heat transfer is either not acceptable or undesirable.

As in CPLs, the operating temperature in LHPs can be actively controlled, if desired. The basic ideas behind both active and passive controls and methods of regulation of LHPs are discussed in Maydanik et al. (1994), Bienert and Wolf (1995), and Nikitkin et al. (1999).

1.2 Motivation and Overall Goal

A desire and commitment, on the part of both the author and his supervisor, to contribute to ongoing worldwide efforts to improve the design or enhance the operating efficiency of energy exchange, storage, and conversion equipment is the main source of the motivation for the work reported in this thesis.

As was mentioned earlier, this work is related to fluid flow and heat transfer phenomena encountered in loop heat pipes (LHPs). It involves complementary experimental and computational investigations. The overall goal of this work is to formulate and develop cost-effective mathematical models and numerical solution methods for computer simulations of LHPs, and validate these models/methods using the

results of complementary experimental investigations. The intention here is to propose models and numerical solution methods that are suitable for the design and optimization of LHPs, augment the available experimental data on LHPs, and also contribute to the understanding of the thermofluid processes that occur within these devices.

1.3 Specific Objectives

The specific objectives of this investigation are summarized below:

- To propose, implement, test, and apply a basic network thermofluid model of conventional LHPs operating under steady-state conditions. The aim is to illustrate the main steps in the formulation of network thermofluid models of LHPs, and to also obtain a model that is capable of at least qualitatively accurate predictions and could serve as a tool in preliminary designs of LHPs. In this context, the aim if to assess the capabilities of this basic model by applying it to an LHP akin to that shown in Figure 1.2 and checking its predictions against experimental results available in the literature.
- To design and implement experimental apparatus and procedures for the measurement of the following properties of sintered powder-metal porous materials that are used as wicks in LHPs:
    - Porosity
    - Maximum effective pore size
    - Effective permeability
    - Effective thermal conductivity when fully saturated with a liquid (distilled water in this work)

  These properties are needed in the design of LHPs and required as inputs in mathematical models of these devices. The aim here is to also apply the aforementioned experimental apparatus and procedures to two sintered powder-metal porous plates, one made of nickel 200 and the other of stainless steel 316, and present and discuss the results.
- To design and construct an LHP with a flat (plate-type) evaporator and a fixed active mass of the working fluid, and conduct an experimental investigation of its steady-state operation. The aim here is to obtain experimental results that

could be used to test network thermofluid models and also to augment the available repertoire of experimental data on LHPs.

- To propose an enhanced version of the aforementioned basic network thermofluid model, and adapt it for computer simulations of the above-mentioned LHP with a flat (plate-type) evaporator and fixed active mass of working fluid.
- To present and discuss the experimental results and the model predictions for the above-mentioned LHP.

1.4 Literature Review

This section is divided into five subsections as follows: 1) textbooks, handbooks, and review articles that provide comprehensive discussions of heat pipes (HPs), loop heat pipes (LHPs), and capillary pumped loops (CPLs); 2) textbooks, handbooks, and review articles that provide detailed discussions of the thermofluid phenomena that occur in HPs, LHPs, and CPLs; 3) publications on numerical methods for the prediction of fluid flow and heat transfer; 4) publications related to the properties of liquid-saturated porous materials; and 5) published works on the unsteady operation of CPLs and LHPs, and the steady-state operation of LHPs.

Comprehensive reviews of the vast number of published works on each of the above-mentioned topics are not intended in this section. Rather, only works that were used in and/or are directly relevant (or closely related) to the research presented in this thesis are reviewed here.

1.4.1 Books and Review Articles on HPs, LHPs, and CPLs

For detailed reviews and discussions of the underlying theory, modeling, design, construction, and operation of HPs, LHPs, and CPLs, the reader is referred to books by Chi (1976), Dunn and Reay (1982), Silverstein (1992), Petersen (1994), and Faghri (1995). Review articles (on these devices) that were found to be particularly informative and useful in this work include the contributions of Ku (1993), Ochterbeck and Peterson (1997), Garimella and Sobhan (2001), Vasiliev (2005), and Maydanik (2005).

1.4.2 Thermofluid Phenomena that Occur in HPs, LHPs, and CPLs

The thermofluid phenomena that occur in HPs, LPHs, and CPLs include the following: Single- and two-phase (vapor-liquid) fluid flow and heat transfer in passages (of circular and noncircular cross section) and fittings; fluid flow and heat transfer in porous media (wick materials); boiling; and condensation.

There are numerous textbooks that cover single-phase Newtonian fluid flow and heat transfer in ducts: Examples include the works of Batchelor (1967), Eckert and Drake (1971), Landau and Lifshitz (1987), Tritton (1988), White (1991), Kays and Crawford (1993), Bejan (1995), Fox and McDonald (1998), Oosthuizen and Naylor (1999), Kaviany (2001), Incropera and DeWitt (2002), Bird et al. (2002), and Currie (2003). Classical works in this area are reviewed in an article by Kays and Perkins (1973). Single-phase laminar flow and heat transfer in ducts have been discussed comprehensively by Shah and London (1978). Detailed discussions of single-phase turbulent flow and heat transfer in ducts are available in the works of Tennekes and Lumley (1972), Hinze (1975), Wilcox (1993), Pope (2000), and Launder and Sandham (2002). Details of single-phase fluid flow and heat transfer topics of particular relevance to this research, such as those covered in the works of Colebrook (1939), Sparrow and Patankar (1977), Gnielinski (1976, 1983), White (1991), and Kays and Crawford (1993), are elaborated in Chapters 2 and 5.

For comprehensive discussions of the rheology of non-Newtonian flows, the reader is referred to books by Dealy and Wissbrun (1990) and Macosko (1994).

Authoritative discussions of the basics and more advanced aspects of fluid flow and heat transfer in porous materials are available in books by Dullien (1992), Kaviany (1999), and Nield and Bejan (2006). For details of the derivations of volume-averaged equations that govern these phenomena and related topics, the reader is referred to the contributions of Beavers and Sparrow (1969), Crapiste et al. (1973), Scheidegger (1974), Slattery (1981), Whitaker (1999), Kaviany (1999), Minkowycz et al. (1999), Alazmi and Vafai (2000), and Nield and Bejan (2006). Specific details of fluid flow and heat transfer in the wicks of LHPs are provided in Chapters 2, 3, and 5.

For comprehensive discussions of two-phase (vapor-liquid) fluid flow and heat transfer in ducts, boiling, and condensation, the reader is referred to books by Wallis

(1969), Collier (1972), Carey (1992), Whalley (1996), Tong and Tang (1997), Levy (1999), Klienstreuer (2003), and Brennen (2005). Reviews of these topics are available in articles by Bouré and Delhaye (1982), Drew (1983), Rohsenow (1985), Griffith (1985), Rose (1998), and Ghajar (2005). Seminal works related to flow regime maps, pressure drops, and heat transfer coefficients for two-phase flows in horizontal and slightly inclined tubes include the contributions of Lockhart and Martinelli (1949), Baker (1954), Chato (1962), Mandhane et al. (1974, 1977), Taitel and Dukler (1976), Jaster and Kosky (1976), Soliman (1982, 1986), Dobson (1994), Dobson and Chato (1998), Ould Didi et al. (2002), and Thome (2003). Details of these works are provided in Chapter 5.

The *Handbook of Single-Phase Convective Heat Transfer* edited by Kakac et al. (1987), the *Handbook of Heat Transfer Fundamentals* edited by Rohsenow et al. (1998), the *Handbook of Phase Change: Boiling and Condensation* edited by Kandlikar et al. (1999), *ASHRAE Fundamentals* (2005), and the *Multiphase Flow Handbook* edited by Crowe (2006) are very useful sources of information on the above-mentioned thermofluid phenomena that occur in HPs, LHPs, and CPLs. Comprehensive reviews of these topics can also be found in Vols. 1 – 38 of the series *Advances in Heat Transfer* edited by Irvine and Hartnett (1964 – 2004).

1.4.3 Numerical Methods for Fluid Flow and Heat Transfer

Numerical methods for the solution of the mathematical models of fluid flow and heat transfer phenomena are usually grouped into the following five main categories: finite difference methods, finite volume methods, finite element methods, boundary element methods, and spectral methods. Hybrid numerical methods that combine the attractive features of the aforementioned categories of methods have also been proposed: Examples include spectral element methods, finite analytic methods, and control-volume finite element methods. The fundamentals of these numerical methods are covered in books authored by Patankar (1980), Tannehill et al. (1997), Roache (1998), Ferziger and Peric (1999), Reddy and Gartling (2000), Gresho and Sani (2000), Zienkiewicz and Taylor (2000), Peyret (2002), Gaul et al. (2003), Jaluria and Torrance (2003), and Karniadakis and Sherwin (2005), among others. Reviews of control-volume finite element methods for fluid flow and heat transfer are available in the works Baliga (1997) and Baliga and

Atabaki (2006). The *Handbook of Numerical Heat Transfer* edited by Minkowycz et al. (2006) and Vols. 1 and 2 of the series *Advances in Numerical Heat Transfer* edited by Minkowycz and Sparrow (1997, 2000), provide many useful review articles on various aspects of computational fluid dynamics and heat transfer. The contributions of Leonard (1979, 1997) are recommended for reviews of upwind procedures.

For authoritative and useful discussions of the numerical modelling of turbulent flow and heat transfer in ducts, the reader is referred to the works of Wilcox (1993), Pope (2000), and Launder and Sandham (2002).

There are numerous books on numerical methods for curve fitting of data, integration and differentiation, solutions of differential equations, and direct and iterative solutions of linear systems of algebraic equations: Concise discussions of these methods and their implementation in computer programs are available in the works of Conte and de Boor (1972), Hamming (1987), and Press et al. (1992). Algorithms for solving tridiagonal and pentadiagonal systems of linear algebraic equations are available in the work of Sebben and Baliga (1995).

1.4.4 Properties of Liquid-Saturated Porous Materials

As was mentioned earlier this chapter, the wicks of HPs, LHPs, and CPLs are liquid-saturated porous materials. Thus, key inputs to the design and mathematical models of these capillary-driven devices include the porosity, the maximum effective pore size, the effective permeability, and the effective thermal conductivity of liquid-saturated wicks.

For discussions of many of the available analytical, semi-analytical, and numerical correlations for effective properties of porous materials made of uniformly sized, regularly spaced, and packed (unconsolidated or consolidated) spherical particles, the reader is referred to the contributions of Maxwell (1954), Kunii and Smith (1960), Chen and Tien (1973), Batchelor and O'Brien (1977), Ogniewicz and Yovanovich (1978), Sangani and Acrivos (1983), Hadley (1986), Bauer (1993), Kaviany (1999), Hsu (2000), Bonnefoy et al. (2004), Bahrami et al. (2004), and Nield and Bejan (2006). Reviews of some of the aforementioned and additional analytical correlations are available in the works of Tsotsas and Martin (1987) and Tavman (1996).

The aforementioned analytical correlations are not applicable to the wicks typically used in HPs, LHPs, and CPLs, as they are made from sintered metal powders or fibers. Furthermore, for sintered metal powders, particles of angular rather than spherical shapes are preferred, and these particles are not uniformly sized or regularly spaced [Goring and Churchill (1961), Batchelor (1974), Hadley (1986); Leong et al. (1997)]. The sintering process creates excellent connections (solid-to-solid contact zones) between the particles or fibers; and most of the available analytical correlations do not properly account for this effect of the sintering process [Kunii and Smith (1960); Hadley (1986); Leong et al. (1997)].

Analytical and experimental investigations of the effective properties of sintered metal powders and fibers have been conducted and reported by Kunz et al. (1967), Soliman et al. (1970), Alexander (1972), Singh et al. (1973), Van Sant and Malet (1975), Hadley (1986), Peterson and Fletcher (1987), Chang (1990), Mantel and Chang (1991), Bonnefoy et al. (2004), and Atabaki and Baliga (2005a).

Details of some of the above-mentioned and other contributions on this topic are presented in Chapter 3 of this thesis.

1.4.5 CPLs and LHPs

This thesis is mainly concerned with loop heat pipes (LHPs). However, because of the conceptual similarities between LHPs and capillary pumped loops (CPLs), published works that deal with computational and experimental studies of both these devices are reviewed in this subsection. Generally, it is easier to start and maintain steady-steady operation of LHPs than that of CPLs. Thus, in the published literature, relatively little attention has been paid to the startup and transient operating aspects of LHPs, while many researchers have described these features and also the role of the two-phase reservoir in CPLs. In addition, some pressure and temperature oscillations (time-periodic and also irregular) could occur during the post-startup operation of CPLs, even with a fixed rate of heat input; and these phenomena too have received attention in the literature. Though such problems are either not present or less frequently encountered in the operation of LHPs, knowledge of the physical phenomena that cause or sustain the aforementioned oscillations in CPLs could be helpful to designers of LHPs.

As was mentioned previously (see Section 1.3), the design, construction, and experiments on a flat-evaporator LHP, and also the formulation and testing of a network thermofluid model for this LHP, are among the specific objectives of this work. This particular LHP does *not* have a compensation chamber integrated with the flat evaporator; in this sense, it is physically and conceptually different from conventional LHPs, such as that shown in Figure 1.2. Rather, an external two-phase reservoir is attached to the liquid-transport line of the proposed LHP for charging purposes and also to facilitate the achievement of a desired phase distribution of the working fluid prior to startup: Subsequent to startup, this reservoir is disconnected (isolated) from the LHP (full details of this LHP and its operation are given in Chapter 4). Therefore, during startup, this LHP behaves like a CPL. Thus, it was essential in this work to develop an understanding of the startup process of CPLs: The related works are reviewed concisely in this subsection.

In this subsection, first, papers that deal with the startup and the transient operations of CPLs and LHPs are reviewed. Following that, attention is devoted to works on modeling and experimental investigations of the steady-state operation of LHPs.

1.4.5.1 Startup and Transient Operation of CPLs and LHPs

Kiper et al. (1990) designed and constructed a CPL and tested it in both transient and steady-state modes of operation, with water as the working fluid. For the transient mode of operation, they applied step-shaped power inputs of 200 W and 300 W to the evaporator of the CPL. For both of these power inputs, they found that the temperature of the evaporator increased linearly with time for the first 65 s, and then asymptotically approached the steady-state operating condition. They also studied the effect of liquid subcooling at the inlet of the evaporator section for power inputs in the range 50 W to 300 W. In these experiments, the liquid was passed through a subcooler before it entered the evaporator section. A significant influence of this subcooling on the CPL performance was reported. In tests with low subcooling, evaporator dry-out occurred even at low power inputs.

Kiper et al. (1990) also proposed a lumped-heat-capacity model to predict the transient operating temperature of their CPL: Their predicted and experimental results

compared quite favorably. They also proposed a model of the steady-state operation of this CPL, in which it is assumed that the heat transfer through the liquid-saturated wick is due to pure conduction and the effect of subcooling (that takes place outside the evaporator and the wick) is introduced via a constant term in the corresponding energy equation (volumetric heat sink). This steady-state model yielded a parabolic temperature profile across the wick, with the minimum temperature located within the wick structure. In their experimental setup, the wick was heated from below and the liquid evaporation took place in the vicinity of its top surface. The subcooled liquid also entered the wick from below. For these conditions, the aforementioned parabolic temperature profile predicted by their steady-state model is physically unrealistic. Thus, it is clear that their steady-state model needs improvements.

Cullimore (1991) has conducted an analytical study of CPL startup transients. In this study, he draws heavily on his laboratory experiences. The work is focused on an analysis of a generic CPL with ammonia as the working fluid. In addition to the start-up behavior, potential failure mechanisms, which might be neglected in the design process, were considered in this study. Cullimore mentions in this article that to start a CPL successfully, the evaporator must be primed or, in other words, the wick must be completely wetted. One way to achieve this condition is to heat the reservoir prior to the startup so that it becomes the hottest component in the CPL and causes all vapor bubbles in the rest of the loop to eventually collapse. Cullimore also points out in this paper that the liquid in all vapor passages (groves, vapor collector, and vapor-transport line) must be cleared off during the startup process; and the displaced liquid must flow to the reservoir through the vapor-transport line and the condenser: Various aspects of this clearing of the liquid in the vapor passages are discussed in Cullimore's work.

Ku (1993) has presented an overview of CPL technology from the late 1970s to 1993. He describes various existing designs, including two experimental CPLs (CPL1 and CPL2) with multiple cylindrical evaporators used at the NASA Goddard Space Flight Center. In these NASA CPLs, ammonia was used as the working fluid and the maximum heat flux (applied to the evaporators) was about 15×10^4 W/m^2. In this paper, Ku has discussed the following performance anomalies observed in CPLs: a) sudden depriming of the evaporators (drying-out of the wick); b) evaporator depriming during rapid step-

down of the power input; and c) pressure oscillations during steady-state operation. The following possible causes of depriming of the evaporators after several hours of steady-state operation have been mentioned: Accumulation of non-condensable gases in the wick; and expansion and penetration of the vapor into the wick during startup. No operating problems were detected during sudden step-up of the power input to the evaporator. However, during rapid power step-downs, the condenser becomes less active, and, therefore, a sudden displacement of the liquid phase of the working fluid from the reservoir towards the condenser (in the reverse direction to the normal fluid flow in the loop) can cause some instabilities [Ku (1993)].

As mentioned earlier in this chapter, the distribution of the liquid phase of the working fluid between the reservoir and the loop in CPLs is governed by the balance between the saturation pressure in the reservoir and that within the loop. As mentioned by Ku (1993), even small changes in the operating temperatures of the fluid in loop or the reservoir during steady-state operation can lead to pressure imbalances and oscillations in the CPL. The interaction between the reservoir, the evaporator, and the condenser during such transient operation of CPLs are quite complex, not very well understood, and require further investigations.

The pressure and temperature oscillations during the operation of CPLs are also the subject of many other studies. High-frequency pressure oscillations are thought to be related to hydrodynamic interactions between the fluid in the reservoir and that in the loop [Muraoka et al. (2001)]. Hoang and Ku (1996) have conducted a theoretical study of the hydrodynamic stability of CPLs. They have proposed an increase in the flow resistance in the line connecting the reservoir to the loop as a means of improving the stability and damping of the aforementioned pressure oscillations.

Kiper et al. (1988, 1990) analytically modeled the transient rate of heat conduction from the evaporator to the piping at its inlet. Their goal was to explain temperature oscillations observed experimentally at the surface of the evaporator inlet pipe in one of the CPLs they tested. They found a criterion for a critical value of the steady-state power input to the evaporator beyond which the inlet pipe surface temperature could oscillate in an unstable way. They compared their model predictions with the results obtained from one of their experimental runs and reported relatively good agreement. Their criterion

implies that at a given steady-state power input to the evaporator, larger values of the following parameters would help in preventing the occurrence of the aforementioned temperature oscillations: Inlet pipe diameter; heat transfer coefficient at the entrance of the evaporator; thermal conductivity of the inlet pipe wall; and degree of subcooling.

In the model of Kiper et al. (1988, 1990), no hydrodynamic oscillations or backward-and-forward motion of the liquid entering the evaporator were considered, and the experimental results (measured temperature) pertain to the pipe wall (not the fluid). Furthermore, they did not provide any measurements of the pressure difference across the evaporator: Such data (if measured) could help to determine if liquid flow oscillations accompany those in the temperature of the wall of the inlet pipe of the evaporator.

Ku (1993) has pointed out the importance of having a proper working fluid phase distribution (charging strategy) in CPLs prior to the startup. He investigated the implications of having the whole loop either fully or only partially flooded with the liquid phase of the working fluid before the startup. In the partially flooded case, the vapor-transport line was filled with the vapor phase while the condenser, the liquid-transport line, and the evaporator were filled with the liquid phase: To ensure that this fluid phase distribution was achieved (at one-g, or in ground tests), the vapor lines of the experimental CPLs studied were located at an elevation of about 0.1 m higher than the rest of the loop: Ku (1993) maintains that the startup under this condition is easier as it leads to lower superheat (amount by which the saturated vapor temperature in the evaporator exceeds the saturation temperature set in the reservoir), and, therefore, less chance of evaporator depriming; in addition, the loop experiences a lower pressure spike during the startup than that associated with a fully-flooded loop (where a sharp pressure spike is caused by rapid emptying of the liquid phase from the vapor-transport line).

The thermodynamics of CPLs has been discussed by Ku (1994). In this paper, a discussion of the steady-state operation of CPLs for both constant- and variable-conductance modes is presented, and the related thermodynamic processes are presented (and interpreted) on pressure-temperature (P-T) and temperature-entropy (T-S) diagrams. In a follow-up paper, Hoang and Ku (1996) have focused on some of the main problems that occur during startup of CPLs (such as depriming of the evaporator). In addition, Hoang and Ku (1996) have stressed the necessity of a detailed study of the onset of

nucleate boiling in a flooded evaporator and presented an equation for calculating the pressure spike at the onset of this nucleate boiling.

Platel et al. (1995) have experimentally studied the heat transport capacity of a CPL with two parallel evaporators and one condenser. Dichloro-difluoro carbon (CCl_2F_2; R12) was used as the working fluid. Tests were performed for an operating temperature of about 30°C (set point in the two-phase reservoir) corresponding to an operating pressure of 7.42 bar. For a polyethylene wick with an effective pore size of 10 μm, the maximum capillary pressure registered was about 2000 Pa. The maximum rate of heat transported was 600 W from the evaporators (300 W from each of the two evaporators) to the condenser, over an equivalent length of 23 m; the minimum rate of heat transported in the tests was 10 W. Startup and transient behaviors of the CPL were also studied, and significant temperature and pressure oscillations in the reservoir were reported.

Platel et al. (1996) formulated a mathematical model to simulate unsteady behavior of the CPL used in the above-mentioned experimental studies of Platel et al. (1995). They developed an expression for the determination of the radius of curvature of the liquid-vapor interface in the pores of the wick as a function of the interface saturation temperature, vapor pressure, and the liquid velocity in the wick. By controlling the saturation temperature in the reservoir, they were able to keep the operating temperatures and pressures in loop of the CPL essentially constant.

Li and Ochterbeck (1999) have presented a numerical and experimental study of the effect of wick thermal conductivity on the startup of a CPL. They showed that thick wicks with low thermal-conductivity are preferable with respect to startup: With thin wicks, they observed sudden generation of vapor bubbles and even boiling directly in the liquid core of the cylindrical evaporator, resulting in rapid dry-out of the wick; similarly, for a wick of high thermal conductivity, they noticed that the high rate of heat conduction through the wick structure could cause the onset of nucleate boiling in the liquid core, and the vapor could penetrate into the wick rather than remain confined in the grooved channels of the evaporator.

LaClair and Mudawar (2000) studied the thermal transients in the evaporator of a CPL prior to the initiation of nucleate boiling. An unsteady heat conduction equation applied to the evaporator was solved analytically (using Green's Function method). They

showed that to maximize the probability of a successful startup, it is necessary to maintain a minimum difference between the temperature of the fluid in the vapor grooves and that in liquid core (initial subcooling level). This was achieved by applying a sufficiently large heat flux to the evaporator. However, they also noted that there were some limits to this technique: For example, a very large heat flux could cause rapid boiling within the liquid in the vapor grooves during startup, and lead to a large pressure surge; if this pressure surge became too large, it could force vapor into the wick and lead to startup failure. LaClair and Mudawar (2000) also pointed out that a wick with high thermal conductivity decreases the degree of subcooling and reduces the chance of a successful startup, confirming similar earlier findings of Li and Ochterbeck (1999).

Muraoka et al. (1998, 2001) have presented numerical and experimental studies of a LHP with a porous element in both the evaporator and the condenser. They formulated a mathematical model (based on a nodal method) to simulate the transient behavior of this LHP. In this method, the physical system is divided into a finite number of isothermal regions and each of these regions is assigned a node; and the system of discretized energy equations for each node is solved numerically. The LHP used in their experimental investigation consisted of a flat (disk-type) evaporator, a flat (disk-type) condenser, and two connecting pipes. The working fluid was ethanol, and disk-type plates made of sintered bronze were used as the wicks in both the evaporator and the condenser. This loop does not have a two-phase reservoir normally used in CPLs or a compensation chamber usually integrated with the evaporator of a LHP. Therefore, their LHP had a fixed mass of the active working fluid and an essentially fixed location of the liquid-vapor interface in the evaporator and the condenser (within the wicks). The reason for not using a two-phase reservoir (akin to that used in CPLs) was to reduce the pressure oscillations (and the related potential for failure) associated with the interactions between the fluid in the reservoir and that in the loop.

Muraoka et al. (1998, 2001) have also presented results for the steady-state performance of their LHP for power inputs of 73W and 120W, and heat-sink temperatures of 30°C, 40°C, and 60°C. The evaporator saturation temperature for these conditions ranged from 61.8°C to 75.6°C, and the total thermal conductance was in the range 2.2 W/°C to 4.4 W/°C (the corresponding total thermal resistance ranged from 0.23

°C/W to 0.45 °C/W). Their results showed that for a constant power input of 120W applied to the evaporator, the total thermal conductance increases with increasing the heat-sink temperature (thermal resistance decreases). They claimed excellent agreement between their numerical predictions and experimental results, with the differences not exceeding 1%: This level of agreement seems a bit exaggerated or it could be a typographical error.

Muraoka et al. (1998, 2001) also did experiments on the transient operation of their LHP, by performing power cycling (120W to 0W) with a constant heat-sink temperature, and also by varying the heat sink temperature between 30°C to 60°C while maintaining a constant power input. They also visualized the fluid flow in the evaporator (designed to be partly transparent) and observed that vapor bubbles were present in the liquid core (liquid pool) below the wick almost all the time during the operation of the loop: These bubbles oscillated; and during the power step-down test, they grew rapidly and pushed the liquid in the reverse direction out of the evaporator and towards the condenser.

1.4.5.2 Steady-State Operation of LHPs

Dickey and Peterson (1994) have conducted experimental and analytical investigations of the thermal performance of a CPL with ammonia as the working fluid. The external two-phase reservoir typically used in CPLs was absent in their loop, thus it resembled LHPs more than conventional CPLs. Both the evaporator and condenser of this loop were 120 mm long pipes with an outside diameter of 12 mm. The vapor- and liquid-transport lines were made of stainless steel pipes of length 3 m with inner diameters of 3 mm and 2 mm, respectively. The wick was made from sintered nickel powder with a maximum effective pore radius of about 1.5 μm and a porosity of 70%.

They studied the influence of the power input to the evaporator and also adverse tilts (operation against gravity) on the steady-state performance of the loop. They also presented an analytical model for the prediction of the steady-state performance of the loop: This model is based on an energy balance on the evaporator and condenser (lumped model), and calculations of pressure loss through the transport lines and the wick; and gravitational heads were incorporated in this model, when needed. However, the two-phase pressure drop in the condenser was neglected. The analytical model presented by

Dickey and Peterson (1994) is relatively simple: For example, the heat transfer from the subcooled section of the condenser to the heat sink was modeled using an average liquid temperature (for the entire subcooled length) and a prescribed constant temperature of the pipe wall. Axial variation of the temperature of the liquid flowing through the subcooled section of the condenser could easily be integrated in this model to provide better estimates of both the rate of heat transfer and the exit temperature. Despite the aforementioned simplicity of their model, relatively good agreements between the model predictions and the experimental data were reported.

Many researchers have studied the thermodynamics of LHPs. For example, the different processes that the working fluid undergoes during the steady-state operation of LHPs are presented and interpreted on P-T diagrams in the works of Dickey and Peterson (1994), Kiseev et al. (1997), Parker (2000), and Atabaki and Baliga (2003). In Chapter 2 of this thesis, the different processes that occur inside a conventional LHP during steady-state operation are demonstrated on a P-T diagram and discussed in detail. In Chapter 5 of this thesis, a P-T diagram is used to represent the processes inside an LHP with a flat (plate-type) evaporator and a fixed active mass of working fluid (water): This LHP was specially designed and used in this research (full details are given in Chapter 4).

Bienert and Wolf (1995) presented an analytical model and test results for an LHP. Unfortunately, full details of the experimental setups were not provided. Their analytical model is based on pressure and energy balances on each element of the LHP; the energy balances are formulated and solved using a combined lumped parameter/nodal approach; the evaporator and the compensation chamber are treated as lumped parameters; and the remainder of the loop is treated using a nodal network approach. They have presented experimental results for the steady-state performance of the LHP, operating in both variable- and fixed-conductance modes. They also noted that these two modes of operation may not be fully established in every test case; furthermore, depending on the thermal coupling to the ambient environment, one or the other mode may be suppressed.

Bienert and Wolf (1995) have also discussed the possibility of using active thermal control in the operation of LHPs. They have presented results obtained with thermostatic control (heating) of the compensation chamber of their LHP, which was operated at temperatures above that of the ambient environment in these tests. They found that for a

given sink temperature, the available control range is limited by the heat rejection capability of the condenser: In other words, for a given temperature setpoint in the compensation chamber, their technique could provide active control of the steady-state operating temperatures in the LHP until the condenser was unable to handle the rejection of the total power input. Thus, when the temperature setpoint was elevated, the heat rejection capability of the condenser increased and thermal control became possible over a wider range of the total power input to the evaporator/compensation chamber assembly.

Wirsch and Thomas (1996) have conducted and reported experimental, analytical, and numerical studies of the performance of an LHP made of stainless steel and operated with ammonia as the working fluid. In their work, for a given power input to the evaporator, the cooling rate in the condenser was adjusted (by increasing or reducing the flowrate of the refrigerant) to keep the temperature of the fluid in vapor-transport line constant (set-point temperature). The evaporator was equipped with a cylindrical sintered nickel-powder wick, and it was fitted in a flat aluminum saddle. Two tests were performed for vapor-transport line temperatures of 40 °C and 50 °C, and the maximum power inputs that could be handled by the LHP were determined. This highest power-input point was 337 W for a vapor-line temperature of 50 °C: At this point, there was insufficient amount of liquid to keep the wick wet, the evaporator temperature rose suddenly, and the evaporator eventually dried out. However, when the vapor-transport line temperature was set at 40 °C, the maximum heat-rejection capacity of the condenser was about 260 W (condenser limit): For this limiting power input, the dry-out condition was not reached in the evaporator. An effective thermal resistance was also calculated from the experimental results, using the input power and the temperature difference between the average steady-state temperatures of the evaporator and the condenser. This effective thermal resistance decreased when the power input was increased: Its minimum sustainable value was 0.085 °C/W. In addition, it was noted that the average effective thermal resistance for a vapor-transport line temperature of 50 °C was lower than that obtained when this temperature was set at 40 °C.

Wirsch and Thomas (1996) used a finite element analysis to model the steady-state conduction heat transfer in the evaporator assembly (aluminum saddle, thermal grease, and stainless steel evaporator shell). This model considered heat transfer from a strip

heater to the saddle, which was then conducted to and through the evaporator stainless wall, and finally lost at the inside radius of the evaporator wall via an evaporative convection boundary condition. Values of the evaporative heat transfer coefficient were calculated using the results obtained from the experiments, as a function of the power input and difference in the temperature of the vapor-transport line and the average evaporator temperature. The numerical predictions of the average evaporator temperature (outer surface) showed relatively good agreement with the corresponding experimental data.

Mulholland et al. (1999) used an analytical model developed by Dynatherm Corporation to predict the operation characteristics of an 800 W LHP tested at the U.S. Air Force Research Laboratory. The liquid-line of this LHP enters the transition section between the evaporator and the compensation chamber (CC), instead of in the CC itself, and this was accounted for by modifying the analytical model. In addition, a weighting factor was introduced to predict the temperature of the liquid entering the wick as a function of its temperatures in the compensation chamber and at the exit of the liquid-transport line. Their model predictions are in relatively good agreement with experimental results for power levels between 50 W and 600 W.

Kaya and Hoang (1999) have put forward a mathematical model of LHPs. This model is based on steady-state energy conservation equations and pressure drop calculations. The model was validated by using it to simulate two different LHPs (labeled the GLAS-LHP and the NRL-LHP) and comparing its predictions to the available experimental data. NASA designed the GLAS-LHP for thermal control of the Geoscience Laser Altimeter System (GLAS), and the NRL-LHP was designed and built for the U.S. Naval Research Laboratory (NRL). Comparisons of corresponding computational and experimental results showed good agreements (within 5%). In the model, it was assumed that the compensation chamber was always filled with a two-phase (liquid and vapor) fluid mixture, and this ensured that the required mass and phase distribution in the loop were automatically satisfied: In other words, the size of the compensation chamber was appropriate to absorb any excess fluid pushed into it from the condenser while maintaining the fluid inside it in a two-phase condition. It was also assumed that in the compensation chamber, the returning subcooled liquid from the condenser would be

heated up to the saturation temperature of the liquid entering the inner surface of the wick, with the required energy coming from heat transfer from the ambient environment (through the compensation chamber envelope) and heat leak from the evaporator. The heat rejection in the condenser was divided into two-phase and subcooled parts. The condenser tube was attached on one side to a plate with embedded pipes through which a coolant (a refrigerant) was circulated to simulate a uniform-temperature thermal sink; the other side of the condenser pipe was exposed to the ambient environment: In the model of this condenser, the heat exchange with the ambient environment (the so-called "parasite heat transfer") was included. However, details of how the heat transfer surface of the condenser tube was divided to take into account heat transfer both to (or from) the ambient environment and to the sink (cooling plate) are not provided.

Kaya and Hoang (1999) observed that the GLAS-LHP operated in the variable-conductance mode for power inputs to the evaporator of less than 100 W. The operating temperature (saturation temperature in the vapor grooves of the evaporator) in this mode decreases to a minimum with increasing power input up to 100 W. For power inputs above 100 W, the LHP operated in the fixed-conductance mode: This was demonstrated by the linear rise in the operating temperature with increase in the power input. These experimental results were used to test a network thermofluid model proposed in this thesis (details are presented in Chapter 2).

Pastukhov et al. (2003) studied miniature LHPs (cylindrical evaporator less than 6 mm in diameter, and connecting lines ranging from 1.5 mm to 2 mm in diameter) designed for applications in electronics cooling. These LHPs could handle power inputs of up to 30 W with heat transfer distances up to 0.25 m, and were used for cooling the central processing unit (CPU) of a mobile personal computer (PC). They built six different LHPs, with different sizes, sink designs, and wick materials. Ammonia and acetone were used as the working fluids. With an air-cooled heat sink, the total thermal resistance (from the source to the sink) ranged from 1.4 °C/W to 4.0 °C/W. These LHPs were tested successfully in the one-g condition for a variety of orientations.

Kaya and Ku (2003) experimentally and computationally studied the thermal characteristics of a small LHP operated with ammonia as the working fluid. The cylindrical evaporator of this LHP was made of aluminum and had an outer diameter of

13 mm and a length of 120 mm; and its transport lines were also made of aluminum and had an inner diameter of 2.5 mm. This LHP has a sintered nickel wick with effective pore radius of less than 1.2μm and porosity of 60%. This LHP was successfully started with evaporator input power as low as 5 W and for different loop orientations (compensation chamber above evaporator, evaporator above the compensation chamber, and condenser above the evaporator). The steady-state performance of this LHP was studied for input power ranging from 5 W to about 250 W and evaporator temperature ranging from 250 K to 325 K. The sink temperature was fixed at about 233 K. For evaporator power input of above 40 W, the steady-state performance of the loop indicated operation in the fixed-conductance mode.

Kaya and Ku (2003) modified and used the mathematical model of Kaya and Hoang (1999) for computer simulations of the steady-state performance of the above-mentioned small LHP. In the modified model of Kaya and Ku (2003), the heat leak formulation accounts for the effect of the radial mass flow rate through the wick, rather than treat this heat transfer as just pure conduction as was done in the model of Kaya and Hoang (1999). The predictions obtained with the modified model were within 8.5 K of the experimental temperature measurements that ranged from 250 K to 320 K (sink temperature was fixed at about 233 K). As noted by the authors, these model predictions for the small LHP are less satisfactory than those obtained for the larger GLAS-LHP.

Atabaki and Baliga (2003) presented a network thermofluid model for steady-state operation of an LHP with a cylindrical evaporator. Mathematical models of the fluid flow and heat transfer in each of the elements of this LHP, and collectively of the entire LHP, were proposed and discussed. Experimental results provided by Kaya and Hoang (1999) for the GLAS-LHP operated with ammonia as the working fluid were used to validate the model. Full detail of this model and its results are discussed in Chapter 2 of this thesis.

Cimbala et al. (2004) used both real-time neutron radioscopy and single-exposure neutron radiography in an experimental study of an LHP to visualize the fluid flow and the phase distribution. This LHP had a cylindrical evaporator made of aluminum and it was operated with ammonia as the working fluid. Aluminum is nearly transparent to thermal neutrons, and the liquid-phase and vapor-phase of ammonia (and also of water) are visually distinguished (liquid is darker), since their mass densities are very different

from each other. With this method, Cimbala and his colleagues were able to visualize partial dry-out of the wick, the liquid-vapor interface location in the condenser, and the fluid flow in the vapor- and liquid-transport lines. This method of visualizing the fluid flow and phase distribution holds great promise, and it is recommended for use in future investigations aimed at improving the understanding and modeling of LHPs (and also HPs and CPLs).

Riehl and Dutra (2005) experimentally studied an LHP made of stainless steel. This LHP had a cylindrical evaporator designed to handle power inputs up to 70 W with acetone as the working fluid. The wick of this LHP was made of an ultra high molecular weight (UHMW) polyethylene. The heat source temperature was limited to 85 °C. The condenser of this LHP was in excellent thermal contact with an aluminum plate embedded with internal channels through which a coolant supplied from constant-temperature bath set at –5 °C was circulated. They used the model proposed by Kaya and Hoang (1999) for the design and prediction of the thermal behavior of this LHP. The experimental results pertaining to the steady-state performance of this LHP were found to be in good agreement with those predicted by the aforementioned model (relative differences less than $\leq$ 5%). The steady-state operating temperature ranged from about 20 °C to 80 °C for the power inputs in the range 2 W to 70 W.

1.5 THESIS ORGANIZATION

In earlier sections of this chapter (Chapter 1), some background discussions (of HPs, LHPs, and CPLs), the motivation for this work, its specific objectives, and a review of the literature relevant to this research were presented.

In Chapter 2, a basic network thermofluid model for conventional LHPs is presented. The application of this basic model to an LHP (with a cylindrical evaporator and ammonia as the working fluid) and a comparison of the predicted results with experimental results taken from the published literature are also presented and discussed in Chapter 2.

In Chapter 3, the experimental apparatus and procedures that were designed and implemented for the determination of the porosity, the maximum effective pore size, the effective permeability, and the effective thermal conductivity of water-saturated sintered

powder-metal plates are presented and discussed. The applications of these techniques to two porous plates, one made of nickel 200 and the other of stainless steel 316, and the results are also presented and discussed in Chapter 3.

In Chapter 4, details of an LHP with a flat (plate-type) evaporator and a fixed mass of active working fluid are presented. This LHP was designed, constructed, and used in this work. The overall setup and procedures that were used in an experimental investigation of this LHP are also described in this chapter.

In Chapter 5, an extended version of the network thermofluid model of LHPs presented in Chapter 2 is presented and discussed. This model is designed for computer simulations of the LHP described in Chapter 4.

Computational and experimental results that pertain to the LHP described in Chapter 4 are presented and discussed in Chapter 6.

In Chapter 7 (the concluding chapter), the contributions of this thesis are summarized and some suggestions for extensions of this work are provided.

Chapter 2:

A Basic Network Thermofluid Model of Loop Heat Pipes

In this chapter, a basic network thermofluid model of loop heat pipes (LHPs) operating under steady-state conditions is presented. The model is formulated for the simulation of a simple LHP, with one cylindrical evaporator, a vapor-transport line, a single condenser, a liquid-transport line, and a compensation chamber, as shown schematically in Figure 2.1. The working fluid considered here is ammonia, but the proposed model can be adapted to any suitable working fluid by simply changing the inputs of thermofluid property data.

The objective of the work described in this chapter is to formulate a basic network thermofluid models of LHPs, based on relatively rudimentary treatments of the fluid flow and heat transfer phenomena in the vapor- and liquid-transport lines, and also in the two-phase and single-phase regions of the condenser, but still capable of at least qualitatively accurate predictions. Such a model would be useful not only in illustrating the main steps in the formulation of network thermofluid models of LHPs, but also a tool for preliminary designs of LHPs akin to that shown in Figure 2.1. In order to check this desired capability of the proposed model, it was applied to an LHP similar to one investigated experimentally by Kaya and Hoang (1999). The details of this exercise, the predicted results, and their comparison with the experimental results of Kaya and Hoang (1999) are presented in this chapter.

An extended version of this basic network thermofluid model is presented in Chapter 5. The extend model is suitable for simulations of LHPs with a flat evaporator and fixed active mass of working fluid, similar to the one designed, constructed, and used in the experimental phase of this research (details are provided in Chapter 4). The proposed extended model also incorporates more sophisticated and/or complete treatments of the fluid flow and heat transfer processes in the vapor- and liquid-transport lines and in the condenser than those used in the basic model described in this chapter.

2.1 THERMODYNAMICS

Figure 2.1 sets the stage for a discussion of the different thermodynamics processes that the working fluid undergoes during the steady-state cyclical operation of the LHPs for which the proposed basic network thermofluid model is formulated. The thermodynamic states of the working fluid at each of the points shown in Figure 2.1 are presented in a pressure-temperature (P-T) diagram given in Figure 2.2. Ku (1994) has presented a similar study for a capillary pumped loop (CPL). In the following presentation, the effects of gravity on the thermofluid processes inside the LHP shown in Figure 2.1 are totally neglected, mainly for convenience in the presentation, and it is assumed the evaporator and condenser sections are at the same elevation.

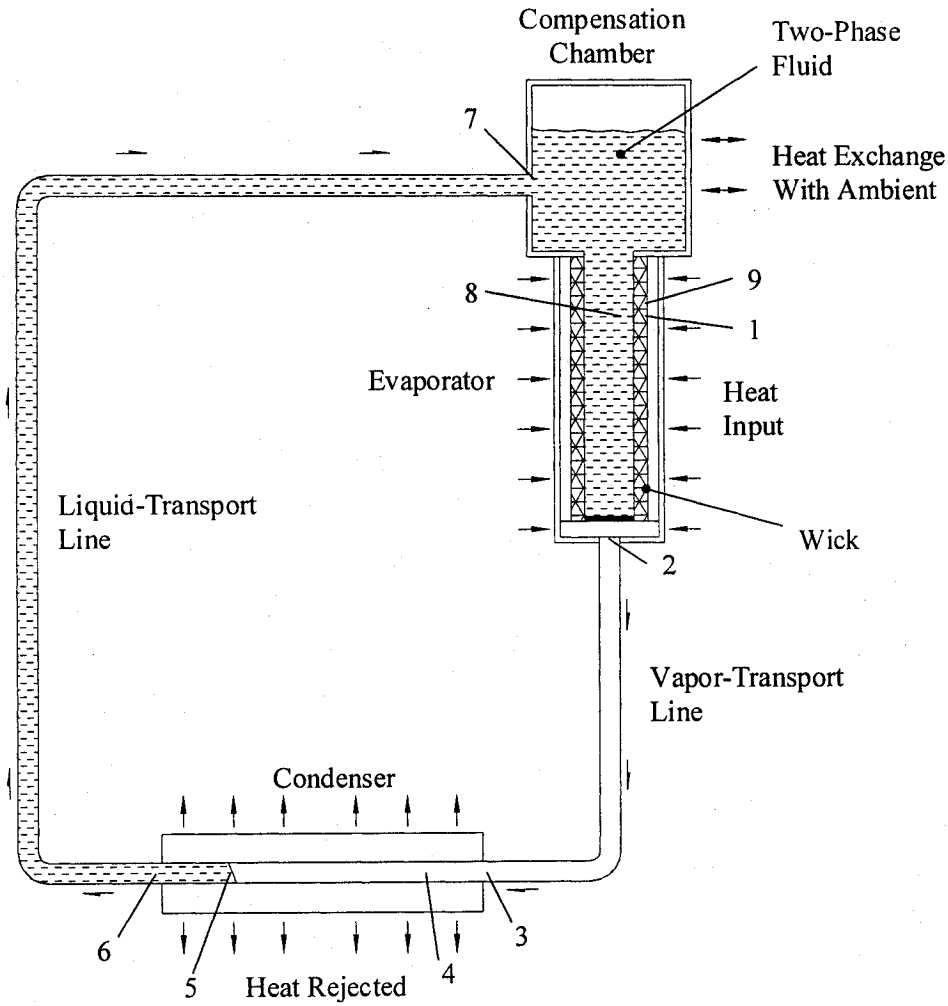

Figure 2.1: Schematic representation of the loop heat pipe considered in the formulation of the basic network thermofluid model.

At point 1 in the evaporator grooves, the fluid is vaporized at the saturation temperature T_1 and the corresponding pressure P_1. This point has the highest thermodynamic (static) pressure in the loop. The vapor then flows through the grooves (channels) and reaches the vapor accumulation area at the end of the evaporator, point 2. A uniform heat flux is added to the entire length of the evaporator, a part of which heats the vapor during its passage between point 1 to the exit of the channels. As shown in Figure 2.2, the vapor undergoes a heating process, accompanied by a pressure drop, during its passage through the channels. Therefore, the saturated vapor at point 1 arrives at point 2 in a slightly superheated state.

The process 2-3 is assumed to be an adiabatic expansion process, as the vapor-transport line is well insulated. In this process, due to shear stress at the inner surface of the pipe wall, the pressure drops, so the vapor expands. The work done by this shear stress on the vapor is converted to heat and this causes its temperature to rise. However, the temperature drop due to vapor expansion and the temperature rise due to friction work counteract each other, and the 2-3 is as an essentially constant-temperature process. Thus, the vapor condition at point 3 could still be slightly superheated.

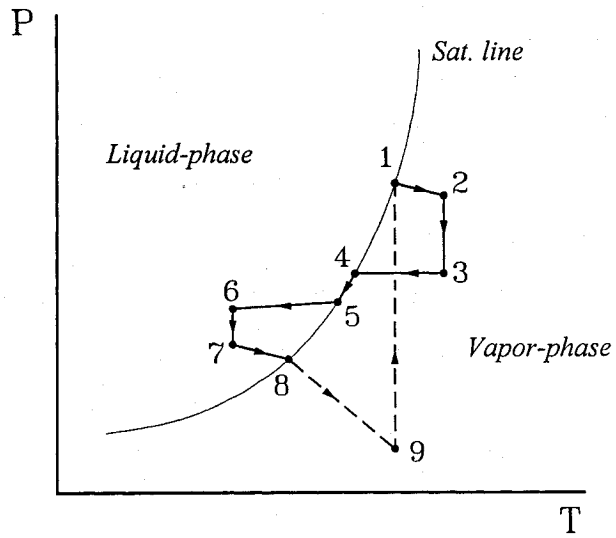

Figure 2.2: Pressure-temperature (P-T) diagram (not to scale) for the LHP considered in the formulation of the basic network thermofluid model.

Under steady-state conditions, the rate at which heat is absorbed by the fluid in the evaporator and compensation chamber ensemble is equal to the rate of heat rejection to a

thermal sink in the condenser. The superheated vapor entering the condenser unit cools to the saturation condition, point 4, usually in a small entrance length of the condenser. In this basic model, 3-4 is considered as a constant-pressure cooling of the vapor from T_3 to T_4, the saturation temperature, at the corresponding saturation pressure P_4 ($P_4 \approx P_3$).

Between points 4 and 5, the saturated vapor (with 100% quality) condenses to saturated liquid (0% quality) and a pressure drop along the condenser pipe accompanies the process. This process is demonstrated on the saturation line in Figure 2.2. If the condenser length is long enough, the saturated liquid exits the condenser at point 6 in a sub-cooled condition. Therefore, the 5-6 is a cooling process with a pressure drop.

The liquid-transport line is very well insulated. Therefore, the process 6-7 is an adiabatic process, with a pressure drop. The viscous dissipation in this process is considered negligible; thus, it is presented on the P-T diagram as an isothermal process. The subcooled liquid then enters the compensation chamber at point 7. Generally, the compensation chamber would be filled with two phases, liquid and vapor, so it accommodates any thermal expansion (or contraction) of the fluid in the rest of the loop. The subcooled liquid enters the compensation chamber and mixes with the warmer two-phase (saturated) fluid. The two-phase fluid is thus slightly cooled, and there is heat transfer from the ambient environment to the compensation chamber. Furthermore, a part of the heat input to the evaporator heats up the fluid in the compensation chamber by means of conduction through the wick material. This heat transfer through the wick is referred to as heat leak [Kaya and Hoang (1999)]. The liquid condition at point 8 is therefore determined by an energy balance on the compensation chamber, considering both heat transfer from the ambient and heat-leak from the evaporator. The process 7-8 is a heating process accompanied by a pressure drop, as presented in the P-T diagram.

At point 8, the saturated liquid enters the wick and then moves up to the liquid-vapor interface. During this passage, the temperature of the saturated liquid rises, due to heat leak from the evaporator, and its pressure drops. At the liquid-vapor interface (point 9), the temperature of the liquid is equal to that of the saturated vapor (point 1). Therefore, the liquid is in a superheated state, because the saturation pressure at point 1 is higher than that of the liquid at point 9 (because of the pressure jump across the interface). That is why the process 9-1 is plotted as a dashed line in the vapor zone of the P-T diagram

(see Figure 2). Due to heat input at the interface, the superheated liquid evaporates in a constant temperature process from point 9 to 1 and its pressure jumps up due to the capillary head developed at the interface. It should be noted that point 9 has the lowest pressure in the loop, and the assumption of local thermodynamic equilibrium at the interface gives $T_9 = T_1$.

It should also be noted that in many practical applications, the changes in temperature and pressure of the working fluid in the entire loop are relatively very small compared to their mean values: For example, as presented by Ku (1994), in an ammonia-CPL with a nominal operating temperature of 25°C and pressure of 1003.08 kPa, the temperature difference due to a pressure drop of 2000 Pa is just 0.07°C. These temperature and pressure changes have been exaggerated (not drawn to scale) in Figure 2.2 in order to aid the presentation.

2.2 NETWORK MODEL

As was discussed earlier, the LHP considered in this paper is composed of the following elements: evaporator, vapor-transport line, condenser, liquid-transport line, and the compensation chamber (see the schematic in Figure 2.1). Mathematical models of the fluid flow and heat transfer in each of these elements, and, collectively, in the whole loop, are presented in this section. Gravitational effects are ignored in these models. Furthermore, in the energy balance equations for the various elements of the LHP, the rates of viscous dissipation and changes in the kinetic energy of the fluid are assumed to be negligible in comparison with the other rates of energy transport.

2.2.1 Evaporator

The cylindrical evaporator is constructed of an internally grooved pipe of circular cross section, with an annular wick installed on its inner surface, as illustrated schematically in Figure 2.3. The wick is made of a sintered powder metal. Under steady-state conditions, the rate of power input applied to the evaporator, q_{app}, can be divided into three portions as follows:

$$q_{app} = q_{vsh} + q_{fg} + q_{hl} \tag{2.1}$$

where q_{vsh} is the rate of heat transfer to the saturated vapor during its passage through the grooved channels, q_{fg} is the rate of heat transfer required for evaporation of the saturated liquid in the wick, and q_{hl} is the rate of heat leak through the wick, from its vapor side to its liquid side.

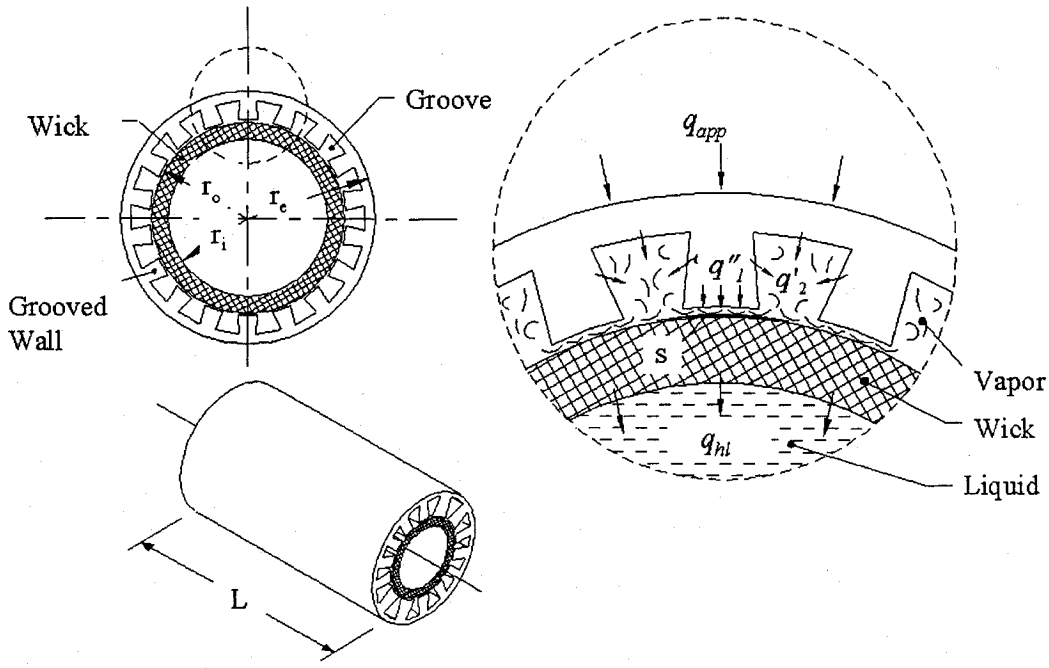

Figure 2.3: Details of the cylindrical evaporator of the LHP.

Liquid-vapor interface inside the wick: Under steady-state conditions, it is assumed that the liquid-vapor interface is located at the outer surface of the wick, and it is stationary there. Of the total input heat flux to the evaporator, a portion q''_1 is transferred by conduction through the grooved metal wall of the pipe to the outer surface of the wick (see Figure 2.3). This heat flux (q''_1) is assumed to be constant, and imposed at the liquid-vapor interface, as shown in Figure 2.4. It is also assumed that the pores of the wick are uniformly distributed at the outer surface of the wick. In addition, the porosity, ε, and permeability, K, of the porous sintered powder-metal wick are assumed to be essentially uniform.

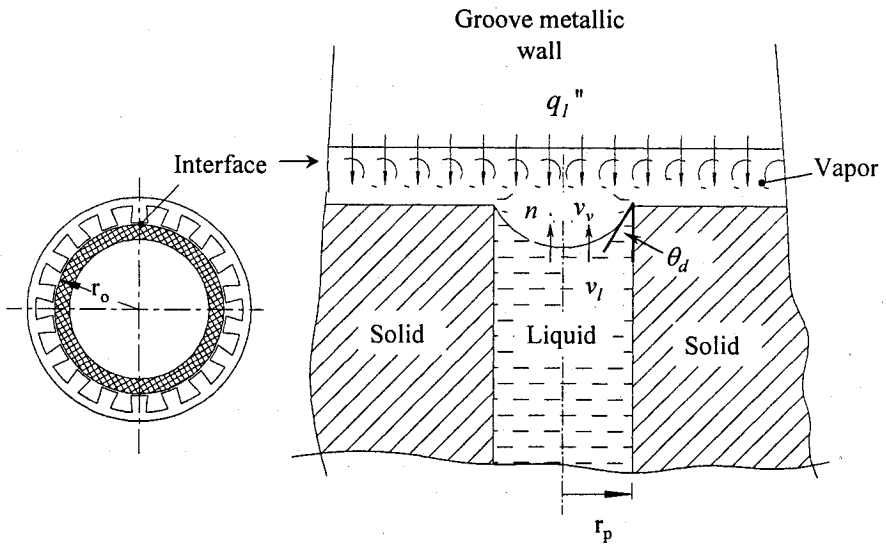

Figure 2.4: Schematic representation of the liquid-vapor interface in one equivalent, or effective, pore at the outer surface of the wick structure.

The conservation of mass at the interface, located at the outer surface of the wick, $r = r_o$, for one pore (see Figure 2.4), implies that the mass flux across the interface is given:

$$\dot{m}_p'' = \rho_v v_v = \rho_l v_l = \dot{m}_{tot} / (\varepsilon 2\pi r_o L) \tag{2.2}$$

where v_v and v_l denote the vapor and liquid absolute velocities, in the direction of $\vec{n}$, averaged across the interface, as shown in Figure 2.4. Thus,

$$v_v = \frac{\dot{m}_{tot}}{\varepsilon 2\pi r_o L \rho_v} \; ; \; v_l = \frac{\dot{m}_{tot}}{\varepsilon 2\pi r_o L \rho_l} \tag{2.3}$$

A simplified momentum conservation statement normal to the curved interface is the following:

$$\dot{m}_p''(v_v - v_l) + (P_v - P_l) = 2\sigma \cos(\theta_d) / r_p \tag{2.4}$$

where σ is the surface tension at the vapor-liquid interface, r_p is the pore radius, and θ_d is the dynamic contact angle of the liquid-vapor interface. In the development of Eq. (2.4), the effect of the net normal viscous stresses acting on the interface has been considered negligible. Using Eqs. (2.2) and (2.3), Eq. (2.4) can be rewritten as follows:

$$(P_v - P_l) = \frac{2\sigma \cos\theta_d}{r_p} - \left(\frac{\dot{m}_{tot}}{\varepsilon 2\pi r_o L}\right)^2 \left(\frac{1}{\rho_v} - \frac{1}{\rho_l}\right) \tag{2.5}$$

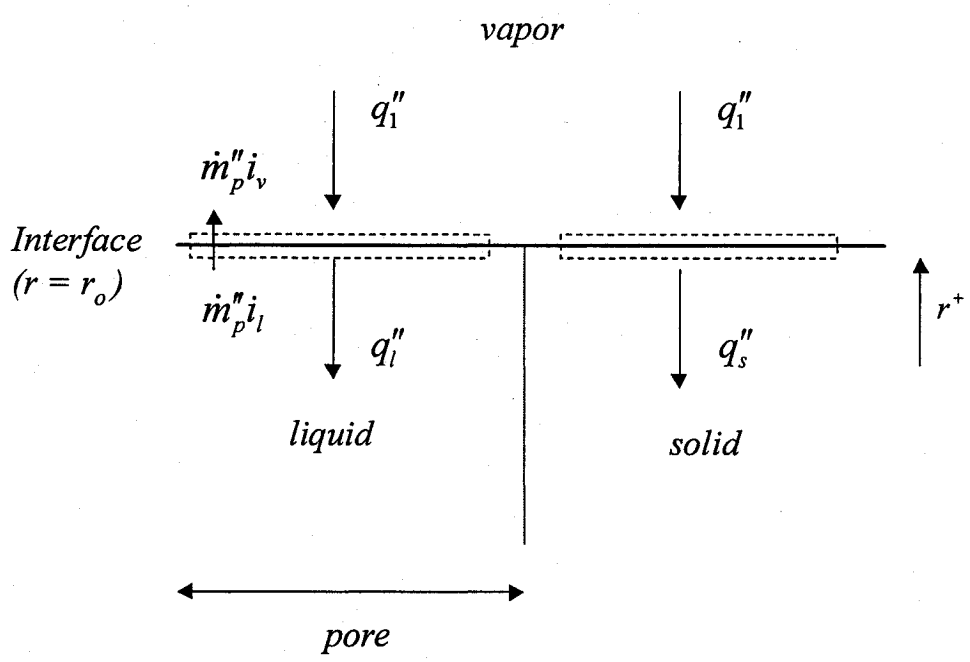

Figure 2.5: Schematic representations of the energy balances at the liquid-solid interface and solid portion of the wick outer surface ($r = r_o$).

With reference to Figure 2.5, a simplified energy balance at the liquid-vapor interface gives:

$$\dot{m}_p''(i_v - i_l) = q_1'' - q_l'' \tag{2.6}$$

where $(i_v - i_l) = i_{fg}$ is the enthalpy of evaporation of the working fluid, and

$$q_1'' = q_s'' = k_s \left.\frac{dT_s}{dr}\right|_{r=r_o} \quad ; \quad q_l'' = k_l \left.\frac{dT_l}{dr}\right|_{r=r_o} \tag{2.7}$$

Combining Eqs. (2.2), (2.6), and (2.7), the energy balance equation at the liquid-vapor interface can be cast in the following form:

$$\dot{m}_{tot} i_{fg} + 2\pi r_o L \left[(1-\varepsilon) k_s \left.\frac{dT_s}{dr}\right|_{r=r_o} + \varepsilon k_l \left.\frac{dT_l}{dr}\right|_{r=r_o} \right] = 2\pi r_o L \; q_1'' \tag{2.8}$$

At this stage, local thermal equilibrium [Whitaker (1999)] is assumed to prevail at the liquid-vapor interface: Thus, $T_s = T_l = T = T_{sat}$. In addition, an effective thermal conductivity of the wick is defined as follows:

$$k_e = [\varepsilon k_l + (1-\varepsilon) k_s)] \tag{2.9}$$

The topic of effective thermal conductivity of liquid-saturated sintered powder-metal wick is discussed in detail in Chapter 3, along with more sophisticated models for k_e. Here, Eq. (2.9), which is commonly known as the parallel model, is considered adequate for illustrating the main steps in the formulation of the basic network thermofluid model. With these assumptions, the energy balance at the liquid-vapor interface, Eq. (2.8), can be expressed as follows:

$$\dot{m}_{tot} i_{fg} + 2\pi r_o L k_e \left.\frac{dT}{dr}\right|_{r=r_o} = 2\pi r_o L \; q_1" \tag{2.10}$$

On the left-hand side of Eq. (2.10), the first term represents the total rate of heat input required for evaporation of the working fluid, q_{fg}, and the second term is the rate of heat leak, q_{hl}. Thus,

$$q_{fg} + q_{hl} = 2\pi r_o L q_1" \tag{2.11}$$

Pressure drop and heat leak across the wick: It is assumed that the Darcy law [Kaviany (1999); Nield and Bejan (2006)] applies to the flow of the working fluid through the wick. Furthermore, preliminary computations revealed that the heat transfer inside the wick could be modeled as pure conduction, with the porous medium being assigned the effective thermal conductivity given in Eq. (2.9). With these assumptions, and with reference to the notation in Figure 2.6, it can be shown that the total pressure *drop* in the liquid and the rate of heat leak across the wick are given by the following expressions:

$$\begin{aligned} \Delta P_{wick} &= \frac{\dot{m}_{tot}\mu_l}{2\pi L \rho_l K} \ln\left(\frac{r_o}{r_i}\right) \\ q_{hl} &= 2\pi L k_e \frac{\left(T_{sat} - T_{w,ent}\right)}{\ln\left(r_o / r_i\right)} \end{aligned} \tag{2.12}$$

Again, it is noted that the expression presented for the effective thermal conductivity in Eq. (2.9) corresponds to what is commonly known as the parallel model. Generally, this model overestimates the effective thermal conductivity of fluid-saturated sintered powder-metal wicks (it provides the upper limit of this property). In Chapter 3 of this thesis, several existing models, including the parallel model, are presented and discussed.

In general, for liquid-saturated sintered powder-metal or fiber-metal wicks used in LHPs, the effective thermal conductivity should be determined experimentally or with more sophisticated (and appropriate) correlations (additional details are presented Chapter 3).

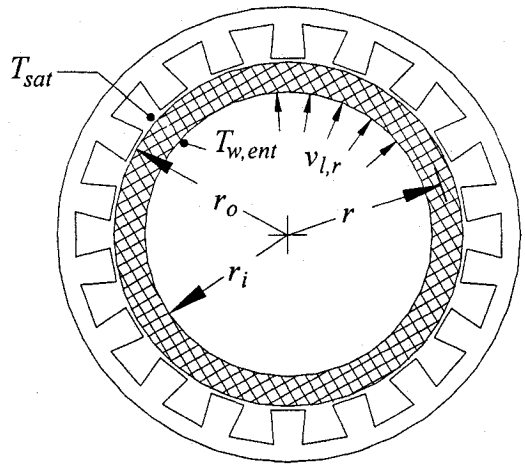

Figure 2.6: Cross section of the wick and related notation.

Grooved channels: It is assumed here (again, just to illustrate the formulation of the basic network thermofluid model) that the pipe of the evaporator has N channels, or grooves, of trapezoidal cross section, as shown in Figure 2.6. Figure 2.7 (top) represents schematically the vapor flow in each groove. The vapor flow in the groove could be laminar or turbulent. The vapor mass flow rate increases from zero at the start of the channel (closed end) to its maximum value at the open end. It is assumed that the rates of vapor flow and heat transfer in each of the N channels are the same.

The vapor mass flux exiting the outer wick surface, $\dot{m}''$, is assumed to be uniform along the channel length: $\dot{m}'' = \varepsilon \dot{m}''_p$. The wick outer perimeter is divided by the number of grooves, N, to obtain the arc length, $S = 2\pi r_o / N$, of the wick cross section associated with each groove, as shown in Figure 2.3. The axial mass flow rate of the vapor through each channel is denoted by $\dot{m}_z$. Then, mass continuity requirements yield the following expressions:

$$\dot{m}_{tot} = \dot{m}'' SNL \; ; \; \dot{m}_z = \dot{m}'' Sz = (\dot{m}_{tot} / N)(z / L)$$
$$u = (\dot{m}_{tot} / N)(z / L) / (\rho_v A_G) \qquad (2.13)$$

where u is the average axial velocity of the vapor inside the groove at any z, and A_G is the cross-sectional area of the groove.

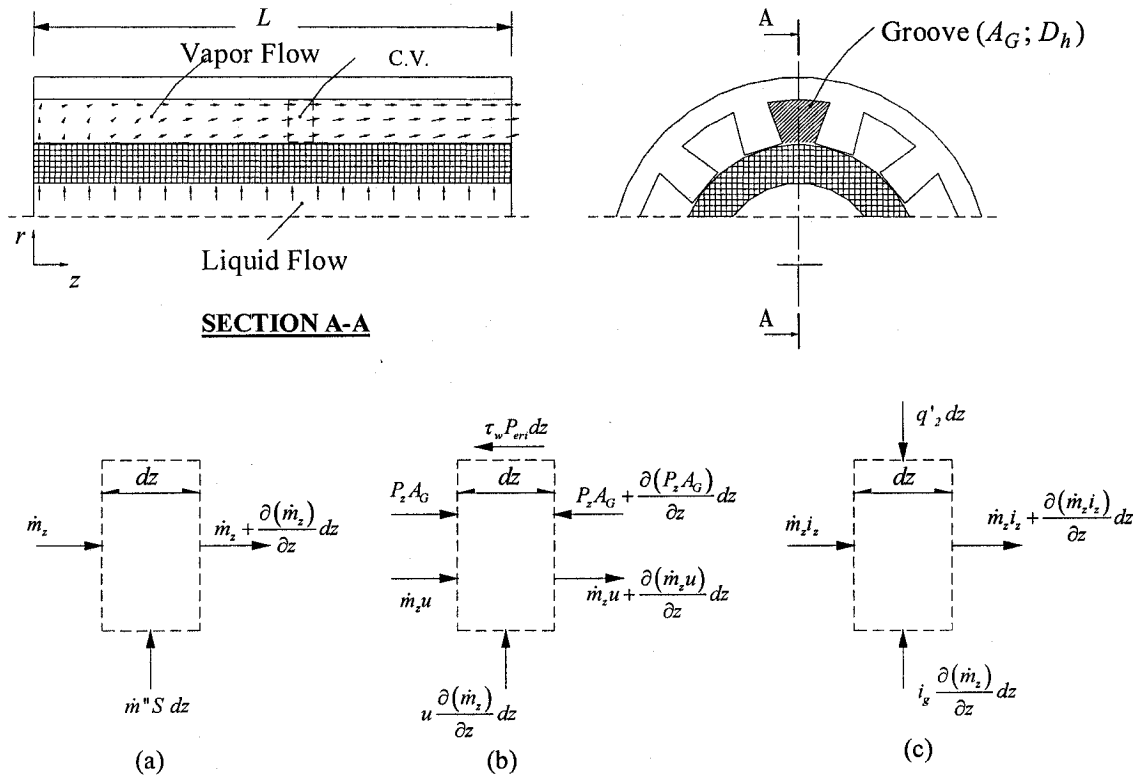

Figure 2.7: Schematic illustrations of the vapor flow through the grooved channel (top): (a) mass balance, (b) axial force and momentum balance, and (c) energy balance, all on a control volume spanning a slice of the channel.

The hydraulic diameter of the groove, D_h, the average Darcy friction factor, f, and the Reynolds number, Re_L, at the end of the channel ($z = L$) are defined as follows:

$$D_h = \frac{4A_G}{Peri_G} \; ; \; f = \frac{4\bar{\tau}_w}{0.5\rho_v u^2} \; ; \; \mathrm{Re}_L = \frac{\dot{m}_{tot} D_h}{NA_G \mu_v} \tag{2.14}$$

In this analysis, it is assumed that the product $f\,\mathrm{Re}_L$ is a constant and corresponds to its fully developed value. For $Re_{vl} \leq 2300$, the flow is considered laminar, and for fully-developed flow $f\,Re_{vl}$ is set equal to 64.0. For Re_{vl} >2300, the flow is considered turbulent, and the Colebrook and White correlation [Colebrook (1939); White (1991)] is used to estimate the friction factor (using an iterative procedure). Thus,

$$f = 64/\mathrm{Re}_L \quad \text{when} \quad \mathrm{Re}_L \le 2300$$
$$1/\sqrt{f} = -2.0\log_{10}\left[\left(e/D_h\right)/3.7 + \left(2.51/\left(\mathrm{Re}_L\sqrt{f}\right)\right)\right] \quad \text{when} \quad \mathrm{Re}_L > 2300 \tag{2.15}$$

With these assumptions, the static pressure *drop* in the grooved channel is given by the following equation:

$$\Delta P_{channel} = \frac{1}{\rho_v A_G^2}\left(\frac{\dot{m}_{tot}}{N}\right)^2 + \frac{f\,\mathrm{Re}_L}{6} L \frac{\mu_v \dot{m}_{tot}}{D_h^2 \rho_v A_G N} \tag{2.16}$$

The vapor flow Mach number is defined as:

$$M_{channel} = \{\dot{m}_{tot}/(N\rho_v A_G)\}/\sqrt{\gamma_v R_v T_{v,abs}} \tag{2.17}$$

where γ_v and R_v are the vapor specific heat ratio, $(c_p/c_v)_v$, and the specific gas constant, respectively. For $M_{channel} > 0.2$, the effect of compressibility on friction factor is taken into account, following the recommendations of Chi (1976), as follows:

$$\frac{f_c}{f} = \left(1 + \frac{\gamma_v - 1}{2} M_{channel}^2\right)^{-1/2} \quad \{Laminar\}$$
$$\frac{f_c}{f} = \left(1 + \frac{\gamma_v - 1}{2} M_{channel}^2\right)^{-3/4} \quad \{Turbulent\} \tag{2.18}$$

The rate of heat input per unit length from the channel walls to the vapor, q_2', is assumed to be uniform over the length of the channel, and the specific enthalpy of the vapor is assumed to be only a function of temperature ($di = c_{p,v}dT$). Thus, the temperature of the vapor in the channel is essentially invariant, and can be expressed as follows:

$$T = T_{sat} + (q_2' NL)/(c_{p,v}\dot{m}_{tot})$$
$$or \tag{2.19}$$
$$T = T_{sat} + q_{vsh}/(c_{p,v}\dot{m}_{tot})$$

2.2.2 Vapor-Transport Line

The vapor that accumulates at the end of the evaporator enters the vapor-transport line (see Figure 2.1). In this model, the vapor-transport line is assumed to be made of a smooth pipe and has no bends (or the effects of any bends in this line are negligible). It is also assumed that entrance effects are negligible and fully-developed vapor flow prevails

throughout this line. The Darcy friction factor and the Reynolds number are defined as follows:

$$f_{vl} = 4\tau_{w,vl} / (0.5\rho_{vl}\bar{u}_{vl}^2) \quad ; \quad \mathrm{Re}_{vl} = \rho_{vl}\bar{u}_{vl}D_{vl} / \mu_{vl} \tag{2.20}$$

where D_{vl} is the inside diameter of the vapor-transport line. The total static pressure *drop* in the vapor-transport line is then given by the following equation [White (1991)]:

$$\Delta P_{vl} = \frac{(f_{vl}\,\mathrm{Re}_{vl})}{2}\frac{\mu_{vl}L_{vl}\dot{m}_{tot}}{\rho_{vl}A_{vl}D_{vl}^2} \tag{2.21}$$

The values of f_{vl} are obtained using Eq. (2.15), with Re_{vl} replacing Re_L.

In the evaporator, if q_{vsh} is negligible in comparison to the other rates of heat transfer, then the vapor enters the vapor-transport line in a saturated condition, rather than a superheated state. The saturation temperature is a direct function of the saturation pressure. Here, the vapor temperature drops along with the pressure in the transport line. Following Ku (1994), the Clapeyron equation is used to estimate the slope of the saturation pressure-temperature curve, and the temperature drop is calculated using this slope. This rudimentary approach was considered to be adequate in this basic transport model. The Clapeyron equation is the following:

$$(dP/dT)_{sat} = \left(i_{fg} / \{T[\frac{1}{\rho_v} - \frac{1}{\rho_l}]\}_{sat} \right) \tag{2.22}$$

2.2.3 Condenser

The net rate of heat input to the ensemble of the evaporator and compensation chamber is rejected to a thermal sink in the condenser. The vapor reaches the condenser in a saturated state, an approximation that was discussed in the last subsection. The temperature of the saturated vapor at the inlet plane of the condenser is $T_{sat,cd}$, which, due to the pressure drop in the vapor-transport line, is a bit lower than T_{sat} ($T_{sat,cd} < T_{sat}$). It is assumed here that the condenser is built from a horizontal pipe covered with a metallic sleeve of high thermal conductivity. The outer surface of this sleeve is maintained at a constant temperature, T_{sink}. The condenser is shown schematically in Figure 2.8.

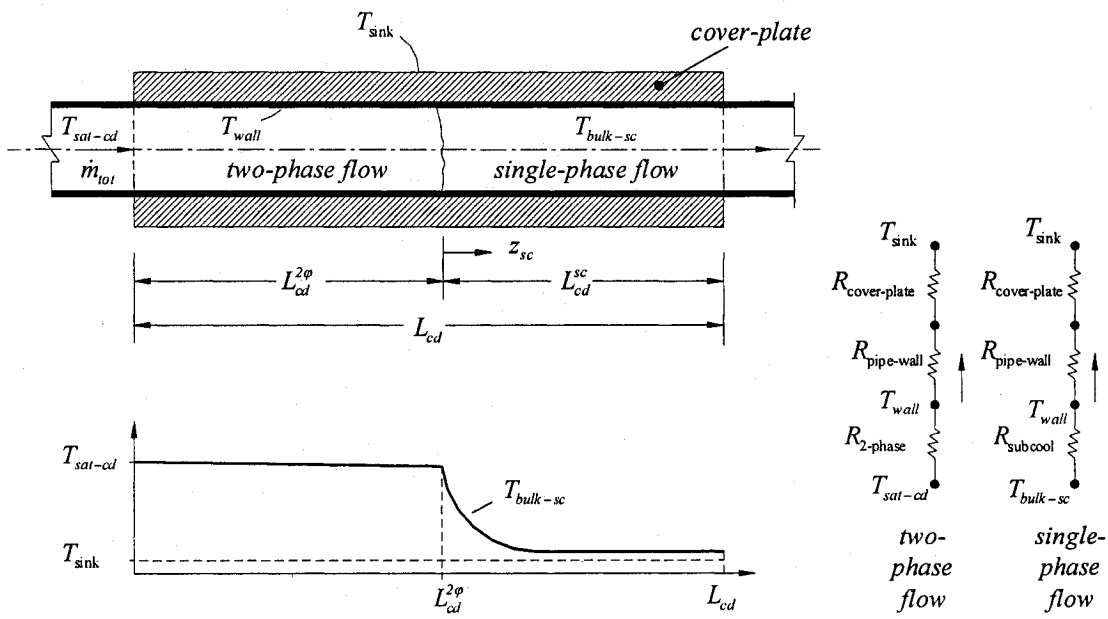

Figure 2.8: Schematic representation of vapor flow through the condenser.

The possible states of the fluid at the exit of the condenser can be categorized as saturated-liquid, subcooled liquid, and two-phase mixture. Figure 2.8 shows a case where the fluid exits the condenser in a subcooled state, and the location where $x = 0$ (full condensation of the vapor) is within the condenser pipe ($L_{cd}^{2\varphi} < L_{cd}$): The saturated vapor entering at temperature T_{sat-cd} is condensed over the length $L_{cd}^{2\varphi}$, and its saturation temperature drops slightly over this length due to the pressure drop. Over the remaining portion of the condenser length, L_{cd}^{sc}, the condensed liquid is cooled further, and it exits in a subcooled condition. Assuming that an average heat transfer coefficient in the subcooled region stays essentially constant, this process is shown in Figure 2.8 as an exponential decay of the fluid temperature.

Two-phase part: In the two-phase region, the rate of heat rejection to the sink is equal to the product of the rate of condensation of the fluid and its latent heat. Furthermore, under steady operating conditions, when the vapor condenses completely within the condenser (as shown in Figure 2.8) $\dot{m}_{cond} = \dot{m}_{tot}$. Thus:

$$q_{fgc} = \dot{m}_{tot} i_{fg,c} = h_m^{2\varphi} \pi D_{cd} L_{cd}^{2\varphi} \left(T_{sat-cd} - T_{wall}\right) \tag{2.23}$$

where q_{fgc} is the rate of heat rejection that is needed from the inlet saturated-vapor to the thermal sink for complete condensation. The latent heat of evaporation of the working fluid at the temperature T_{sat-cd} is $i_{fg,c}$. The average heat transfer coefficient in this region of the condenser is denoted by $h_m^{2\varphi}$. D_{cd} is the condenser pipe internal diameter. $L_{cd}^{2\varphi}$ is the length of the two-phase region measured from the entrance of the condenser, and T_{wall} is the pipe wall inner-surface temperature, which is considered constant in the two-phase region. In Eq. (2.23), $h_m^{2\varphi}$, T_{wall}, and $L_{cd}^{2\varphi}$ are not known *a priori*.

As was noted by Rohsenow (1985), at low condensation rates, the vapor velocities are low, permitting the liquid condensate inside the horizontal pipe to run off in a stratified condition. In this case, the condensate formed in the upper portion of the tube flows around the periphery to the bottom layer, which flows off in a kind of open-channel flow. Chato (1962) has presented the following correlation for calculating the average heat transfer-coefficient, $h_m^{2\varphi}$, for this type of condensing flow:

$$h_m^{2\varphi} = 0.728\,\Im\left[\frac{g\rho_l(\rho_l-\rho_v)k_l^3 i_{fg,c}^{'}}{\mu_l(T_{sat-cd}-T_{\text{wall}})D_{cd}}\right]^{\frac{1}{4}} \tag{2.24}$$

where $\Im = 0.76$ and

$$i_{fg,c}^{'} = i_{fg,c} + \frac{3}{8}c_{p,l}(T_{sat-cd}-T_{\text{wall}}) \tag{2.25}$$

Eq. (2.24) is valid when the Reynolds number associated with the inlet vapor flow, $\text{Re}_v = \frac{\rho_v D_{cd} V}{\mu_v} = \frac{\dot{m}_{tot} D_{cd}}{\mu_v A_{cd-pipe}}$, is lower than 35,000. In the current study, it is assumed that the Reynolds number is always less than this critical value. It should be noted that for higher values of Re_v, the condensate liquid flow becomes annular, with a vapor core; at even higher values of Re_v, the vapor core may contain a mist of liquid droplets [Rohsenow (1985)]. For these situations, Rohsenow (1985) presents a set of correlations for the calculation of the local heat transfer coefficient and the pressure-drop, based on the work of Traviss et al. (1973). For high mass flow rates, these correlations should be incorporated in the model, a task that is left for future works. Additional discussions of these and related issues are given in Chapter 5.

Eqs. (2.23) - (2.25) contain the term T_{wall}, which is not known *a priori*. Using the resistance analogy presented for the two-phase region in Figure 2.8, the following relation are used to relate T_{wall} to T_{sink} :

$$\frac{T_{sat-cd}-T_{\text{wall}}}{R_{2\text{-}phase}}=\frac{T_{sat-cd}-T_{\text{sink}}}{R_{2\text{-}phase}+R_{pipe-wall}+R_{\text{cover}-plate}} \tag{2.26}$$

Here, $R_{2\text{-}phase}$ is the thermal resistance between the saturated vapor and the inner pipe surface, and is given by $R_{2\text{-}phase}=1/\{h_m^{2\varphi}(\pi D_{cd}L_{cd}^{2\varphi})\}$. $R_{pipe-wall}$ and $R_{\text{cover}-plate}$ are, respectively, the pipe wall and the cover plate (sleeve) thermal resistances. These thermal resistances are calculated using the relations $R_{pipe-wall}=\ln\left(D_{po}/D_{cd}\right)/\left(2\pi L_{cd}^{2\varphi}k_{c,pipe}\right)$ and $R_{\text{cover}-plate}=\ln\left(D_{so}/D_{po}\right)/\left(2\pi L_{cd}^{2\varphi}k_{c,sleeve}\right)$; here, $k_{c,pipe}$ and $k_{c,sleeve}$ are, respectively, the condenser pipe wall and sleeve-material (cover-plate) thermal conductivities; and D_{so} and D_{po} are the outside and inside diameters of the cover plate (sleeve), respectively. A thermal conductance that is based on the inner diameter of the pipe and includes both pipe-wall and cover-plate thermal resistances is given by the following equation:

$$U_{p\text{-s}}(\pi D_{cd}L_{cd}^{2\varphi})=1/\left(R_{pipe-wall}+R_{cover-plate}\right) \tag{2.27}$$

where $U_{p\text{-s}}$ depends on the geometry of the condenser and is considered to be known for the particular problem. An overall heat transfer coefficient based on the inner diameter of the pipe is now defined as follows:

$$U_{tot}^{2\varphi}(\pi D_{cd}L_{cd}^{2\varphi})=1/\left(R_{2\text{-}phase}+R_{pipe-wall}+R_{cover-plate}\right)$$

or (2.28)

$$U_{tot}^{2\varphi}=1/\left(\frac{1}{h_m^{2\varphi}}+\frac{1}{U_{p\text{-s}}}\right)$$

Substituting Eq. (2.28) into Eq. (2.26) and rearranging the terms, the following equation is obtained:

$$T_{sat-cd}-T_{\text{wall}}=U_{tot}^{2\varphi}\left(T_{sat,cd}-T_{\text{sink}}\right)/h_m^{2\varphi} \tag{2.29}$$

For given values of T_{sat-cd}, $\dot{m}_{tot}$, and T_{sink}, the three unknown values, $h_m^{2\varphi}$, T_{wall} and $L_{cd}^{2\varphi}$, can be determined using an iterative method to solve Eqs. (2.23) to (2.25), (2.28),

and (2.29). It should be noted that all fluid properties are determined at the saturation temperature inside the condenser, T_{sat-cd}.

Eq. (2.23) can also be written as:

$$\dot{m}_{tot} i_{fg,c} = U_{tot}^{2\varphi} \pi D_{cd} L_{cd}^{2\varphi} (T_{sat-cd} - T_{sink}) \tag{2.30}$$

Once $L_{cd}^{2\varphi}$ is determined, it is compared to the total condenser pipe length, L_{cd}. As mentioned previously, three possible cases could exist:

a) $L_{cd}^{2\varphi} = L_{cd}$

In this case, the fluid exits the condenser in the saturated liquid state. The saturation temperature is essentially T_{sat-cd}. The vapor quality at the exit is $x_{vqual,cdexit} = 0$, and the total rate of heat rejected in condenser section is:

$$q_{cd-reject} = q_{fgc} = \dot{m}_{tot} i_{fg,c} = U_{tot}^{2\varphi} \pi D_{cd} L_{cd}^{2\varphi} \left(T_{sat-cd} - T_{\text{sink}}\right) \tag{2.31}$$

b) $L_{cd}^{2\varphi} > L_{cd}$

This situation occurs when the capability for the rate of heat rejection in the condenser is not enough to condense the vapor completely. Therefore, the fluid at the exit would be in a two-phase condition at the saturation temperature T_{sat-cd}. The quality of the fluid at the exit would be $0 < x_{vqual,cdexit} < 1$. The total rate of heat rejected in the condenser section is:

$$q_{cd-reject} = \dot{m}_{tot} \left(i_v - i_{exit,c}\right) = U_{tot}^{2\varphi} \pi D_{cd} L_{cd}^{2\varphi} \left(T_{sat-cd} - T_{\text{sink}}\right) \tag{2.32}$$

Here, $q_{cd-reject} < q_{fgc}$, $i_{exit,c}$ is the fluid enthalpy at the exit of the condenser, and i_v is the enthalpy of saturated vapor measured at T_{sat-cd}. Both $i_{exit,c}$ and $q_{cd-reject}$ can be determined from Eq. (2.32). Once $i_{exit,c}$ is calculated, the vapor quality at the exit can be determined from:

$$i_{exit,c} = i_v x_{vqual,cdexit} + (1 - x_{vqual,cdexit}) i_l \tag{2.33}$$

where h_l is the enthalpy of the saturated liquid measured at T_{sat-cd}.

c) $L_{cd}^{2\varphi} < L_{cd}$

This situation could occur for low rates of heat transfer across the loop. The ability of the condenser to reject heat is more than that required for complete condensation of inlet saturated vapor, and the x = 0 position is located within the condenser pipe. The heat

rejection to the sink is continued over the rest of the condenser pipe, and the fluid exits in a subcooled condition. The total rate of heat rejection is calculated as follows:

$$q_{cd-reject} = q_{fgc} + q_{sc} \tag{2.34}$$

where q_{sc}, the rate of heat rejection from the condensed liquid which brings it to the subcooled state at the exit of the condenser, is given by the following equation:

$$q_{sc} = \dot{m} c_{p,l} \left(T_{sat-cd} - T_{exit,c} \right) \tag{2.35}$$

To obtain q_{sc}, $T_{exit,c}$ should be known first. The method for the determination of $T_{exit,c}$ is presented in the next subsection.

In this work, the pressure drop in the two-phase part of the condenser is considered negligible, compared to the absolute value of the average pressure of the fluid in the condenser. In Chapter 5 of this thesis, a procedure is presented for the estimation of the two-phase pressure drop in the condenser section of LHPs.

Single-phase part: In the subcooled region, neglecting viscous dissipation and axial diffusion terms, the energy balance on an infinitesimally thin control volume is presented schematically in Figure 2.9.

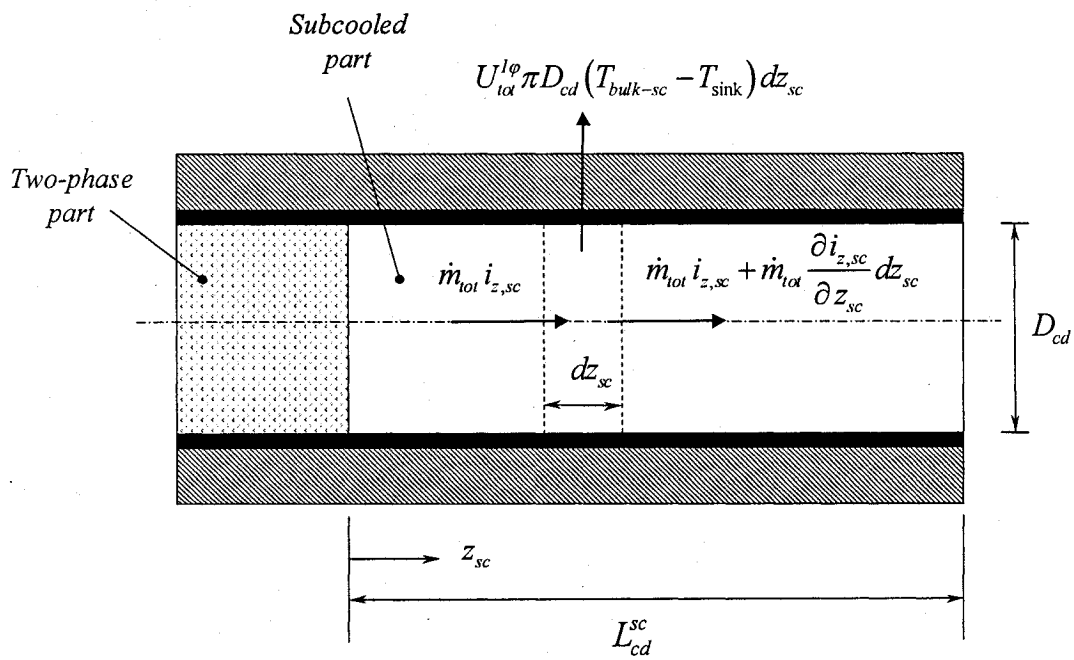

Figure 2.9: Schematic representation of energy balance on a slice of the subcooled portion of the condenser.

Assuming that the specific enthalpy of the subcooled liquid is just a function of temperature ($di_{z,sc} = c_{p,l} dT_{bulk-sc}$), the energy equation in the subcooled region can be written as follows:

$$\frac{d\left(T_{bulk-sc} - T_{\text{sink}}\right)}{\left(T_{bulk-sc} - T_{\text{sink}}\right)} = -\frac{U_{tot}^{1\varphi} \pi D_{cd}}{\dot{m}_{tot} c_{p,l}} dz_{sc} \tag{2.36}$$

with the following boundary condition: at $z_{sc} = 0$, $T_{bulk-sc} = T_{sat-cd}$. The overall heat transfer coefficient is given by:

$$U_{tot}^{1\varphi} = 1 / \left(\frac{1}{h_{sc}^{1\varphi}} + \frac{1}{U_{p-s}} \right) \tag{2.37}$$

The cover-plate and pipe wall are made from a material of relatively high thermal conductivity, thus T_{wall} would be quite close to T_{sink} and essentially constant. Thus, assuming hydrodynamically and thermally fully-developed laminar flow and heat transfer in the subcooled region of the condenser, the Nusselt number in this region is given by:

$$Nu = (h_{sc}^{1\varphi} D_{cd} / k_l) = 3.657 \tag{2.38}$$

The solution to the energy equation in the subcooled region is the following:

$$\left(T_{bulk-sc} - T_{\text{sink}}\right) / \left(T_{sat-cd} - T_{\text{sink}}\right) = e^{-\left(\frac{U_{tot}^{1\varphi} \pi D_{cd}}{\dot{m}_{tot} c_{p,l}}\right) z_{sc}} \tag{2.39}$$

The fluid temperature at the condenser exit, if there is a subcooled region, could be estimated by substituting $z_{sc} = L_{cd}^{sc}$ in Eq. (2.39), which gives:

$$T_{exit,c} = T_{\text{sink}} + \left(T_{sat-cd} - T_{\text{sink}}\right) e^{-\left(\frac{U_{tot}^{1\varphi} \pi D_{cd}}{\dot{m}_{tot} c_{p,l}}\right) L_{cd}^{sc}} \tag{2.40}$$

Once $T_{exit,c}$ is calculated, Eqs. (2.34) and (2.35) can be used to calculate the total rate of heat rejection in the condenser section.

Assuming single-phase fully-developed flow, the pressure *drop* along the subcooled length of the condenser pipe is calculated using the following equation:

$$\Delta P_{sc,cd} = \frac{\left(f_{sc} \operatorname{Re}_{sc}\right)}{2} \frac{\mu_{l,sc} L_{cd}^{sc} \dot{m}_{tot}}{\rho_{l,sc} A_{cd,pipe} D_{cd}^2} \tag{2.41}$$

Here again, depending on the value of Re_{sc}, it is first determined whether the flow is laminar or turbulent, and then appropriate correlations are used to calculate the product $f_{sc}\,\mathrm{Re}_{sc}$ [see Eq. (2.15)].

2.2.4 Liquid-Transport Line

The liquid-transport line, which connects the condenser to the compensation chamber, is made of a smooth pipe. Assuming the fluid exiting the condenser is in a saturated or subcooled liquid condition, this transport line is considered to convey an incompressible, single-phase fluid flow.

The liquid-transport line is very well insulated; thus it is considered to be adiabatic. The enthalpy of the liquid flowing through this line is constant, as the kinetic and potential energy changes, and also the viscous dissipation, are negligible. Furthermore, the contribution of the *Pv* term in the specific enthalpy is also negligible. Therefore, it is assumed the temperature of the liquid remains constant.

For laminar and turbulent fully-developed flow, the pressure *drop* through the liquid-transport line is estimated using appropriate correlations [see Eq. (2.15)].

2.2.5 Compensation Chamber

The compensation chamber is usually a small reservoir that is connected in series with the evaporator (see Figure 2.1). In essence, it is an accumulator filled with a liquid-vapor mixture, and it performs the following functions: It ensures that enough saturated liquid is always available in the evaporator, and thus decreases the risk of depriming; it stores the excess working fluid that is not required in the loop at specific operating conditions; and it acts as an expansion tank in a closed system, absorbing all thermal and hydrodynamic surges that may occur during transient variations of the power input or the startup process. In this model, it is assumed, and ensured by using an appropriate charging strategy, that during the operation of the LHP, over the full range of desired rates of heat input, the compensation chamber is always filled with a two-phase mixture.

An energy balance on the entire LHP gives the following equation:

$$q_{app} - q_{cc-amb} = q_{cd-reject} \tag{2.42}$$

where q_{cc-amb} represents the rate of heat transfer from the fluid stocked in the compensation chamber to the ambient. Assuming that this fluid is in the saturated state, the following equation applies:

$$q_{cc-amb} = \bar{U}_{cc-amb} A_{cc} \left(T_{sat-cc} - T_{amb}\right) \tag{2.43}$$

where $\bar{U}_{cc-amb}$ is an overall heat transfer coefficient, A_{cc} is the corresponding heat transfer surface area (envelope of the compensation chamber), T_{amb} is the ambient temperature, and T_{sat-cc} is the saturation temperature of the fluid inside the compensation chamber. Neglecting the heating up of the saturated liquid entering the evaporator section by the heat leak exiting the inner surface of the wick, T_{sat-cc} can be considered equal to the saturated temperature of the liquid entering the wick structure, $T_{w,ent}$. It should be noted that q_{cc-amb} could be negative or positive depending on the operating temperature of the LHP (or the rate of heat input applied to the evaporator).

2.2.6 Total Pressure Drop in the Loop Heat Pipe

The total pressure *drop* in the entire LHP should not be higher than the maximum capillary pressure that is developed at the liquid-vapor interface in the wick structure. The total loop pressure drop, in its general form, is calculated as follows:

$$\Delta P_{tot} = P_v - P_l = \Delta P_{channel} + \Delta P_{vl} + \Delta P_{cd}^{2\varphi} + \Delta P_{sc,cd} + \Delta P_{ll} + \Delta P_{cc} + \Delta P_{ev,ent} + \Delta P_{wick} \tag{2.44}$$

Here, $\Delta P_{channel}$ is the vapor pressure drop through the evaporator grooved channel; ΔP_{vl} is the vapor pressure drop through the vapor-transport line; $\Delta P_{cd}^{2\varphi}$ is the liquid-vapor mixture pressure drop in the two-phase part of the condenser; $\Delta P_{sc,cd}$ denotes the liquid pressure drop in the subcooled region of the condenser (single-phase part); ΔP_{ll} indicates the liquid pressure drop through the liquid-transport line; ΔP_{cc} is the liquid-vapor mixture pressure drop thorough the compensation chamber; $\Delta P_{ev,ent}$ is the liquid pressure drop from the compensation chamber exit to the annular wick entrance in the evaporator; and ΔP_{wick} denotes the liquid pressure drop during its passage in the radial direction through

the wick. In addition, it is essential to ensure that ΔP_{tot} is less than the maximum capillary pressure, $\Delta P_{cap,\max}$:

$$\Delta P_{tot} < \Delta P_{cap,\max}$$

$$\Delta P_{cap,\max} = \frac{2\sigma_{lv}\cos\theta_c}{r_p} \tag{2.45}$$

Here, θ_c is the contact angle at the static equilibrium condition. In this basic network thermofluid model, the terms $\Delta P_{cd}^{2\varphi}$, ΔP_{cc}, and $\Delta P_{ev,ent}$ are considered negligible.

2.2.7 Model Implementation

The proposed network thermofluid model was incorporated in a computer program. This program is written in FORTRAN and it is designed to simulate an LHP akin to that shown in Figure 2.1, with ammonia as the working fluid. It calculates the steady-state operating temperature and mass flow rate as a function of the power input, q_{app}, to the evaporator. The program starts by reading the input geometry of the loop, T_{sink}, and T_{amb}. Then, the operating temperature of the loop, T_{sat}, is guessed. Here, T_{sat} is the saturation temperature of the working fluid (ammonia, in this case) at the liquid-vapor interface in the wick inside the evaporator section.

The sequence of the various calculations and checks performed by the program, and its overall iterative solution procedure, are presented in the flow chart in Figure 2.10.

2.3 Results and Discussions

The proposed network thermofluid model and its overall iterative solution procedure described in the earlier sections of this chapter were used to predict the performance of an LHP akin to that shown schematically in Figure 2.1. Details of this LHP and the results obtained in this investigation are presented and discussed in this section.

2.3.1 Details of the LHP

In order to allow comparisons of the results of this investigation with those available in the literature, the characteristics of the LHP considered here were chosen to be as close

as possible to those of the GLAS LHP (LHP1) investigated by Kaya and Hoang (1999). Where specific data were not available, some logical guessed values were substituted.

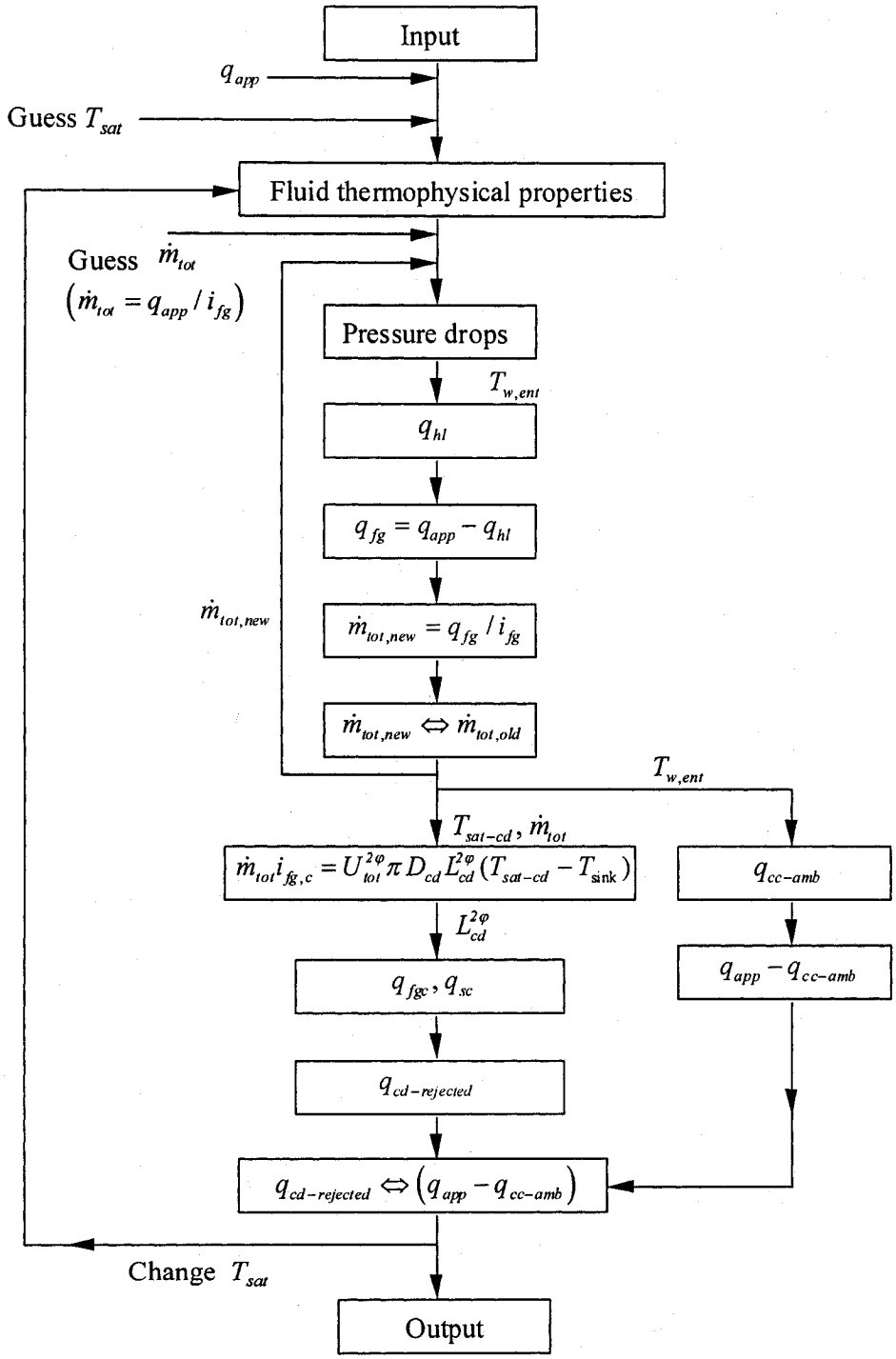

Figure 2.10: Flow chart depicting key elements of the overall iterative solution procedure of the basic network thermofluid model.

The LHP considered in this work is schematically illustrated in Figure 2.1, with details given in Figures 2.2, 2.4, 2.6-2.9. It has a cylindrical, internally grooved, evaporator, with an external diameter of 25.4 mm and a length of 150 mm. The total number of grooves in the evaporator is $N = 16$, each with an average cross-sectional area of $A_G = 4$ mm², and a hydraulic diameter of $D_h = 2$ mm. The evaporator is equipped with a nickel 200 sintered powder-metal wick with an effective pore radius of $r_p = 1.2$ μm. The porosity and permeability of the wick are set equal to 50 % and 2.7×10^{-10} cm², respectively, and its inside and outside radii are, respectively, $r_o = 10$ mm and $r_i = 6$ mm. The compensation chamber (CC) has an internal diameter of 46 mm and a length of 76 mm (giving a CC volume of 126.3 ml). This chamber exchanges heat with the ambient environment through its envelope. The ambient temperature, T_{amb}, is fixed at 295 K.

It is assumed that the compensation chamber is initially filled (at ambient temperature) with a two-phase mixture of 50% quality. The charging strategy is the following: The liquid-transport line, the condenser pipe, the liquid core of the evaporator, and the void volume of the wick structure are filled with saturated liquid ammonia; and the vapor-transport line and the evaporator grooves are filled with saturated ammonia vapor at this temperature. To estimate the rate of heat transfer through the envelope of the CC, to or from the ambient, an average overall heat transfer coefficient, $\bar{U}_{cc-amb}$, is set equal to 10 W/m²-K. This coefficient, $\bar{U}_{cc-amb}$, is based on the internal surface area of the cylindrical container of the CC.

Both the vapor- and the liquid-transport lines of the LHP are made of identical smooth-walled tubes (made of stainless steel), each with an inner diameter of 5.54 mm and a length of 460 mm. These transport lines are very well insulated, and assumed to have adiabatic boundaries.

The condenser is a single-pass heat exchanger, with a tube of length 4.06 m and internal diameter of 5.54 mm. The thermal conductance per unit length from the inner surface of the condenser tube to the outer surface of the condenser cover plate (sleeve) is set equal to 4 W/m-K. It is assumed that this conductance is constant over the entire length of the condenser, therefore, the related heat transfer coefficient, U_{p-s}, is calculated as 229.8 W/m²-K, using the definition given in Eq. (2.27).

The working fluid in the LHP is ammonia. The required thermophysical property data for this fluid were obtained from the book by Faghri (1995): Appropriate curves were fitted to this data for use in the aforementioned computer program. In this investigation, the range of the power input to the evaporator, q_{app}, was limited to ensure that the saturation temperature of the ammonia was in the range $200\ \text{K} < T_{sat} < 400\ \text{K}$; the critical point temperature of ammonia is 405.4 K [Avallone and Baumeister III (1987)].

The performance of the LHP was examined for q_{app} in the range 0 to 400 W and three different values of the sink temperature: T_{sink} = 273 K, 283 K, and 290 K. The results for these sink temperatures are qualitatively similar. In this chapter, therefore, attention in limited to the results for $T_{sink} = 273$ K.

2.3.2 Variation of T_{sat} and $T_{exit,c}$ with q_{app}

In Figure 2.11, the variations of the saturation temperature of the ammonia at the liquid-vapor interface in the wick structure, T_{sat}, and the fluid temperature at the exit of the condenser, $T_{exit,c}$, with the power input to the evaporator, q_{app}, are presented, for $T_{sink} = 273$ K and $T_{amb} = 295$ K. For low power inputs ($q_{app} < 80$ W), the saturation temperature first decreases as q_{app} increases and then reaches a minimum value. For higher values of power input, T_{sat} increases almost linearly as q_{app} increases. For low power inputs, $T_{exit,c}$ remains almost constant and very close to the sink temperature, and when this temperature starts to rise with q_{app}, so does T_{sat}.

Similar results have been reported by Bienert and Wolf (1995) and Kaya and Hoang (1999). In both of these investigations, the researchers concluded that at low power inputs, the fluid exits the condenser as a subcooled liquid and the LHP operates as a variable conductance device; and beyond the minimum point of the T_{sat} *vs.* q_{app} curve, the condenser becomes fully "open" (in that its entire length is filled with a two-phase flow), the LHP operates as a constant conductance device, and T_{sat} increases almost linearly

with q_{app}. This explanation is essentially correct, but not precise, as is indicated by the results presented in the following subsections.

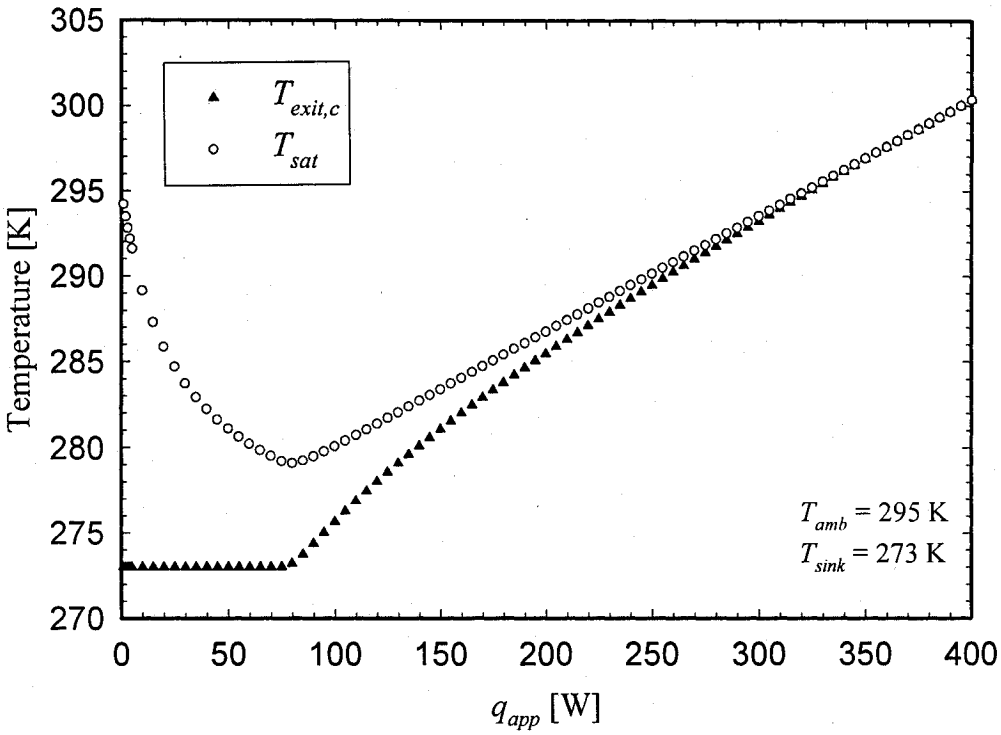

Figure 2.11: Variation of T_{sat} and $T_{exit,c}$ with q_{app} for $T_{sink} = 273$ K and $T_{amb} = 295$ K.

2.3.3 Length of the Two-Phase Flow Region inside the Condenser

The variation of dimensionless length of the two-phase flow region in the condenser with q_{app}, for $T_{sink} = 273$ K and $T_{amb} = 295$ K, is depicted in the results presented in Figure 2.12. These results show that when $q_{app} = 80$ W, roughly 90% of the condenser length is occupied by the two-phase flow region. Thus, the location of the minimum point in Figure 2.11 does *not* coincide with the condenser becoming fully open, as proposed by Bienert and Wolf (1995) and Kaya and Hoang (1999). Indeed, at the location of the minimum point in the loop operating temperature, the rate of growth of the two-phase region inside the condenser is decreased and an inflection point is evident in Figure 2.12, around $q_{app} = 80$ W.

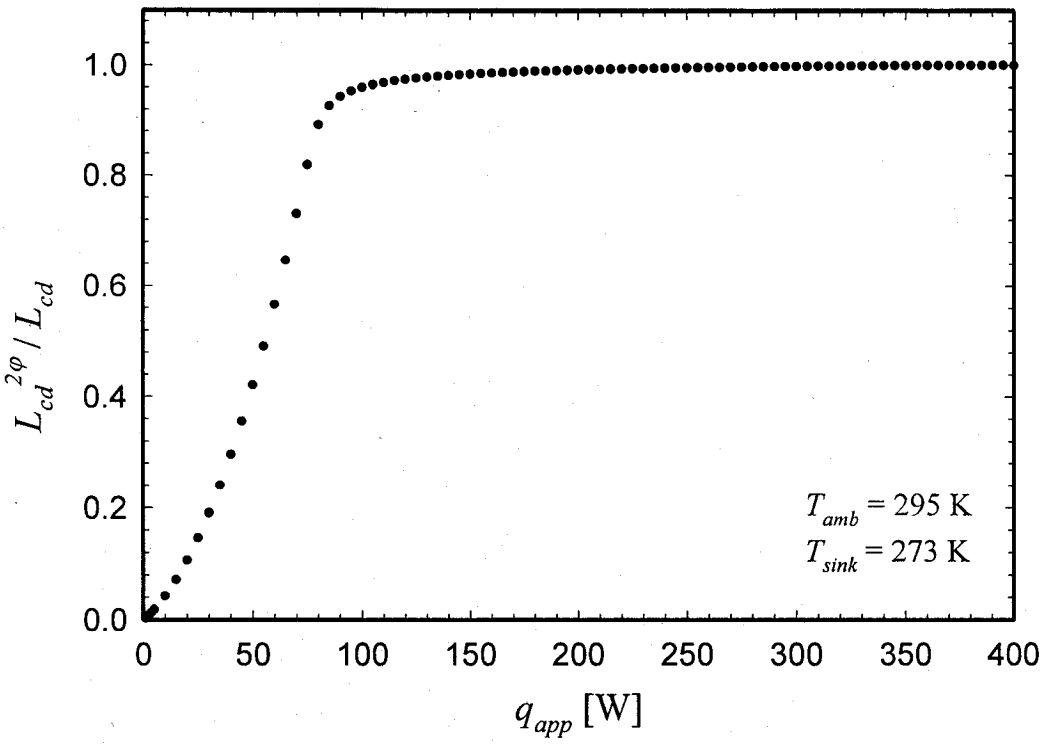

Figure 2.12: Dimensionless length of the two-phase flow region in the condenser as a function of q_{app}, for $T_{sink} = 273$ K and $T_{amb} = 295$ K.

2.3.4 Variation of q_{sc}, q_{cc-amb}, and q_{hl} with q_{app}

These results for $T_{sink} = 273$ K and $T_{amb} = 295$ K are presented in Figure 2.13. The negative values of the heat transfer rates in this figure imply heat loss from the system, and heat gains are indicated by the positive values.

The results in Figure 2.13 show that for $0 \le q_{app} \le 80$ W, the rate of heat rejection in the subcooled region of the condenser, q_{sc}, increases from zero to about 1.7 W (negative values), reaching its highest value at about q_{app} = 80 W. Simultaneously, the rate of heat gained in the compensation chamber, q_{cc-amb}, increases and reaches its highest value (1.7 W) at point *A*. In this range, the heat leak, q_{hl}, is almost zero because the loop mass flow rates and pressure drops are relatively very small. For $q_{app} > 80$ W, q_{sc} starts to decrease with increasing power input and reaches zero at q_{app} = 355 W (point *D*), where the condenser becomes totally open. At point *B*, the rate of growth of q_{hl} is increased due to

the transition from laminar to turbulent flow in the vapor-transport line. In this case, the total pressure drop in the loop is increased, and, in consequence, a higher temperature difference across the wick is achieved. From point A to C, q_{cc-amb} is decreased, and at point C, the loop operating temperature reaches the ambient temperature yielding a zero value for q_{cc-amb}. It should be noted that before reaching point C (q_{app} = 320 W), the sum of q_{cc-amb} and q_{hl}, which represents the total rate of heat gained in the compensation chamber, is equal to q_{sc}.

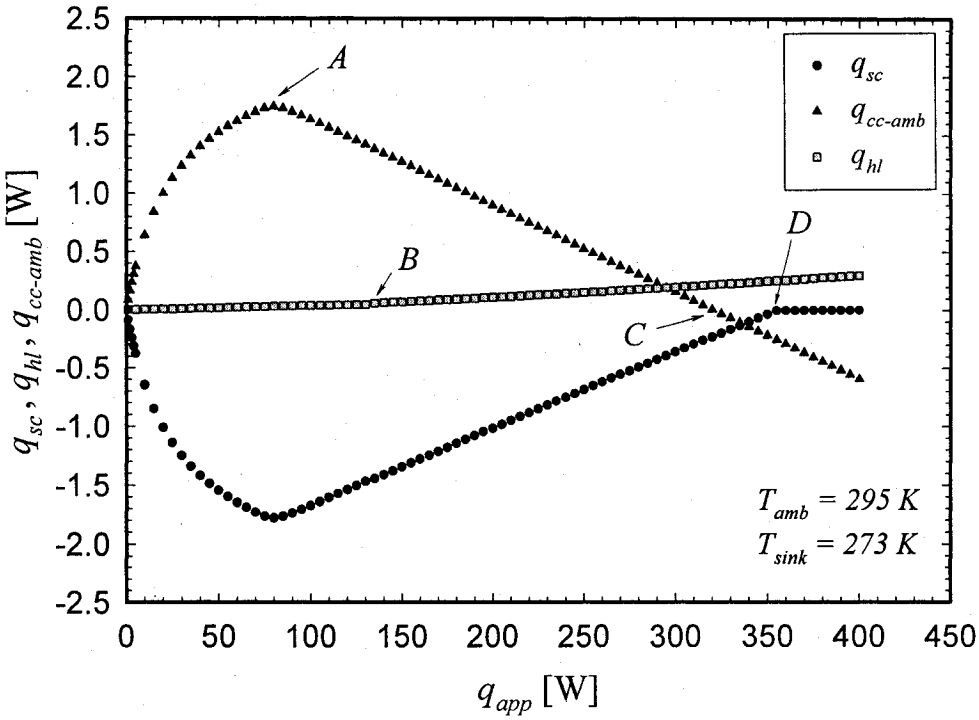

Figure 2.13: Variation of q_{sc}, q_{cc-amb}, and q_{hl} with q_{app}, for T_{sink} = 273 K and T_{amb} = 295 K.

At point C, the rate of heat leak, q_{hl}, is adequate to compensate for q_{sc}. For q_{app} > 320 W (beyond point C), the LHP operating temperature becomes higher than the ambient temperature resulting in a negative value of q_{cc-amb}.

Between points C and D, the rate of heat leak is adequate to compensate for both q_{sc} and q_{cc-amb}. At point D, q_{sc} becomes zero and the rate of heat leak is balanced by the rate of heat rejected to the ambient from the compensation chamber. For q_{app} > 355 W

(beyond point *D*), the rate of heat rejected to the ambient in the compensation chamber is higher than the rate of heat leak gained from the evaporator. To investigate the reason for this, it is necessary to consider the condenser again. After reaching point *D*, where the condenser becomes totally open, for increasing values of the applied power, the condenser section does not allow complete condensation of the inlet saturated vapor. In this case, the fluid exits the condenser as a two-phase liquid-vapor mixture, and the temperature of the fluid at the exit of condenser remains essentially constant and equal to T_{sat}. However, the enthalpy of this two-phase fluid is higher than that of the saturated liquid, and because the quality at the exit of the condenser increases with increasing power input, the fluid enthalpy also rises. Therefore, the fluid entering the compensation chamber carries more and more enthalpy with increasing power input, which, along with the heat leak, must be dissipated to the ambient environment from the compensation chamber envelope, under steady-state conditions. Therefore, as is seen in Figure 2.13, with increasing power input (beyond point *D*), q_{cc-amb} decreases more rapidly than q_{hl}.

2.3.5 Comparison of Model Predictions with Experimental Data

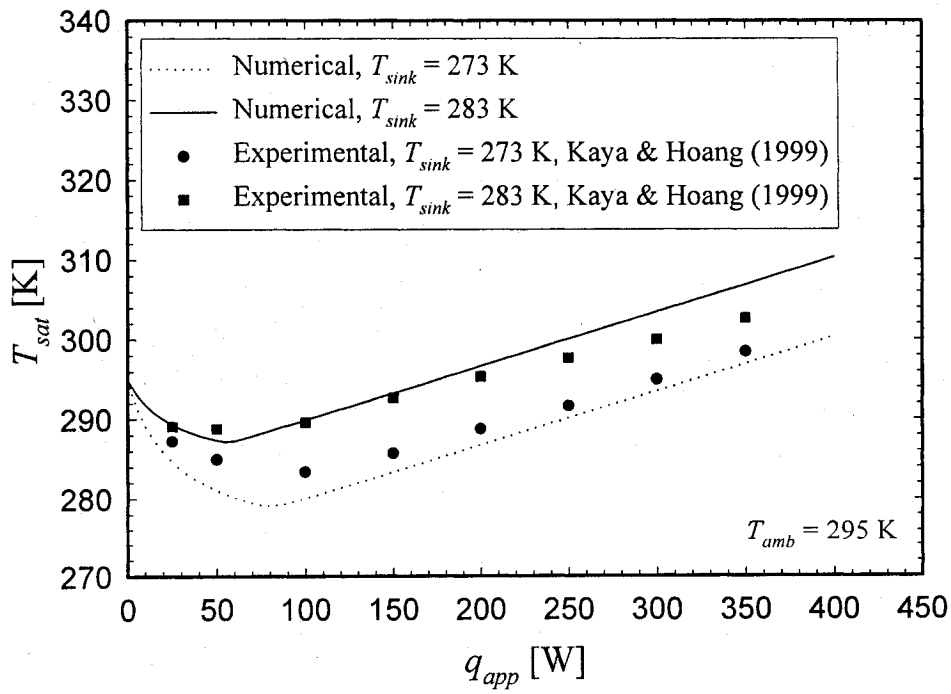

Figure 2.14: Comparisons of the experimental data of Kaya and Hoang (1999) with the numerical predictions obtained with the proposed model, for T_{amb} = 295 K.

As was mentioned earlier in this section, the geometry and other parameters of the LHP investigated in this work were chosen to match, as closely as possible, those of an LHP investigated experimentally by Kaya and Hoang (1999). A comparison of the numerical predictions obtained in this work with the experimental results of Kaya and Hoang (1999) is presented in Figure 2.14. Considering the difficulty experienced in duplicating the geometry and other parameters of the LHP investigated by Kaya and Hoang (1999), mainly because of lack of sufficient information in their paper, the comparisons in Figure 2.14 are regarded as being quite encouraging.

2.4 SUMMARY

A basic network thermofluid model of a loop heat pipe (LHP) operating under steady-state conditions was presented and discussed in the earlier sections of this chapter. Attention was focused on a simple LHP, with one evaporator, a vapor-transport line, a single condenser, a liquid-transport line, and a compensation chamber. Quasi one-dimensional mathematical models of the fluid flow and heat transfer in each of the elements of the LHP, and collectively of the entire LHP, were proposed and discussed.

The basic network thermofluid model was used to simulate an LHP similar to one investigated experimentally by Kaya and Hoang (1999). Results pertaining to the performance of this LHP over a range of operating conditions were presented, and their implications were discussed. These results show the basic network model proposed in this chapter produces results that compare quite well (at least qualitatively) with the corresponding experimental results of Kaya and Hoang (1999). In this sense, this basic network thermofluid model could serve as a simple, but effective, tool in the preliminary designs of LHPs akin to the one shown in Figure 2.1.

As was mentioned at the start of this chapter, an extended version of this basic network thermofluid model is presented and discussed in Chapter 5. This extended model is suitable for simulations of LHPs with a flat evaporator and fixed active mass of working fluid, similar to the one designed, constructed, and used in the experimental phase of this research (details are provided in Chapter 4).

Chapter 3:

Determination of the Properties of Sintered Powder-Metal Wicks

Porous materials of good rigidity, and low effective pore size can be readily fabricated by sintering metal powders. The aforementioned characteristics have made sintered powder metals the materials of choice for the construction of wicks employed in heat pipes (HPs), capillary pumped loops (CPLs), and loop heat pipes (LHPs) [Dunn and Reay (1986); Silverstein (1992); Faghri (1995); Leong et al. (1997)]. For discussions and derivations of volume-averaged equations that govern fluid flow and heat transfer in porous media and the corresponding effective thermofluid properties, the reader is referred to the contributions of Hadley (1986), Kaviany (1999), Whitaker (1973, 1999), Minkowycz et al. (1999), Alazmi and Vafai (2000), and Nield and Bejan (2006).

Key inputs required in network thermofluid models and designs of LHPs, such as the one presented in Chapter 2, include the porosity, the maximum effective pore size, the effective permeability, and the effective thermal conductivity of the liquid-saturated wicks used in these devices. In this chapter, the theoretical considerations, the experimental apparatus, and the procedures that were used to determine these properties for two sintered powder-metal plates, one made of nickel 200 and the other of stainless steel 316, are presented. A square piece cut from this stainless steel 316 sintered powder-metal plate was used as the wick in the LHP that was designed, constructed, and used in the experimental part of this work (details are given in Chapter 4).

3.1 Overview of the Sintered Powder-Metal Porous Plates

As was mentioned above, two sintered powder-metal plates, one made of nickel 200 and the other of stainless steel 316, were used in this work. These plates were purchased from a manufacturer of specialized filters (Mott Corporation, Connecticut, U.S.A.) in the form of disks with nominal dimensions of 185.4 mm (7.3") diameter and 6.35 mm (1/4") thickness. Laser machining was used to cut the following samples from each of these plates: a square of nominal dimensions of 127 mm × 127 mm (5.5" x 5.5") and few disks

of 22.23 mm (7/8") nominal diameter. The laser machining ensured that the peripheral surfaces (cut edges) of these samples were sealed (impermeable to the working fluid).

A scanning electron microscope (Hitachi S-4700) was used to obtain photomicrographs of the samples of both the nickel 200 and stainless steel 316 sintered powder-metal porous plates. Examples of these photomicrographs at 300X and 1000X magnifications are given in Figures 3.1 and 3.2 for the nickel 200 and the stainless steel 316 samples, respectively.

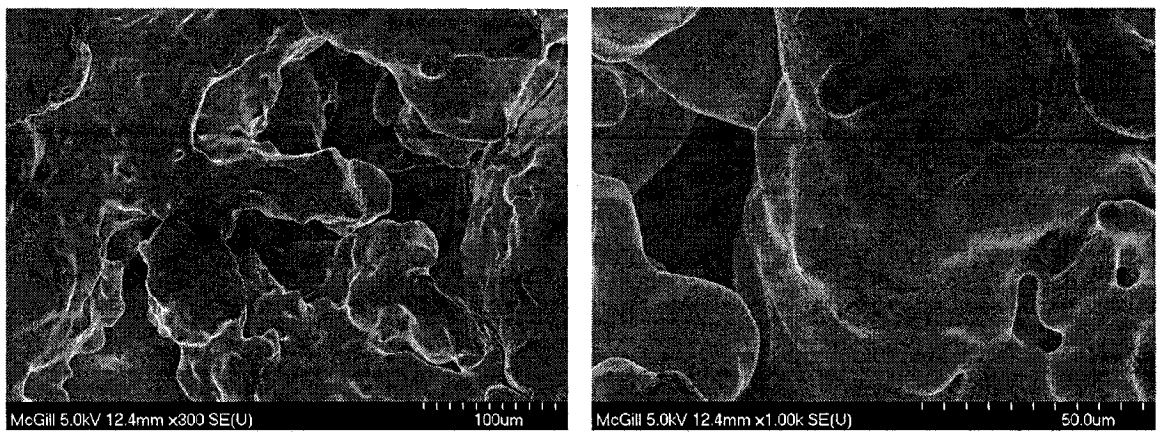

(a) **(b)**

Figure 3.1: Scanning electron microscopy images of samples of the sintered powder-metal plate made of nickel 200 at magnifications of (a) 300X and (b) 1000X.

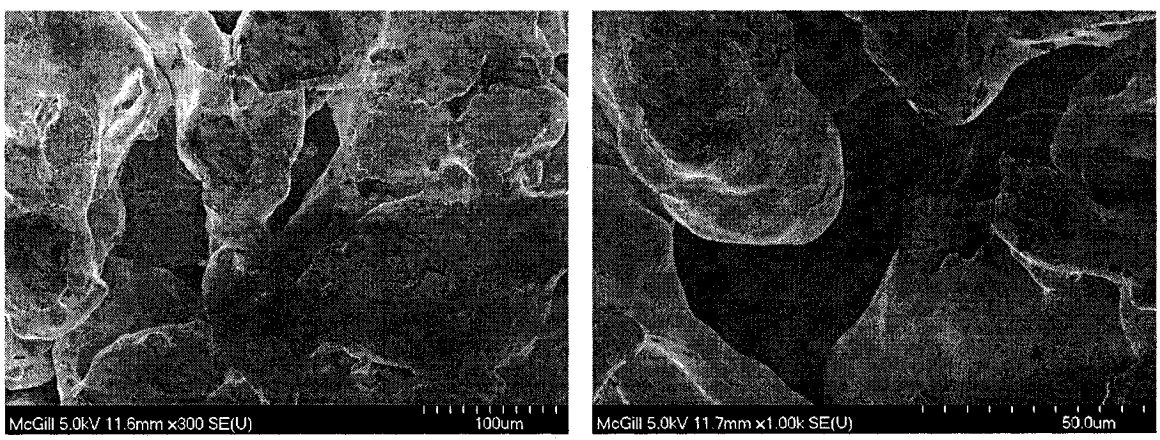

(a) **(b)**

Figure 3.2: Scanning electron microscopy images of samples of the sintered powder-metal plate made of stainless steel 316 at magnifications of (a) 300X and (b) 1000X.

The photomicrographs presented in Figures 3.1 and 3.2 clearly show that the particles of the metal powders used in the fabrication of the sintered porous plates are not spherical

in shape. Rather, these particles are randomly shaped and not uniformly sized. Furthermore, the sintering process creates excellent connections (solid-to-solid contact zones) between these particles. Thus, it is clear that available analytical, semi-analytical, and numerical correlations [Kunii and Smith (1960); Chen and Tien (1973); Ogniewicz and Yovanovich (1978); Hadley (1986); Kaviany (1999); Hsu (2000); Bahrami et al. (2004), Nield and Bejan (2006)] for effective properties of porous materials made of uniformly sized, regularly spaced, and packed (unconsolidated or consolidated) spherical particles are not applicable to the sintered powder-metal porous plates considered here. Therefore, in this work, experimental methods were used to measure the effective properties of these porous plates.

3.2 POROSITY

The porosity of a porous medium is defined as the ratio of the volume of the voids within it to its total volume, and it accounts for all pores in the porous medium. On the other hand, the term *effective* porosity, accounts for only the volume of the interconnected pores within the porous material. Kunz et al. (1967) examined photomicrographs of sintered metal fibers and screens, and observed that the pores in these types of porous materials are, for the most part, interconnected. However, as they have also noted, during the compacting of powders to form sintered materials, isolated voids can form. Nevertheless, they claimed that by suitably packing the powder before the compacting and sintering process, the probability of the formation of isolated voids could be minimized. Based on these observations, it is assumed here that for well-fabricated porous materials made of both sintered fibers and powders, the porosity and the effective porosity are essentially equal. Furthermore, following the arguments of Kunz et al. (1967), the porosity of sintered porous materials is estimated as follows:

$$\varepsilon = \frac{V_{void}}{V_{total}} = 1 - \frac{m_{dry\_porous\_matl}}{\rho_s V_{total}} \tag{3.1}$$

where V_{void} is the total volume of the voids inside the porous material; V_{total} is the total volume of the porous material; $m_{dry\_porous\_matl}$ is the total mass of the dry porous material;

and ρ_s is the mass density of the solid. In this equation, the mass of the air filling the voids is neglected in comparison to the mass of the solid part of the porous material.

Procedures for measuring the porosity of porous metal plates are discussed in Dullien (1992). A simple procedure, the so-called density method [Dullien (1992)], was used in this work for the determination of the porosity of each sample. It is described below:

- Measure the dimensions of the sample several times, and average the measurements to obtain their mean values. Use these mean values to calculate the total volume of the porous sample.
- Measure the ambient temperature, and then obtain the value of the mass density (ρ_s) of the solid component of the porous sample at this temperature.
- Dry the porous sample and then weigh it (in this work, an electronic balance with an accuracy of ±0.1g was used).
- Use Eq. (3.1) to estimate the porosity of the sample.

As was mentioned earlier, two different sintered powder-metal plates were considered in this work: One made of nickel 200 and the other of stainless steel 316. In the experiments to determine the porosity of these plates, the mass of a 126.8 mm × 126.8 mm × 6.65 mm sample of the nickel 200 plate was measured to be 683.4 g; the sample of the stainless steel 316 plate had dimensions of 126.6 mm × 126.6 mm × 6.54 mm, and its mass was measured to be 462.4 g. The ambient temperature during these experiments was about 27°C throughout. At this temperature, the mass density of solid nickel 200 and stainless steel 316 are, respectively, 8890 kg/m^3 [Special Metals (2002)] and 8238 kg/m^3 [Incropera and DeWitt (2002)].

Using the abovementioned data and Eq. (3.1), the porosity of the above-mentioned two sintered powder-metal plates were determined to be the following:

Nickel 200	$\varepsilon = 0.281$ (±0.010)
Stainless steel 316	$\varepsilon = 0.465$ (±0.016)

The uncertainties in these values of the porosity were calculated using the method described in ASHRAE Standard 41.5-75 (1976).

3.3 MAXIMUM EFFECTIVE PORE SIZE

Another important property of the wicks used in capillary driven heat transfer devices is the maximum effective pore size. This property is needed for the determination of the maximum capillary pressure that can be developed at the liquid-vapor interface in the wick and, consequently, the associated heat transfer limit for HPs, CPLs, and LHPs. In this section, an experimental apparatus that was designed, constructed, and used for the determination of this property of the wicks is described. The experiments were conducted with cylindrical (disk-shaped) samples cut (using laser machining) from sintered powder-metal porous plates made of nickel 200 and stainless steel 316. The results of these experiments are also presented and discussed in this section.

3.3.1 Theoretical Considerations

Figure 3.3 shows a schematic representation of a liquid-vapor interface that is concave with respect to the vapor. The interface is characterized by two principal radii of curvature, R_1 and R_2. In static equilibrium and with no mass transfer across the interface, the normal components of the surface tension forces are in balance with the force caused by the pressure jump from the liquid phase to the vapor phase. This statement is strictly true only for portions of the curved liquid-vapor interface that are far from solid walls. However, as discussed by de Gennes (1985), in many applications, the extent of a near-wall region that is affected by the Van der Waals force of the solid is less than 100 Å. With reference to Figure 3.3, the difference in pressure across the liquid-vapor interface is given by the Young-Laplace equation [Silverstein (1992)]:

$$\Delta P_{cap} = (P_v - P_l) = 2\sigma_{lv} / r_c \;\; ; \;\; \frac{1}{r_c} = \left(\frac{1}{R_1} + \frac{1}{R_2} \right) / 2 \tag{3.2}$$

In this equation, P_v and P_l denote, respectively, the thermodynamic pressure in the vapor and the liquid phases adjacent to the interface; σ_{lv} represents the surface tension at the liquid-vapor interface; and r_c is the mean radius of curvature. As is commonly done [Alexander (1972); Stepanov et al. (1977); Silverstein (1992)], it is assumed here that the liquid-vapor surface tension is essentially equal to that of the liquid-air interface, and both are referred to as the liquid surface tension, σ. In HPs, LHPs, and CPLs, it is

necessary to obtain a positive value of the pressure jump ($P_v - P_l$), to balance the overall pressure drop in the rest of the working fluid circuit. Therefore, a working fluid that wets the solid in the porous wick is needed.

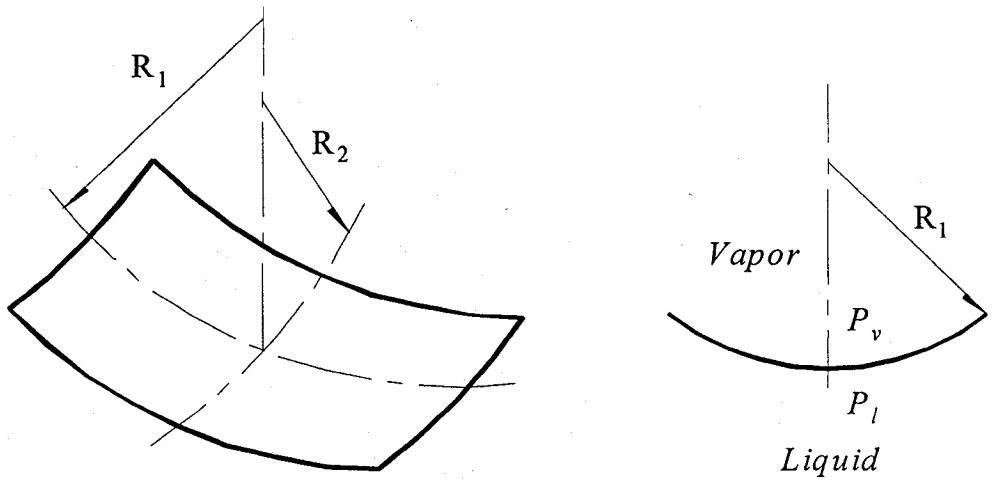

Figure 3.3: Liquid-vapor interface and associated notation.

In the setup shown schematically in Figure 3.4, the capillary force causes the liquid inside the vertical pipe of small diameter to rise to an equilibrium height of h_{cap}. Neglecting the weight of the air column in comparison to that of the liquid column, the following equation applies:

$$(P_a - P_l) = (2\sigma / r_c) = \rho_l g h_{cap} \;\; ; \;\; r_c = r_p / \cos(\theta_c) \qquad (3.3)$$

In Eq. (3.3), ρ_l is the mass density of the liquid; σ is the surface tension at the liquid-air interface; g is the gravitational acceleration; r_p is the inner radius of the pipe; and θ_c is the contact angle at static equilibrium [Stepanov et al. (1977)].

The experiment illustrated schematically in Figure 3.4 could be repeated with the pipe replaced by a cylinder made of a porous material. The equilibrium height of the liquid column that would rise up in the porous cylinder could then be used in Eq. (3.3) to compute a value of r_p, which would represent the effective pore radius of the interstices of the porous material under "rising" conditions.

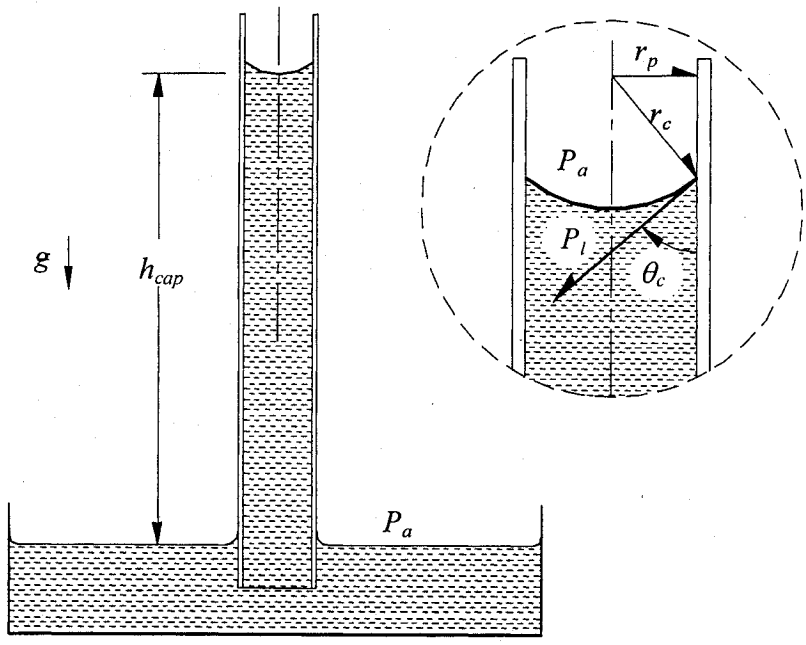

Figure 3.4: Schematic illustration of capillary action inside a pipe of small diameter.

Another experiment with a disk of porous material inserted in a sample holder with a pipe attached to its *bottom* could be run as follows: This assembly is immersed completely in a pool of liquid contained in a vertical tube of larger diameter; after the porous disk is fully saturated and the tube at the bottom of the sample holder is completely filled, the liquid in the larger tube is slowly withdrawn until the liquid column inside the bottom tube breaks away from the porous sample; the height of this liquid column is then used in Eq. (3.3) to compute a value of r_p. This value of r_p would represent the effective pore radius under "falling" conditions.

In earlier experimental works [Alexander (1972), Stepanov et al. (1977)], values of the effective pore size ($d_p = 2r_p$) obtained under rising conditions have been found to be consistently less than those obtained under falling conditions, but no convincing explanation has been advanced for this finding. However, an examination of the data shows that these rising and falling values are established by the minimum and maximum effective pore radii, respectively, of the interstices of the porous material. Furthermore, in HPs, LHPs, and CPLs operating just beyond their capillary limit [Silverstein (1992)], the vapor pushes the liquid out of the wick material, and the corresponding capillary pressure

is that obtained with the falling (or maximum) value of the effective pore size. The determination of this maximum effective pore size is the focus of this experimental work.

3.3.2 Experimental Apparatus and Procedure

The apparatus that was designed, constructed, and used in this work is schematically shown in Figure 3.5. It is an improved version of an apparatus designed by Alexander (1972).

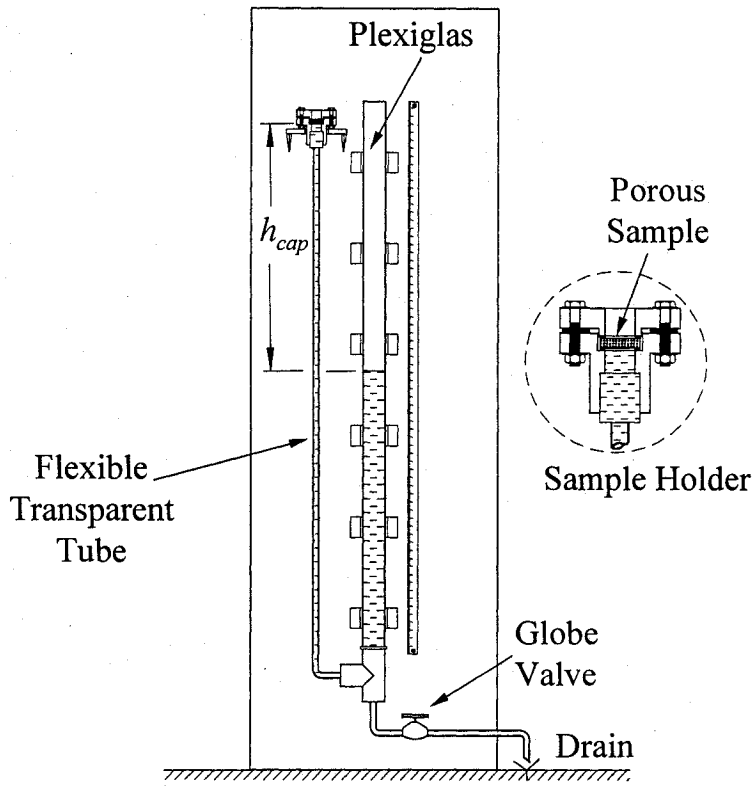

Figure 3.5: Schematic of the experimental apparatus used for measurements of the maximum effective pore size.

This apparatus is designed to accommodate cylindrical (disk-shaped) test samples of 22.23 mm diameter and 6.35 mm thickness (nominal). As was mentioned earlier, in this study, cylindrical samples cut from 6.35 mm thick (nominal) sintered powder-metal plates of nickel 200 and stainless steel (SS) 316 were tested. It is noted again that these cylindrical samples were cut out of the porous plates using laser machining, which ensured that their curved surface (cut edge) was water-tight.

In the apparatus illustrated in Figure 3.5, the straight Plexiglas tube has 50.8 mm outer diameter and 2 m length. The porous metal samples were sandwiched between two specially designed flanges, along with ring-shaped gaskets (see inset in Figure 3.5). At the start of each experimental run, the porous sample was thoroughly cleaned by using high-pressure nitrogen to sequentially push (several times) isopropyl alcohol and all-glass double-distilled deaerated water through it. Then the test cell was located in its fixed position (as shown in Figure 3.5), the globe valve was fully closed, and the whole system was completely filled with all-glass double-distilled deaerated water. Following that, the globe valve was opened slightly to allow the water to drain very slowly out of the system. In the early stages of this draining process, the water levels both in the Plexiglas tube and on top of the porous sample descend. However, once the liquid-air interface enters the porous sample, a capillary pressure jump is created, and water drains only from the Plexiglas tube. In each run, the water in the Plexiglas tube was allowed to continue draining until the column of water in the flexible transparent tube (supported by capillary forces in the porous material) broke away from the sample: The height of this water column in the flexible transparent tube, h_{cap}, was recorded and used in Eq. (3.3) to calculate the maximum (falling) effective pore size ($d_p = 2r_p$) of the sample.

3.3.3 Results and Discussions

Table 3.1: Maximum effective pore size: Experimental data and results

	h_{cap} [m]	ΔP [Pa]	θ_c [deg]	d_p [μm]
nickel 200	1.130	11074	34	21.82
	1.120	10976	34	22.02
	1.140	11172	34	21.63
	1.100	10780	34	22.42
	1.080	10584	34	22.83
	1.090	10682	34	22.63
316 SS	0.555	5439	40	41.06
	0.545	5341	40	41.81
	0.550	5390	40	41.43
	0.540	5292	40	42.20
	0.535	5243	40	42.59
	0.550	5390	40	41.43

The final results obtained from six runs with each of the two porous samples considered in this work are reported in Table 3.1. The contact angles were obtained from Stepanov et al. (1977). The average water temperature in the experiments was 20.7°C. For the porous samples tested, the values of the maximum effective pore size, $d_p = 2r_p$, were repeatable to within ± 2.7% and ± 2.0% of the mean value for nickel 200 and stainless steel 316, respectively.

The overall relative uncertainties in the maximum effective pore sizes were calculated using the method described in ASHRAE Standard 41.5-75 (1976). The final results for the mean values of the maximum effective pore size, d_p, for the nickel 200 and stainless steel 316 samples are the following:

Nickel 200	$d_p = 22.22\ \mu m$ (±7.5%)
Stainless steel 316	$d_p = 41.75\ \mu m$ (±7.6%)

3.4 Effective Permeability

In mathematical models of LHPs (and also HPs and CPLs), the effective permeability of the wick structure is needed to determine the liquid pressure drop through the wick, as was illustrated in Chapter 2. Depending on the geometry of the wick, the working fluid properties, and the flow rate, this pressure drop could be a significant portion of the total pressure drop encountered in a LHP. An experimental/numerical method was used in this work to determine the permeabilities of two 6.35 mm thick (nominal) sintered powder-metal porous plates, one made of nickel 200 and the other of stainless steel 316.

3.4.1 Theoretical Considerations

In 1856, Darcy performed what is now regarded as a classical experiment on laminar flow through a homogenous porous medium [Scheidegger (1974)]. A schematic representation of Darcy's experimental setup is shown in Figure 3.6. It consists of a homogeneous porous medium of height h packed inside a pipe of cross-sectional area A_{c-s}. An incompressible liquid is circulated through this porous medium, and its volumetric flow rate, Q, is measured. A manometer is used to measure the pressure drop across the upper and lower boundaries of the porous medium. Darcy performed numerous

experiments with this setup and observed that the volumetric flow rate of the liquid varied linearly with the pressure gradient across the porous media.

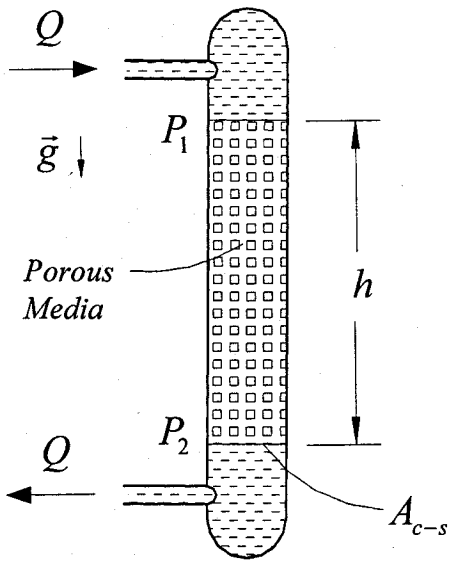

Figure 3.6: Schematic representation of Darcy's experimental setup for measurements of effective permeability.

Assuming that the mass density of the liquid, ρ_l, and the gravitational acceleration, g, are constant, Darcy's observation can be represented mathematically by the following equation:

$$U = \frac{K}{\mu}\frac{(P_1 - P_2 + \rho_l g h)}{h} = \frac{K}{\mu}\frac{(\Delta P)_{fric}}{h} \tag{3.4}$$

where U is the area-averaged velocity of the fluid ($U = Q/A_{c\text{-}s}$), μ is the dynamic viscosity of the fluid, K is the effective permeability of the porous medium, and $(\Delta P)_{fric}$ is the friction pressure drop associated with the flow through the porous medium. Beavers and Sparrow (1969) showed that departures of experimental results from Darcy's law, as expressed in Eq. (3.4), occur at Reynolds number (based on the square-root of the permeability of the porous material as the characteristic dimension) of the order of one or greater. As the sintered powder-metal porous materials normally used in LHPs have fine pores, they typically have very low effective permeabilities. In addition, in LHPs, the flow rate in the wick is usually very small. Thus, in this study, it is assumed that Darcy's law governs the liquid flow through the wick in LHPs.

The effective permeability is a geometrical property of porous materials. For wicks with simple and regular geometries, analytical relations are available for the determination of the effective permeabilities: Some of these relations are presented in the works of Scheidegger (1974), Chi (1976), Dunn and Reay (1982), Faghri (1995), and Ochterbeck and Peterson (1997). However, as can be seen from the photomicrographs presented in Figures 3.1 and 3.2, the geometries of the sintered powder-metal porous plates used in this work are quite complex and highly irregular: Thus, the aforementioned analytical relations cannot be used to determine their effective permeability; and this task is best accomplished using experiments.

In experimental techniques for the determination of the effective permeability of a porous medium, it is common to construct a setup similar to that of Darcy's (see Figure 3.6), assume macroscopically one-dimensional flow through the test section, and use an equation akin to Eq. (3.4). For this approach to be strictly correct, the porous material must be fitted in the flow passage in such a way that at its interface with the walls of the test section, the effective permeability is unaltered. For example, if the porous medium presented in Figure 3.4 is made up of a packed bed of solid spheres, then the corresponding hemispheres could be carefully glued to the inside surface of the confining walls of the test section. While the construction of this sort of specialized test section is feasible for uniform and regular porous media (such as a packed bed of solid spheres), it is not practical for porous materials made of sintered powder metals (such as those shown in Figures 3.1 and 3.2).

One approach to achieving good accuracy of the aforementioned one-dimensional approach with sintered powder-metal porous media is to weld, solder, or press-fit them into the test section, assume that this would change their porosity and permeability in a region immediately adjacent to the confining walls, say over a cross-sectional area $A_{c-s,peripheral}$, and ensure that $A_{c-s,peripheral} / A_{c-s} << 1$. However, this approach may not always be convenient, practical, or cost-effective. Another approach is to use laser machining to cut the sample of the sintered powder-metal porous medium (which seals its cut edge) and then use flat gaskets over peripheral regions of its top and bottom surfaces to seal it into the test section. Even with this approach, in order to ensure the validity of the one-dimensional approach, it is necessary to make $(A_{c-s} - A_{open,c-s}) / A_{c-s} << 1$, where

$A_{open,c-s}$ is the cross-sectional area on the top and bottom surfaces of the sample that is open to the flow (not blocked by the gaskets). In cases where it is not practical to make $(A_{c-s} - A_{open,c-s})/A_{c-s} << 1$, it is necessary to use a multidimensional formulation of Darcy's law to model the flow in the porous medium in between the gaskets, and use a numerical solution of the governing equations, with inputs of experimental data, to obtain the effective permeability. Such an experimental/numerical approach was used in this work to determine the effective permeability of the sintered powder-metal porous plates. The experimental setup is explained in the next subsection, followed by subsections describing the experimental data, the experimental/numerical procedure, and the results. A parametric numerical study of flow through the cylindrical sample was also conducted to assess how small $(A_{c-s} - A_{open,c-s})/A_{c-s}$ should be to ensure the validity of the aforementioned one-dimensional approach to the calculation of the effective permeability: The results of this parametric study are presented concisely in the final subsection.

3.4.2 Experimental Setup and Procedure

A schematic illustration of the experimental setup designed, constructed, and used to measure the effective permeability of samples of the sintered powder-metal plates is given in Figure 3.7. All-glass double-distilled deaerated water was used as the working fluid in the experiments. As shown in this figure, this water was gravity fed from a reservoir (a glass flask), which could be located at five different levels, 3.0, 2.5, 2.1, 1.6, and 1.2 m above the floor of the laboratory. A flexible tube was used to connect this reservoir to the test cell (labeled as sample holder in the figure) in which the porous material was held. A plug valve was used to turn the flow on and off, and a globe valve was used to control the flow rate. Two digital pressure gauges (Omega DPG1000B, 0-15 psig) were used for measuring the static pressure right before and just after the test cell. The mass flow rate of the water was obtained by collecting it in a small glass flask (250 ml Erlenmeyer flask) until it was almost full, recording the related time, weighing the flask plus the water (using an electronic balance accurate to ±0.01 g), subtracting out the mass of the empty (dry) flask, and dividing the mass of the water by the recorded time.

Two test cells were constructed for use with this setup: one for cylindrical (disk-shaped) test samples of 22.23 mm diameter (nominal); and the other for 127 mm x 127 mm (nominal) square test samples. As was mentioned earlier, two 6.35 mm thick (nominal) sintered powder-metal porous plates, one made of nickel 200 and the other of stainless steel 316, were investigated in this work. For each of these materials, the cylindrical and the square test samples were cut (using laser machining) from the same porous plate. Thus, if the experimental apparatus is designed and constructed properly, and the proposed procedures are valid, the effective permeability values obtained with the cylindrical and square samples cut from the same plate should be identical (within the experimental uncertainty).

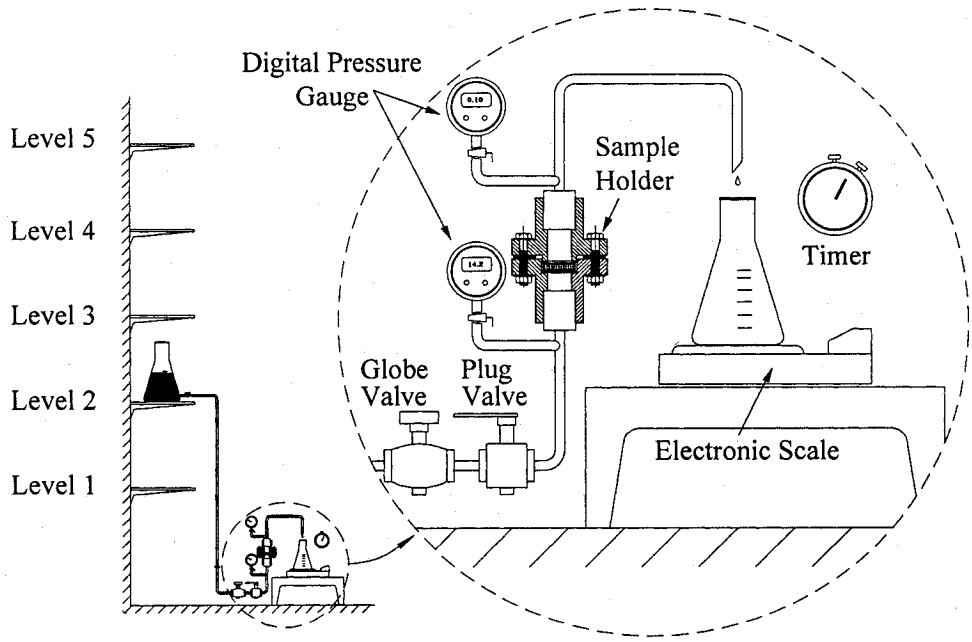

Figure 3.7: Schematic illustration of the experimental setup used for measurements of effective permeability.

As was mentioned earlier, flat gaskets were used for sealing the porous samples in the test cells. The areas sealed by gaskets on the top and bottom surfaces of the square and cylindrical samples are schematically presented in Figures 3.8 and 3.9. The peripheral surfaces of the samples were also sealed (water tight), as they were cut using laser machining.

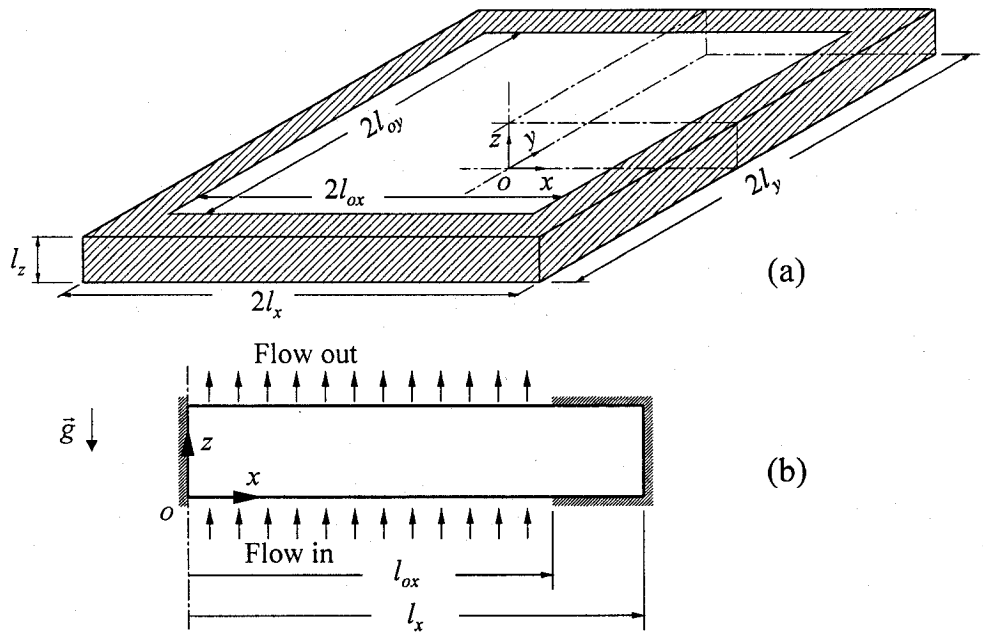

Figure 3.8: Geometrical description of the square porous samples: (a) isometric view of the sample (hatched regions represent areas sealed by the gaskets or the laser cutting); and (b) the $y = 0$ plan view of a quarter of the sample.

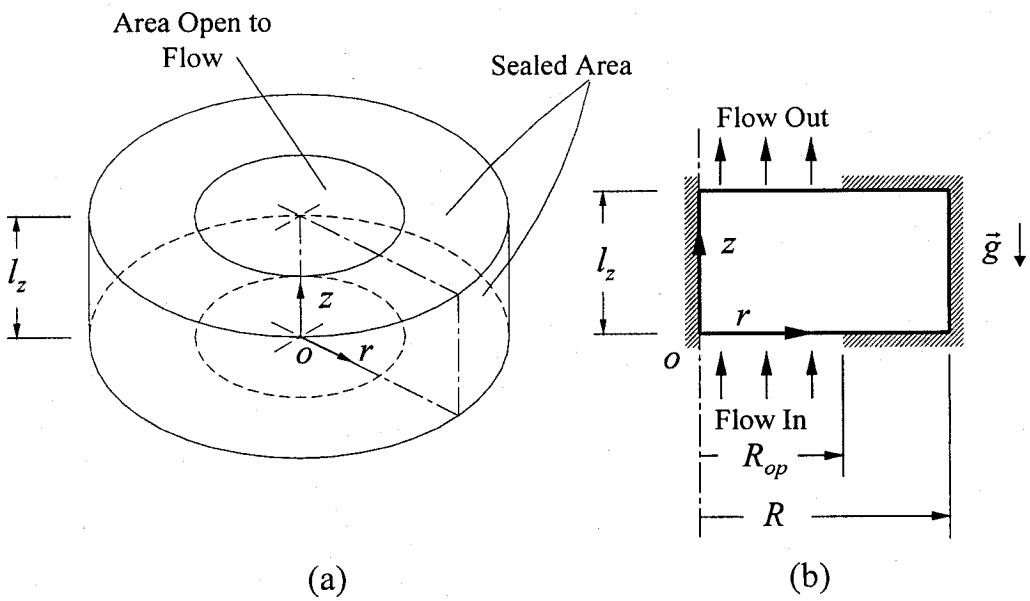

Figure 3.9: Geometrical description of the cylindrical (disk-shaped) porous samples: (a) isometric view of the sample; and (b) the rz plan view of the sample.

The dimensions of the square and cylindrical porous samples shown in Figures 3.8 and 3.9 are tabulated in Table 3.2.

Table 3.2: Dimensions of the square and the cylindrical porous samples.

	Square Porous Samples				
	l_x [m]	l_y [m]	l_z [m]	l_{ox} [m]	l_{oy} [m]
Nickel 200	6.34×10^{-2}	6.34×10^{-2}	6.65×10^{-3}	5.08×10^{-2}	5.08×10^{-2}
S.S. 316	6.33×10^{-2}	6.33×10^{-2}	6.54×10^{-3}	5.08×10^{-2}	5.08×10^{-2}

	Cylindrical Porous Samples		
	R [m]	l_z [m]	R_{op} [m]
Nickel 200	1.10×10^{-2}	6.65×10^{-3}	5.74×10^{-3}
S.S. 316	1.10×10^{-2}	6.54×10^{-3}	5.74×10^{-3}

In terms of the notation shown in Figures 3.8 and 3.9, the open (unblocked) area for flow through the bottom and top surfaces of the square and the cylindrical porous samples, respectively, are $A_{o,sq} = 4l_{ox}l_{oy}$ and $A_{o,cyl} = \pi R_{op}^2$.

Before starting the experiments, the test samples were cleaned using the same procedure as that used in the experiments to measure the maximum effective pore size (see Subsection 3.3.2). Then, the desired test sample and test cell combination were installed in the setup, and the entire flow circuit shown in Figure 3.7 was filled with double-distilled deaerated water. The reservoir was located at level 5 (highest point), and all valves were fully opened, allowing the water to flow through the porous sample. About six liters of water were circulated through the porous sample in order to purge any residual air or nitrogen inside it. Then the plug valve was closed, the empty 250 ml Erlenmeyer flask was weighed, and the water temperature was measured. The two electronic pressure gauges were turned on, and their readings were recorded: The difference between these readings in the no-flow condition represents the hydrostatic pressure drop across the porous sample. This hydrostatic pressure drop is subtracted from

the difference in the readings of these pressure gauges with the water flowing through the porous sample to obtain the friction pressure drop (assuming that the minor losses in the fittings at the low flow rates used in these experiments are negligible compared to the friction pressure drop through the porous material).

After the above-mentioned preparations and preliminary measurements, the experimental setup was considered ready for the final measurements. For each sample of the porous plates and each level of the reservoir, the arithmetic means of at least three sets of measurements of the mass flow rate of the water and the associated frictional pressure drop across the porous sample with both the plug valve and the globe valve fully open were recorded first; and then several additional sets of these measurements were obtained at lower flow rates (using the globe valve for flow control).

3.4.3 Experimental Data

The experimental data obtained for the cylindrical and the square samples made of nickel 200 are presented in Figures 3.10 and 3.11, respectively; these data for the cylindrical and square samples made of stainless steel 316 are presented Figures 3.12 and 3.13, respectively. The symbols in these figures represent the experimental data, and the straight lines are least-square fits to these data and forced to pass through the origin (0,0): The equations that represent these lines are given for each figure separately in its caption. As is seen in these figures, for both geometries and both materials, the friction pressure drop across the porous sample, $(\Delta P)_{fric}$, varies linearly with the mass flow rate, $\dot{m}$, indicating that the flow is in the Darcy regime for all cases considered here.

The absolute uncertainties in the pressure-drop measurements were all less than ±365.5 Pa. The vertical error bars in Figures 3.10 to 3.13 represent these absolute uncertainties in the measurements of the friction pressure drop across the porous samples. The maximum relative uncertainties in the pressure-drop measurements for the square and cylindrical nickel 200 samples (Figures 3.10 and 3.11) are ±7.12% and ±4.33%, respectively; for the cylindrical stainless steel 316 sample (Figure 3.12), this maximum relative uncertainty is ±5.15%. For the square stainless steel 316 sample, however, the friction pressure drops are relatively low and thus the relative uncertainties in these data are very high, as can be seen from the data presented in Figure 3.13: Thus, these data are

useless and were discarded. The uncertainties in the mass flow rate data were found to be less than ±1.0%.

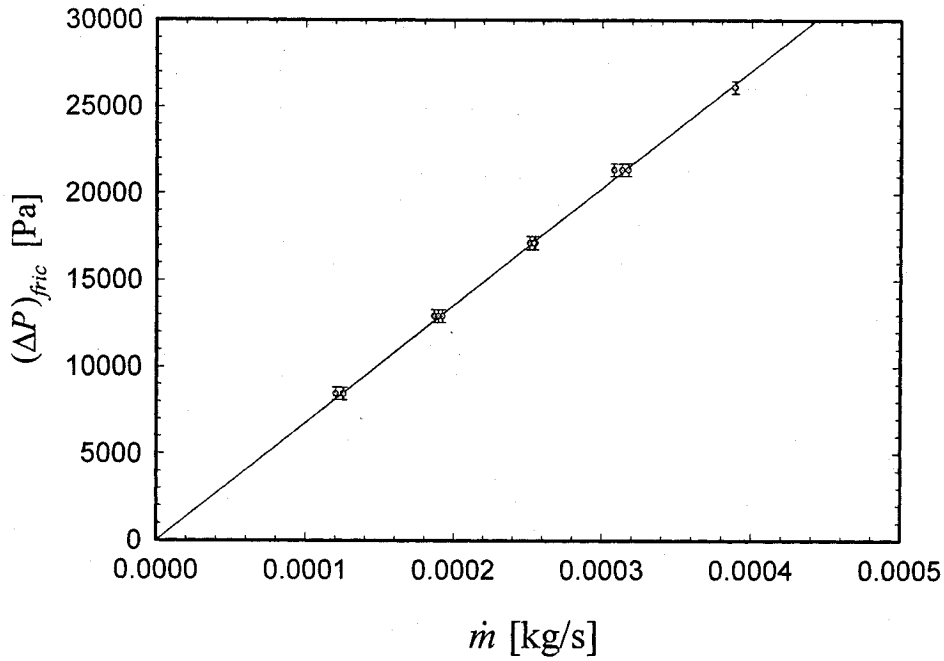

Figure 3.10: Data from the permeability experiments on cylindrical samples of nickel 200. Least-squares straight line: $(\Delta P)_{fric}\,[\text{Pa}] = 67{,}731{,}847.63\ \dot{m}\ [\text{kg/s}]$.

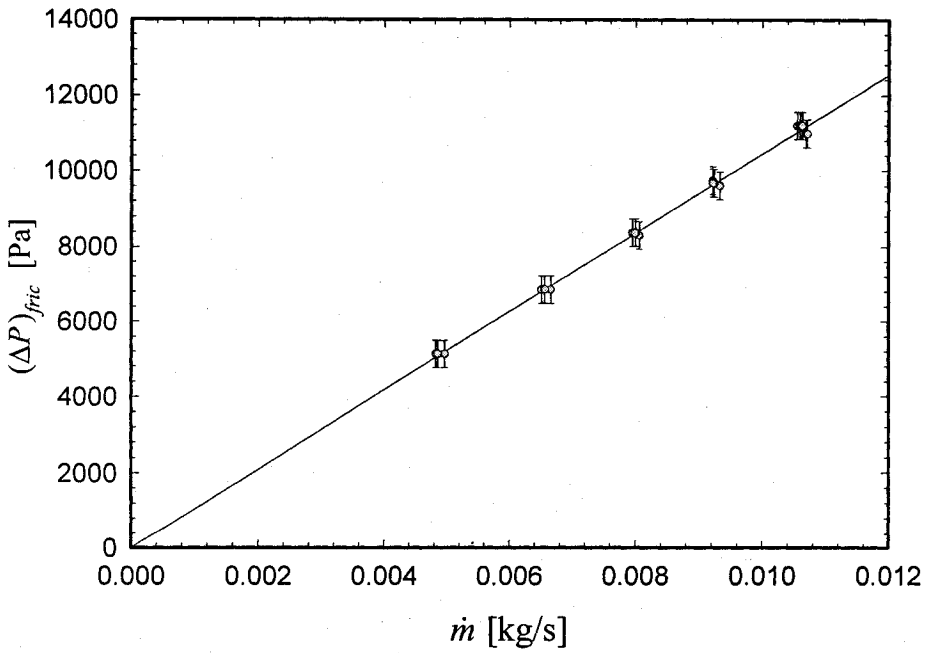

Figure 3.11: Data from the permeability experiments on square samples of nickel 200. Least-squares straight line: $(\Delta P)_{fric}\,[\text{Pa}] = 1{,}045{,}388.23\ \dot{m}\ [\text{kg/s}]$.

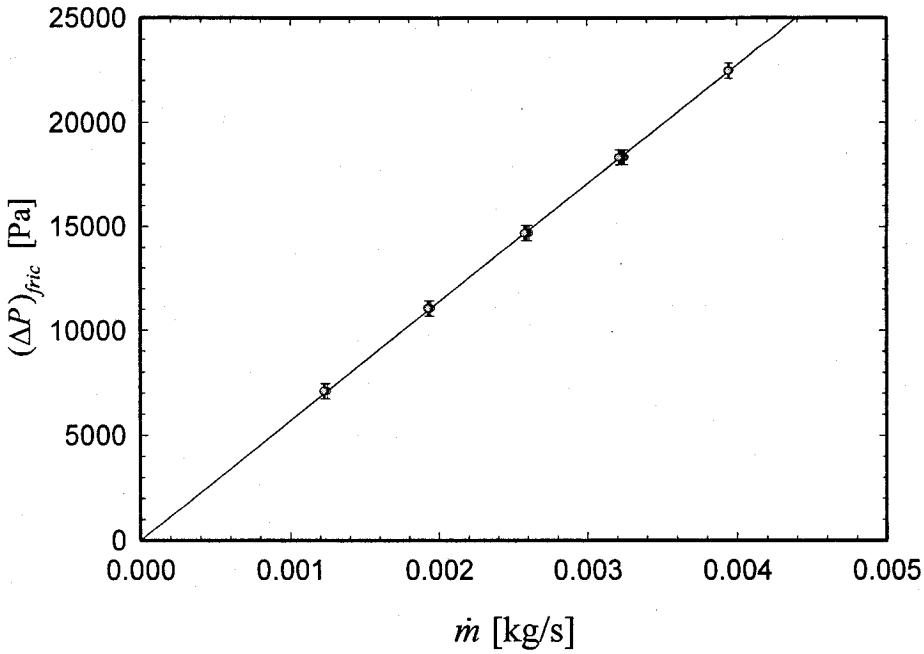

Figure 3.12: Data from the permeability experiments on cylindrical samples of stainless steel 316. Least-squares straight line: $(\Delta P)_{fric}\,[\text{Pa}] = 5{,}688{,}804.79\ \dot{m}\ [\text{kg/s}]$.

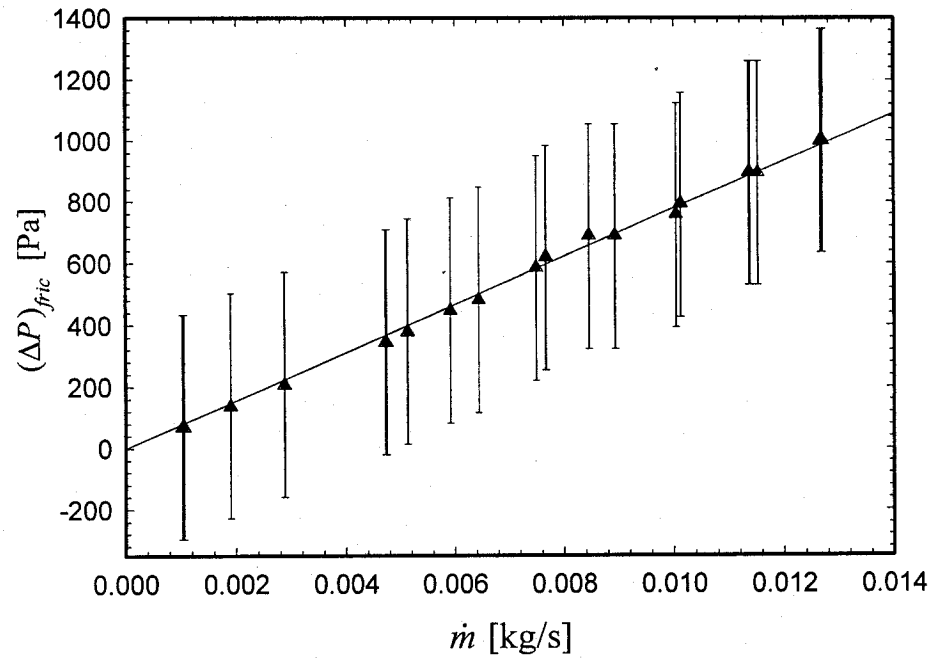

Figure 3.13: Data from the permeability experiments on square samples of stainless steel 316. Least-squares straight line: $(\Delta P)_{fric}\,[\text{Pa}] = 77{,}955.72\ \dot{m}\ [\text{kg/s}]$.

3.4.4 Calculation of Effective Permeability Based on the Assumption of One-Dimensional Flow and Related Difficulties

If one-dimensional flow through the samples of the porous media is assumed, then the area-averaged liquid velocity is given by the following expressions:

$$\text{For the square samples: } U = \dot{m}/(\rho A_{o,sq}) = \dot{m}/(\rho 4 l_{ox} l_{oy})$$
$$\text{For the cylindrical samples: } U = \dot{m}/(\rho A_{o,cyl}) = \dot{m}/(\rho \pi R_{op}^2) \qquad (3.5)$$

In this equation, l_{ox}, l_{oy}, and R_{op} are the dimensions of the open (unblocked) flow areas on the top and bottom surfaces of the samples (see Figures 3.8 and 3.9, and also Table 3.2). The area-averaged velocity, U, given by Eq. (3.5) is used in the one-dimensional formulation of Darcy's law, Eq. 3.4, to calculate the permeability K.

The experiments were run at a temperature of 24 °C. At this temperature, the values of mass density and dynamic viscosity of distilled water are the following [Incropera and DeWitt (2002)]: ρ_l = 998.06 kg/m³ and μ = 9.175×10^{-04} kg/m-s. With these properties of water, the experimental data presented in Figures 3.10 and 3.11, the U values calculated using Eq. 3.5, and Eq. (3.4), the following values of the effective permeability of the nickel 200 plate were determined:

$$\text{For the square samples: } K = 5.669\text{x}10^{-13}\ \text{m}^2$$
$$\text{For the cylindrical samples: } K = 8.719\text{x}10^{-13}\ \text{m}^2 \qquad (3.6)$$

The results presented in Eq. (3.6) show that the permeability of the nickel 200 sintered porous plate calculated using data obtained with the cylindrical sample is about 1.54 times that obtained with the square sample. As was stated earlier, both the cylindrical and the square samples were cut from the same nickel 2000 sintered porous plate, thus the permeability values obtained with these samples should be identical (within the experimental uncertainty). Thus, the inconsistent results given in Eq. (3.6) show that the assumption of one-dimensional flow is questionable in this case. To explore this issue further, it is necessary to solve a multidimensional formulation of Darcy's law, with the above-mentioned experimental data as inputs, and check the corresponding values of the effective permeability. This multidimensional experimental/numerical approach to the calculation of the effective permeability and the results are presented in the following subsection.

3.4.5 A Multidimensional Experimental/Numerical Approach to the Determination of Effective Permeability

For flow through a porous medium with a constant permeability, K, Darcy's law in the Cartesian coordinate system (x, y, z) can be written as follows [Kaviany (1999); Nield and Bejan (2006)]:

$$u_x = -\left(\frac{K}{\mu}\right)\frac{\partial \mathrm{P}}{\partial x};\quad u_y = -\left(\frac{K}{\mu}\right)\frac{\partial \mathrm{P}}{\partial y};\quad u_z = -\left(\frac{K}{\mu}\right)\frac{\partial \mathrm{P}}{\partial z} \tag{3.7}$$

In this equation, u_x, u_y and u_z are the velocity components in x, y, and z directions, respectively, and P is the reduced pressure: $\mathrm{P} = P + \rho_l g z$, where P is the static pressure, g is the gravitational acceleration, and the term $\rho_l g z$ represents the hydrostatic pressure. It is assumed here that the gravitational acceleration vector is directed along the negative z direction.

Assuming steady-state, constant property, incompressible fluid flow in the porous medium, the continuity equation is

$$\frac{\partial u_x}{\partial x} + \frac{\partial u_y}{\partial y} + \frac{\partial u_z}{\partial z} = 0 \tag{3.8}$$

Combining Eqs. (3.7) and (3.8), the following equation is obtained:

$$\frac{\partial^2 \mathrm{P}}{\partial x^2} + \frac{\partial^2 \mathrm{P}}{\partial y^2} + \frac{\partial^2 \mathrm{P}}{\partial z^2} = 0 \tag{3.9}$$

For an axisymmetric, constant property flow through a porous material with constant permeability, K, the Eqs. (3.7) to (3.9) can be written with respect to the cylindrical coordinate system as follows:

$$u_r = -\left(\frac{K}{\mu}\right)\frac{\partial \mathrm{P}}{\partial r};\quad u_z = -\left(\frac{K}{\mu}\right)\frac{\partial \mathrm{P}}{\partial z} \tag{3.10}$$

$$\frac{1}{r}\frac{\partial (r u_r)}{\partial r} + \frac{\partial u_z}{\partial z} = 0 \tag{3.11}$$

$$\frac{1}{r}\frac{\partial}{\partial r}\left(r\frac{\partial \mathrm{P}}{\partial r}\right) + \frac{\partial^2 \mathrm{P}}{\partial z^2} = 0 \tag{3.12}$$

With reference to the schematic representations of the calculation domains and the notations given in Figures 3.8 and 3.9, the following two sets of equations give the boundary conditions that apply to the square and cylindrical samples, respectively:

$$
\begin{aligned}
&x=0;\ 0\le y\le l_y;\ 0\le z\le l_z \quad \frac{\partial \mathrm{P}}{\partial x}=0 \\
&x=l_x;\ 0\le y\le l_y;\ 0\le z\le l_z \quad \frac{\partial \mathrm{P}}{\partial x}=0 \\
&y=0;\ 0\le x\le l_x;\ 0\le z\le l_z \quad \frac{\partial \mathrm{P}}{\partial y}=0 \\
&y=l_y;\ 0\le x\le l_x;\ 0\le z\le l_z \quad \frac{\partial \mathrm{P}}{\partial y}=0 \\
&z=0;\ 0\le x\le l_{ox};\ 0\le y\le l_{oy} \quad \mathrm{P}=\mathrm{P}_1 \\
&z=l_z;\ 0\le x\le l_{ox};\ 0\le y\le l_{oy} \quad \mathrm{P}=\mathrm{P}_2 \\
&z=0;\ l_{ox}\le x\le l_x;\ 0\le y\le l_y \quad \frac{\partial \mathrm{P}}{\partial z}=0 \\
&z=0;\ 0\le x\le l_{ox};\ l_{oy}\le y\le l_y \quad \frac{\partial \mathrm{P}}{\partial z}=0 \\
&z=l_z;\ l_{ox}\le x\le l_x;\ 0\le y\le l_y \quad \frac{\partial \mathrm{P}}{\partial z}=0 \\
&z=l_z;\ 0\le x\le l_{ox};\ l_{oy}\le y\le l_y \quad \frac{\partial \mathrm{P}}{\partial z}=0
\end{aligned}
\tag{3.13}
$$

$$
\begin{aligned}
&r=0;\ 0\le z\le l_z \quad \frac{\partial \mathrm{P}}{\partial r}=0 \\
&r=R;\ 0\le z\le l_z \quad \frac{\partial \mathrm{P}}{\partial r}=0 \\
&z=0;\ 0\le r\le R_{op} \quad \mathrm{P}=\mathrm{P}_1 \\
&z=l_z;\ 0\le r\le R_{op} \quad \mathrm{P}=\mathrm{P}_2 \\
&z=0;\ R_{op}\le r\le R \quad \frac{\partial \mathrm{P}}{\partial z}=0 \\
&z=l_z;\ R_{op}\le r\le R \quad \frac{\partial \mathrm{P}}{\partial z}=0
\end{aligned}
\tag{3.14}
$$

In these equations, P_1 and P_2 are the reduced pressures that prevail over the inlet and outlet flow areas of the porous samples.

Equations (3.9) and (3.12) are akin to the equations that govern steady-state, constant-property, diffusion-type problems with a diffusion coefficient of one (unity) and no (zero) volumetric source term. A well-established finite volume method proposed by Patankar (1980) was used to discretize and solve Eqs. (3.9) and (3.12) subject to the boundary conditions given by Eqs. (3.13) and (3.14), respectively: In these numerical solutions, P_2 was set equal to zero (for convenience), and P_1 was set equal to a specified value, such that ($P_1 - P_2$) covered the range of the friction pressure drops involved in the permeability experiments (see Figures 3.10 – 3.12). It should be noted here that as the working fluid (water in the permeability experiments) is assumed to be incompressible, the absolute level of pressure is not important (so it can be set to any convenient value) and it is the pressure difference imposed across the porous sample that drives the flow through it [Patankar (1980)]. In each case, once the pressure field was computed, the corresponding

inlet (or outlet) mass flow rate was calculated with velocity components calculated using Eq. (3.7) for the square sample and Eq. (3.11) for the cylindrical sample, and prescribed values of the liquid mass density, ρ_l, and dynamic viscosity, μ: These calculated mass flow rates were in the form $\Im K$, where $\Im$ is a computed number and K is the (unknown) permeability of the porous medium. The experimental data were used to determine the permeability K as follows: For each sample and a prescribed value of ($P_1 - P_2$), the computed mass flow rate, $\Im K$, was equated to the corresponding experimentally measured value, $\dot{m}$, and the permeability was calculated using $K = \dot{m} / \Im$.

To test for grid independence of the numerical results, the computations were conducted with $(K/\mu) = 1$ on two different grids for each sample: For the cylindrical sample with grids of 101×401 and 126x501 nodes (in the r and z directions) the relative difference between the calculated values of permeability was less than ±0.05%; and for the square sample with grids of 61x61x31 and 71x71x36 nodes (in the x, y, and z directions), the relative difference between the calculated values of permeability was less than ±0.15%. Based on these findings, in the final computations, a grid of 101x401 nodes was used for the cylindrical sample and a grid of 61x61x31 nodes was used for the square sample.

The numerical results obtained for the cylindrical and square samples of the sintered powder-metal plate made of nickel 200 plate subjected to an overall pressure difference ($P_1 - P_2$) of 1.0 kPa are presented in Figures 3.12 and 3.13, respectively.

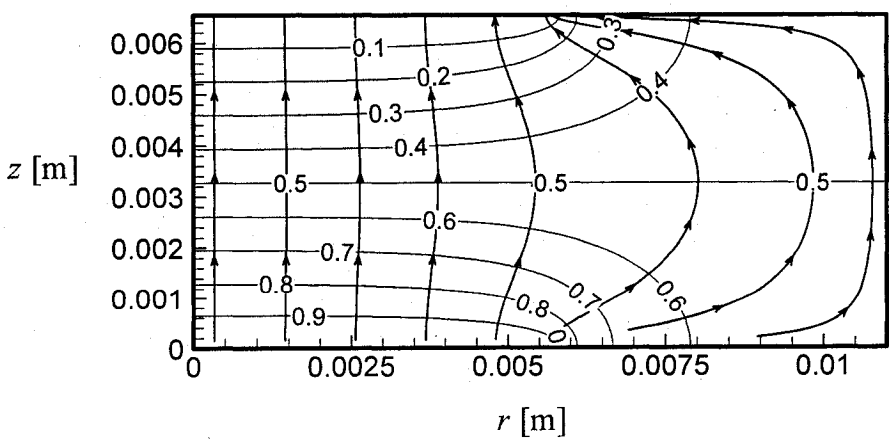

Figure 3.14: Numerically calculated isobars and streamlines (not to scale) in a diametrical cross section of the cylindrical sample of the nickel 200 porous plate: Pressures imposed at the inlet and outlet planes are P_1=1 kPa and P_2= 0 kPa, respectively.

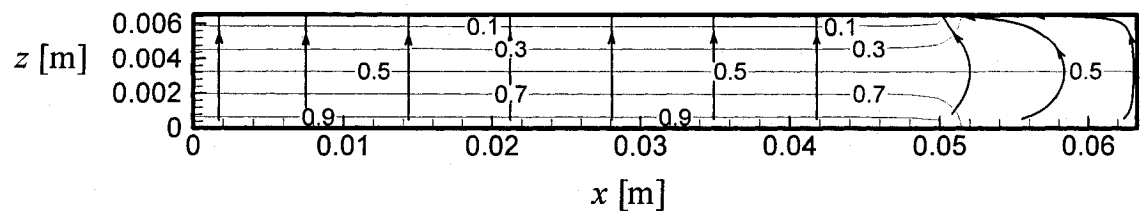

Figure 3.15: Numerically calculated isobars and streamlines (not to scale) in the $y = 0$ plane of the square sample of the nickel 200 porous plate: Pressures imposed at the inlet and outlet planes are P_1=1 kPa and P_2= 0 kPa, respectively (only half of the width of the sample is presented here).

The results for the cylindrical sample (R = 1.10 x 10^{-2} m, l_z = 6.65 x 10^{-3} m, and R_{op} = 5.74 x 10^{-3} m) presented in Figure 3.14, show that the streamlines (lines with arrow heads) are significantly bent (indicating two-dimensional flow) in the outer regions, over almost half of the radius: This is because the sealing gaskets block significant portions of the top and bottom surfaces of this sample (see Figure 3.9): $(R - R_{op})/R$ = 0.478. For the square sample ($l_x = l_y$ = 6.34 x 10^{-2} m, l_z = 6.65 x 10^{-3} m, and $l_{ox} = l_{oy}$ = 5.08 x 10^{-2} m), the portions of the top and bottom surfaces blocked by the gaskets (see Figure 3.8) are not as large as those for the cylindrical sample, with $(l_x - l_{ox})/l_x = (l_y - l_{oy})/l_y$=0.203: Correspondingly, the results presented in Figure 3.15 show that the streamlines are significantly bent only over about 20% of the outer portion of the half-width.

The values of the permeability obtained using the proposed experimental/numerical method for the cylindrical and the square samples of the nickel 200 porous plate are 5.563×10^{-13} m^2 and 5.409×10^{-13} m^2, respectively. In comparison with the corresponding results obtained using the simple one-dimensional method (see the previous subsection), the permeability for the cylindrical sample is about 36.2% lower (as the multidimensional effects are quite pronounced, and the effective flow area in the central region of the sample in between the gaskets is quite a bit larger than the open areas in the inlet and outlet planes), while the permeability for the square sample is only about 4.6% lower (as the multidimensional effects are not too pronounced). Furthermore, the proposed experimental/numerical method yields consistent results, in that the relative difference between the values of the permeability obtained for the cylindrical and square samples is only 2.77%, which is well within the uncertainty in the experimental measurements of the pressure difference across the samples.

In the permeability experiments, the pressure drops across the cylindrical sample were much higher than those across the square sample. As a result, there is much less uncertainty in the experimental results for the cylindrical sample than those in the results for the square sample. Thus, the value of the permeability obtained with the cylindrical sample is assumed to apply to the nickel 200 sintered powder-metal plate.

The permeability values obtained with the proposed numerical/experimental approach for the cylindrical samples of the nickel 200 and the stainless steel 316 porous plates are the following:

Nickel 200	$K = 5.563 \times 10^{-13}$ m^2 ($\pm$7.22%)
Stainless steel 316	$K = 6.576 \times 10^{-12}$ m^2 ($\pm$7.75%)

3.4.6 Flow through Cylindrical Samples: A Parametric Numerical Study

A parametric numerical study of flow through cylindrical samples (see Figure 3.9) of a porous medium was conducted to assess when the simple one-dimensional approach described in Subsection 3.4.4 is adequate for the calculation of the effective permeability. With reference to the schematic illustration of the cylindrical sample in Figure 3.9, two geometrical parameters were investigated in this study, the ratio of the radius to the thickness, $\gamma = R / l_z$, and the ratio of the radius of the open area to the radius of the sample, $\omega = R_{op} / R$. The results of this parametric study are presented concisely in this subsection.

The variation of the ratio of the permeability obtained with the one-dimensional model, $K_{1\text{-}D}$, to that yielded by the numerical/experimental method (multi-dimensional flow model), $K_{Multi\text{-}D}$, for a range of values of γ and ω for the cylindrical sample (Figure 3.9) are presented in Figure 3.16. These results show that for a fixed value of γ, as ω is increased, the overestimation of K by the one-dimensional model is decreased, and, when $\omega = 1$, $K_{1\text{-}D}$ becomes equal to $K_{Multi\text{-}D}$, as expected. For a fixed value of ω, $K_{1\text{-}D} / K_{Multi\text{-}D}$ decreases (approaching 1) with an increase of γ. Furthermore, $K_{1\text{-}D} / K_{Multi\text{-}D}$ is more sensitive to variations in γ at small values of ω. Similar results were obtained for the square sample: In order to avoid unnecessary repetition, they are not presented here.

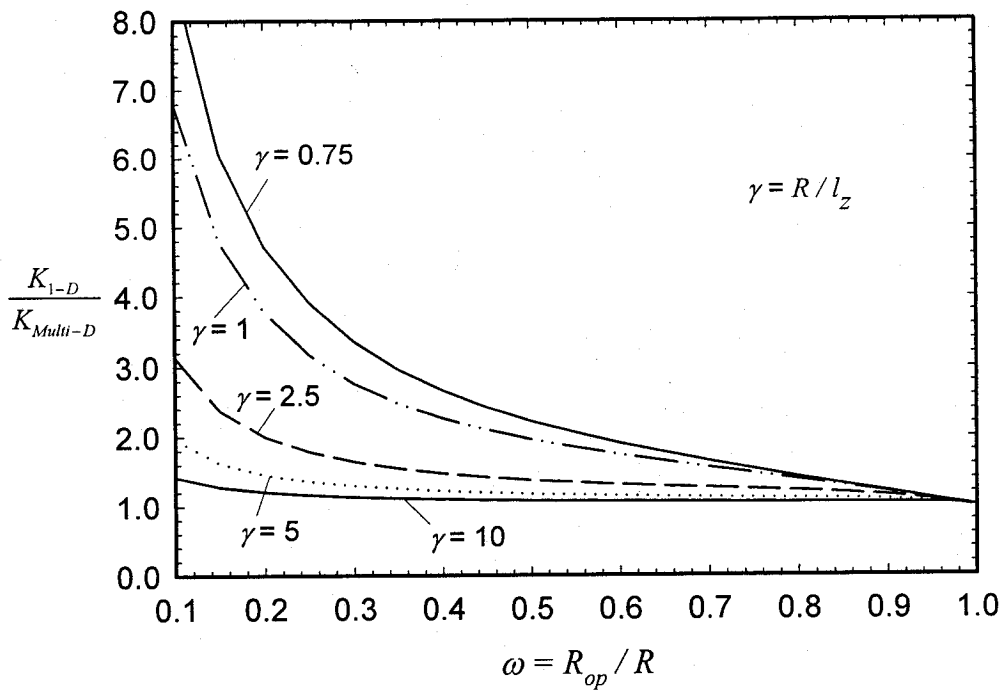

Figure 3.16: Results of a parametric numerical study of flow through cylindrical samples of a porous medium.

The results in Figure 3.16 show that with cylindrical samples of a porous medium (akin to that shown in Figure 3.9), for $\gamma \geq 5$ and $\omega \geq 0.5$, the one-dimensional model provides a simple and effective way of estimating the permeability from experimental data on $(P_1 - P_2)$ and $\dot{m}$ (see Subsection 3.4.3). The graph presented in Figure 3.16 can also be used to correct the permeability values obtained with the simple one-dimensional model for any combination of values of γ and ω.

3.5 Effective Thermal Conductivity

In this section, first, some available analytical and semi-analytical correlations for the effective thermal conductivity of porous media are reviewed. Following that, the experimental apparatus and procedure that were used for measuring the effective thermal conductivity of the sintered power-metal plates made of nickel 200 and stainless steel 316 saturated with water (all-glass, double-distilled, and deaerated) are described. Then, benchmarking tests of the experimental apparatus and procedure are presented. Next, the experimental results are presented and discussed. Finally, a new empirical correlation is

proposed for the effective thermal conductivity of liquid-saturated sintered powder-metal porous materials. This empirical correlation is formulated by extending the theoretical ideas proposed earlier by Hadley (1986).

Many researchers have proposed analytical and numerical correlations for the prediction of the effective thermal conductivity of fluid-saturated porous materials as a function of the fluid and the solid thermal conductivities and the geometrical details of the porous structure. Examples of such attempts include the contributions of Maxwell (1954), Kunii and Smith (1960), Dul'nev (1965), Ofuchi and Kunii (1965), Hadley (1986), Prasad et al. (1989), Bauer (1993), Hsu et al. (1995), Calmidi and Mahajan (1999), Boomsma and Poulikakos (2001), and Bahrami et al. (2004). In order to predict the effective thermal conductivity of porous beds made of *spherical* particles subjected to a compressive load, the area of contact between the particles must be accounted for in the model. For such porous beds, when the area of contact can be calculated by assuming elastic deformation of the particles, the effects of surface roughness and coatings on the particles are negligible, and the arrangements of the spherical particles are regular (simple cubic, body-centered cubic, or face-centered cubic), analytical models and correlations have been proposed by Chen and Tien (1973), Batchelor and Obrien (1977), Ogniewicz and Yovanovich (1978), and Sangani and Acrivos (1983). Reviews of several of the aforementioned and additional analytical correlations are available in the works of Tsotsas and Martin (1987), Tavman (1996), Kaviany (1999), and Hsu (2000). Analytical models for the effective thermal conductivity of packed beds of rough spherical particles have been proposed by Bahrami et al. (2004). Such analytical correlations do not provide reliable predictions of the effective thermal conductivity of fluid-saturated sintered powder-metal plates for the following reasons: The metal particles are usually angular shaped, as spherical powders do not press together well [Hadley (1986)]; the geometry of the solid porous structure may be considered random (see Figures 3.1 and 3.2) and quite different from a packed bed of uniform solid spheres with a regular arrangement [Hadley (1986); Leong et al. (1997)]; and the available analytical correlations do not properly account for the effects of the sintering process [Kunii and Smith (1960)]. Therefore, empirical or semi-empirical correlations based theoretical considerations supplemented

by inputs of data from experimental investigations are required for accurate predictions of the effective thermal conductivity of fluid-saturated sintered powder-metal plates.

In the published literature, there are many experimental investigations, and corresponding correlations, of the effective thermal conductivity of porous materials made of sintered powders and fibers, with a liquid, gas, or vacuum in the interstices or voids. Examples of such investigations include the works of Alexander (1972), Singh et al. (1973), Hadley (1986), and Mantle and Chang (1991). The works of Singh et al. (1973) and Mantle and Chang (1991) pertain to sintered metal fibers; Alexander (1972) investigated both sintered metal fibers and powders; and Hadley considered porous mediums made of unconsolidated and consolidated (cold-pressed) packed metal powders. A semi-empirical correlation for the effective thermal conductivity of consolidated porous media, such as sandstone or sintered porous metals, has also been proposed by Kunii and Smith (1960). In the aforementioned investigations, not much attention has been paid to the variation of the effective thermal conductivity with the average temperature of the porous material. However, an experimental investigation by Peterson and Fletcher (1987) does focus on the variation of the effective thermal conductivity of dry (air filled) and water-saturated sintered nickel 200 and sintered copper (C102) powders with mean temperature in the range 25°C to 100°C.

In this work, the emphasis is on the experimental determination of the effective thermal conductivity of water-saturated sintered powder-metal plates as a function of their mean temperature in the range 20°C to 150°C. This temperature range exceeds that considered by Peterson and Fletcher (1987). Two sintered powder-metal plates, one made of nickel 200 and the other of stainless steel 316, each of nominal dimensions 127 mm x 127 mm x 6.35 mm, were used as the test samples in the experiments. As was presented in the Section 3.2, the porosities of these test samples were measured to be 28.10% and 46.45% for the nickel 200 and the stainless steel 316 plates, respectively. The experimental measurements obtained in this work and also the data presented by Peterson and Fletcher (1987) were used to propose a novel empirical correlation for the variation of the effective thermal conductivity of water-saturated sintered powder-metal plates with mean temperature in the range 20°C to 150°C. This correlation is formulated by extending the theoretical ideas proposed by Hadley (1986), as was stated earlier in this

subsection, and also borrowing some ideas from the earlier work of Kunii and Smith (1960).

3.5.1 Overview of Some Available Correlations

Some well-know analytical and semi-analytical correlations are briefly reviewed here, in order to facilitate comparisons with the experimental results and set the stage for the development of a new correlation in a subsequent subsection. The correlations reviewed in this section relate the *effective* thermal conductivity of a porous media, k_e, to its porosity, ε, and the thermal conductivities of the fluid and solid phases, k_f and k_s, respectively.

The parallel and series arrangements of the solid and the fluid are the simplest geometrical structures considered in analytical models of the effective thermal conductivity of porous media; and these arrangements yield upper and lower limits, respectively, of this property [Batchelor and Obrien (1977); Hadley (1986); Kaviany (1999)]. The parallel model yields the following result:

$$k_e = \varepsilon k_f + (1-\varepsilon) k_s \tag{3.15}$$

The following expression is obtained using the series model:

$$k_e = \frac{k_f k_s}{\varepsilon k_s + (1-\varepsilon) k_f} \tag{3.16}$$

Maxwell (1954) conducted analytical studies of two solid-fluid systems and proposed equations for the prediction of their effective specific resistance (electrical). His work can be adapted to obtain the corresponding effective thermal conductivity of these solid-fluid systems akin to fluid-saturated porous media [Hadley (1986)]. The first such system consists of a dilute suspension of solid spherical particles in an infinite uniform fluid, and its effective thermal conductivity is given by the following equation:

$$\frac{k_e}{k_f} = \frac{2\varepsilon + (k_s / k_f)(3-2\varepsilon)}{3-\varepsilon + (k_s / k_f)\varepsilon} \tag{3.17}$$

This equation has been referred to by Hadley (1986) as the "lower Maxwell formula". The second system analyzed by Maxwell consists of a solid body containing a dilute dispersion of fluid-filled voids. The effective thermal conductivity of this second system

is given by the following equation, referred to by Hadley (1986) as the "upper Maxwell formula":

$$\frac{k_e}{k_f}=\frac{2\left(k_s/k_f\right)^2(1-\varepsilon)+(1+2\varepsilon)\left(k_s/k_f\right)}{(2+\varepsilon)\left(k_s/k_f\right)+1-\varepsilon} \tag{3.18}$$

Dul'nev (1965) modeled porous materials as a combination of cubic unit cells with interconnected pores. He applied a resistance analogy to obtain an effective thermal conductivity of the unit cell, based on an assumption of unidirectional heat conduction. His analytical solution is presented below:

$$\begin{aligned}&\frac{k_e}{k_s}=s^2+\frac{k_f}{k_s}(1-s)^2+\frac{2\left(k_f/k_s\right)s(1-s)}{1-s\left(1-\left(k_f/k_s\right)\right)}\\&s=y/(0.5-y)/\left[1-y/(0.5-y)\right]\\&4y^3-3y^2+(1-\varepsilon)/4=0\end{aligned} \tag{3.19}$$

Alexander (1972) experimentally determined the effective thermal conductivities of some samples of porous materials saturated with water (wet) or air (dry). These samples were made of metal felts, sintered powders, layers of wire cloth, and unconsolidated bead beds. He used his experimental data to propose the following empirical correlation:

$$k_e=k_f\left(k_s/k_f\right)^{(1-\varepsilon)^\delta} \tag{3.20}$$

The following values are recommended for the parameter δ in this equation [Alexander (1972)]: For metal felts, δ = 0.34; sintered powders, δ = 0.53; layers of wire cloth, δ = 0.59; and for unconsolidated beads, δ = 0.44.

Hadley (1986) has proposed a general approach to the modeling of the effective thermal conductivity of packed metal powders. The approach involves a combination of a theoretical expression that is appropriate for conduction through a contiguous solid (the upper Maxwell formula) and another such expression that is suitable for conduction through a suspension (not necessarily dilute) of solid particles. For a solid-fluid (two-phase) system, where the solid is connected (consolidated by cold pressing), Hadley (1986) proposed the following equation for the effective thermal conductivity:

$$\frac{k_e}{k_f}=(1-\alpha_{con})\left[\frac{\varepsilon f_0+(k_s/k_f)(1-\varepsilon f_0)}{1-\varepsilon(1-f_0)+(k_s/k_f)\varepsilon(1-f_0)}\right] + \alpha_{con}\left[\frac{2(k_s/k_f)^2(1-\varepsilon)+(1+2\varepsilon)(k_s/k_f)}{(2+\varepsilon)(k_s/k_f)+1-\varepsilon}\right] \tag{3.21}$$

where the values of the parameters α_{con} and f_o are to be determined with reference to experimental data. The parameter α_{con} depends strongly on what Hadley (1986) refers to as the "degree of consolidation"; so it will be referred to here as the consolidation parameter. The value of the parameter f_o lies between the theoretical upper and lower limits provided by Maxwell's formulas: Thus,

$$f_{o,\min}=\frac{2}{3} \quad ; \quad f_{o,\max}=\frac{2(k_s/k_f)}{2(k_s/k_f)+1} \quad ; \quad f_{o,\min}<f<f_{o.\max} \tag{3.22}$$

Here, $(k_s/k_f)\geq 1$. For the experimental data of Hadley (1986), $0.8\leq f_o\leq 0.9$. The values of the parameter α_{con} as a function of $(1-\varepsilon)$ for evacuated samples $(k_s/k_f\rightarrow\infty)$ have been presented graphically by Hadley (1986): Nonlinear (semi-log) curve fits to Hadley's data for α_{con}, as proposed by Kaviany (1999), are given below:

$$\log(\alpha_{con})=\begin{cases}-4.898\varepsilon & for\ 0\leq\varepsilon\leq 0.0827\\ \left(-0.405-3.154(\varepsilon-0.0827)\right) & for\ 0.0827<\varepsilon\leq 0.298\\ \left(-1.084-6.778(\varepsilon-0.298)\right) & for\ 0.298<\varepsilon\leq 0.580\end{cases} \tag{3.23}$$

Bauer (1993) has presented an analytical approach for the determination of the effective thermal conductivity of porous media. He started with the theoretical lower formula of Maxwell, Eq. (3.17), for dilute suspensions of spherical particles, and then extended it to suspensions of solid particles of random shape and any concentration. He proposed the following implicit correlation for the calculation of the effective thermal conductivity of porous materials with a single type of randomly oriented pores:

$$\frac{k_e-k_p}{k_o-k_p}\left(\frac{k_o}{k_e}\right)^{1-2/(3\beta)}=1-\varepsilon \tag{3.24}$$

Here, k_o and k_p denote, respectively, the thermal conductivities of the continuous medium and the material inside the pores. The term, β, in this equation is a shape factor: Its value

lies in the range $2/3 < \beta \leq 1$, with the upper limit of unity applicable to spherical pores. Its value for specific materials is determined using corresponding experimental data.

3.5.2 Experimental Investigation

Apparatus

An apparatus for measuring the effective thermal conductivity of water-saturated sintered porous metals was designed and built for use in this work. Its design is based on the so-called *steady-state comparative method* [Touloukian et al. (1970)]. In this method, a reference sample of known thermal conductivity is placed in series with the sample for which this property is to be determined. One end of the assembly of these two samples is heated while the other end is cooled. When steady-state conditions of operation are reached, it is assumed that the same heat flux flows through the centerlines of both samples. With this assumption and measurements of the temperature drops across each sample (along their centerline), the unknown thermal conductivity is obtained.

The goal in this work was to measure the effective thermal conductivity of water-saturated sintered powder-metal plates with average temperatures in the range 20°C to 150°C. To achieve this goal, two special requirements had to be successfully met in the design of the porous metal sample holder: It had to allow pressurization to a level that was sufficiently high to prevent boiling of the water at temperatures up to 150°C; and it had to safely and reliably accommodate the thermal volumetric expansion of the liquid water. The experimental apparatus was also designed to meet some additional requirements elaborated by Singh et al. (1973): The porous metal sample had to be fully saturated with liquid water at all times; radiation and natural convection in the porous metal samples had to be negligible compared to the heat conduction; all thermal contact resistances had to be minimized; and soldering or welding of the porous metal had to be avoided in order to ensure that it properties were not altered.

A schematic illustration of the experimental apparatus is given in Figure 3.17. It consists of a heating section, a sample holder, a reference sample, and a cooling section. Two plate-type electrical heaters (139.7 mm x 139.7 mm x 6.35 mm), each with a nominal maximum power rating of 900 W, were used in the heating section. These two heaters were installed back-to-back and sandwiched between two 9.53 mm (3/8-inch)

thick copper plates, in order to ensure essentially uniform temperatures at the contact interfaces with other sections. The two heaters were wired in parallel. A DC power supply (Xantrex XKW 150V/20A; maximum capacity of 3000W) was used, ensuring continuously adjustable and stable power inputs to these heaters.

The sample holder was designed to hold porous metal plates with nominal dimensions of 127 mm x 127 mm x 6.35 mm, sandwiched in between two copper plates. The copper plates were designed to provide 139.7 mm x 139.7 mm interfaces, externally, and were in contact with the heating section at the top and the reference sample (stainless steel, SS 303) at the bottom (see Figure 3.17). In the temperature range of interest, this arrangement also provides thermally stable density stratification in the water that saturates the horizontal porous metal plate, and thus eliminates natural convection.

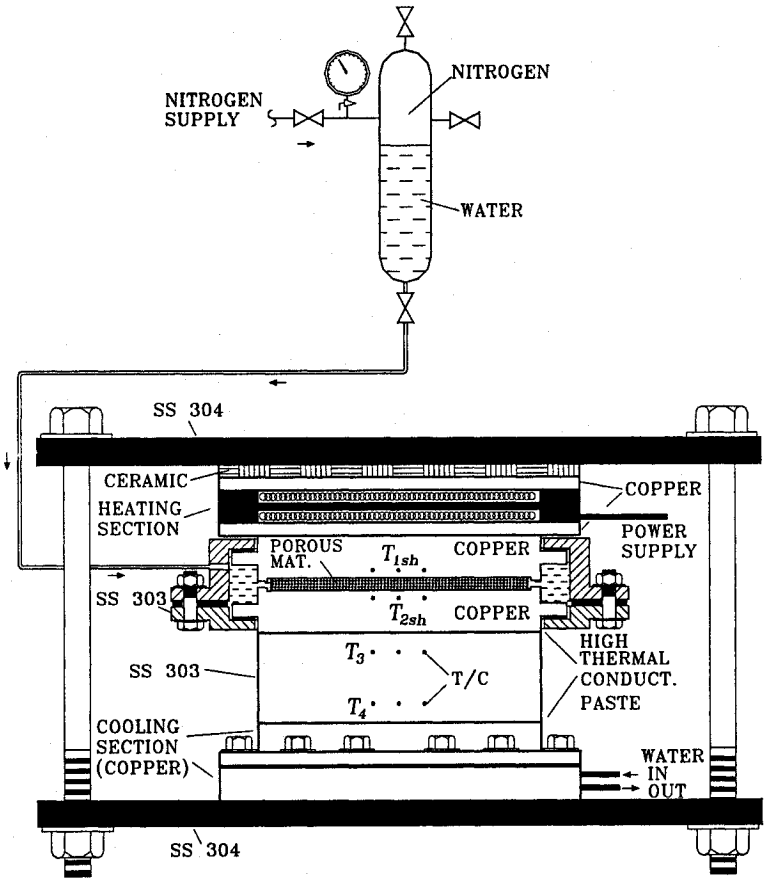

Figure 3.17: Schematic illustration of the experimental apparatus used for measuring the effective thermal conductivity.

(perpendicular to the direction of heat flow) passing through the center of the sample. With this arrangement, the temperatures in the central region of the plate, over a separation distance of 25.4 mm, could be measured.

The cooling section was made of an assembly of copper plates with a thermal interface area of 139.7 mm × 139.7 mm. This section had four inlets and four outlets ports connected to counter-flow passages milled inside one of the copper plates: Water was circulated through these counter-flow passages, and this arrangement provided an essentially uniform temperature at the interface between the cooling section and the reference sample. Two inline water heaters, each with a maximum power rating of 1000 W, and a tank-type water heater with a maximum power rating of 3000 W were used in series to provide preheating of the water supplied to the cooling section. This setup allowed the average temperature of the whole setup to be boosted without increasing the electrical power inputs to the plate heaters in the heating section. The power inputs to the inline water heaters were adjustable, while the tank water heater could only be turned off or on, either manually or automatically with a thermostatic control (55°C set point).

The heating section, sample holder, reference sample, and the cooling section were held together (in compression mode) by means of two perforated rectangular stainless steel (SS 304) plates (355.6 mm × 355.6 mm × 12.7 mm) and eight heavy-duty (12.7 mm) stainless steel bolts and nuts. The degree of compression of this assembly could be adjusted by changing (equally) the torque on all eight bolt/nut combinations. In order to introduce a significant thermally resistance between the heating section and the upper stainless steel holding plate, a 6.35 mm thick ceramic plate was deployed between them (see Figure 3.17). The flexibility provided by this overall design allowed the contact (compression) pressure at the copper-porous metal interfaces to be increased externally: This compression was necessary in order to minimize the related thermal contact resistance. In addition, this overall compression system also helped to improve the thermal contact between the other sections of the apparatus. A high-thermal conductivity paste (Omegatherm 201; $k \cong 2.31$ W/m-°C) was used on both square surfaces of the reference sample, in order to reduce the corresponding thermal contact resistances and ensure essentially one-dimensional heat conduction in the central region of this sample.

The entire experimental setup was insulated with 152.4 mm thick fiberglass insulation (R20, RSI3.5). A box built from 25.4 mm thick polystyrene material (R5, RSI0.86) was used to hold this fiberglass insulation in place. A second layer of the aforementioned 152.4 mm thick fiberglass insulation was used to cover the outside surface of polystyrene box, and this insulation was packed inside a second (outer) box also made of the 25.4 mm thick of polystyrene material. The efficiency of this double-insulation system was tested later by letting the whole preheated setup to cool with no power input to the heaters: Under essentially steady-state conditions, the highest difference between the temperatures readings yielded by the installed thermocouples was about ±0.09°C. This value is in good agreement with the summation of the uncertainties in the readings provided by any two individual thermocouples (that is, ±0.1°C).

Experimental Procedure

Two water-saturated sintered porous metal plates, one made of nickel 200 and the other made of stainless steel 316 (nominal dimensions of 127 mm × 127 mm × 6.35 mm), were used as the test samples. As was mentioned in Section 3.1, the porosities of the test samples were determined to be 28.10% and 46.45% for the nickel 200 and the stainless steel (SS 316) porous plates, respectively. Before the installation of a porous metal plate in the sample holder of the experimental apparatus, it was thoroughly cleaned as follows: All-glass redistilled isopropyl alcohol was pushed several times through the pores of the test sample, using a specially designed cleaning chamber that was fitted with a tubing system and could be pressurized using nitrogen gas; all-glass double-distilled deaerated water was then used to dissolve (and push out) all of remaining alcohol in the sample; and then the sample was soaked in all-glass double-distilled deaerated water. To prevent the accumulation of air bubbles, the assembly of each water-saturated porous metal plate inside the sample holder was carried out entirely under water in a relatively large plastic tub (also filled with all-glass double-distilled deaerated water). Once the sample holder was completely assembled and installed in the experimental apparatus, the pressure inside it was increased to an absolute value of nine bars (about 120 psig), which is well above the 4.76 bar saturation pressure of distilled water at 150°C [Van Wylen et al. (1994)].

After checking to make sure that there were no leaks, the entire apparatus was insulated, as described in the previous subsection.

Each series of tests was initiated by turning on power to the electrical plate heaters and starting the water circulation through the cooling section. The power input to the heaters and the flow rate and temperature of the cooling water were then set. The thermocouples were connected to a data acquisition and control system (HP 3497A) hooked up to a personal computer. The data acquisition and control were effected via a computer program written using the VEE OneLab (Agilent Technologies) software. Once the temperature measurements were initiated, data were periodically saved (at 10-second intervals) on a hard disk in the personal computer. When the differences between two consecutive sets of temperature readings were all less than or equal to ±0.05°C, it was assumed that the steady-state condition prevailed. It could take up to 12 hours to reach this steady-state condition in each experimental run.

3.5.3 Benchmarking of Experimental Setup and Procedure

The experimental setup and procedure were benchmarked before they were used to determine the effective thermal conductivity of the water-saturated porous metal samples. In the benchmarking tests, the sample holder in the experimental setup (shown in Figure 3.17) was replaced by a second reference sample made of stainless steel 303, with the same dimensions as those presented earlier. This benchmarking arrangement of the experimental apparatus is shown schematically in Figure 3.18.

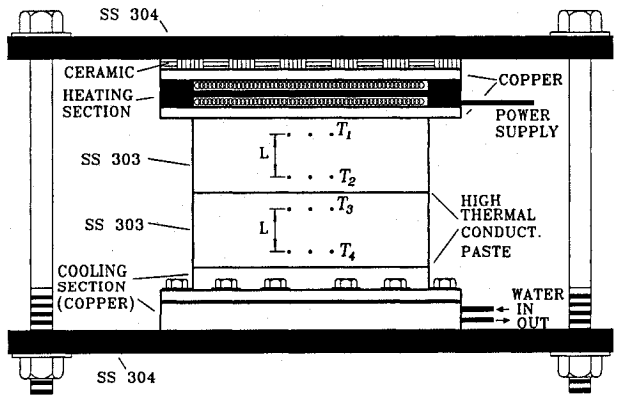

Figure 3.18: Schematic illustration of the arrangement used in benchmarking tests of the thermal conductivity apparatus.

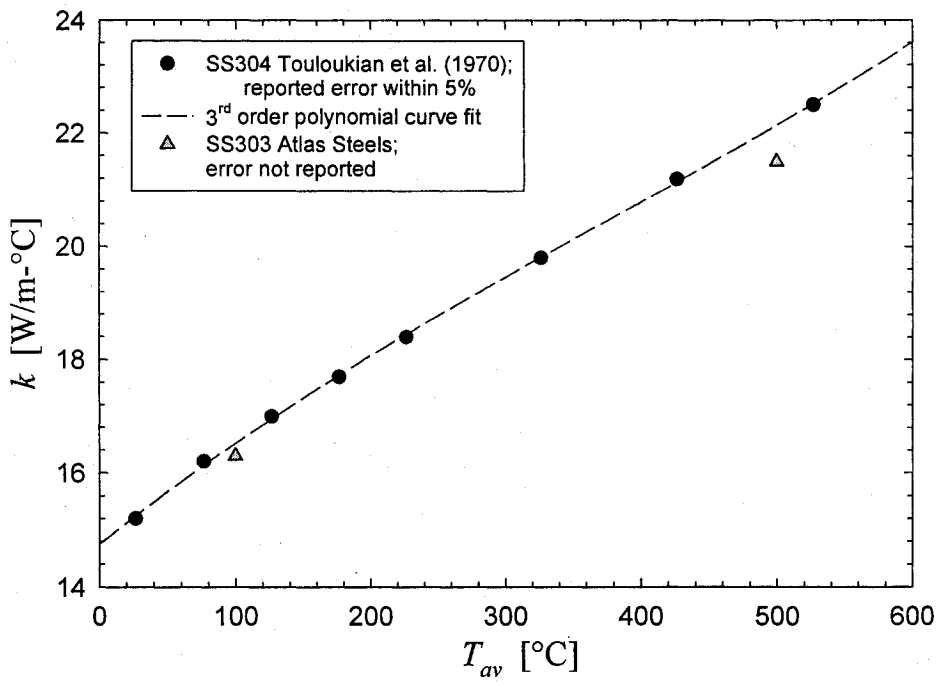

Figure 3.19: Thermal conductivity of stainless steel 304 and 303.

The heat *flux* through the central region of the two reference samples (SS 303) is assumed to be one-dimensional and given by the following equation:

$$q''_x = -k(T)\frac{dT}{dx} \tag{3.25}$$

In this equation, *k(T)* denotes the thermal conductivity of the reference sample material as a function of the local temperature. With the assumption of essentially one-dimensional heat flow in the central region of the two reference samples, installed in series as shown in Figure 3.18, a suitable *k(T)* should lead to the same value of the heat flux, calculated using Eq. (3.25), through each of the reference samples when steady-state conditions prevail. During each test, the mean temperature of the upper reference sample was higher than that of the lower reference sample: Thus, the values of $k(T_{mean})$ in these reference samples were different. Therefore, if the heat fluxes through the central regions of these samples were constant and equal to one another, the related temperature differences across these samples would be different.

Figure 3.19 shows the variation of the thermal conductivity of SS 304 as a function of temperature: The uncertainty in these data, which are taken from Touloukian et al.

(1970), is ±5% (in the temperature range 300 K to 800 K). For SS 303 (which was used in this work mainly because of the ease of machining it offers relative to SS 304), no reliable data on thermal conductivity were found in the published literature, except for two values reported by some metallurgical industries (for example, Atlas Steels): These values are 16.3 W/m-°C and 21.5 W/m-°C at temperatures of 100°C and 500°C, respectively. These two data points are also included in Figure 3.19. As is illustrated by the data in this figure, at 100°C, the values of the thermal conductivities of SS 304 and SS 303 are quite close, while at 500°C, the values are appreciably different. The temperature range in the benchmarking tests conducted in this work was 30°C to 150°C. It was assumed that in this range of temperature, the thermal conductivity of SS 303 is the same as that of SS 304. The data provided by Touloukian et al. (1970) were curve fitted for temperatures in the range 26.0°C to 200°C: The following third-order polynomial curve gives an excellent fit ($r^2 \approx 1$) to these data:

$$k_{SS303} = aT^3 + bT^2 + cT + d$$
$$a = 1.333\times10^{-7};\quad b = -7.072\times10^{-5} \qquad (3.26)$$
$$c = 2.617\times10^{-2};\quad d = 14.547$$

In this equation, T is in °C and k_{SS303} is in W/m-°C.

With reference to the benchmarking setup illustrated in Figure 3.18, the temperatures averaged over the central region of the top and bottom measurement planes (where the thermocouples are located) of the upper reference sample plate are denoted as T_1 and T_2, respectively; and L is used to indicate the perpendicular distance between these two horizontal planes (here, L is 25.4 mm or 1 inch). The polynomial presented in Eq. (3.26) for the function $k(T)$ is substituted into Eq. (3.25). Then, assuming q''_x is constant, Eq. (3.25) is integrated along the heat flow path (noting that at $x = 0$, $T=T_1$; and at $x = L$, $T=T_2$): This yields the following expression for the heat flux in the upper reference sample plate (SS 303):

$$q''_{upper} = \frac{1}{L}\left[\frac{a}{4}\left(T_1^4 - T_2^4\right) + \frac{b}{3}\left(T_1^3 - T_2^3\right) + \frac{c}{2}\left(T_1^2 - T_2^2\right) + d\left(T_1 - T_2\right)\right] \qquad (3.27)$$

Following a similar process, the following expression was derived for the heat flux in the lower reference sample plate (SS 303):

$$q''_{lower} = \frac{1}{L}\left[\frac{a}{4}\left(T_3^4 - T_4^4\right) + \frac{b}{3}\left(T_3^3 - T_4^3\right) + \frac{c}{2}\left(T_3^2 - T_4^2\right) + d\left(T_3 - T_4\right)\right] \tag{3.28}$$

where T_3 and T_4 denote, respectively, the temperatures averaged over the central areas of the upper and lower measurement planes in the lower reference sample plate (SS 303).

Table 3.3: Results yielded by the benchmarking tests.

T_1 [°C]	T_2 [°C]	q''_{upper} [W/m²] Eq. (3.27)	T_3 [°C]	T_4 [°C]	q''_{lower} [W/m²] Eq. (3.28)	Difference ±( )%
58.3	45.6	7891.4	33.4	19.8	8123.5	2.941
69.3	56.5	8028.8	44.3	31.2	7950.2	0.978
78.0	65.1	8174.1	52.6	39.2	8213.3	0.480
103.1	91.5	7542.8	80.4	68.7	7473.9	0.914
109.0	96.9	7956.5	85.1	72.6	7956.3	0.003
124.2	112.9	7509.4	102.0	90.6	7455.9	0.713
139.6	128.3	7671.5	117.3	105.6	7740.8	0.903
144.3	133.2	7521.1	122.5	111.1	7564.9	0.582
154.5	144.0	7167.8	133.9	123.3	7107.1	0.847

The results yielded by the benchmarking tests are given in Table 3.3. These results indicate the following: The values of q''_{lower} calculated using Eqs. (3.26) and (3.28) can be used to estimate the heat flux passing through the sample holder, q''_{upper}, with a deviation of less than ±3%. It should also be noted that in the temperature range of interest, and for the particular experimental apparatus designed and used in this work, the relatively simpler expression, $k_{SS303}^{T_{mean,lower}}(T_3 - T_4)/L$, with $T_{mean,lower} = (T_3 + T_4)/2$, could be used to estimate q''_{lower} with a difference of less than 0.01% from the values listed in Table 3.3.

3.5.4 Experimental Results and Discussions

As was mentioned earlier in the paper, two water saturated sintered powder-metal plates, one made of nickel 200 and the other of stainless steel 316, were used as the test samples. Several experiments were performed with each sample. The temperature differences across the sample holder and the reference sample were monitored, and these data were saved when steady-state conditions were achieved. The results are presented in Tables 3.4 and 3.5 for the nickel 200 and the SS 316 samples, respectively. The last columns in these tables give the relative uncertainties in the values of the effective thermal conductivity. They were obtained using the error propagation method explained in ASHRAE Standard 41.5-75 (1976).

Table 3.4: Experimental results for effective thermal conductivity of water-saturated nickel 200 sintered powder-metal plate (t = 6.65 mm and ε = 28.10%)

T_{1sh} [°C]	T_{2sh} [°C]	T_{mean} [°C]	ΔT [°C]	q'' [W/m²]	R''_{tot} [m²-°C/W]	k_e [W/m-C]	Rel. uncer. ±( )%
34.8	33.7	34.24	1.17	5323.0	2.2008E-04	32.58	9.87
44.4	42.6	43.48	1.75	8078.6	2.1716E-04	33.06	7.55
53.0	50.8	51.90	2.22	10300.1	2.1549E-04	33.34	6.69
64.3	61.4	62.89	2.89	13523.0	2.1364E-04	33.66	6.04
73.7	70.3	72.02	3.46	16274.8	2.1247E-04	33.87	5.73
82.2	78.2	80.15	4.00	18799.2	2.1272E-04	33.83	5.55
90.9	86.4	88.67	4.53	21363.8	2.1209E-04	33.94	5.42
99.2	94.2	96.71	5.04	23832.2	2.1127E-04	34.08	5.33
110.0	104.3	107.13	5.73	27163.4	2.1096E-04	34.14	5.25
118.1	111.8	114.96	6.24	29704.7	2.1014E-04	34.29	5.20
125.6	118.9	122.24	6.75	32090.3	2.1020E-04	34.28	5.17
135.4	128.0	131.73	7.38	35136.2	2.1004E-04	34.31	5.13
143.5	135.6	139.54	7.92	37747.2	2.0988E-04	34.34	5.11
148.2	140.0	144.09	8.21	39140.0	2.0981E-04	34.35	5.10

Table 3.5: Experimental results for effective thermal conductivity of water-saturated stainless steel 316 sintered powder-metal plate (t = 6.56 mm and ε = 46.45%)

T_{1sh} [°C]	T_{2sh} [°C]	T_{mean} [°C]	ΔT [°C]	q'' [W/m²]	R''_{tot} [m²-°C/W]	k_e [W/m-C]	Rel. uncer. ±( )%
25.0	21.5	23.25	3.51	2719.8	1.2890E-03	5.15	5.71
36.8	30.3	33.55	6.54	5241.9	1.2476E-03	5.33	5.18
49.1	39.5	44.30	9.64	7993.1	1.2061E-03	5.51	5.06
58.7	46.7	52.66	12.01	10176.6	1.1803E-03	5.63	5.02
67.4	52.5	59.95	14.84	12864.3	1.1539E-03	5.77	5.00
72.0	57.3	64.65	14.75	12917.7	1.1421E-03	5.83	5.00
82.2	64.4	73.27	17.75	15838.2	1.1209E-03	5.94	4.98
86.5	72.5	79.49	13.94	12459.4	1.1192E-03	5.95	5.00
91.8	78.2	85.04	13.61	12244.9	1.1117E-03	5.99	5.00
100.9	86.4	93.67	14.49	13269.8	1.0918E-03	6.10	5.00
108.3	94.8	101.54	13.52	12478.8	1.0836E-03	6.15	5.00
115.1	102.0	108.57	13.11	12139.7	1.0800E-03	6.17	5.01
119.4	105.4	112.44	13.99	13072.3	1.0702E-03	6.22	5.00
129.8	113.3	121.58	16.47	15579.7	1.0569E-03	6.30	4.99
145.1	129.2	137.14	15.84	15033.3	1.0539E-03	6.32	4.99
151.9	133.9	142.90	18.01	17352.0	1.0380E-03	6.42	4.98

In Tables 3.4 and 3.5, T_{1sh} and T_{2sh} denote, respectively, the average temperatures at measurement planes inside the top and the bottom copper plates of the sample holder, shown schematically in Figures 3.17 and 3.20. T_{mean} and ΔT represent, respectively, the overall mean temperature, $(T_{1sh} + T_{2sh})/2$, and the overall temperature difference, $(T_{1sh} - T_{2sh})$. The measured values of T_3 and T_4 across the reference sample are used as inputs to Eqs. (3.26) and (3.28) to calculate q''_{lower}, which in turn is used to estimate the heat flux through the test sample, $q'' \simeq q''_{lower}$. R''_{tot} represents the total thermal resistance (in m²-°C/W) between the measurement points across the sample holder. With reference to the schematic in Figure 3.20, R''_{tot} is calculated using the following equation:

$$R''_{tot} = \frac{\Delta T}{q''} = R''_w + \sum R''_c + \sum R''_{cu} \tag{3.29}$$

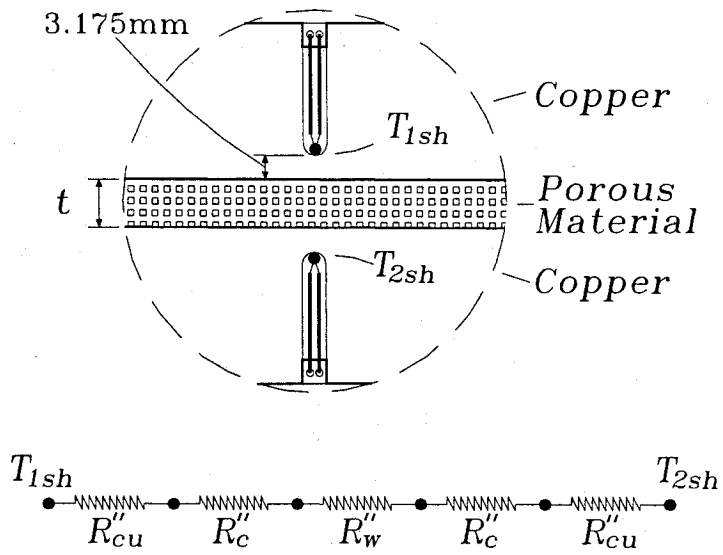

Figure 3.20: Schematic of the thermocouples in the sample holder of the thermal conductivity apparatus and the related thermal resistances.

In Eq. (3.29) and Figure 3.20, R''_w represents the thermal resistance of the water-saturated porous metal sample, R''_{cu} represents the thermal resistance of the copper plates (the thickness of these copper plates on each side of the porous metal sample is t_{cu} = 3.175 mm or 1/8"), and R''_c denotes the thermal contact resistance at the interfaces between the sample and the copper plates. The inner surfaces of the copper plates were smooth and they were pushed snugly against the surfaces of the water-saturated porous metal sample. Therefore, the thermal contact resistance R''_c was assumed to be negligible in this work. Support for the validity of this assumption was also derived from the results presented by Singh et al. (1973). Therefore, for each test, the thermal resistance of the sample, R''_w, could be calculated from Eq. (3.29) by only compensating for $R''_{cu} = t_{cu} / k_{cu,av}$. Once R''_w was calculated, the effective thermal conductivity of the water-saturated powder-metal sample at the mean temperature of the sample, T_{mean}, was obtained using the relation $k_e = t / R''_w$.

The results given in Tables 3.4 and 3.5 (and the corresponding graphical presentations in Figures 3.21 and 3.22) show that the effective thermal conductivities of the nickel 200

and the stainless steel 316 porous metal samples both increase with the mean temperature (indicated in these figures as T_{av}). For the stainless steel 316 sample, these results are not surprising, as the thermal conductivities of the metal (SS316) and the water are both increasing functions of temperature in the range investigated here. However, the thermal conductivity of nickel 200 is a decreasing function of temperature in the range of interest; the porosity of the nickel 200 sintered sample is relatively low (ε = 28.10%); and the ratio of k_s / k_f for this sample is relatively high. Therefore, these results indicate that the thermal conductivity of the water, k_f, *perhaps* has a relatively greater influence than that of the solid (nickel 200), k_s, in the determination of the effective thermal conductivity of this water-saturated nickel 200 sintered powder-metal sample: The word *perhaps* is used in this statement because the maximum difference (full variation) of the effective thermal conductivity of this sample over the temperature range of interest is almost fully within the error bands shown in Figure 3.22. However, in this context, it should be noted that Peterson and Fletcher (1987) also experimentally investigated the temperature dependency of the effective thermal conductivities of three different water-saturated sintered nickel 200 powder-metal samples (of porosity ε = 43.0%, 64.0% and 69.0%) with mean temperatures in the range 20°C to 100°C: Their results also show that the effective thermal conductivity increases with mean temperature, for all three samples.

Figures 3.21 and 3.22 show graphical comparisons of the experimental results obtained in this investigation for the effective thermal conductivity of the water-saturated porous stainless steel 316 and nickel 200 plates, respectively, with those predicted by the correlations presented earlier. The predictions were obtained by using the thermal conductivities of water, stainless steel 316, and nickel 200 as functions of temperature, while assuming that the porosities of the water-saturated samples remain unchanged. For the Dul'nev (1965) correlation, the nonlinear polynomials given in Eq. (3.19) were solved iteratively, and values of y = 0.26184 and y = 0.32527 were found to give physically meaningful values of k_e for stainless steel 316 (ε = 46.45%) and nickel 200 (ε = 28.1%), respectively. The correlation proposed by Alexander (1972), Eq. (3.20), was used with δ = 0.53. In the correlation of Hadley (1986), Eq. (3.21), α_{con} was calculated using the curve fits provided by Kaviany (1999), Eq. (3.23), and f_o was set equal to 0.85.

The Bauer (1993) correlation was fitted using β =1.0, and Eq. (3.24) was solved iteratively for k_e. As is clearly seen in Figures 3.21 and 3.22, the parallel and series model represent, respectively, the upper and lower limits for the effective thermal conductivities.

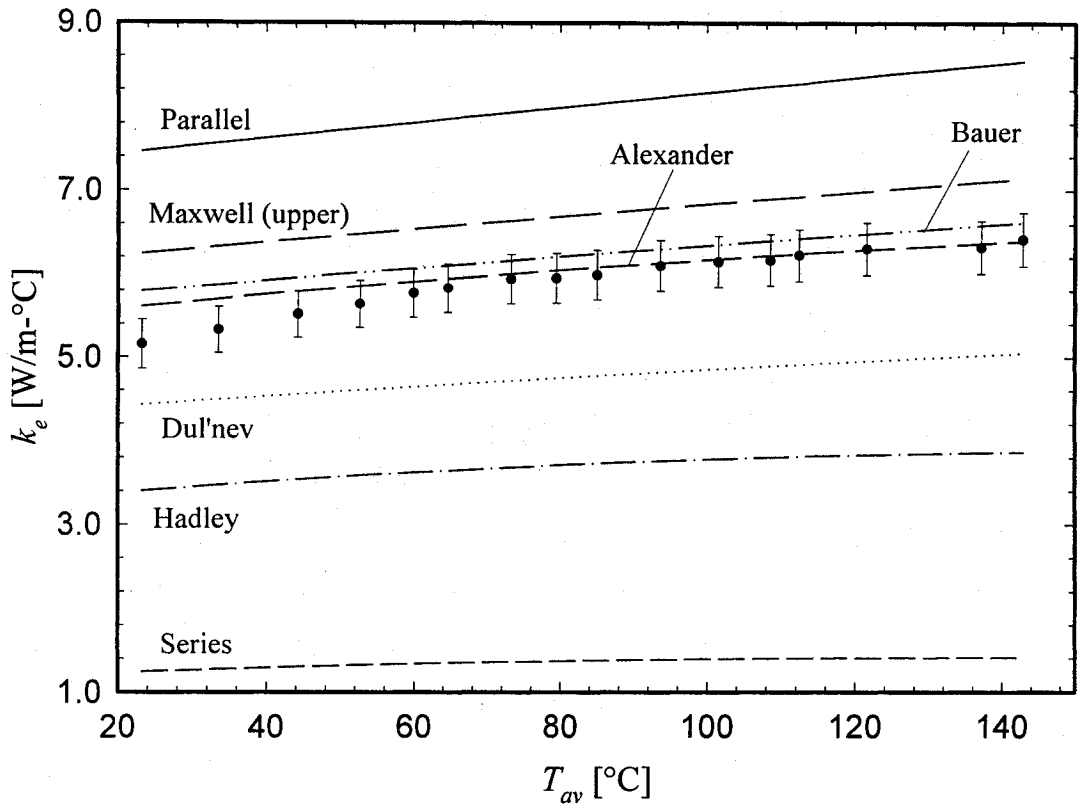

Figure 3.21: Comparison of the experimental values of the effective thermal conductivity of water-saturated sintered stainless steel 316 powder-metal plate (ε = 46.45%) obtained in the current study with those predicted by some available correlations.

The results presented in Figure 3.21 show that for the stainless steel 316 sample, all of the correlations considered here predict that the effective thermal conductivity increases with the mean temperature (T_{av}). The correlation of Alexander (1972) gives the best predictions, with the maximum percentage difference between the experimental and predicted values being E_r = +8.8% for a mean temperature of 23.3°C: Here, it should be noted that $E_r = 100 \text{ x } (k_{e,correl} - k_{e,expt}) / k_{e,expt}$. This difference decreases with increasing mean temperature for this sample as follows: +3.0% $\leq E_r \leq$ +8.8% for 23.3°C $\leq T_{av} \leq$ 55°C; and $|E_r|$ is within 3.0% for $T_{av} >$ 55°C.

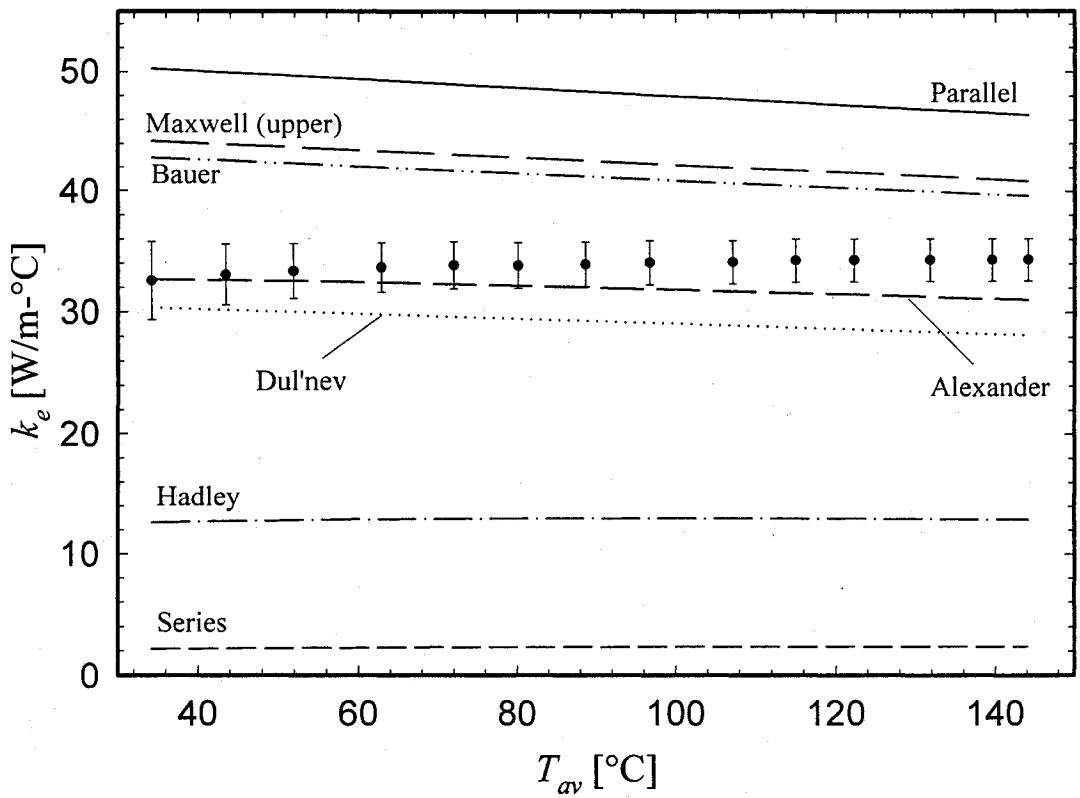

Figure 3.22: Comparison of the experimental values of the effective thermal conductivity of water-saturated sintered nickel 200 powder-metal plate (ε = 28.1%) obtained in the current study with those predicted by some available correlations.

For the nickel 200 sample, as can be seen from the results presented in Figure 3.22, the parallel, Maxwell (1954), Bauer (1993), Alexander (1972) and Dul'nev (1965) correlations predict that the effective thermal conductivity should decrease with an increase of T_{av}, while the Hadley (1986) and series correlations predict an increase of this property with the mean temperature. The best predictions are again given by the correlation of Alexander (1972): E_r = -9.6% for T_{av} = 144.1°C and E_r = +0.28% for T_{av} = 34.2°C. However, Alexander's correlation predicts a decrease of k_e with an increase of T_{av}, whereas the experimental results show an opposite trend. Again, it should be noted that these statements about opposing trends in the experimental results and the values predicted by some of the aforementioned correlations are not definitive as the maximum difference (full variation) of the experimental values in the temperature range 20°C to 150°C is within the error bands shown in Figure 3.22. Here, it should also be noted that the experimental results of Peterson and Fletcher (1987) compare quite well with those

predicted by the correlation of Alexander (1972), in terms of overall deviations (Dev_{max} = ±32.27% and Dev_{mean} = ±11.15% values), but these sets of results also show opposite trends with respect to the variation of k_e with T_{av}.

3.5.5 Proposed Correlation

As was discussed in the previous subsection, the empirical correlation of Alexander (1972), which is based on experiments with porous materials made of sintered fibers and powders, gives predictions that agree quite well with the effective thermal conductivity data obtained experimentally in this work (see Figures 3.21 and 3.22). However, a correlation that is less empirical than Alexander's correlation and provides better predictions is proposed in this subsection. As was mentioned earlier, this correlation was formulated by extending the theoretical ideas put forward earlier by Hadley (1986).

As was discussed in Subsection 3.5.1, Hadley (1986) proposed an approach that involves a combination of a theoretical expression that is appropriate for conduction through a contiguous solid (the upper Maxwell formula) and another such expression that is suitable for conduction through a suspension (not necessarily dilute) of solid particles. Hadley's combined expression for a solid-fluid (two-phase) system, where the solid is connected (consolidated by cold pressing), is given in Eq. (3.21): This equation involves two parameters, α_{con} and f_o, which are to be determined with reference to experimental data. Hadley (1986) has proposed a graph of α_{con} as a function of $\delta = (1-\varepsilon)$, based on experimental measurements of the effective thermal conductivity of packed powders saturated with either air or nitrogen at pressures that were low enough to eliminate the influence of the pore fluid ($k_s / k_f \to \infty$); and using experimental data obtained with packed (cold-pressed) powders of stainless steel and brass, with water as the pore fluid, he found $0.8 \le f_o \le 0.9$.

In this work, the focus is on the effective thermal conductivity of water-saturated *sintered* powder-metal plates. These sintered porous metal plates are different from the *cold-pressed* packed metal-powder porous media used by Hadley (1986), in that the thermal conduction across the solid-to-solid contacts zones between the metal particles created by the sintering process is better than that across similar contact zones created by

the cold-pressing process. Thus it is not surprising that the effective thermal conductivity values of both the water-saturated stainless steel 316 and nickel 200 porous plates obtained using the correlation proposed by Hadley (1986) lie well below the corresponding values yielded by the experiments undertaken in this work (see Figure 3.21 and 3.22).

In the proposed correlation, the basic combined expression, Eq. (3.21), proposed by Hadley (1986) is retained. However, it is postulated that the parameters α_{con} and f_o in this combined expression are functions of not only the porosity, ε, as proposed by Hadley (1986), but also of the conductivity ratio k_s / k_f. The inspiration for this postulate was derived from the earlier work of Smith and Kunii (1960). The following function is proposed for the consolidation parameter, α_{con}:

$$\ln(1-\alpha_{con}) = \frac{-\Lambda\left(\frac{1-\varepsilon}{\varepsilon}\right)^m}{\left[1-\left(\frac{k_s}{k_f}\right)^{-n}\right]} \quad \text{or} \quad \alpha_{con} = 1-\exp\left\{\frac{-\Lambda\left(\frac{1-\varepsilon}{\varepsilon}\right)^m}{\left[1-\left(\frac{k_s}{k_f}\right)^{-n}\right]}\right\} \tag{3.30}$$

This expression applies to systems for which $(k_s / k_f) \geq 1$: Note that when $(k_s / k_f) \to 1$ and $0 < \varepsilon < 1$, $\alpha_{con} \to 1$. The parameter f_o is assumed to be the following porosity-weighted average of the values corresponding to Maxwell's upper and lower limits:

$$f_{o,\min} = \frac{2}{3} \quad ; \quad f_{o,\max} = \frac{2(k_s / k_f)}{2(k_s / k_f)+1} \quad ; \quad f_o = f_{o,\min}\varepsilon + f_{o,\max}(1-\varepsilon) \tag{3.31}$$

Equations (3.30) and (3.31) ensure that when the porosity approaches very small values ($\varepsilon \to 0$), $\alpha_{con} \to 1$ and $f_o \to f_{o,\max}$; and when the porosity approaches its highest value ($\varepsilon \to 1$), $\alpha_{con} \to 0$ and $f_o \to f_{o,\min}$. For the water-saturated nickel 200 and stainless steel 316 sintered powder-metal plates considered in this work with temperatures in the range 20°C to 150°C, and also the water-saturated nickel 200 and copper (C102) sintered powder-metal plates used by Peterson and Fletcher (1987) in the temperature range 25°C to 100°C, the values of f_o obtained using Eq. (3.31) lie in the range $0.768 \leq f_o \leq 0.903$.

Using curve fitting techniques with the experimentally determined values of the effective thermal conductivity in this work, and also the experimental results reported by Peterson and Fletcher (1987), as inputs, the constants in the Eq. (3.30) were determined to be the following:

$$\Lambda = 0.148 \quad ; \quad m = 0.283 \quad ; \quad n = 0.04 \tag{3.32}$$

The variation of the consolidation parameter, α_{con}, with the porosity, ε, is depicted in Figure 3.23 for five different values of the conductivity ratio, k_s / k_f, and the above-mentioned values of the constants in Eq. (3.30). For comparison purposes, the values of α_{con} obtained with the curve fit proposed by Kaviany (1999) to Hadley experimental data, Eq. (3.23), are also shown in Figure 3.23. As is evident from these results, the influence of k_s / k_f and the sintering on α_{con} is significant.

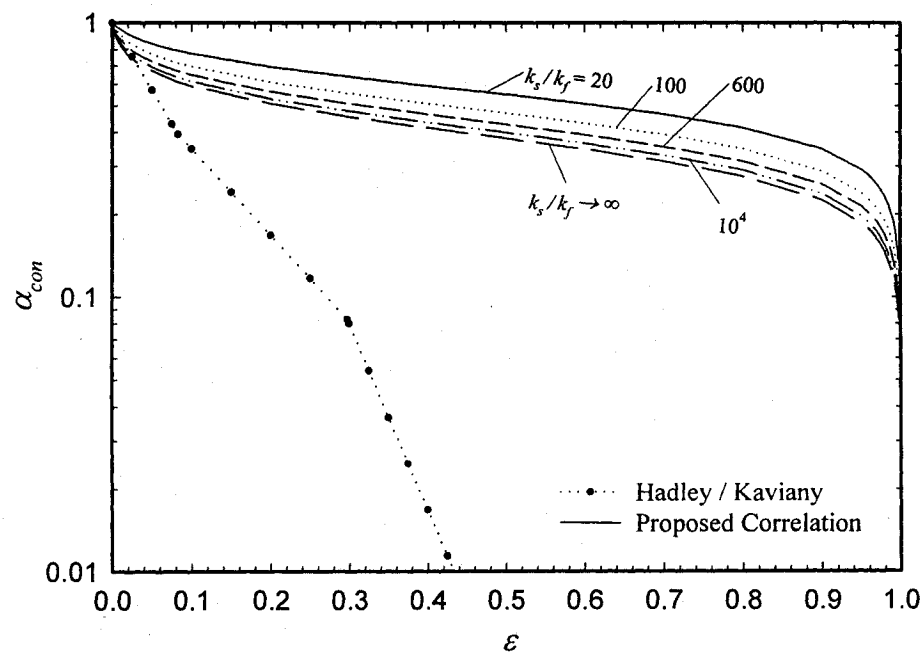

Figure 3.23: Variation of the consolidation parameter, α_{con}, with the porosity, ε, predicted by the proposed correlation for six different values of the thermal conductivity ratio, k_s / k_f.

With this proposed correlation, all of the values of the effective thermal conductivity experimentally determined in this work, and also those reported by Peterson and Fletcher

(1987), are predicted with a mean deviation of less than ±5.67% and a maximum deviation of ±19.39%. The maximum and mean deviations of the predictions from the experimentally determined results of the effective thermal conductivity in *this* work are the following:

$$\begin{aligned} &\text{Nickel 200:} && \text{Dev}_{max} = \pm 5.83\% \;\; ; \;\; \text{Dev}_{mean} = \pm 3.04\% \\ &\text{Stainless Steel 316:} && \text{Dev}_{max} = \pm 5.55\% \;\; ; \;\; \text{Dev}_{mean} = \pm 2.45\% \end{aligned} \tag{3.33}$$

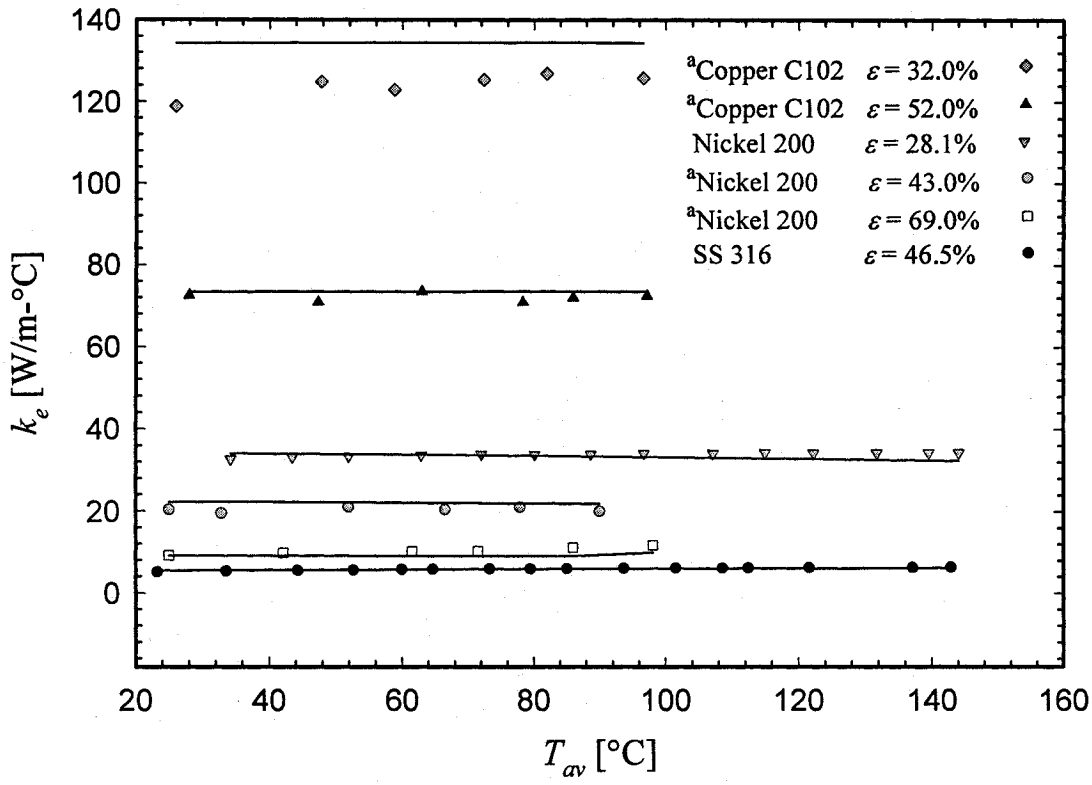

Figure 3.24: Variation of effective thermal conductivity of water-saturated sintered powder-metal porous plates with T_{av}: Values predicted by the proposed correlation and the corresponding experimental results obtained in this investigation and by [a]Peterson and Fletcher (1987).

Graphical presentations of the predictions obtained with the proposed correlation, the experimental results of this investigation, and the experimental results of Peterson and Fletcher (1987) are given in Figures 3.24 and 3.25. In Figure 3.24, the experimental results pertaining to nickel 200 with ε = 28.1% and stainless steel (S.S.) 316 with ε = 46.5% were obtained in this work; and the experimental results pertaining to copper C102 with ε = 32.0%, copper C102 with ε = 52.0%, nickel 200 with ε = 43.0%, and nickel

200 with ε = 69.0% were reported by Peterson and Fletcher (1987). These results show that the proposed correlation provides predictions of the effective thermal conductivity of the aforementioned water-saturated sintered powder-metal plates that are significantly better than the corresponding predictions yielded by the correlations proposed by Alexandre (1972) and Hadley (1986).

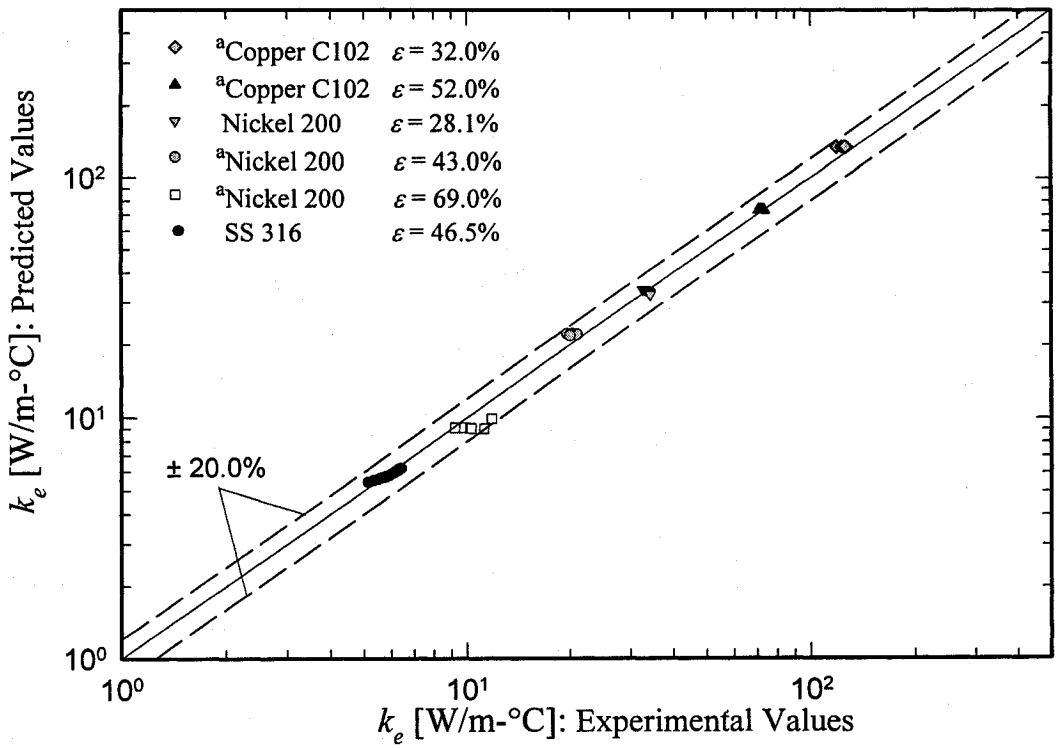

Figure 3.25: Comparison of the values of effective thermal conductivity of water-saturated porous metal plates predicted by the proposed correlation and the corresponding experimental results obtained in this investigation and by [a]Peterson and Fletcher (1987).

Chapter 4:

A Loop Heat Pipe with a Flat Evaporator and Fixed Active Mass of Working Fluid: Experimental Setup and Procedures

In this chapter, a loop heat pipe (LHP) that was designed, constructed, and used in the experimental phase of this investigation is described, along with the overall setup and procedures. A schematic illustration of this LHP is given in Figure 4.1: It has one flat (plate-type) evaporator, a vapor-transport line, a single condenser, and a liquid-transport line.

As was mentioned in the literature review presented in Chapter 1, the flat evaporator configuration was chosen for this experimental work as it has received comparatively less attention than evaporators with a cylindrical geometry; and the intention here is not only to obtain experimental results that would be useful for checking a network thermofluid model of LHPs proposed in this thesis (described in Chapter 5), but also to augment the available repertoire of experimental data on these devices. In addition, it was decided to design a flat evaporator that was fairly straightforward to fabricate, assemble, and operate with a flat sintered powder-metal plate as the wick. This flat evaporator is *not* integrated with a compensation chamber; rather, as shown in Figure 4.1, an external two-phase reservoir is attached to the LHP, as is done in capillary pumped loops (CPLs). However, the proposed LHP is different from CPLs [Nikitkin and Cullimore (1998)] in that after charging (that is, filling the LHP with the working fluid), this external two-phase reservoir is isolated and the active fluid mass in the loop is kept fixed during its operation (additional details are provided later in this chapter).

In the published literature on LHPs (see Chapter 1, Section 1.4), there are fewer works that deal with water as the working fluid than those that consider other working fluids (such as ammonia, methanol, and ethanol). In this context, for the same reasons as those mentioned above, it was decided to operate the proposed LHP with water as the working fluid.

4.1 DETAILS OF THE LHP

As is shown in Figure 4.1, the LHP considered in this work has the following components: a flat (plate-type) evaporator; a condenser made of a serpentine-type pipe that is fully submerged in a constant-temperature oil bath (that was designed and constructed specially for use in this work); a vapor-transport line made of a serpentine-type pipe; and a liquid-transport line also made of a serpentine-type pipe. A two-phase reservoir is also attached externally to this LHP, as shown in Figure 4.1: This reservoir is used only in the charging operation (details are given in a later section of this chapter).

One of the objectives in the design of this LHP was to mimic conditions encountered in practical applications: This is the main reason for the use of serpentine pipes in the construction of the vapor-transport line, the condenser, and the liquid-transport line. These serpentine pipes also allow rather long vapor- and liquid-transport lines to be convenient accommodated in limited laboratory space and fit a condenser with a relatively large surface area (for heat transfer) inside an oil-bath that is not overly large.

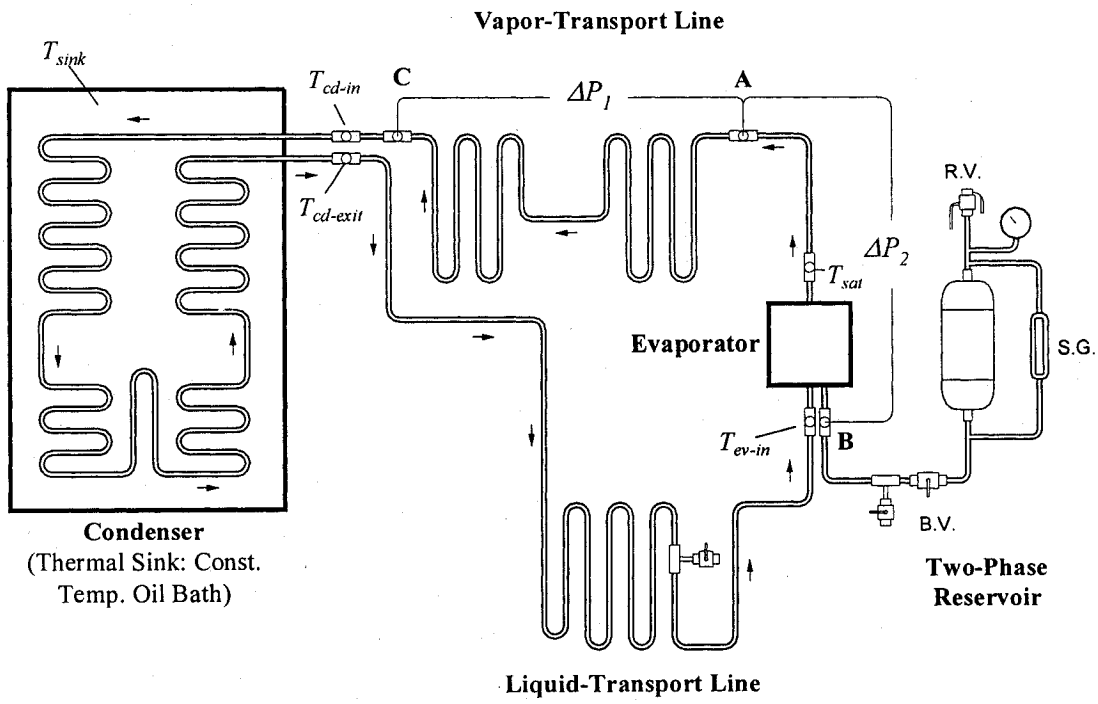

Figure 4.1: Schematic representation of the LHP (not to scale).

The dimensions of the various elements of the LHP, the materials used to construct them, and some characteristics of the sintered powder-metal wick used in this work are summarized in Table 4.1. Geometrical details of the tubes used in the construction of this LHP are given in Appendix C.

Table 4.1: Dimensions and characteristics of the different elements of the LHP.

EVAPORATOR		CONDENSER	
Overall Dimensions		Pipe Material:	SS 316L
Upper Piece (SS 316): 177.8×177.8×19.05 mm^3		Outside Diameter:	9.53 mm
Lower Piece (SS 316): 177.8×177.8×31.75 mm^3		Inside Diameter:	7.75 mm
Heat Transfer Interface		Length:	6.36 m
At the Center of the Upper Piece: 100.8×100.8 mm^2		Cross Sectional Area:	4.72×10^{-5} m^2
Liquid Pool		Volume:	300 mL
Dimensions:	101.6×101.6×12.7 mm^3	VAPOR-TRANSPORT LINE	
Volume:	131 mL	Pipe Material:	SS 316L
Wick:		Outside Diameter:	9.53mm
Sintered Metal Powder:	SS 316	Inside Diameter:	7.75 mm
Porosity:	46.45%	Effective Length:	4.3 m
Dimensions:	126.6 ×126.6×6.54 mm^3	Cross-Sectional Area	4.72×10^{-5} m^2
Effective Permeability:	6.576×10^{-12} m^2	Volume:	203 mL
Max. Effective Pore Size:	41.75 μ m	LIQUID-TRANSPORT LINE	
Total Volume of Pores:	49 mL	Pipe Material:	SS 316L
Grooves		Outside Diameter:	9.53mm
Number of Grooves:	13	Inside Diameter:	7.75 mm
Groove Length:	107.9mm	Effective Length:	4.6m
Groove C.S. Area:	12.1mm^2	Cross-Sectional Area	$4.72\times10^{-5}$$m^2$
Groove Hydraulic Diameter:	3.1mm	Volume:	217mL
Total Volume of Grooves:	17mL	TWO-PHASE RESERVOIR	
Grooves Collector Volume:	11mL	Volume:	2035mL

4.1.1 Evaporator

Details of the flat evaporator of the LHP are presented in Figure 4.2. It is made of the following parts: An upper piece, machined out of a stainless steel plate, with vapor-transport grooves of trapezoidal cross section on its bottom face; a lower piece, also machined out of a stainless steel plate, with a cavity of rectangular cross section that serves as the liquid pool in the evaporator during the operation of the LHP; and a sintered

powder-metal wick sandwiched between the upper and lower pieces. The overall dimensions of these parts and some of the characteristics of the wick are listed in Table 4.1. As indicated in this table, the wick used in this LHP was made of a sintered powder-metal plate of stainless steel 316.

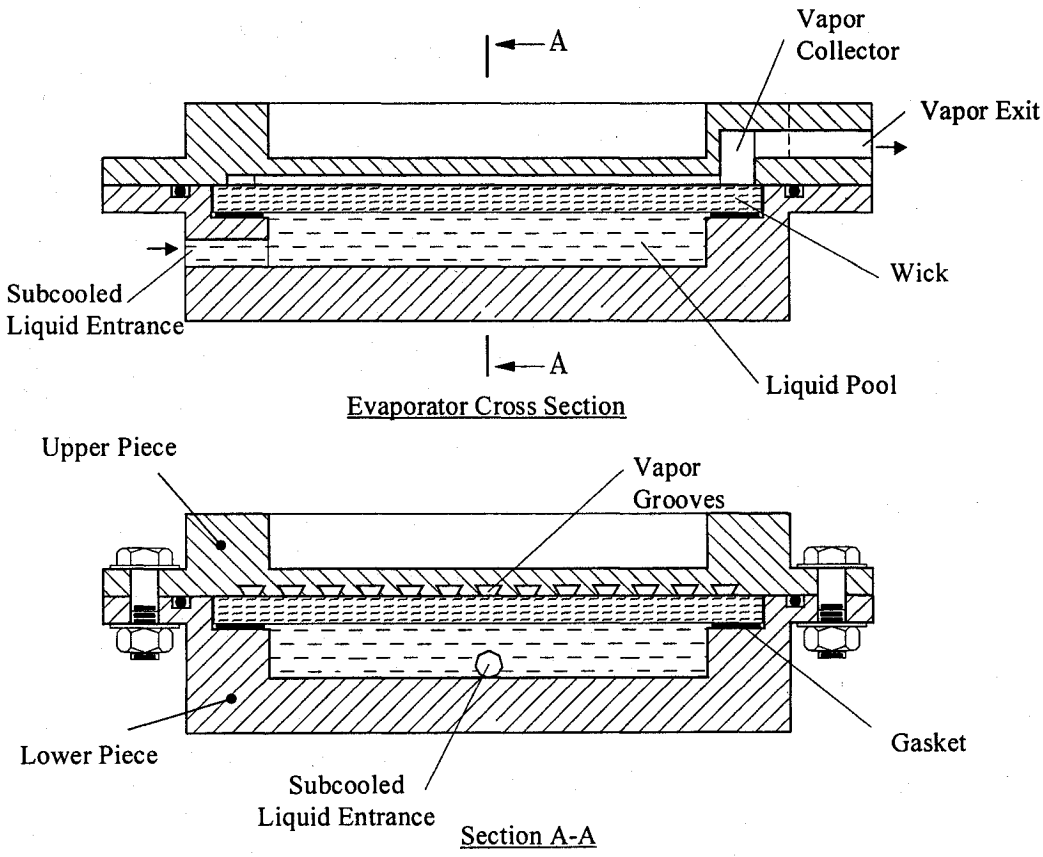

Figure 4.2: Details of the flat evaporator. Note: Bolts, nuts, and washers are not shown in the upper figure in order to avoid cluttering in the presentation.

The upper and the lower pieces of the evaporator are assembled and then clamped together using twenty sets of bolt, nut, and washers. This configuration allows easy opening of the evaporator and access to its internal parts for inspection and cleaning, or replacement of the wick. The sealing between the liquid in the rectangular cavity in the lower piece (liquid pool) and the vapor at top of the wick was achieved using a flat silicon rubber gasket of 1.59 mm (1/16-inch) thickness; and the sealing between the upper and lower pieces was effected using Viton® o-rings (3.18 mm diameter). Both the

silicon rubber gaskets and the Viton® o-rings were rated for a maximum operating temperature of 250°C.

The full evaporator-assembly is illustrated schematically in Figure 4.3. It consists of the evaporator presented in Figure 4.2, a heating section, a heat-flux measuring plate, ceramic tiles, and supporting plates with bolts and nuts. The heating section was made of two plate-type electrical heaters (139.7 mm x 139.7 mm x 6.35 mm), each with a nominal maximum power rating of 900 W. These two heaters were installed back-to-back with a thin copper plate (3.18 mm thick) sandwiched in between. This heating system was then sandwiched between two thin copper plates (3.18 mm thick), in order to ensure essentially uniform temperatures at the contact interfaces with other sections. The two heaters were wired in parallel. A DC power supply (Kepco1000, 100 V/10 A, maximum capacity of 1000 W) was used, ensuring continuously adjustable and stable power inputs to these heaters.

Seventy chromel-constantan thermocouples (type E; AWG-30) were fabricated. These thermocouples plus ten additional sheathed thermocouples (type E, each installed in a stainless sheath of 152.4 mm length and 1.59 mm diameter) were calibrated in the temperature range of 5°C – 155°C. A special constant-temperature oil bath was designed and constructed for the calibration of these thermocouples in the temperature range of 60°C – 155°C. This constant-temperature oil bath was later used as the heat sink for the condenser of the LHP (see Figure 4.1); its details, along with those of the condenser, are explained later in this chapter. For calibration of these thermocouples at temperatures below 60°C, a constant-temperature water bath (Neslab RTE 220) was used. The uncertainties in the temperature readings provided by the calibrated thermocouples were determined to be less than or equal to ±0.05°C, using the method described in ASHRAE Standard 41.5-75 (1976). The procedure used for the calibration of these thermocouples is presented and discussed in Appendix A of this thesis. The calibrated thermocouples were used to measure temperatures in the evaporator and also other elements of the LHP, as described in some of the following sections of this chapter.

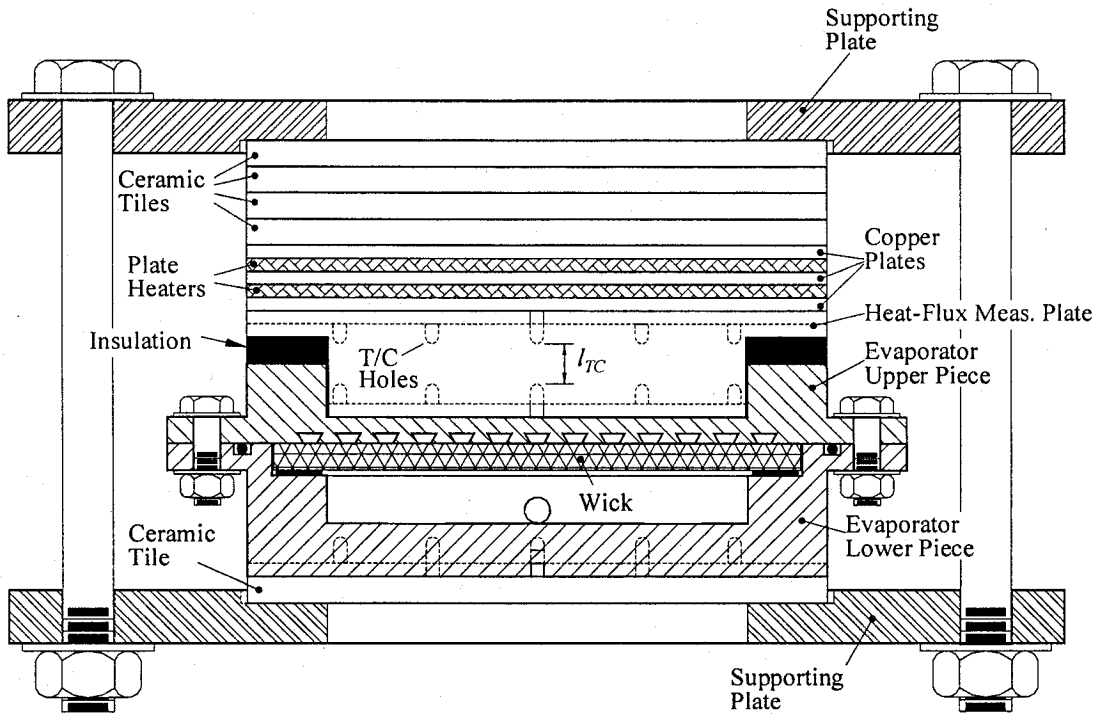

Figure 4.3: Details of the full evaporator-assembly.

As is shown in Figure 4.3, a heat-flux measuring plate is inserted in between the heating section and the evaporator. This plate is made of stainless steel (SS303); its top side has a surface area of 139.7 mm × 139.7 mm and is in contact with the bottom surface of the heating section; on its lower side, it fits snugly into a cavity machined in the upper piece of the evaporator, and has a bottom contact interface surface of 100.8 mm × 100.8 mm (the cavity in the upper piece of the evaporator has a cross-sectional area of 101.6 mm × 101.6 mm). Nine thermocouples were installed inside the top and bottom surfaces of the heat-flux measuring plate, over a 95.2 mm × 95.2 mm region around the center; the holes for these thermocouples are 7.94 mm deep and drilled symmetrically with respect to the horizontal plane (perpendicular to the direction of heat flow) passing through the center of the sample. With this arrangement, the average temperatures of two horizontal planes inside the heat-flux measuring plate, separated by a distance of 9.53 mm (l_{TC} in Figure 4.3), could be measured. Once these average temperatures are obtained, assuming one-dimensional heat transfer in the central part of the heat-flux measuring plate and with

the known (predetermined) thermal conductivity of the plate, the downward heat flux and, consequently, the total power input to the evaporator can be estimated.

In order to introduce significant thermal resistances (and thus reduce heat loss) in between the top of the heating section and the upper supporting plate, and also in between the bottom of the evaporator and the lower supporting plate, 6.35 mm thick ceramic tiles were used (see Figure 4.3). Specifically, four such tiles were installed at the top of the heating section to promote the downward flow of the heat generated in the electrical heaters, towards the evaporator.

The evaporator, the heating section, the heat-flux measuring plate, and the ceramic tiles were held together (in compression mode) by means of two perforated rectangular stainless steel (SS 303) plates (254 mm × 254 mm × 12.7 mm) and six sets of heavy-duty (12.7 mm) bolts, nuts, and washers. The degree of compression in this assembly could be adjusted by changing (equally) the torque on all six bolt-nut-washer sets. This compression was necessary to minimize the related thermal contact resistances, especially between the bottom of the heat-flux measuring plate and the top of the evaporator. A high-thermal conductivity paste (Omegatherm 201; $k \cong 2.31$ W/m-°C) was used at the contact interfaces between the heat-flux measuring plate, the heating assembly, and the evaporator, in order to reduce the corresponding thermal contact resistances, and ensure essentially one-dimensional heat conduction in the central region of the heat-flux measuring plate.

The full evaporator-assembly presented in Figure 4.3 was insulated with 152.4 mm thick fiberglass insulation (R20, RSI3.5). A box built from 19 mm thick wood planks was used to hold this fiberglass insulation in place.

In order to estimate the heat loss from the evaporator body to the ambient environment, and also better understand the thermal phenomena that occur in this portion of the LHP, nine thermocouples were installed inside the bottom side of the lower piece of the evaporator. These thermocouples were installed over a 95.2 mm × 95.2 mm region around the center of this piece. The blind holes for these thermocouples were stopped 3.2 mm from the bottom surface of the liquid pool in the evaporator (see Figure 4.3).

A high-accuracy differential pressure transducer (Omega PX838; 0-10,000 Pa; ±0.25%FS) was calibrated (for 0-1500 Pa; ±7.2 Pa) using an Askania manometer and

used for measuring the difference in pressure between the subcooled liquid entering the evaporator and the vapor leaving it. This pressure transducer is denoted as ΔP_2 in Figure 4.1, and it is attached to measurement ports denoted as A and B in the figure.

4.1.2 Condenser

The condenser of the LHP was made of stainless steel (SS 316L) pipe (7.75 mm ID; 6.36 m long) which was bent smoothly (23.8 mm internal bend radius) at several location along its length to allow its installation inside the space available in the constant-temperature oil bath (see Figure 4.1). This constant-temperature oil bath served as the heat sink for the LHP.

The constant-temperature oil bath was made of a 0.305 m x 0.610 m x 0.915 m stainless steel tank; it was filled with approximately 140 liters of mineral oil. With this mineral oil (flash temperature of about 173°C), continuous operating temperatures up to 155°C could be accommodated. The tank was fitted with a total of three electrical heaters; two of these were hooked up to a temperature controller; and the third was supplied with a continuous power input, when required, and functioned as a booster heater. A casing made of fiberglass boards (63.5 mm thick) was built and installed on the outside of the stainless steel tank, in order to minimize heat losses to the surroundings. For controlling the temperature of the oil inside the bath, it is necessary to have not only the aforementioned heaters inside the tank, but also a means to cool it when needed. Tap water was circulated in a counter flow manner through two coolant-transport pipes installed inside the oil in the tank to provide this cooling capability; the flow rate of this coolant water was adjusted (manually) by a stainless steel metering valve. A three-blade (152.4 mm diameter) propeller attached to a variable-speed agitator (Talboys Stirrer Model 138) was incorporated in this bath to mix the mineral oil and facilitate achievement of isothermal operating conditions. Furthermore, the oil bath was mounted on a base that allowed its height to be varied. Photographs of this oil bath are provided in Appendix A.

The condenser pipe was installed inside the bath above both heaters and the coolant-transport pipes. The elevation of the inlet of the condenser pipe was 50.8 mm above that of its outlet. This difference in elevation provided an overall downward slope of about

1% in the flow direction. This slight downward slope aided in establishing a stable phase distribution (liquid and vapor) inside the condenser pipe and ensured repeatable steady-state of operation of the LHP.

The fluid temperatures at the inlet and outlet (exit) of the condenser, $T_{cd\text{-}in}$ and $T_{cd\text{-}exit}$, were measured using sheathed thermocouples (see Figure 4.1). Using especial compression fittings, the tips of these thermocouples were positioned at the axis of the condenser pipe, allowing direct measurements of the fluid at the inlet and outlet of the condenser. Other sheathed thermocouples were used to measure the temperature of the oil at several locations in the bath, and these measurements were averaged to obtain the sink temperature, T_{sink}, for each experimental run of the LHP.

The heat transfer coefficient on the external surface of the condenser pipe (subjected to cross flows of the mineral oil in the stirred bath), h_{oil}, was measured experimentally using a steady-state method. A custom-made tubular electrical heater having the same geometry as that of the condenser pipe was designed, constructed, and used inside the oil-bath (replacing the condenser pipe) in this method. Power supply to this heater was provided by a DC supply (Kepco1000, 100V/10A; maximum capacity of 1000W), ensuring continuously adjustable and stable power inputs during these experiments. Twelve thermocouples were attached to the outer surface of this custom-designed tubular electrical heater; during these experiments, the readings from these thermocouples were averaged to obtain the mean outer surface temperature of the tubular heater. In each run of these experiments, the agitator speed and the sink (oil-bath) temperature were set, the tubular electrical heater was powered up, and the thermocouple outputs were monitored. Once steady-state condition was achieved in each run, the sink (oil-bath) temperature, the power input to the tubular heater, and the average temperature of outer surface of the tubular heater were recorded. Using a steady-state energy balance on the heater, h_{oil} was determined. In each of these experiments, the agitator speed setting was kept fixed at the same value (4/10) as that used in all of the LHP experiments. The results obtained for h_{oil}, with sink (oil-bath) temperatures of 41.9°C, 51.3°C, and 62.0°C are 290.2 W/m^2-°C, 320.4 W/m^2-°C, and 344.9 W/m^2-°C, respectively. These conditions are essentially the same as those used in the LHP experiments. The relative uncertainties in these values of h_{oil} were estimated to be less than ±3.4%. Simple linear interpolation or extrapolation of

these values was used to estimate h_{oil} when the sink temperature differed slightly from the aforementioned values in the LHP experiments.

4.1.3 Vapor- and Liquid-Transport Lines

The vapor- and the liquid-transport lines were made of smooth stainless steel (SS 316) pipes of circular cross section (dimensions given in Table 4.1). These pipes were bent into serpentine shapes, using several smooth bends of 23.8 mm internal radius, as shown in Figure 4.1, to allow their installation in the limited space of the laboratory and also to mimic conditions encountered in LHP applications. These pipes were connected using stainless steel compression fittings. Two of these fittings were specially designed and constructed to allow connection of a differential pressure transducer across a finite length of the vapor-transport line, indicated by the symbols A and C in Figure 4.1. A high-accuracy differential pressure transducer (Omega PX938; 0-1,000 Pa) was calibrated (±0.15% FS) using an Askania manometer and then used for these measurements, indicated by $\Delta P_1 = (P_A - P_C)$ in Figure 4.1.

As shown in Figure 4.1, the fluid temperatures at the inlet of the vapor-transport line, T_{sat}, and at the exit of the liquid-transport line, $T_{ev\text{-}in}$, were measured. Sheathed thermocouples, positioned at the center of these pipe using special compressions fittings, were used for these temperature measurements.

Both the vapor- and the liquid-transport lines were very well insulated on their outside surface with fiberglass insulation (R20, RSI3.5), in order to minimize heat losses to the ambient environment. A box built from 19 mm thick wood planks was used to hold this fiberglass insulation in place.

The thermal resistance for the vapor-transport line from the inside surface of the pipe to the ambient environment, $R_{th-vl-out}$, and that for the liquid-transport line, $R_{th-ll-out}$, were both determined using special experiments. In these experiments, distilled water at about 70°C, supplied from a constant-temperature bath, was circulated through the vapor- and liquid-transport lines, and the drops in the temperature of this water as it flowed through these lines were monitored. In each run of these experiments, once a steady-state condition was established, the aforementioned temperature drops were recorded, and the corresponding mass flow rate of the water was measured using a simple

stopwatch/bucket/mass balance method. These experimental data and a steady-state energy balance for each transport line were used to determine the corresponding values of the above-mentioned thermal resistances. In order to achieve good accuracy in these measurements, the steady-state mass flow rates of the distilled water were adjusted, using a fine stainless steel metering valve, to be low enough to obtain temperature drops of the order of 10°C. In this context, it is noted that the thermal resistances associated with laminar and fully-developed convective heat transfer inside the pipe of the vapor- and liquid-transport lines were negligible compared to $R_{th-vl-out}$ and $R_{th-ll-out}$, respectively. After several runs of these experiments, the results were averaged to obtain the following results: $R_{th-vl-out}$ = 3.56 °C/W and $R_{th-ll-out}$ = 14.7 °C/W. The uncertainties in these values were determined to be less than ±16.0%.

4.1.4 Two-Phase Reservoir

As was mentioned earlier, a two-phase reservoir is attached to the LHP (see Figure 4.1). This reservoir was designed primarily for use during the filling (charging) of the LHP. A stainless steel ball valve (indicated by B.V. in Figure 4.1) is used to isolate this reservoir from the LHP after completion of the filling process, and the LHP is operated with a fixed active mass of the working fluid. However, this two-phase reservoir could also serve to run the loop as a capillary pumped loop (CPL), if desired, in future extensions of this work.

This two-phase reservoir was made of fully welded 101.6 mm (4-inch nominal) stainless steel pipe (SS 304) and standard end-cap fittings also made of stainless steel (SS 316). The total internal volume of this reservoir is 2035 mL. The reservoir was equipped with a sight glass (denoted as S.G. Figure 4.1) to allow viewing of the liquid-vapor interface, and a pressure gage capable of operating from vacuum to about 7 bars (-30 inch of Hg to 100 psig). A relief valve (denoted as R.V. in Figure 4.1) was attached to this reservoir for safety purposes. Two cartridge electrical heaters, each rated for 500 W, were installed at two different levels inside the reservoir for heating and temperature control purposes. A sheathed thermocouple was also installed at a fixed level inside the reservoir allowing monitoring of the saturation temperature of the liquid-vapor mixture in the

reservoir. A manually operated vent valve and a drain were also attached to the reservoir (not shown in the figure). The whole reservoir was thermally insulated using fiberglass, and the whole assembly (except the relief valve, the sight glass, the vent valve, and the drain) was mounted in a box made from wood planks.

4.1.5 Data Acquisition and Control

All thermocouples and differential pressure transducers were connected to a data acquisition and control system (HP 3497A). This system was connected to a personal computer. The data acquisition and control were effected via a computer program written using the VEE OneLab (Agilent Technologies) software. Once the measurements of temperature and pressure drop were initiated, data were periodically saved (at 10-second time intervals) on a hard disk in the personal computer. The input voltage and current supplied to the various heaters were measured using suitable multimeters (HP 3478A); currents greater than 1 A were deduced from measurements of voltage drop across a resistive shunt. These voltage and current measurements were also acquired and recorded using the aforementioned data acquisition and control system, and these measurements were used to calculate the corresponding power inputs.

4.2 Filling Strategy and Procedure

For stable steady-state operation of the LHP presented in Figure 4.1, it is necessary to have the following phase distribution of the working fluid: The grooves in the evaporator (see Figures 4.2 and 4.3) should be filled with the vapor; the vapor-transport line should be filled mostly with the vapor phase (some condensation in this line was unavoidable in this work, and it is accounted for in the proposed network thermofluid model proposed in Chapter 5); and the liquid-transport line, the evaporator liquid pool, and the void volume of the wick structure should be filled with the liquid phase. In addition, it is desirable to have full condensation of the vapor inside the condenser; in other words, the condenser pipe should be only partly filled with the two-phase (vapor-liquid) mixture, and the rest of it should be filled with only the condensed liquid. The filling strategy and procedure that were designed and employed to achieve this desirable phase distribution during the steady-state operation of the LHP are presented in this section. The two-phase reservoir

(discussed in Section 4.1.4 and shown in Figure 4.1) played a crucial role in the proposed filling strategy and procedure.

After the LHP was assembled (including the two-phase reservoir), it was fully flushed several times with all-glass double-distilled water, using a gravity-feed overhead tank to supply the water and pressurized nitrogen to effect forced draining. This flushing process is necessary to get rid of dust and some other solid particles that might get inside the LHP during its assembly.

After the completion of this flushing process, the LHP was connected to a vacuum pump (Boc-Edwards-RV8; 8.0 m^3/hr; 3×10^{-2} mbar) at an access port located in between the evaporator and the two-phase reservoir. Then the ball valve in the pipe that connects the two-phase reservoir to the LHP was opened and the vacuum pump was turned on. The vacuuming process was continued until a pressure lower than 1.33 mbar (±0.53 mbar; or 1.0 torr) was sustained; this pressure was monitored using a vacuum gauge (Boc-Edwards-CG 16K; 0-20 torr; ±2%F.S.) installed on the vacuum line. At this stage, the two-phase reservoir was disconnected from the LHP by shutting off the isolating ball valve, but the vacuum pump was left on. The reservoir was then connected to the above-mentioned gravity-feed overhead tank, located about 2.0 m above it, and was filled completely with all-glass double-distilled water. Then the two cartridge heaters in the two-phase reservoir were turned on to heat and deaerate the water and also get rid of any trapped air bubbles: During this process, due to thermal expansion and degasification, the water pressure rises inside the isolated reservoir. The reservoir was kept isolated and closed until the pressure gauge installed on it indicated a pressure of 0.5 bar above the local atmospheric pressure. The vent valve on the reservoir was then opened, and the heating at atmospheric condition was continued until the water started to boil (at about 100°C). At this stage, the water vapor was continuously vented from the system for about 10 min. Then the vent valve was closed, and the heating was continued until a pressure of 1 bar above the local atmospheric pressure was built up inside the reservoir. At this stage, the reservoir was pressurized and filled with a two-phase liquid-vapor water mixture that was essentially free of air.

The vacuum pump was then shut off and disconnected from the LHP, and the isolating ball valve was opened gradually allowing the liquid phase to flow from the

reservoir into the loop: It should be noted that the connecting pipe from the LHP was attached to the point of lowest elevation of the reservoir, in order to ensure that only the liquid phase of the water flowed into the loop. As the amount of the liquid inside the reservoir was much higher than the total LHP volume, after a while, the whole LHP was fully filled with liquid phase of the working fluid. During this filling process, the liquid-vapor interface in the two-phase reservoir was monitored via the sight glass (see Figure 4.1), and its final level was recorded. At this stage, the LHP (fully filled with liquid water) and the connected two-phase reservoir were ready for initiation of a process that was designed to obtain the desired phase distribution (inside the LHP).

To achieve the desired phase distribution, the LHP (fully filled with water) and the attached to the two-phase reservoir are together started as a CPL. The first sequence of steps in this startup procedure are the following: The oil-bath temperature was set to about 40°C and one of the cartridge heaters installed at the bottom of the two-phase reservoir (submerged in the liquid phase) was turned on; once the fluid temperature in the two-phase reservoir was about 70°C, the electrical power input to the cartridge heater inside it was reduced (via a variac) to about 15 W and then maintained (this level of power input was enough to compensate for heat losses in the reservoir and keep its temperature relatively constant at about 70 °C); an automatic on/off controller was not used with this cartridge heater in order to avoid excessive pressure oscillations inside the LHP during this startup process; and after the oil-bath and the two-phase temperatures attained and maintained their set values, a total power input of about 250W was applied to the heaters in the evaporator assembly (see Figure 4.3). It should be noted that only a part of this power input applied to the heaters in the evaporator assembly is actually transmitted to the evaporator (about 200W), and the rest of it is lost to the ambient environment.

The startup procedures and the related transient behaviors of CPLs are explained and discussed in several published works, for example in the works of Cullimore (1991) and Hoang and Ku (1996). As heat is applied to the initially fully flooded evaporator, the temperature of the fluid inside of it starts to rise and reaches a value close to the one set in the two-phase reservoir (about 70°C). At this temperature, the pressure inside the evaporator reaches the saturation pressure of the two-phase system (the ensemble of the

loop and the reservoir), and nucleate boiling is initiated within the vapor grooves, accompanied by vapor bubbles generation and accumulation. As the heat transfer to the vapor bubbles is continued, they expand and the surrounding liquid in the vapor grooves is displaced to accommodate the vapor growth: This process is indicated by spikes in the pressure difference across the evaporator, as mentioned by Hoang and Ku (1996). Once the vapor grooves in the evaporator are cleared of the liquid, the liquid-vapor interface enters the wick structure, and the capillary pressure that is built there prevents the vapor from flowing backwards into the liquid pool. Heat is conducted from the metal ridges in between the vapor groves to the liquid-saturated wick, and it causes the liquid to change phase at the liquid-vapor interface. The resulting vapor pushes out the liquid from the vapor-transport line into the condenser, then into the liquid-transport line, and finally into the liquid pool of the evaporator (see Figure 4.1); the excess liquid is accommodated in the connected two-phase reservoir. Due to capillary action, the liquid is continuously supplied to the liquid-vapor interface in the evaporator, sustaining the evaporation there. Eventually, a part of the condenser opens up (is filled with vapor), and the condensation of the vapor in the condenser is initiated. As was mentioned above, the excess liquid from the initially flooded LHP collects in the two-phase reservoir; this process is indicated by the rise in the level of the liquid-vapor interface in the two-phase reservoir, monitored via visual observation of the sight glass (see Figure 4.1).

The temperature and pressure measurements at the previously indicated locations, spread out over the LHP, allow close monitoring of its behavior during this startup procedure, and also its progress from the transient to the steady-state mode of operation. Once the LHP reached its steady-state condition of operation, the mean level of the vapor-liquid interface in the two-phase reservoir, as indicated in the sight glass, was recorded and compared to its initial value (just after the flooding of the LHP with the liquid water): The related difference in the volume of the liquid in the two-phase reservoir is equal to total volume of the grooves, the groove collector, the vapor-transport line, and the part of the condenser that is filled by the vapor phase; this volume, along with the known geometry of the LHP and the reservoir, was used establish that the zero-quality (full condensation of the vapor) point is indeed located at the desired position inside the condenser pipe.

The choice of the set-point temperature in the two-phase reservoir ultimately determines the steady-state operating conditions in the LHP: At the end of the above-mentioned startup process, the steady-state saturation temperature in the evaporator and also that in the condenser take on values very close to the initial set-point temperature in the two-phase reservoir. For a given power input to heaters in the evaporator-assembly and a constant thermal sink temperature, an increase in the reservoir set point temperature produces a corresponding increase in the mean steady-state operating temperature of the LHP; this, in turn, leads to a higher overall difference between the temperature of the fluid in the condenser pipe and the oil in the bath (thermal sink), and, consequently, less surface area is needed for the complete condensation of the saturated vapor that enters the condenser. Therefore, an increase in the initial set-point temperature of the two-phase reservoir causes the condenser to become less open, and the mass of the liquid phase (and also the mass of active working fluid) inside the LHP loop to be higher. On the other hand, a decrease in this initial set-point temperature forces the zero-quality point towards the end of the condenser pipe (and more excess liquid to accumulate inside the two-phase reservoir), and results in a lower mass of liquid (and active working fluid) inside the LHP. Thus, the initial set-point temperature of the two-phase reservoir, the initial level of power input to the heaters in the evaporator-assembly, and the set-point temperature of the oil bath together allow the mass of active working fluid, the phase distribution, and the mean steady-state operating temperature of the LHP to be determined.

During the above-mentioned steady-state operation of the combination of the LHP and the two-phase reservoir in the CPL mode, the pressure drop across the evaporator (see Figure 4.1) was not quite constant (steady), in the sense that it continually oscillated about a mean value. These time-periodic, but not necessarily harmonic, pressure oscillations, which have also been observed and reported by Cullimore (1991), Muraoka et al. (1998, 2001), and Hoang and Ku (1996), are generally caused by dynamic interactions between the fluid in the two-phase reservoir and the active fluid in the loop: The elevation of the liquid-vapor interface in the two-phase reservoir was observed (through the sight glass) to oscillate about ±25.4 mm (equivalent of about ±250 Pa) about its mean level during such pressure oscillations in the loop; furthermore, the temperature measured at the inlet of the evaporator also oscillated by about ±3.5°C, showing some

inflow and backflow from the two-phase reservoir to the liquid pool, and also from the liquid pool into the liquid-transport line.

In this study, it was decided to avoid (or considerably reduce) the above-mentioned time-periodic oscillations that characterize the CPL mode of operation of the loop and two-phase reservoir combination. Therefore, once the above-mentioned time-periodic steady-state conditions were reached in the CPL mode, the two-phase reservoir was isolated from the loop by shutting off the ball valve (denoted as B.V. in Figure 4.1). Then all power inputs were shut down fully, and the system was allowed to cool down to the ambient environment temperature. At this stage, the LHP is charged with a fixed amount of the active working fluid (an amount that provides the phase distribution and the mean operating temperature desired in the LHP during its steady-state mode of operation). Furthermore, it was found that with this filling strategy and procedure, when this LHP is restarted (with the two-phase reservoir isolated), it reaches a steady-state operating condition that involves considerably smaller pressure oscillations than those observed in the aforementioned CPL mode.

4.3 Experimental Procedure

At the rest condition of the charged LHP isolated from the two-phase reservoir (that is, prior to the start of its operation), the elevation of the condenser was adjusted so that the zero-quality point inside it is slightly higher than that of the top surface of the wick in the evaporator. This ensures that the whole evaporator (and perhaps even a part of the vapor-transport line), a part of the condenser, and the liquid-transport line are completely filled with the liquid phase. The startup of the LHP was initiated by setting the temperature of the oil-bath and turning on the power input to the evaporator heaters, at the desired levels. The acquisition and recording of data from all thermocouples, differential pressure transducers, and multimeters (used to measure the voltages and currents supplied to the heaters) were initiated at least two hours before this startup of the LHP, and continued all through the experiment. When the differences between two consecutive sets of temperature readings (taken at 10 second intervals) were all less than or equal to $\pm 0.05^{\circ}C$ over a period of at 30 minutes, it was assumed that the steady-state

conditions prevailed. This condition could take up to eight hours to be reached for each experimental run.

In the next chapter, the network thermofluid model presented in Chapter 2 is extended and adapted to the LHP described in this chapter. The corresponding experimental and numerical results are presented and discussed in Chapter 6.

Chapter 5:

A Loop Heat Pipe with a Flat Evaporator and Fixed Active Mass of Working Fluid: Network Thermofluid Model

In this chapter, the network thermofluid model presented in Chapter 2 is extended and adapted to the geometry and conditions of the loop heat pipe (LHP) presented in Chapter 4. Figures 4.1 and 5.1 schematically illustrate this LHP: It has a flat (plate-type) evaporator, a vapor-transport line, a condenser, and a liquid-transport line. As shown in this figure, an external two-phase reservoir is attached to the LHP.

The basic network thermofluid model presented in Chapter 2 is designed for LHPs with a cylindrical evaporator integrated with a compensation chamber (a two-phase reservoir; see Figure 2.1). As was discussed in the earlier chapters, such an integrated compensation chamber in the LHP automatically adjusts the active fluid mass inside the loop when there are variations in the heat input or in the sink temperature. However, in the LHP considered here (see Figures 4.1 and 5.1), as was described in Chapter 4, after charging (that is, filling the LHP with the working fluid), the external two-phase reservoir is isolated from the system, and the active fluid mass in the loop is kept fixed. Thus, the modeling of such an LHP requires the imposition of an additional condition, namely, the conservation of the active fluid mass inside the loop: This is done in the network thermofluid model proposed in this chapter.

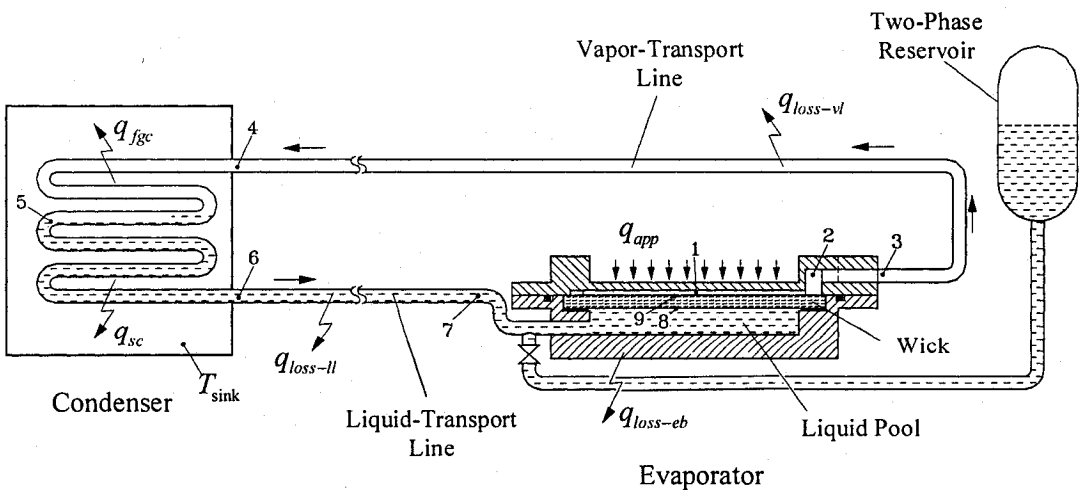

Figure 5.1: Schematic representation of the loop heat pipe considered in the formulation of the proposed network thermofluid model.

The pressure drop in the two-phase region of the condenser and the heat exchange with the ambient environment from (or to) the fluid in the vapor- and liquid-transport lines, which were neglected in the network thermofluid model presented in Chapter 2, are included in the new model presented in this chapter. Furthermore, some simplifications in the modeling of the evaporator are incorporated via a lumped model.

In the enhanced network thermofluid model presented here, a special procedure is presented (and incorporated) for estimating the augmented pressure drops associated with fluid flow (single- and two-phase) through the bent portions of the serpentine vapor-transport line (see Figure 5.1 and 5.7), where there is a possibility of condensation of the vapor. This special procedure was essential for obtaining accurate simulations, because a significant portion of the overall pressure drop in the LHP occurred in the vapor transport line. On the other hand, it was not necessary (with respect to overall accuracy) to incorporate any special procedures to account for heat transfer augmentations in the bends of the vapor-transport line, as the rate of heat loss from this line to the ambient environment is controlled primarily by the thermal resistance of the excellent insulation used outside it, rather than the convective heat on its inside surface. Furthermore, with respect to the serpentine pipe of the condenser (see Figures 4.1 and 5.1), it was not necessary to incorporate special procedures for estimating either the augmented pressure drops or heat transfer in the bent portions, as preliminary calculations and experiments showed that most of the vapor condensed in the initial straight portion of this pipe.

In this chapter, first, the various thermodynamic processes that the working fluid undergoes during steady-state operation of the LHP are presented with reference to a pressure-temperature (P-T) diagram. Then, a network thermofluid model of this LHP operating under steady-state conditions is presented. Following that, quasi-one-dimensional mathematical models of the fluid flow and heat transfer in each of the elements of the LHP (and, collectively, in the entire LHP) are proposed and discussed.

Distilled water is used as the working fluid in the LHP considered here, but the proposed network model can work with any suitable fluid, with appropriate inputs of thermophysical property data. Furthermore, the development of this model is done in the context of the specific LHP shown in Figure 5.1, but the formulations of the various

elements of the model are quite general, in the sense that they can be readily adapted for the modeling and design of other LHPs.

5.1 THERMODYNAMICS

The thermodynamics of the different processes that the working fluid undergoes during the steady-state cyclical operation of the LHP shown in Figure 5.1 are discussed in this section. The thermodynamic states of the working fluid at each of the numbered points shown in Figure 5.1 are presented on a pressure-temperature (P-T) diagram in Figure 5.2.

At point 1 in the evaporator grooves, the fluid is vaporized at the saturation temperature T_1, and the corresponding saturation pressure P_1 is the highest thermodynamic (static) pressure in the loop. The power input to the LHP manifests itself as a uniform heat flux over the entire length of the grooves in the evaporator. A part of this power input heats the vapor during its passage between points 1 and 2: Thus, as is shown in Figure 5.2, the vapor undergoes a heating process and a pressure drop during its passage through these grooves, and it arrives at point 2 in a slightly superheated state.

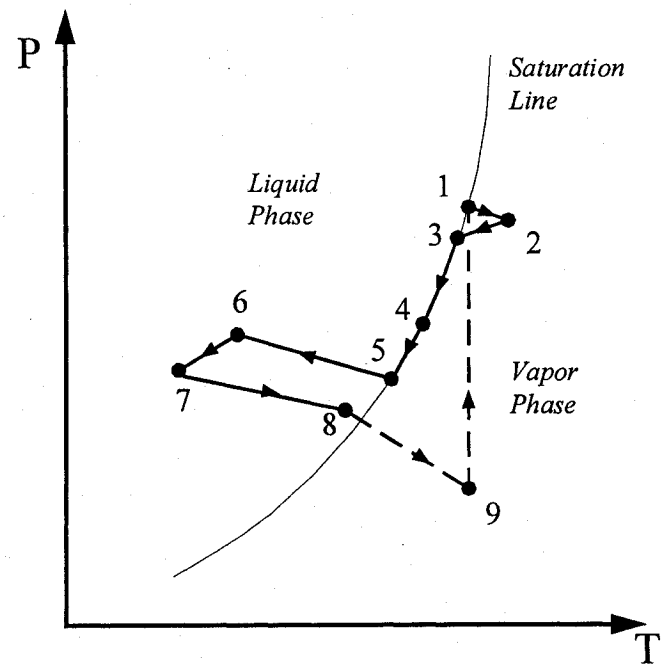

Figure 5.2: Pressure-temperature (P-T) diagram (not to scale) for the loop heat pipe considered in the formulation of the proposed network thermofluid model.

The LHP, with distilled water as the working fluid, was operated with a saturation temperature (at point 1) well above the ambient environment temperature and a minimum temperature of about 40°C in the condenser heat sink (the constant-temperature oil bath in which the condenser pipe is immersed). It was necessary to operate the LHP at these conditions in order to obtain an absolute saturated vapor pressure at point 1 that was high enough to easily overcome the total pressure drop in the LHP. Therefore, even with the entire LHP (except the condenser) well insulated, for the whole range of the power input to the evaporator, the heat losses to the ambient environment (from the evaporator, and the vapor- and liquid-transport lines) were not negligible.

After reaching the vapor-accumulation region at point 2, the vapor flows through some passages inside the evaporator and then exits it at point 3. Due to heat losses from the peripheral areas of the evaporator, the vapor undergoes a cooling process, in addition to a pressure drop, during its passage from point 2 to 3. As shown in Figure 5.2, it is assumed here that the vapor exits the evaporator (point 3) in a saturated state.

The process 3-4 is a cooling process. It also involves a static pressure drop that is needed to overcome frictional losses and minor losses (in the bends of the vapor-transport line). The vapor-transport line is well insulated, thus the vapor condenses only partially inside it. In practice, the fluid at point 4 is at a saturation temperature that is slightly lower than that at point 3 and has a quality that is slightly less than unity, as the rates of heat loss (and the accompanying rates of condensation) are low and the changes in saturation temperature due to the pressure drops (with distilled-water as the working fluid) are small. As an example, for this LHP, at an average operating temperature of 80°C, the change in saturation temperature due to a pressure drop of 2000 Pa is just 1.05°C [determined using the water saturation tables given in Van Wylen et al. (1994)]. The process 3-4 is demonstrated on the saturation line in Figure 5.2.

Under steady-state conditions, the net rate of heat absorbed by the fluid in the evaporator and in the vapor- and liquid-transport lines is rejected to a thermal sink in the condenser. Assuming that complete condensation takes place inside the condenser pipe between points 4 and 5, the two-phase fluid that enters at point 4 with a quality of slightly less than unity condenses to saturated liquid (0% quality) at point 5. If the condenser pipe length is long enough, the condensed liquid exits the condenser at point 6 in a subcooled

condition. The physical elevation (with respect to the vertical direction parallel to the gravitational acceleration vector) of the inlet of the condenser of the LHP presented in Figure 5.1 is slightly higher than that of the liquid-vapor interface inside the evaporator pipe (by about 50.8 mm): The condenser pipe of this LHP is sloped slightly downward (slope of about 1%) from the inlet (point 4) toward the exit (point 6), with point 6 having almost the same elevation as the liquid-vapor interface inside the wick in the evaporator (point 9). Despite this change in elevation, in the two-phase region of the condenser, the friction and minor losses are high enough to cause a static pressure drop between points 4 and 5: The process 4-5 is a cooling process with a static pressure drop, in which the fluid reaches the saturated liquid state at point 5, as shown on the saturation line in Figure 5.2. However, in the subcooled region of the condenser, the friction and minor losses are very low and the density of the condensed liquid is very high (relative to that of the vapor). As a result, the elevation (gravity related) head causes an increase in the static pressure as the condensed liquid flows inside the condenser pipe from point 5 to point 6 (here, it should be noted that the sum of the pressure, elevation, and velocity heads at point 5 is higher than that at point 6): Therefore, process 5-6 is a cooling process with a static pressure rise, in which the condensed liquid reaches a subcooled state at point 6. At point 6, the liquid enters the horizontal liquid-transport line, where it undergoes another cooling process (due to heat losses to the ambient environment) accompanied by another static pressure drop: This process is demonstrated by line 6-7 in Figure 5.2.

The subcooled liquid exits the liquid-transport line at point 7 and enters the liquid pool inside the evaporator. For the particular LHP used in this investigation, the liquid-transport line (points 6 to 7) is horizontal with a mean elevation that is almost the same as that of the liquid-vapor interface in the evaporator (point 9). A small length of pipe with two 90° bends is used to connect point 7 to the entry point in the liquid pool of the evaporator, located at the lowest elevation inside the evaporator. This small length of pipe is very well insulated and the mass flow rate of the liquid in this pipe is very small: Thus it is assumed that the friction and minor losses and also the temperature change in this small segment of pipe are all negligible compared to their values in other portions of the LHP.

A part of the heat input to the evaporator leaks through to the fluid in the liquid pool, due to conduction through the liquid-saturated wick material and also the metallic body of the evaporator. Following terminology commonly used in the HP and LHP literature, this heat transfer (which heats up the liquid in the liquid-pool) is referred to in this work as heat leak [Kaya and Hoang (1999)]. Point 8 is located at the entrance of the wick inside the evaporator. As a result of the heat leak, 7-8 is a heating process. It is also involves a static pressure drop due to friction and minor losses. The liquid at point 8 could be in a slightly subcooled state (as shown in Figure 5.2), or it could be at the saturated or even slightly superheated state.

After entering the wick inside the evaporator, the liquid moves up to the liquid-vapor interface. During this passage through the wick, the temperature of the liquid continues to rise, due to the heat leak, and its static pressure drops. At the liquid-vapor interface, it is assumed that the temperature of the liquid (point 9) equals that of the saturated vapor (point 1): Thus, this liquid is in a superheated state, because, due to surface tension effects and the consequent capillary head developed at the liquid-vapor interface, the saturation pressure at point 1 is higher than that of the liquid at point 9. The superheated liquid processes (part of the process 8-9 and the process 9-1) are plotted as dashed lines in the vapor zone of the P-T diagram (see Figure 5.2). Due to heat input at the liquid-vapor interface, the superheated liquid evaporates in a constant-temperature process from point 9 to 1, and the pressure of the vapor jumps up due to the capillary head developed there. Point 9 has the lowest and point 1 has the highest static pressure in the LHP.

5.2 NETWORK MODEL

The network model of the LHP presented in Figure 5.1 is based on the requirements of conservation of mass (of the active fluid), momentum, and energy.

This LHP is charged with a fixed amount of a working fluid (all-glass double-distilled water), denoted by $m_{charged}$. The distribution of this total mass of the fluid over the LHP is expressed as follows:

$$m_{total} = m_{charged} = m_{lpool} + m_{lwick} + m_{vgroove} + m_{vline} + m_{cd-2\varphi} + m_{cd-sc} + m_{lline} \tag{5.1}$$

In this equation, m_{total} is the total mass of the working fluid in the LHP, m_{lpool} is the mass in the evaporator liquid pool, m_{lwick} is the liquid mass in the wick inside the evaporator, $m_{vgroove}$ is the vapor mass in the evaporator grooves and vapor-accumulation region, m_{vline} is the fluid mass in the vapor-transport line, $m_{cd-2\varphi}$ is the fluid mass in the two-phase region of the condenser, m_{cd-sc} is the liquid mass in the subcooled region of the condenser, and m_{lline} is the liquid mass in the liquid-transport line.

With regard to the requirement of steady-state momentum balance, in each segment of the LHP, the vector sum of the surface and body forces acting on the fluid must equal the rate of increase of its momentum as it flows through the segment.

Under steady-state conditions, an overall energy balance on the LHP, which is a closed system with no work inputs or outputs, yields:

$$q_{app} = q_{loss-vl} + q_{cd-reject} + q_{loss-ll} + q_{loss-eb} \tag{5.2}$$

where q_{app} is the net rate of heat input to the evaporator, $q_{loss-vl}$ is the rate of heat loss from the fluid in the vapor-transport line, $q_{loss-ll}$ is the rate of heat loss from the liquid in the liquid-transport line, $q_{loss-eb}$ is the rate of heat loss from the evaporator body, and $q_{cd-reject}$ is the rate of heat rejected in the condenser to the heat sink (constant-temperature oil bath). All the heat loss terms in this equation refer to the corresponding rates of heat transfer from the working fluid to the ambient environment.

Mathematical models of the fluid flow and heat transfer in each of the LHP elements are presented in the remainder of this section.

5.2.1 Evaporator

As was discussed in Chapter 4 (see Section 4.1.1), the flat evaporator of the LHP is constructed from two square machined plates, with a porous flat-plate sintered powder-metal wick sandwiched between them: Details of this evaporator are provided in Figures 5.3 and 5.4.

Under steady-state conditions, the net rate of heat input to the evaporator, q_{APP}, can be divided into four portions (see Figure 5.4):

$$q_{app} = q_{vsh} + q_{fg} + q_{hl} + q_{loss-eb} \tag{5.3}$$

where q_{fg} is the part of q_{app} that goes into the evaporation of the working fluid in the evaporator, q_{hl} is the rate of heat leak from the evaporator to the liquid pool, q_{vsh} is the rate of heat transfer that is used up in the superheating of the vapor during its passage through the grooved channels, and $q_{loss-eb}$ is the part of q_{app} that is lost to the ambient environment from the evaporator body.

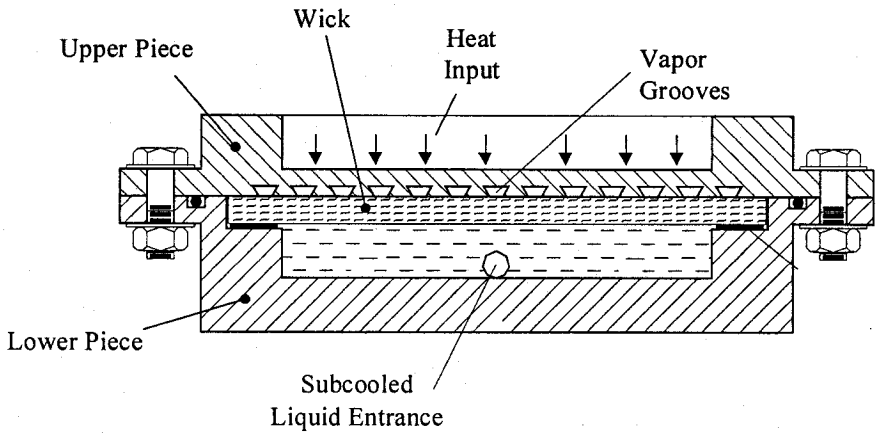

Figure 5.3: Details of the flat evaporator.

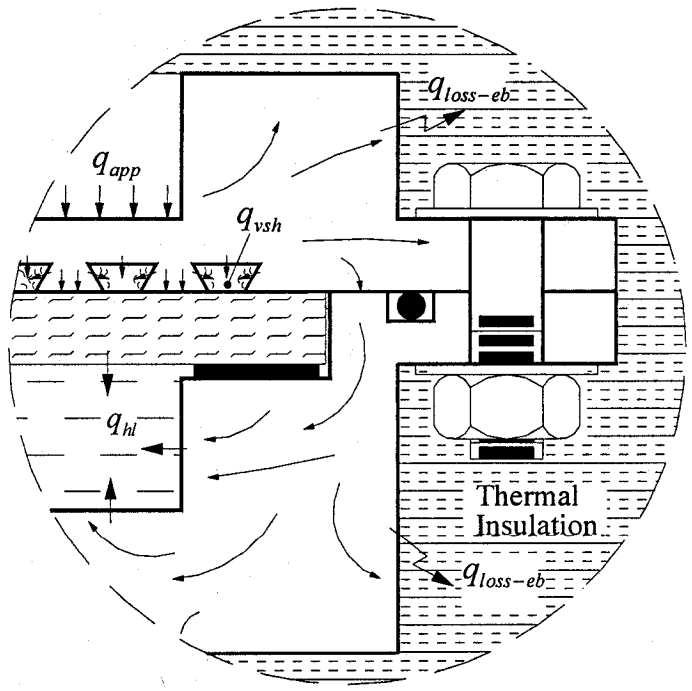

Figure 5.4: Additional details of the flat evaporator.

In the present study, q_{vsh} is assumed to be negligible: Thus, with reference to the notation in Figure 5.2, the vapor is assumed to exit the evaporator in a saturated state and point 3 is on the saturation line. This saturation temperature (T_3) is different from that of the saturated vapor inside the grooves and adjacent to the liquid-vapor interface in the evaporator, T_{sat} (= T_1). If the pressure drop ΔP_{vl-ent} (between point 1 and 3 in Figures 5.1 and 5.2) can be estimated, the vapor-transport line entrance temperature can be determined using

$$T_{sat-vl-in} = T_{sat} - \Delta P_{vl-ent} / \left(\frac{dP}{dT} \right)_{sat} \tag{5.4}$$

In the present study, ΔP_{vl-ent} is quite low. So it was assumed that the corresponding change in saturation temperature is negligible: Thus, $T_1 = T_3 = T_{sat}$ and $T_{sat-vl-in} = T_{sat}$.

In the context of the above-mentioned assumptions, the entire evaporator is treated as one subsystem (lumped model) with the subcooled liquid (at $T_{ev\text{-}in}$) entering from one side and saturated vapor (at T_{sat}) exiting from the other side.

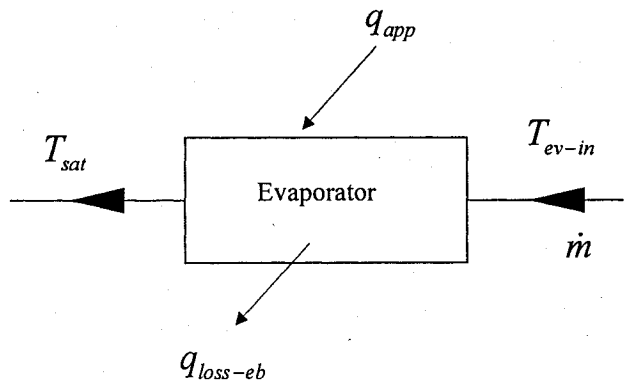

Figure 5.5: Schematic of energy balance on the evaporator.

An energy balance on the evaporator (see Figure 5.5) gives the following:

$$q_{app} - q_{loss-eb} = \dot{m}\left(i_g|_{T_{sat}} - i|_{T_{ev-in}} \right) \tag{5.5}$$

In this equation, $\dot{m}$ is the mass flow rate; $i_g|_{T_{sat}}$ and $i|_{T_{ev-in}}$ are, respectively, the specific enthalpies of the saturated vapor leaving and the subcooled liquid entering the evaporator; and $q_{loss-eb}$ is the rate of heat loss from the evaporator body.

The evaporator of the LHP studied in this work was well insulated. In spite of this, when the operating saturation temperature is well above the temperature of the ambient environment, the rate of heat loss from the evaporator body becomes important in the determination of the net rate of heat transported by the LHP. Most of the surface of the upper portion of the evaporator is in direct contact with an electrical heating element, and thus it mostly receives (rather than losses) heat. Heat is conducted through metal-to-metal contact and also through the wick from the upper to the lower portion of the evaporator (heat leak). A part of this heat leak goes into heating up the subcooled liquid entering the evaporator, and the rest of it is lost to the ambient environment. Here, it is assumed that the main rate of heat loss from the evaporator body to the ambient occurs from its lower portion (see Figures 5.3 and 5.4). Precise prediction of $q_{loss-eb}$ could be done via complete three-dimensional numerical modeling of the fluid flow and heat transfer inside the evaporator: This type of detailed modeling of the evaporator is not within the scope of this thesis; rather, it is suggested as one of the possible extensions of this work. Here, to estimate $q_{loss-eb}$ for use in the proposed network thermofluid model, a semi-empirical approach based on the experimental data (obtained in this work) is adopted. This semi-empirical approach is discussed in the next couple of paragraphs.

In steady-state operation of the LHP, for each value of power heat input to the evaporator, q_{app}, the average temperature at the bottom surface of the lower piece of the evaporator, T_{ev-bot}, was measured and recorded. For the whole ranges of power inputs to the evaporator and the sink temperatures used in this experimental study, the measured values of T_{ev-bot} were plotted against the corresponding values of q_{app}. A third-order polynomial curve was then fitted to these experimental data to obtain the following equation: $T_{ev-bot} = 31.63 + 0.282 q_{app} - 6.01\times10^{-4} q_{app}^2 + 5.03\times10^{-7} q_{app}^3$, where T_{ev-bot} is in °C and q_{app} is in W. This correlation is valid for $80\ \text{W} \le q_{app} \le 460\ \text{W}$ and $40°\text{C} \le T_{\text{sink}} \le 62°\text{C}$. Using this correlation, in steady-state operation, for each value of power input to the evaporator, the corresponding temperature at the bottom surface of the evaporator can be estimated. Knowing T_{ev-bot}, the rate of heat loss to the ambient environment from the evaporator body can be estimated using the following equation:

$$q_{loss-eb} = U_{ev} A_{lp} \left(T_{ev-bot} - T_{amb} \right) \tag{5.6}$$

In this equation, U_{ev} is an overall heat transfer coefficient, A_{lp} is the total heat transfer surface area of the lower piece of the evaporator, and T_{amb} is the ambient environment temperature. In this study, U_{ev} was estimated experimentally as follows: Hot water (single-phase) was passed through the evaporator, *without* the wick and with no heat input; the mass flow rate and the change in the bulk temperature of this water stream were measured; $q_{loss-eb}$ was calculated with this data; T_{ev-bot} and T_{amb} were measured; and then Eq. (5.6) was used to calculate the overall heat transfer coefficient. This procedure yielded U_{ev} = 5.75 W/m^2-K, and this value was used in the proposed network thermofluid model.

In principle, assuming one-dimensional Darcy-flow through a homogeneous porous material, the friction pressure *drop* as the liquid phase of the working fluid flows through the wick inside the evaporator, ΔP_{wick}, can be estimated as follows:

$$\Delta P_{wick} = \frac{l_{wick}}{A_{ef-wick}} \frac{\dot{m}}{K_{wick}} \frac{\mu_l}{\rho_l} \tag{5.7}$$

where l_{wick} is the thickness of the wick, $A_{ef-wick}$ is an effective open flow area of the wick, and K_{wick} is the effective permeability of the wick. As was discussed in Chapter 3, the permeability of the wick was measured using a numerical/experimental approach. The results are reported in Chapter 3 (Section 3.4.5) and in Table 4.1.

In this work, however, as shown in Figures 5.3 and 5.4, the upper surface of the wick is partially blocked by the solid ridges in between the grooves in the upper plate of the evaporator; and a 12.7 mm wide strip around the perimeter of its lower surface is covered by a flat rubber gasket. With this arrangement inside the evaporator, the liquid flow pattern inside the porous wick is quite complex and it is invalid to assume that this flow is essentially one-dimensional. Therefore, it was assumed that the wick is a homogeneous porous material with a known permeability, K_{wick}, and the steady-state three-dimensional governing equations for Darcy-flow were solved numerically. The numerical results were then used to obtain the following correlation:

$$\Delta P_{wick} = C_{wick} \frac{\mu_l}{\rho_l} \dot{m} \tag{5.8}$$

The coefficient C_{wick} in this equation depends on the geometrical characteristics of the wick. For a given wick, this coefficient was found to be essentially constant and independent of the working fluid properties. The characteristics of the stainless steel (material # 1) and nickel 200 (material # 2) porous materials used as the wicks in this study are listed in Table 4.1, and the corresponding values of coefficients C_{wick-1} and C_{wick-2} are, respectively, 1.0796×10^{11} and 1.4409×10^{12} m^{-3}.

In the LHP considered in this study, the velocities of the subcooled liquid as it flows into and through the liquid pool inside the evaporator are very low: Thus, the corresponding pressure drops are negligibly small compared to those in other portions of the LHP.

5.2.2 Vapor-Transport Line

The vapor-transport line connecting the evaporator to the condenser of the LHP was made of a serpentine pipe (see Figure 5.1). Depending on the values of the loop operating temperature (T_{sat}) and the ambient environment temperature (T_{amb}), the vapor flowing through the vapor-transport line could be either heated or undergo heat loss to the ambient environment. The heat transfer and pressure drop calculations for these two cases are discussed in this subsection.

Case a) $T_{sat} < T_{amb}$

In this case, heat is transferred from the ambient environment to the vapor (heat gain), there is no condensation, and the static pressure drops as the vapor flows through the vapor-transport line.

Heat Transfer

For steady-state conditions, an energy balance over the vapor-transport line yields the following relation:

$$q_{gain-vl} = \dot{m} c_{p,v} \left(T_{cd-in} - T_{sat}\right) = UA_{vl} \left[\frac{\left(T_{cd-in} - T_{sat}\right)}{\ln\left(\left(T_{cd-in} - T_{amb}\right)/\left(T_{sat} - T_{amb}\right)\right)} \right] \tag{5.9}$$

where UA_{vl} is the overall thermal conductance for the heat transfer between the vapor flowing in the vapor-transport line and the ambient environment, and $T_{cd\text{-}in}$ is the vapor

temperature at the exit of this line. The overall thermal conductance takes into account convective heat transfer inside the pipe, radial heat conduction in the pipe wall and the insulation (if present), and external heat transfer (free convection, forced convection, radiation, or a combination of them). This overall thermal conductance can be expressed as follows:

$$UA_{vl} = \frac{1}{R_{th-vl-in} + R_{th-vl-out}} \tag{5.10}$$

In this equation, $R_{th-vl-in}$ and $R_{th-vl-out}$ are, respectively, the thermal resistance for the internal convection in the vapor-transport line and the external thermal resistance (sum of the thermal resistances associated with the pipe wall, insulating material, and the external heat transfer). Here, it is assumed that the rate of axial heat conduction through the pipe wall and the insulation are negligible compared to that in the radial direction, the convective heat transfer inside the pipe is fully developed. In this context, the two thermal resistances in Eq. (5.10) are defined as follows:

$$\begin{aligned} R_{th-vl-in} &= \frac{1}{h_{vl-in}\pi D_{vl} L_{vl}} \\ R_{th-vl-out} &= \frac{1}{h_{vl-out}\pi D_{vl} L_{vl}} \end{aligned} \tag{5.11}$$

where, h_{vl-in} and h_{vl-out} are heat transfer coefficients, both based on the inside surface area of the vapor-transport line, and D_{vl} is its internal diameter.

As was discussed earlier in this chapter, the heat loss from the vapor-transport line to the ambient environment is primarily controlled by the thermal resistance of the excellent insulation used outside it; thus, no special procedures were incorporated (or necessary, with respect to overall accuracy) to account for the influence of the U-bends on the heat transfer coefficients on its inside surface. Therefore, h_{vl-in} inside the vapor-transport line is estimated here by first calculating the Reynolds and Prandtl numbers, and then using appropriate analytical solutions or available empirical correlations for fully developed heat transfer in straight pipes. The Reynolds number is defined as follows:

$$\mathrm{Re}_{vl} = \frac{\dot{m} D_{vl}}{\mu_g A_{vl}} \tag{5.12}$$

Following the usual practice in heat transfer calculations [Incropera and DeWitt (2002)], for Re_{vl} <2300, the flow is considered to be laminar, and, for fully-developed conditions, available analytical and numerical solutions [Kays and Crawford (1993); Sparrow and Patankar (1977); Atabaki and Baliga (2005b)] show that the Nusselt number, $Nu_{vl\text{-}in}$ ($=h_{vl\text{-}in} D_{vl} / k_v$), is in the range $3.65 \leq Nu_{vl\text{-}in} \leq 4.36$: A value in the middle of this range, $Nu_{vl-in} = 4.0$, is used for this case.

For Re_{vl} >2300, a correlation proposed by Gnielinski (1976) is used to estimate the value of $Nu_{vl\text{-}in}$: For $0.5 < Pr < 2000$ and $2300 < \mathrm{Re_{vl}} < 5\times10^6$:

$$Nu_{vl-in} = \frac{(f/8)(\mathrm{Re}_{vl}-1000)\mathrm{Pr}}{1+12.7(f/8)^{1/2}(\mathrm{Pr}^{2/3}-1)} \tag{5.13}$$

where f is the Darcy friction factor, and Pr is the Prandtl number of the vapor.

The heat transfer coefficient h_{vl-out} that appears in Eq. (5.11) depends on the LHP geometry and material configurations. Figure 5.6 shows the geometry and the insulating system of the vapor- and liquid-transport lines of the LHP studied here. A detailed numerical simulation could be used for the determination of a conduction shape factor for this insulating system. However, as was mentioned in Chapter 4, a convenient and reliable experimental method was used to obtain $R_{th-vl-out}$. The following value applies here: $R_{th-vl-out} = 3.56$ °C/W.

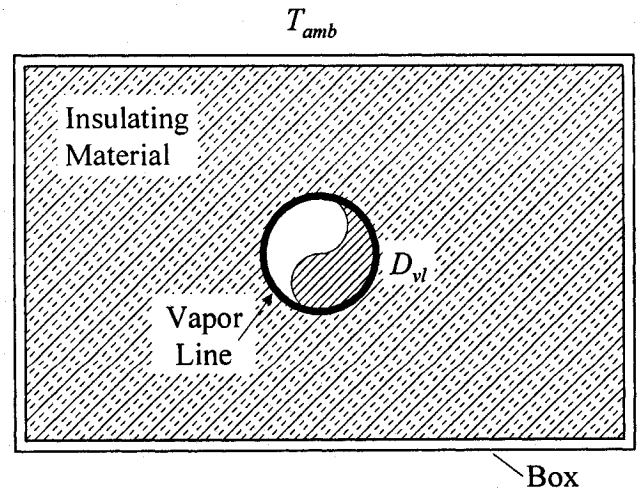

Figure 5.6: Details of the insulation used outside the vapor-transport line.

Pressure Drop

For single-phase vapor flow in the vapor-transport line, the static pressure drop, ΔP_{vl}, is calculated as follows (note that gravitational effects are assumed to be negligible here):

$$\Delta P_{vl} = \frac{(f \operatorname{Re}_{vl})}{2} \frac{\mu_g L_{vl} \dot{m}}{\rho_g A_{vl} D_{vl}^2} + \Delta P_{fittings} \tag{5.14}$$

where the second term on the right hand side accounts for the extra pressure drop that is needed to overcome losses in fittings and bends (if any are present).

For Re_{vl} <2300, the flow is considered to be laminar and fully-developed, and the Darcy friction factor, f, is calculated using the analytical solution [Kays and Crawford (1993)] $fRe_{vl} = 64.0$.

For Re_{vl} >2300, the flow is to be considered turbulent and fully developed, and the Colebrook-White correlation [Colebrook (1939); White (1991)] is used to estimate the Darcy friction factor:

$$\frac{1}{\sqrt{f}} = -2.0 \log\left[\frac{e/D_{vl}}{3.7} + \frac{2.51}{\operatorname{Re}_{vl}\sqrt{f}}\right] \tag{5.15}$$

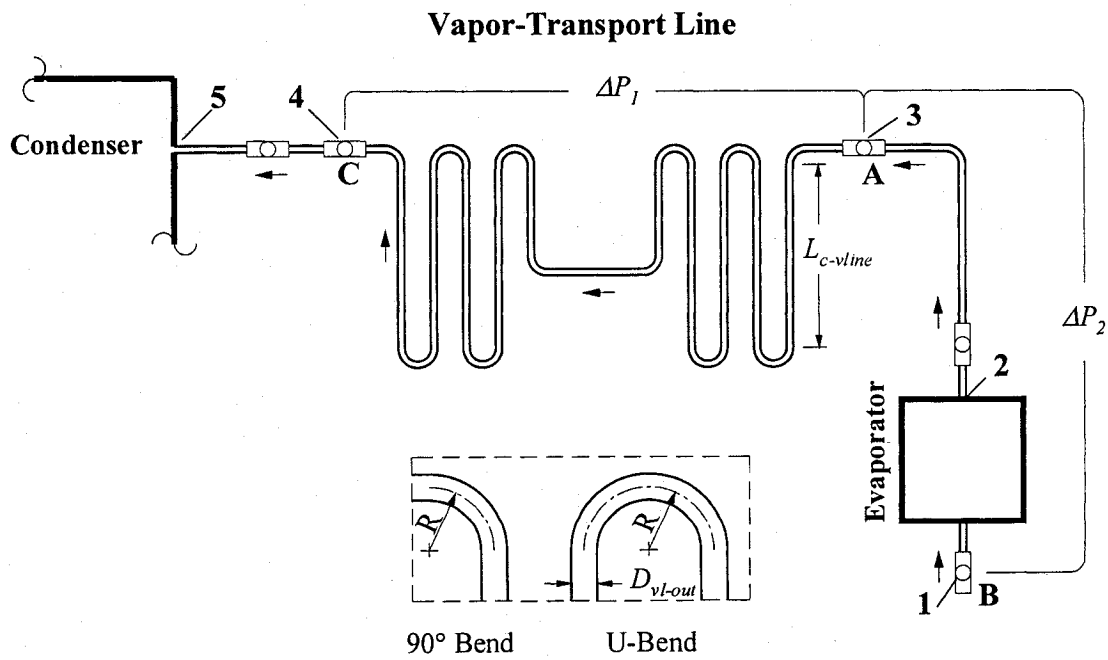

Figure 5.7: Schematic of the vapor-transport line.

Figure 5.7 schematically shows the serpentine vapor-transport line of the LHP studied here: The central part of this line has several U-bends, forming a serpentine pipe. All of these bends have the same radius: $R/D_{vl\text{-}out} = 3$, where R is the bend radius, and $D_{vl\text{-}out}$ is the pipe outside diameter. Because of the complexity of this bending pattern and also the presence of fittings, an experimental method was used to determine a correlation for the single-phase pressure drop through the vapor-transport line as a function of the fluid properties and flow rate. In this method, using nitrogen, for a wide range of flow rates (measured using five rotameters), the pressure drop through the vapor-transport line was measured. Details of these measurements are presented in Appendix B. Briefly, the vapor-transport line was divided into three sections. Referring to Figure 5.7, section 2 includes the empty evaporator (without the wick) and the portion of the vapor-transport line between points 2 and 3 (*B-A* in Figure 5.7); section 1 includes the serpentine part of the vapor-transport line located between points 3 and 4 (*A-C* in Figure 5.7); and section 3 is the portion located between points 4 and 5. The pressure drop in section 3 is estimated using the analytical and theoretically correlations discussed earlier for a straight pipe (neglecting the pressure drop through the single tee-junction present there). Two precise pressure transducers (details presented earlier in Chapter 4) were used to measure the pressure drops in sections 1 and 2: Denoted as ΔP_2 and ΔP_1, respectively, in Figure 5.7.

Pure nitrogen (99.9%) was used as the working fluid in the aforementioned experimental tests to determine the pressure drops for single-phase flow in the vapor-transport line. After passing through calibrated rotameters, this nitrogen entered the liquid-pool region of the empty (*wickless*) evaporator at point 1, and exited at point 5. In each test, the pressure drops, ΔP_1 and ΔP_2, and the corresponding flow rate were recorded. Noting that the evaporator was wickless during these experiments, and neglecting the pressure drop through the liquid-pool region and its entrance, ΔP_2 represents the pressure drop through the vapor grooves + the groove collector region + the internal passage of the evaporator exit + the pipe section 2-3 (see Figure 5.7) of the vapor-transport line. The pressure drops and the corresponding flow rates were then plotted in a dimensionless format: These curves are presented in Appendix B. A nonlinear least-squares curve fitting technique was then used to obtain the following empirical correlations for ΔP_2 and ΔP_1:

$$C_{f-1} = \frac{\Delta P_1}{\rho \bar{V}^2} = \frac{14{,}360}{\mathrm{Re}} + 9.77 \quad \text{for } \mathrm{Re} \le 2{,}300)$$

$$C_{f-1} = 14.7 - 1.42\times10^{-3}\,\mathrm{Re} + 5.27\times10^{-7}\,\mathrm{Re}^2 - 3.49\times10^{-11}\,\mathrm{Re}^3 \quad (5.16)$$

$$\text{for } 2{,}300 < \mathrm{Re} \le 10{,}000$$

$$C_{f-2} = \frac{\Delta P_2}{\rho \bar{V}^2} = \frac{2{,}047}{\mathrm{Re}} + 5.62 \quad \text{for } \mathrm{Re} \le 2{,}300$$

$$C_{f-2} = 3.45 + 6.82\times10^{-4}\,\mathrm{Re} + 1.03\times10^{-7}\,\mathrm{Re}^2 - 9.86\times10^{-12}\,\mathrm{Re}^3 \quad (5.17)$$

$$\text{for } 2{,}300 < \mathrm{Re} \le 10{,}000$$

In these equations, C_{f-1} and C_{f-2} represent dimensionless pressure drops for the corresponding sections of the vapor-transport line; Re is the single-phase flow Reynolds number based on the internal diameter of the vapor-transport line; and $\bar{V}$ is the mean (area-averaged) axial velocity of the vapor flowing inside the vapor-transport line.

Case b) $T_{sat} > T_{amb}$

In this case, the vapor loses heat to the ambient ($q_{loss-vl}$) and condenses (partially) in the vapor-transport line, and this two-phase flow also involves a pressure drop. Again, the heat loss from the vapor-transport line to the ambient environment is primarily controlled by the thermal resistance of the excellent insulation used outside it; thus, no special procedures were incorporated (or necessary, with respect to overall accuracy) to account for the influence of the U-bends on the heat transfer coefficients on its inside surface.

Heat Transfer

Assuming a quality of unity for the vapor at the entrance of the vapor-transport line, the rate of heat loss $q_{loss-vl}$, can be calculated from:

$$q_{loss-vl} = \dot{m}\left(i_g\big|_{T_{sat}} - i_{cd-in}\right)$$

$$i_{cd-in} = x_{cd-in} i_g\big|_{T_{cd-in}} + \left(1 - x_{cd-in}\right) i_f\big|_{T_{cd-in}} \quad (5.18)$$

However, the saturation temperature at the exit of the vapor line, T_{cd-in}, and the vapor quality at the exit of the vapor line, x_{cd-in}, are not known *a priori*. It is assumed here that

the vapor condenses only partially (not completely) in the vapor-transport line, as this line was very well insulated during all tests.

In order to obtain $q_{loss-vl}$, the length of the vapor line is divided into a total of M segments, and in each of these segments, it is assumed that the saturation temperature is constant: M can be adjusted to obtain any desired level of accuracy (within machine precision) of this assumption. An energy balance applied to each segment k implies that:

$$q_{loss-vl,k} = \left(UA_{vl}^{'}\right)_k \Delta z_k \left(T_{sat-vl,k} - T_{amb}\right) = \dot{m}\, \Delta x_{vl,k} i_{fg}\Big|_{T_{sat-vl,k}} \tag{5.19}$$

In this equation, $\left(UA_{vl}^{'}\right)_k$ is a thermal conductance per unit length for segment k; Δz_k is the pipe length for segment k; $T_{sat-vl,k}$ is the average saturation temperature for segment k; and $\Delta x_{vl,k}$ is the change in the quality over the segment k.

$(UA_{vl}^{'})_k$ can be calculated using equations akin to Eqs. (5.10) and (5.11). However, the internal heat transfer coefficient $(h_{vl-in})_k$ for the condensing vapor inside segment k of the vapor-transport line is needed in such equations. As the vapor-transport line is well insulated, the vapor condenses only partially and a two-phase (vapor-liquid) fluid enters the condenser. In addition, the mass flow rates and the corresponding mass fluxes in the LHP considered here are relatively low ($\dot{m}_{\max} < 1.97\times10^{-4}$ kg/s; and $G_{\max} < 4.18$ kg/m^2-s). As was noted by Chato (1962) and Rohsenow (1985), at low condensation rates and low vapor velocities (inlet Reynolds number of the vapor below 35,000), the liquid condensate inside the horizontal pipe runs off in a stratified condition, and the flow is gravity dominated. In this case, the condensate formed in the upper portion of the tube flows down its inside surface to the bottom region, and the liquid accumulated in this bottom region flows off in manner akin to open-channel flow. In this study, the two-phase flow over the entire length of the vapor-transport line and also in the condenser may be assumed stratified. This assumption was justified with reference to available flow pattern maps, as discussed in the next few paragraphs.

Depending on the flow rates, fluid properties, and pipe diameter, the flow patterns in co-current vapor-liquid two-phase flows in horizontal and slightly inclined pipes could be stratified smooth, stratified wavy, intermittent (plug/slug flow), annular flow, or dispersed bubbly [Dobson and Chato (1998)]; and the vapor and liquid flows could be laminar or

turbulent. These flow regimes and related issues for two-phase flows in horizontal and slightly inclined tubes are discussed in detail in the works of Lockhart and Martinelli (1949), Baker (1954), Thom (1964), Chisholm (1967), Collier (1972), Mandhane et al. (1974), Taitel and Dukler (1976), Soliman (1982, 1986), Rohsenow (1985), Griffith (1985), Carey (1992), Nitheanandan and Soliman (1994), Dobson and Chato (1998), and Thome (2003). Dobson and Chato (1998) compared the predictions of several flow-regime maps with their own experimental observations: They state that the flow regime map of Taitel and Dukler (1976) is one of the most theoretically based and it provided satisfactory predictions for all of their experiments that involved stratified smooth and stratified wavy flow regimes (the regimes which were encountered at mass fluxes below 75 kg/m^2-s). In the LHP experiments undertaken in this work, the mass fluxes were all below 4.18 kg/m^2-s. Furthermore, as noted by Dobson and Chato (1998), the flow regime map of Taitel and Dukler (1976) was developed for adiabatic flows, but it has been used with success by other investigators for diabatic flows [Barnhart (1992); Wattelet et al. (1994)]. Thus, the flow regime map of Taitel and Dukler (1976) was deemed suitable for the present study. The related conclusions were also confirmed using the recommendations of Soliman (1982).

Figure 5.8 illustrates plots for the full condensation of the vapor ($0 < x < 1.0$) in the vapor-transport line and the two-phase portion of the condenser pipe on the flow regime map of Taitel and Dukler (1976), for the upper extreme conditions in the LHP experiments: Note that $\dot{m}_{\max} = (q_{app})_{\max} / i_{fg}|_{T_{sat}=118.35\,^{o}C}$; and $G_{\max} = \dot{m}_{\max} / (\pi D_{vl}^2 / 4)$. The abscissa, X, is a parameter introduced by Lockhart and Martinelli (1949). This Lockhart-Martinelli parameter, often referred to as just the Martinelli parameter [Griffith (1985)], is defined as follows:

$$X^2 = \frac{C_l}{C_g}\frac{\left(Re_g\right)^m}{\left(Re_l\right)^n}\frac{\rho_g\left(\dot{m}_l\right)^2}{\rho_l\left(\dot{m}_g\right)^2} = \frac{\left|\left(dP/dz\right)_l^s\right|}{\left|\left(dP/dz\right)_g^s\right|}$$

$$\dot{m}_l = (1-x)\dot{m} \;;\; \dot{m}_g = x\dot{m} \;;\; G_l = \dot{m}_l/(\pi D_{vl}^2/4) \;;\; G_g = \dot{m}_g/(\pi D_{vl}^2/4) \qquad (5.20)$$

$$Re_l = G_l D_{vl}/\mu_l \;;\; Re_g = G_g D_{vl}/\mu_g$$

In this equation, C_l, C_g, m, and n are constants; u is the fluid velocity; ρ is the mass density; μ is the dynamic viscosity; D_{vl} is the internal diameter of the pipe (identical for

the vapor-transport line and the condenser in this study); dP/dz is the axial gradient of the static pressure; and the subscripts l and g denote, respectively, variables applicable to the liquid and the vapor phases. The values of the constants C_l, C_g, m, and n depend on the four possible particular combinations of laminar and turbulent flows of the liquid and vapor phases: The recommendations of Taitel and Dukler (1976) are given in Tables 5.1 and 5.2.

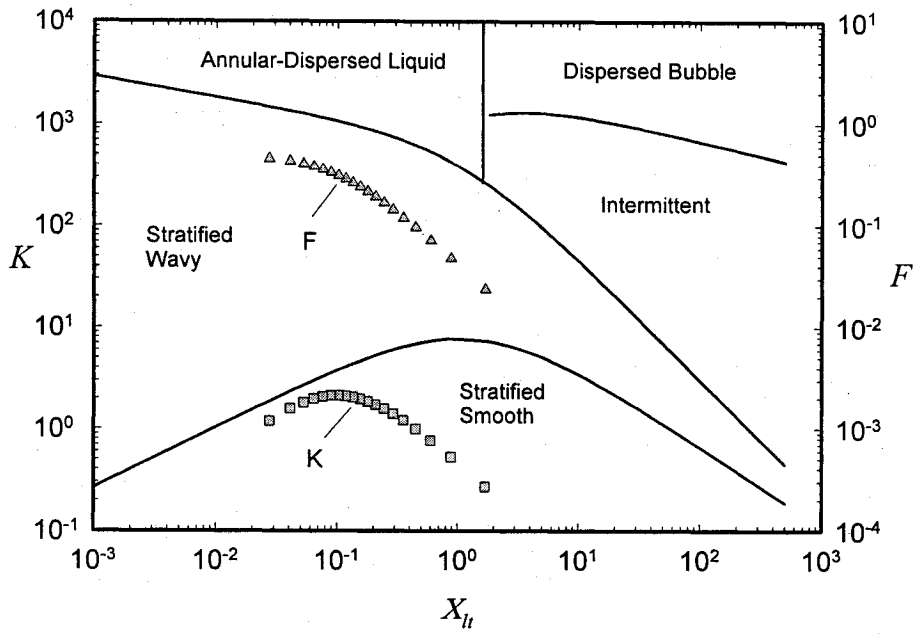

Figure 5.8: Establishment of flow regimes using the map of Taitel and Dukler (1976): The triangle and square symbols correspond to $0 < x < 1.0$ and the upper extreme conditions in the LHP experiments: $\dot{m}_{max} = 1.97 \times 10^{-4}$ kg/s, $G_{max} = 4.18$ kg/m^2-s, $D_{vl} = 7.75$ mm, $T_{sat} = 118.35$ °C, $T_{sink} = 61.80$ °C, $T_{amb} = 25.27$ °C, and $(q_{app})_{max} = 434.57$ W.

Table 5.1: Laminar and turbulent combinations of the liquid and vapor flows [Taitel and Dukler (1976)].

Liquid Flow	Vapor Flow	Symbol	$Re_l = u_l^s D_{vl} \rho_l / \mu_l$	$Re_g = u_g^s D_{vl} \rho_g / \mu_g$
Turbulent	Turbulent	$t-t$	> 2000	> 2000
Laminar	Turbulent	$l-t$	< 1000	> 2000
Turbulent	Laminar	$t-l$	> 2000	< 1000
Laminar	Laminar	$l-l$	< 1000	< 1000

Table 5.2: Constants in the Lockhart-Martinelli parameter [Taitel and Dukler (1976)].

Constants	$t-t$	$L-t$	$t-l$	$l-l$
N	0.2	1.0	0.2	1.0
M	0.2	0.2	1.0	1.0
C_l	0.046	16.0	0.046	16.0
C_g	0.046	0.046	16.0	16.0

The right-hand ordinate in Figure 5.8 is a dimensionless parameter, F, which is a modified Froude number (ratio of inertial to gravity forces in the vapor, modified by a density ratio):

$$F = \sqrt{\frac{\rho_g}{\rho_l - \rho_g}} \frac{u_g^s}{\sqrt{D_{vl} g \cos\theta}} \tag{5.21}$$

Here, g is the gravitational acceleration, and θ is the angle between the pipe axis and the horizontal. The left-hand ordinate in Figure 5.8 is a dimensionless parameter, K, which is the product of the modified Froude number, F, and the square root of the superficial liquid Reynolds number:

$$K = F\sqrt{\left(u_l^s D_{vl} \rho_l / \mu_l\right)} = \left[\frac{\rho_l \rho_g u_l^s \left(u_g^s\right)^2}{\left(\rho_l - \rho_g\right) g \mu_l \cos\theta}\right]^{1/2} \tag{5.22}$$

The following deductions apply for the upper extreme conditions in the LHP experiments (see the title of Figure 5.8): The vapor flow is laminar, except at high values of quality (close to one) when it can become turbulent; the liquid flow is always laminar. Therefore, adopting a conservative approach to the determination of the flow regimes, it was decided to use the laminar-liquid/turbulent-vapor combination for choosing the values of the constants in the Lockhart-Martinelli parameter X, as is indicated by the subscript lt given to this parameter in Figure 5.8.

For the abovementioned upper extreme conditions (highest mass flux and saturated vapor temperature investigated in this work), and for values of quality in the range 0.05 to 0.95, the dimensionless parameters F, K and X_{lt} are plotted in Figure 5.8: The left-hand ordinate is K; the right-hand ordinate is F; and X_{lt} is the abscissa. The F-X_{lt} curve (triangle symbols) in this figure shows that the two-phase flows encountered this

investigation are in the stratified regime. The type of stratified flow is indicated by the K-X_{lt} curve (square symbols) in Figure 5.8: The flow is stratified-smooth throughout. Therefore, for the full range of conditions considered in the LHP experiments, the two-phase flows in the vapor-transport line and in the condenser are in the stratified smooth regime.

In the work of Soliman (1982), a Froude number (Fr_{so}) is defined as follows:

$$Fr_{so} = 0.025 Re_l^{1.59} \left(\frac{1+1.09 X_{tt}^{0.039}}{X_{tt}} \right)^{1.5} \frac{1}{Ga^{0.5}} \quad Re_l \leq 1250$$
$$Fr_{so} = 1.26 Re_l^{1.04} \left(\frac{1+1.09 X_{tt}^{0.039}}{X_{tt}} \right)^{1.5} \frac{1}{Ga^{0.5}} \quad Re_l > 1250 \tag{5.23}$$

The Galileo number, Ga, and the liquid Reynolds number, Re_l, are defined as follows:

$$Ga = \frac{g\rho_l (\rho_l - \rho_g) D_{vl}^3}{\mu_l^2} \; ; \; Re_l = \frac{(1-x) G D_{vl}}{\mu_l} \; ; \; G = \frac{\dot{m}}{\pi D_{vl}^2 / 4} \tag{5.24}$$

Values of the Froude number of Soliman (1982) corresponding to the above-mentioned upper extreme conditions in the LHP experiments (see title of Figure 5.8) and $0.05 \leq x \leq 0.95$ are plotted in Figure 5.9: All of these values of Froude number are much less than 7, indicating that the flow is in the wavy regime of Soliman (1982). As noted by Dobson and Chato (1998), the wavy regime of Soliman (1982) includes flows commonly referred to as stratified, slug, and wavy.

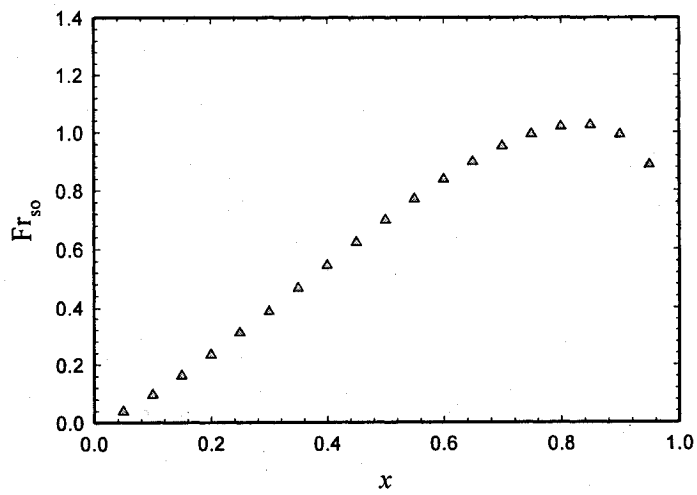

Figure 5.9: Variation of the Froude number of Soliman (1982) with quality for the upper extreme conditions in the LHP experiments.

With the above-mentioned deduction that the two-phase flows in the vapor-transport line and in the condenser are in the stratified regime for all conditions tested in the LHP experiments, an appropriate correlation can be used for the estimation of the heat transfer coefficient, $(h_{vl-in})_k$, that is required in determination of $\left(UA'_{vl}\right)_k$ [see Eq. (5.19), (5.10), and (5.11)]. Again, it is assumed that the influence of the U-bends on the rate of heat loss is negligible. Chato (1962) has presented the following correlation for the Nusselt number, *Nu*, in stratified flow condensation in horizontal pipes:

$$Nu = \frac{h_{vl-in} D_{vl}}{k_l} = 0.728\,\Im \left[\frac{g\rho_l \left(\rho_l - \rho_g\right) i'_{fg} D_{vl}^3}{k_l \mu_l \left(T_{sat-vl} - T_{wall}\right)} \right]^{\frac{1}{4}} \tag{5.25}$$

where $\Im = 0.76$ and, following the recommendations of Dobson and Chato,

$$i'_{fg} = i_{fg}(1 + 0.68 Ja_l)\ ;\ Ja_l = c_{p,l}(T_{sat} - T_{wall}) / i_{fg} \tag{5.26}$$

In Eqs. (5.25) and (52.6), k_l represents the thermal conductivity of the liquid phase; $c_{p,l}$ is the specific heat at constant pressure for the liquid phase; T_{wall} is the temperature of the inside surface of the pipe wall; D_{vl} is internal diameter of the vapor-transport line; $T_{sat\text{-}vl}$ is the saturation temperature inside the vapor-transport line; and Ja_l is the liquid Jakob number. To account for the variation of the depth of the liquid pool in the bottom region of the tube, Jaster and Kosky (1976) suggested replacing $\Im = 0.76$ in the correlation of Chato (1962), Eq. (5.23), with a function of the vapor void fraction: $\Im = \alpha^{3/4}$, with the vapor void fraction, α, determined using a correlation proposed by Zivi (1964):

$$\frac{1}{\alpha} = 1 + \frac{1-x}{x}\left(\frac{\rho_g}{\rho_l}\right)^{2/3} \tag{5.27}$$

where x is the local quality. Combining careful analyses of experimental data and physical guidance obtained from analytical solutions, Dobson and Chato (1998) amalgamated the rates of heat transfer by film condensation along the upper part of the inner wall and forced convection in the liquid pool at the bottom of the horizontal tube, and proposed the following correlation for the Nusselt number:

$$Nu = \frac{h_{vl} D_{vl}}{k_l} = \frac{0.23 Re_{vo}^{0.12}}{1 + 1.11 X_{tt}^{0.58}} \left[\frac{GaPr_l}{Ja_l}\right]^{0.25} + (1 - \theta_l / \pi) Nu_{forced} \tag{5.28}$$

In this equation, θ_l is the angle subtended at the center of the tube cross-section by the portion of the inner wall that is above the liquid level; Ga is the Galileo number and Ja_l is the liquid Jakob number, defined in Eqs. (5.24) and (5.26), respectively; $Re_{vo} = GD_{vl} / \mu_g$ is the vapor-only Reynolds number; $Pr = \mu_l c_{p,l} / k_l$ is the liquid Prandtl number; and

$$Nu_{forced} = 0.0195 Re_l^{0.8} Pr_l^{0.4} \varphi_l$$
$$\varphi_l = \sqrt{1.376 + \frac{c_1}{X_{tt}^{c_2}}} \tag{5.29}$$

Re_l is the superficial liquid Reynolds number as given in Eq. (5.24). The turbulent-turbulent Lockhart-Martinelli parameter, X_{tt}, and the parameters c_1 and c_2, both functions of the liquid Froude number, $Fr_l = G^2 / (\rho_l^2 g D_{vl})$, are given by the following equations:

$$X_{tt} = \left(\frac{\rho_g}{\rho_l}\right)^{0.5} \left(\frac{\mu_l}{\mu_g}\right)^{0.1} \left(\frac{1-x}{x}\right)^{0.9} \tag{5.30}$$

For $0 < Fr_l \leq 0.7$
$c_1 = 4.172 + 5.48 Fr_l - 1.56 Fr_l^2$; $c_2 = 1.773 - 0.169 Fr_l$
and for $Fr_l > 0.7$
$c_1 = 7.242$; $c_2 = 1.655$ (5.31)

Dobson and Chato (1998) have proposed the following approximate equation for calculating the angle, θ_l, based on the earlier work of Jaster and Kosky (1976):

$$(1 - \theta_l / \pi) \cong \frac{\arccos(2\alpha - 1)}{\pi} \tag{5.32}$$

In this equation, α is the vapor void fraction, determined using the correlation proposed by Zivi (1964), given in Eq. (5.27). The Nu values yielded by the correlations of Chato (1962), Jaster and Kosky (1976), and Dobson and Chato (1998), for the upper extreme conditions in the LHP experiments (see title of Figure 5.8) and $0.05 \leq x \leq 0.95$, are plotted in Figure 5.10.

As noted by Dobson and Chato (1998), the Nu values predicted by correlation of Jaster and Kosky (1976) for all vapor qualities greater than 0.2 exceed those obtained

using the correlation of Chato (1962) and also their own experimental data. The correlation of Chato (1962) matches the experimental data of Dobson and Chato quite well (mean deviation of 12.8%), but it does not show any dependence on the quality, x. This difficulty does not afflict Eq. (5.28), the correlation proposed by Dobson and Chato (1998), and it also matches their experimental data very well (mean deviation of 6.6%). Therefore, the correlation of Dobson and Chato (1998) was used in this work to compute the value of the internal heat transfer coefficient $(h_{wl-in})_k$ inside each segment k of the vapor-transport line and also the two-phase portion of the condenser pipe; and was discussed earlier, this heat transfer coefficient is needed for the calculation of the thermal conductance per unit length for segment k, $(UA'_{wl})_k$, as indicated in Eqs. (5.10), (5.11), and (5.19).

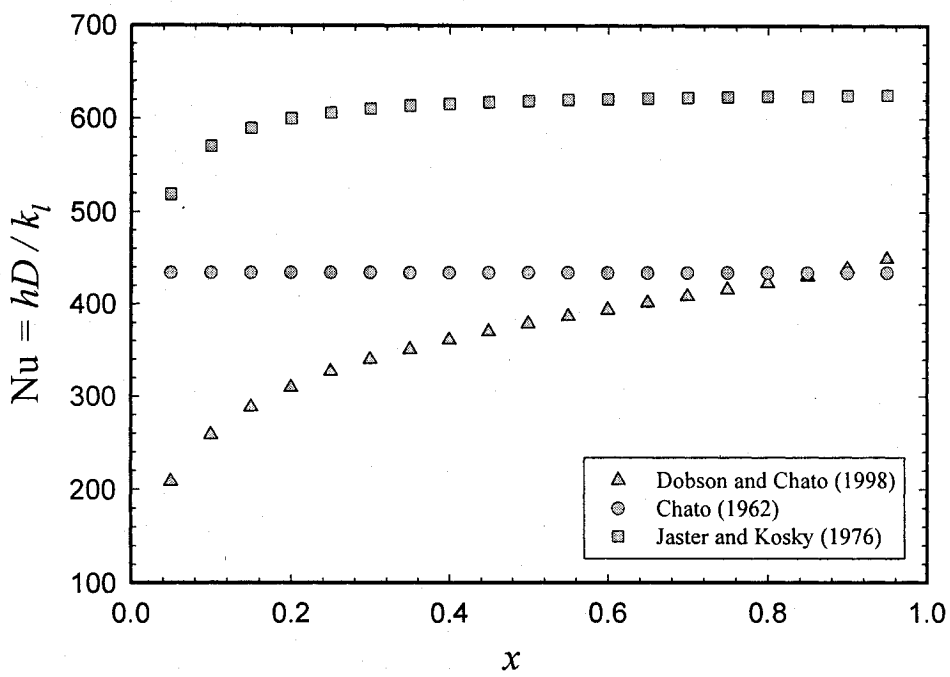

Figure 5.10: Variation of the Nusselt number with quality for the upper extreme conditions in the LHP experiments: Predictions obtained with the correlations of Chato (1962), Jaster and Kosky (1976), and Dobson and Chato (1998).

Eqs. (5.24) and (5.28) show that correlation of Dobson and Chato (1998) contains the temperature of the inner surface of the tube wall, T_{wall}, which is not known *a priori*.

However, using the resistance analogy, the following relation can be used to relate T_{wall} to T_{sat-vl} and the temperature of the ambient environment, T_{amb}, which is known:

$$\frac{T_{sat-vl} - T_{wall}}{R_{th-vl-in}} = \frac{T_{sat-vl} - T_{amb}}{R_{th-vl-in} + R_{th-vl-out}} \tag{5.33}$$

The total rate of heat loss from the vapor-transport line is obtained by adding together the rates of heat loss from all of the segments, k, each given by Eq. (5.19):

$$\begin{aligned} q_{loss-vl} &= \sum_{k=1}^{M} q_{loss-vl,k} = \sum_{k=1}^{M} (UA'_{vl})_k \Delta z_k \left(T_{sat-vl,k} - T_{amb}\right) \\ &= \dot{m} \sum_{k=1}^{M} \Delta x_{vl,k} i_{fg}\Big|_{T_{sat-vl,k}} \end{aligned} \tag{5.34}$$

The saturation temperature in the segment k+1, $T_{sat-vl,k+1}$, is obtained from that in the previous segment, $T_{sat-vl,k}$, using the slope of the liquid-vapor saturation line (P-T diagram) and the pressure drop ΔP_{vl-k}:

$$T_{sat-vl,k+1} = T_{sat-vl,k} - \Delta P_{vl-k} \Big/ \left(\frac{dP}{dT}\right)_{sat\,@T_{sat-vl,k}} \tag{5.35}$$

For the first segment in the vapor-transport line, k = 1, the saturation temperature is T_{sat}, the saturation temperature at the exit of the evaporator.

The procedure for determining the pressure drops ΔP_{vl-k} for two-phase flow is described in the next subsection.

Pressure Drop

For a fixed mass flow rate, the pressure drop in the two-phase flow is needed to overcome the wall friction (shear) and gravity forces, and sustain the momentum changes during the condensation process [Griffith (1985); Ould Didi et al. (2002); Thome (2003)]. In addition, if fittings and/or bends are used, additional pressure drops are needed to overcome the associated losses: In this work, if applicable, such additional pressure drops are included by suitably augmenting the friction pressure drop. Thus, the two-phase pressure drop is expressed as follows:

$$\Delta P_{2\varphi} = (\Delta P)^{2\varphi}_{fric} + (\Delta P)_{mom} + (\Delta P)_{grav} \tag{5.36}$$

where the terms $(\Delta P)_{fric}^{2\varphi}$, $(\Delta P)_{mom}$, and $(\Delta P)_{grav}$ denote, respectively, the pressure drops caused by the wall friction force (and also bends and fittings), the momentum changes during the condensation process, and the gravity force: These pressure drops are referred to in this thesis as the friction pressure drop, the momentum pressure drop, and the gravity pressure drop, respectively.

A) Friction Pressure Drop

The two-phase friction pressure drop $(\Delta P)_{fric}^{2\varphi}$ is different for the different flow regimes that may be encountered. Using the classification of Taitel and Dulker(1976), two-phase (liquid-vapor) flows in ducts could be in the stratified smooth, stratified wavy; annular, intermittent (plug and slug), or dispersed bubble regimes. Furthermore, the vapor and liquid flows could be either laminar or turbulent. For such flows in vertical and inclined ducts, the direction of flow (assisting or opposing with respect to the gravitational acceleration vector) could influence the friction pressure drop. The type of fluid (refrigerants, water-steam, water-air, refrigerant blends), size of the duct, and the shape of the duct also have to be taken into account. For elaborations of these issues and overviews of related calculation procedures, the reader is referred to the works of Lockhart and Martinelli (1949), Wallis (1969), Agarwal et al. (1973), Mandhane et al. (1974, 1977), Taitel and Dukler (1974), Friedel (1979), Grönnerud (1979), Soliman (1982), Griffith (1985), Müller-Steinhagen and Heck (1986), Carey (1992), Barnhart (1992), Wattelet et al. (1994), Awwad et al. (1995), Whalley (1996), Tribbe (1998), Dobson and Chato (1998), Tribbe and Müller-Steinhagen (2000), Ould Didi et al. (2002), Thome (2003), Cavallini et al. (2003), Coleman and Garimella (2003), Bassi and Bansal (2003), Wilson et al. (2003), Wang et al. (2003), Wang et al. (2003a, 2003b), and Chen et al. (2004a, 2004b, 2005), and also to ASHRAE Fundamentals (2005).

As was discussed earlier in this chapter, in the LHP experiments undertaken in this work, the two-phase (water-steam) flows are all in the stratified (smooth or wavy) regime; the liquid flows are all laminar; and the vapor flows may be laminar or turbulent. The vapor-transport line and the condenser tube are both stainless-steel pipes of circular cross-section (both of internal diameter 7.75 mm), and these pipes are horizontal or only

slightly inclined. The geometry of the vapor-transport line is shown schematically in Figure 5.7, and full details are given in Chapter 4. The upper extreme conditions that apply to the two-phase (water-steam) flows in the LHP experiments in this work are given in the title of Figure 5.8.

Many of the available approaches to the calculation of the friction pressure drop for stratified (smooth and wavy) two-phase flows in *straight* horizontal pipes have been reviewed and assessed by Tribbe (1998), Tribbe and Müller-Steinhagen (2000), and Ould Didi et al. (2002), and some of the most used of these approaches have also been reviewed in ASHRAE Fundamentals (2005): Tribbe and Müller-Steinhagen (2000) recommend use of the method of Agarwal et al. (1973) for stratified smooth flows and the method of Hart et al. (1989) for flows in the stratified wavy regime; and for stratified wavy flows, Ould Didi et al. (2002) rate the methods of Grönnerud (1979) and Müller-Steinhagen and Heck (1986) as the best, and state that the method of Lockhart and Martinelli (1949) gave results which are considered reasonable for two-phase flows (standard, mean, and average deviations of 67.41%, 46.31%, and 17.72%, respectively, for pressure drops greater than 0.5kPa). It should be noted that these assessments are based on comparisons with experiments data sets in which the mass fluxes are mostly considerably larger than the maximum of 4.18 kg/m^2-s applicable to the LHP experiments in this work. Furthermore, in the method of Lockhart and Martinelli (1949), the two-phase friction drop in *straight* horizontal pipes is obtained by multiplying the single-phase (liquid or vapor) friction pressure drop by a corresponding two-phase multiplier (details are given later in this section); and adaptations of this approach are used in some of the latest available methods for the calculation of friction pressure drops in horizontal pipes with *U-bends* [Wang et al. (2003); Chen et al. (2004a, 2004b, 2005)] and in horizontal *helicoidal* pipes [Awwad et al. (1995)]. Lastly, the original correlation proposed by Lockhart and Martinelli (1949) applies to isothermal two-phase two-components flow in straight pipes; but Griffith (1985) states that this correlation applies quite well for low-pressure (close to one atmosphere) two-phase flows in non-adiabatic pipes; and the absolute pressures in the LHP experiments in this work are in the range 0.451 bars to 1.894 bars. Based on these observations, the method of Lockhart and Martinelli (1949) was chosen for the calculation of two-phase friction pressure drops in

the *straight* portions of the vapor-transport line and the condenser pipe; and a modified version of the methods of Awwad et al. (1995) and Chen et al. (2004a, 2004b, 2005) is used for the calculation of this pressure drop in the bent portions of these pipes. The details are given in the remainder of this subsection.

The two-phase friction pressure drops in the straight and the bent portions of the vapor-transport line are determined separately. The friction pressure drop in the vapor grooves, the vapor collector, and the vapor passage at the exit of the evaporator is determined in a special way. Then, these pressure drops are combined to obtain the overall two-phase friction pressure drop for the vapor-transport line, *using a segmented approach* similar to that used to calculate the heat loss from this line (see Eq. (5.34) and related discussions in the previous subsection).

A-1) Straight Portions

For each segment in straight portions of the vapor-transport line, first, the Lockhart-Martinelli parameter, given in Eq. (5.20), is calculated using the combinations of liquid/gas flow regimes and the corresponding constants given in Tables 5.1 and 5.2. Then, a two-phase multiplier (based on liquid phase) is calculated using the following equation [Chisholm (1967)]:

$$\varphi_l^2 = 1 + \frac{C}{X} + \frac{1}{X^2} \tag{5.37}$$

The value of the coefficient C in this equation depends on the combinations of liquid/gas flow regimes [Collier (1972)], as given in Table 5.3.

Table 5.3 Values of the coefficient, C, in the two-phase multiplier.

Liquid-phase	Gas-phase	Subscript	C
turbulent	*turbulent*	*(tt)*	20
laminar	*turbulent*	*(lt)*	12
turbulent	*laminar*	*(tl)*	10
laminar	*laminar*	*(ll)*	5

Once φ_l^2 is obtained, the two-phase friction pressure drop for each segment in straight portions of the vapor-transport line is calculated using the following equation:

$$(\Delta P)_{f,st}^{2\varphi} = \varphi_l^2 (\Delta P)_{l,st}^{1\varphi} \tag{5.38}$$

where $(\Delta P)_{l,st}^{1\varphi}$ is the single-phase friction pressure drop with the liquid phase flowing alone in the pipe at *its* mass velocity and is defined as

$$(\Delta P)_{l,st}^{1\varphi} = -(dP/dz)_{l,st}^{s} L_{st} = f_{st} \frac{\rho_l (u_l^s)^2}{2} \frac{L_{st}}{D_{vl}} \tag{5.39}$$

where L_{st} is the length of the segment in the straight portion. For laminar fully-developed liquid flow, $f_{st} = 64/Re_l$, and Eq. (5.39) can be rewritten as follows:

$$(\Delta P)_{l,st}^{1\varphi} = \frac{32\mu_l u_l^s}{D_{vl}^2} L_{st} = \frac{32\mu_l (1-x) G}{D_{vl}^2 \rho_l} L_{st} \tag{5.40}$$

In this equation, x is the average vapor quality in the particular segment of the straight portion, and G is the mass flux ($G = \dot{m}/A_{cs}$).

A-2) Bent Portions

The first step for each segment in bent portions of the vapor-transport line is again the calculation of the Lockhart-Martinelli parameter, but now defined using the single-phase pressure gradients for the bent portions [Chen et al. (2005)]:

$$X_b^2 = \frac{|(dP/dz)_{l,b}^{s}|}{|(dP/dz)_{g,b}^{s}|} \tag{5.41}$$

In this equation, the single-phase pressure gradients for the liquid and gas phases flowing alone in the bent portion, at *their respective* mass velocities, are calculated as follows:

$$-(dP/dz)_{l,b}^{s} = f_{b,l} \frac{\rho_l (u_l^s)^2}{2D_{vl}}; \quad -(dP/dz)_{g,b}^{s} = f_{b,g} \frac{\rho_g (u_g^s)^2}{2D_{vl}} \tag{5.42}$$

Here, f_b denotes the friction factor for single-phase flow in the bent portion. This friction factor is a function of the *Re* number and a geometric parameter that characterizes the bend. It can be calculated using available correlations, if applicable, or determined experimentally for the particular bent-pipe geometry. The latter approach was adopted in this work. As was described in an earlier subsection, an experimental set-up was built and used to determine the single-phase pressure drop for entire the serpentine part of the

vapor-transport line (the section located between points 3 and 4 in Figure 5.7), ΔP_1, with pure nitrogen (99.9%) as the working fluid for a suitable range of flow rates. Then, a correlation for $C_{f-1} = \Delta P_1 / \rho \bar{V}^2$ as a function of the Reynolds number, *Re*, was obtained: It is presented in Eq. (5.16). Referring to Figure 5.7, the single-phase pressure drops in all *straight* portions of the pipe located between the points 3 and 4 are estimated using available analytical solutions or empirical correlations for the corresponding friction factor: For laminar flow, this single-phase friction is only a function of the Reynolds number; for turbulent flow, it is also a function of the relative roughness of the inside surface of the pipe. Using ΔP_1 and subtracting from it the single-phase pressure drops through the straight portions, the single-phase pressure drop contribution of the bent portions is obtained. This single-phase pressure-drop contribution of the bent portions is then divided by their total length, to obtain the *average single-phase* pressure drop per unit length of the bent portions, $-(dP/dz)_b^s$:

$$-(dP/dz)_b^s = \frac{\Delta P_1 - \Delta P_{st,3-4}}{L_{b,tot,3-4}} \tag{5.43}$$

where $\Delta P_{st,3-4}$ is the sum of pressure drops in all straight portions located between the points 3 and 4, and $L_{b,tot,3-4}$ is the total length of the bent portions located between the points 3 and 4.

Once the value of $(dP/dz)_b^s$ is calculated using Eq. (5.43), the single-phase friction factor in the bent portions is obtained as follows:

$$f_b = \frac{-(dP/dz)_b^s D_{vl}}{\rho \bar{V}^2 / 2} \tag{5.44}$$

This procedure is used to calculate the single-phase frictions factors in the bent portions for the both the liquid-phase and vapor-phase, $f_{b,l}$ and $f_{b,g}$, respectively, and then X_b is calculated using Eqs. (5.41) and (5.42): In each segment, *k*, lying in the bent portions of the vapor-transport line, this calculation requires as inputs the corresponding values of $(Re_l)_k$, $(\rho_l (u_l^s)^2)_k$, $(Re_g)_k$, and $(\rho_g (u_g^s)^2)_k$.

Once the Lockhart-Martinelli parameter, X_b, for the segment, k, lying in bent portions of the vapor-transport line is calculated, a two-phase multiplier for this segment, based on the liquid-phase, $\varphi_{b,l}$, is determined. This two-phase multiplier is then used to calculate the corresponding value of $(\Delta P)_{f,b}^{2\varphi}$ in the segment of interest. These procedures are based on ideas put forward by Awwad et al. (1995) and Chen et al. (2004): The details are given in the remainder of this subsection.

Awwad et al. (1995) studied air-water two-phase flow in horizontal *helicoidal* pipes and proposed a corrected Lockhart-Martinelli two-phase multiplier, by introducing a function of a modified liquid Froude number, $Fr_{l,aw}$, and the corresponding Lockhart-Martinelli parameter, X_{helic}:

$$\varphi_{helic,l} = \left[1 + \frac{X_{helic}}{C_{l,aw}\left(Fr_{l,aw}\right)^n}\right]\left(1 + \frac{12}{X_{helic}} + \frac{1}{X_{helic}^2}\right)^{1/2}$$
$$Fr_{l,aw} \le 0.3, \quad C_{aw} = 7.79; \quad n = 0.576$$
$$Fr_{l,aw} > 0.3, \quad C_{aw} = 13.56; \quad n = 1.3 \qquad (5.45)$$
$$Fr_{l,aw} = \frac{\left(u_l^s\right)^2}{gd}\left(\frac{d}{D_{coil}}\right)^{0.1}$$

In this equation, d is the inside diameter of the pipe and D_{coil} is the coil diameter.

Chen et al. (2004a) have proposed an empirical correlation for a corrected Lockhart-Martinelli two-phase multiplier for U-bends. Their correlations is based on experimental data for air-water two-phase mixture flows, at values of mass flux (G) between 100 to 700 kg/m^2-s, in serpentine (U-type wavy) tubes of diameter (D) between 3.43 to 8.29 mm, curvature ratio of R/D = 1.85 to 3.94, and the spacer length ratio (L_c/D) between 1.93 to 30.5 (where R is the radius of the centerline of the U bends; and L_c is the length of the straight pipe that connecting any two consecutive U-bends, akin to $L_{c\text{-}vline}$ in Figure 5.7). The correlation of Chen et al. (2004a) is given below:

$$\varphi_{b,l} = \left[0.9116 X_b^{-0.0546} Fr_{l,Chen}^{0.0785}\right]^{1/2}\left(1 + \frac{10}{X_b} + \frac{1}{X_b^2}\right)^{1/2} \qquad (5.46)$$
$$Fr_{l,Chen} = \frac{\left(u_l^s\right)^2}{gD}$$

The geometry of the serpentine vapor-transport line used in the LHP experiments conducted in this work falls well in the range of geometrical parameters investigated by Chen et al. (2004a). However, the mass fluxes in these LHP experiments ($\dot{m}_{max}$ = 4.18 kg/m^2-s) are significantly lower than those in the experiments of Chen et al. (2004). The study of Awwad et al. (1995) applies to horizontal helicoidal pipe (rather than serpentine pipes with U-bends), and the mass fluxes they considered are also significantly higher than those in the LHP experiments undertaken here. Thus, the correlations of Awwad et al. (1995) and Chen et al. (2004a) were not used directly in this work. Rather, some of the key ideas in their correlations were adapted to propose and fine tune a new correlation for a two-phase multiplier that is applicable to the LHP investigated in this work.

The proposed two-phase multiplier for segments in the bent portions of the vapor-transport line and the condenser pipe is the following:

$$\varphi_{b,l} = \left[1+\frac{X_b}{A_1\left(Fr_{l,m}\right)^m}\right]\left[1+\left(\frac{D}{L_c}\right)^n\right]\left(1+\frac{12}{X_b}+\frac{1}{X_b^{\,2}}\right)^{1/2}$$

$$A_1 = 0.8; \quad m = 0.283; \quad n = 0.6 \tag{5.47}$$

$$Fr_{l,m} = \frac{\left(u_l^s\right)^2}{gD}\left(\frac{2R}{D}\right)$$

The first term in the square brackets on the right-hand side of Eq. (5.47) is inspired by a similar term in the correlation of Awwad et al (1995); this term goes to zero when the ratio R/D goes to infinity (the pipe is straight, and the modified liquid Froude number, $Fr_{l,m}$, goes to infinity). The second term in square brackets on the right-hand side of Eq. (5.47) is introduced to account for possible non-fully-developed conditions at the entrance to the U-bend when L_c is not long enough, in a manner akin to that used to incorporate entrance effects in heat transfer studies [Gnielinski (1983)]. The constant 12 used in the third term in square brackets on the right-hand side of Eq. (5.47) corresponds to the value of C in the Lockhart-Martinelli two-phase multiplier for laminar-turbulent conditions (see table 5.3). The values of the constants A_1, m, and n were fined-tuned with reference to the data collected in the LHP experiments: With this fine-tuning, the mean deviation of the predictions from the measured data in the vapor-transport line is ±4.11%.

For each segment, k, in the bent portions of the vapor-transport line, once $\varphi_{b,l}$ is estimated using Eq. (5.47), the two-phase friction pressure drop is estimated as follows:

$$(\Delta P)_{f,b}^{2\varphi} = \varphi_{b,l}^2 (\Delta P)_{l,b}^{1\varphi} = \varphi_{b,l}^2 (-dP/dz)_{b,l}^{s} L_b \tag{5.48}$$

In this equation, L_b is the length of the segment, k, in the bent portion along its centerline, and $(\Delta P)_{l,b}^{1\varphi}$ is the friction pressure drop for the liquid-phase flowing alone (single-phase flow) at *its* mass velocity in this segment. The procedure for estimating $(\Delta P)_{l,b}^{1\varphi}$ was presented earlier in this subsection; see Eq. (5.42) and the two paragraphs that follow it.

A-3) Vapor Grooves, Vapor Collector, and Evaporator Exit Passage

The two-phase friction pressure drop from the location of the liquid-vapor interface inside the wick to the entrance of the vapor-transport line (point 2 in Figure 5.7) is calculated using a procedure similar to that explained in the previous subsection for the bent portions. As was mentioned earlier [see the three paragraphs that follow Figure 5.7, and also Eqs. (5.16) and (5.17)], the pressure drop for single-phase flow through the evaporator grooves to the entrance of the serpentine section of the vapor-transport line was obtained experimentally; and a correlation for estimating this pressure drop is presented in Eq. (5.17). Neglecting the pressure drop for single-phase flow in the one smooth 90° bend existing in this section of the vapor-transport line (between point 2 and 3 in Figure 5.7), and subtracting out the corresponding pressure drops in the straight portions of this section, the pressure drop for single-phase flow inside the vapor grooves + vapor collector + evaporator exit pipe is estimated for both the vapor-phase and liquid-phase (flowing alone at their respective mass flow rates), to obtain $(\Delta P)_{l,ev}^{s}$ and $(\Delta P)_{g,ev}^{s}$. Using this approach, for each operating condition, the Lockhart-Martinelli parameter for this section of the LHP (vapor grooves, vapor collector and evaporator exit pipe) is calculated:

$$X_{eva-exit}^2 = \frac{|(\Delta P)_{l,ev}^{s}|}{|(\Delta P)_{g,ev}^{s}|} \tag{5.49}$$

Then, using Eq. (5.37), a two-phase multiplier (based on the liquid-phase), $\varphi_{l,ev}$, is obtained, and the two-phase pressure drop for this section of the LHP (vapor grooves, vapor collector, and the evaporator exit pipe), $(\Delta P)_{f,ev}^{2\varphi}$, is estimated as follows:

$$(\Delta P)_{f,ev}^{2\varphi} = \varphi_{l,ev}^2 (\Delta P)_{l,ev}^{s} \tag{5.50}$$

A-4) Overall Vapor-Transport Line

The overall friction pressure drop for two-phase flow in the vapor-transport line is calculated by summing up $(\Delta P)_{f,ev}^{2\varphi}$, and the pressure drops in all the segments, *k*, in the straight and bent portions of the vapor-transport line as follows:

$$(\Delta P)_{fric}^{2\varphi} = (\Delta P)_{f,ev}^{2\varphi} + \sum_{k=1}^{M} \left[\xi (\Delta P)_{f,st}^{2\varphi} + (1-\xi)(\Delta P)_{f,b}^{2\varphi} \right]_k \tag{5.51}$$

In this equation, for segments, *k*, located in straight portions of the vapor-transport line, $\xi = 1$; and for those located in the bent portions, $\xi = 0$.

B) Momentum Pressure Drop

For each segment, *k*, for a fixed total mass flow rate, $\dot{m}$, the pressure drop required to sustain the momentum changes due to condensation, $(\Delta P_{mom})_k$, is calculated as follows:

$$(\Delta P_{mom})_k = G^2 \left\{ \left[\frac{(1-x)^2}{\rho_l (1-\alpha)} + \frac{x^2}{\rho_g \alpha} \right]_{ex,k} - \left[\frac{(1-x)^2}{\rho_l (1-\alpha)} + \frac{x^2}{\rho_g \alpha} \right]_{en,k} \right\} \tag{5.52}$$

where the subscripts *ex,k* and *en,k* denote the conditions at the exit and entrance cross-sections of the segment, *k*, respectively; and α denotes the vapor void fraction. In this work, α is calculated using Eq. (5.27), which is a correlation proposed by Zivi (1964).

The total momentum pressure drop for the vapor-transport line is calculated by summing this pressure drop in each of the segments, *k*:

$$(\Delta P)_{mom} = \sum_{k=1}^{M} (\Delta P_{mom})_k \tag{5.53}$$

C) Gravity Pressure Drop

The gravity pressure drop for a segment, k, is calculated using the following equation:

$$\left(\Delta P_{grav}\right)_k = \left[\alpha\rho_g + (1-\alpha)\rho_l\right]_k g\Delta z_k \sin\theta \tag{5.54}$$

In this equation, θ is the inclination angle measured upwards from the horizontal, and α is the average vapor void fraction in the segment. Again, α is calculated using Eq. (5.25), a correlation proposed by Zivi (1964).

The total gravity pressure drop for the vapor-transport line is calculated by summing this pressure drop in each of the segments, k:

$$(\Delta P)_{grav} = \sum_{k=1}^{M}\left(\Delta P_{grav}\right)_k \tag{5.55}$$

Mass of Fluid inside the Vapor-Transport Line and Quality at its Exit Section

The total mass of the two-phase mixture (vapor + liquid) in the vapor-transport line is calculated using the following equation:

$$m_{vline} = \sum_{k=1}^{M}[\alpha\rho_g + (1-\alpha)\rho_l]_k(\pi D_{vl}^2/4)\Delta z_k \tag{5.56}$$

In this equation, α_k is the average vapor void fraction in the segment. Again, α_k is calculated using Eq. (5.25), a correlation proposed by Zivi (1964).

The quality of the two-phase mixture at the exit of the vapor-transport line, $x_{vl\text{-}ex}$, is same as that at the entrance to the condenser of the LHP, x_{cd-in}. This quality is calculated as follows:

$$x_{vl-ex} = x_{cd-in} = 1 - \sum_{k=1}^{M}\Delta x_k \tag{5.57}$$

5.2.3 Condenser

The condenser of the LHP is built from a serpentine pipe of circular cross-section (see Figure 5.1). However, as was noted earlier in this chapter, it was not necessary to incorporate special procedures for estimating either the augmented pressure drops or heat transfer in the bent portions, as preliminary calculations and experiments showed that most of the vapor condensed in the initial straight portion of this pipe. Furthermore, the

mass flow rate (and Reynolds number) of the condensed liquid flowing in the condenser pipe is very small; thus the effects of the U-bends on the pressure drops and heat transfer in the subcooled region of the condenser are negligibly small.

As was mentioned in Chapter 4, in order to create a constant sink temperature boundary condition in the LHP experiments, the entire condenser pipe was submerged in an oil-bath with a controlled environment (temperature and stirrer speed).

The fluid could exit the condenser as a saturated-liquid, a subcooled liquid, or a two-phase mixture. Figure 5.11 shows a case where the fluid exits the condenser in a subcooled state, and the location where $x = 0$ (full condensation of the vapor) is within the condenser pipe ($L_{cd}^{2\varphi} < L_{cd}$). As presented at the bottom left of this figure, the vapor entering at temperature T_{cd-in} is condensed over the length $L_{cd}^{2\varphi}$, and its temperature drops slightly over this length, due to the drop in pressure. Over the rest of the condenser length, L_{sc}, the condensed liquid is cooled further and it exits in a subcooled state. If the condenser tube were long enough, the subcooled liquid temperature at the exit of the condenser for this case would asymptotically approach the sink temperature.

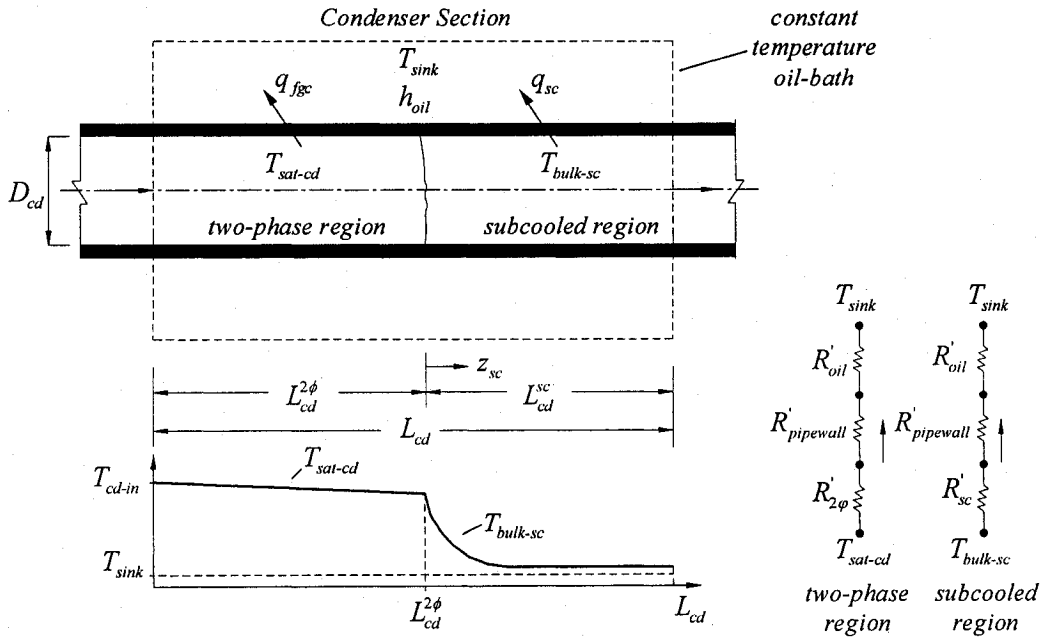

Figure 5.11: Schematic of the fluid flow through the condenser when $L_{cd}^{2\varphi} < L_{cd}$.

The heat transfer and pressure drop in the condenser are examined for two distinct flow regions: Two-phase region and subcooled region. These regions are schematically illustrated in Figure 5.11.

Two-Phase Region

As presented in Figure 5.11, the saturated vapor enters the condenser pipe at T_{cd-in} and fully condenses in the two-phase region of length $L_{cd}^{2\varphi}$. As was mentioned earlier, the thermodynamic process in this region involves a pressure drop, and associated slight lowering of the saturation temperature, and the fluid reaches the saturated liquid state at the start of the subcooled region. However, $L_{cd}^{2\varphi}$ is not known *a priori*, and the rate of heat loss and the pressure drop in the condenser depend on this length. The procedure presented in Rohsenow (1985) for sizing condensers is adapted here to evaluate $L_{cd}^{2\varphi}$.

The two-phase region is divided into N segments of equal quality change. The lengths of the corresponding pipe segments are not necessarily equal. Over the length of each such segment, Δz_i, the saturation temperature, $T_{sat-cd,i}$, is assumed constant (the value of N can be increased to achieve any desired accuracy of this procedure, to within machine precision). The two-phase pressure drop over each segment depends on whether it is in the straight or bent portions of the condenser pipe, and it is obtained using the same procedures as those used to obtain the two-phase pressure drops for the segments located in the vapor-transport line (discussed in the last subsection). After the pressure drop is calculated for each segment, i, the saturation temperature for the next segment, $i+1$, is updated as follows:

$$T_{sat-cd,i+1} = T_{sat-cd,i} - \Delta P_i \Big/ \left(\frac{dP}{dT}\right)_{sat.@T_{sat-cd,i}} \qquad i = 2,3...,N \tag{5.58}$$

The saturation temperature for the first section is $T_{sat-cd,1} = T_{cd-in}$. The saturation temperature at the exit of the two-phase region, $T_{2\varphi-exit}$, is obtained by solving Eq. (5.58) for $i = N$: $T_{2\varphi-exit} = T_{sat-cd,N+1}$.

The quality at the entrance of the condenser and the exit of the two-phase region are, respectively, $x_{cd\text{-}in}$, and zero. Thus, the change in quality over each of the N segments is given by

$$\Delta x = x_{cd-in} / N \tag{5.59}$$

The average quality for the first segment is $x_1 = x_{cd-in} - \Delta x/2$, and for other segments it is calculated from

$$x_i = x_{i-1} - \Delta x \qquad i = 2,3,...N \tag{5.60}$$

The energy balance on each segment, i, can be expressed as

$$(UA'_{2\varphi})_i \Delta z_i \left(T_{sat-cd,i} - T_{sink}\right) = A_{cd} G i_{fg}\big|_{T_{sat-cd,i}} \Delta x \tag{5.61}$$

where Δz_i is the length of the segment i; G is the mass flux ($G = \dot{m}/A_{cd}$); $i_{fg}\,|_{T_{sat-cd,i}}$ is the latent heat of evaporation in the segment i; and $(UA'_{2\varphi})_i$ is the total thermal conductance for heat loss from the segment i, defined as follows:

$$(UA'_{2\varphi})_i = \left(\frac{1}{R'_{2\varphi} + R'_{pipewall} + R'_{oil}} \right)_i \tag{5.62}$$

where, referring to Figure 5.11, $R'_{2\varphi}$, $R'_{pipewall}$, and R'_{oil}, respectively, are the thermal resistances (per unit length of the pipe) for the internal two-phase flow, radial heat conduction through the pipe wall, and the external convection over the condenser pipe immersed in the oil bath: These thermal resistances are defined as

$$\begin{aligned} R'_{2\varphi} &= \frac{1}{h_{2\varphi} \pi D_{cd}} \\ R'_{pipewall} &= \frac{\ln\left((D_{cd} + 2t)/D_{cd}\right)}{2\pi k_{pipe}} \\ R'_{oil} &= \frac{1}{h_{oil} \pi (D_{cd} + 2t)} \end{aligned} \tag{5.63}$$

where D_{cd} is the internal diameter of the condenser pipe; t is the thickness of this pipe; $h_{2\varphi}$ is the heat transfer coefficient for the two-phase flow inside the pipe; k_{pipe} is the thermal conductivity of the pipe wall material; and h_{oil} is the heat transfer coefficient on the external surface of the condenser pipe immersed in the oil bath.

R'_{oil} is a function of the oil properties, the sink temperature, T_{sink}, and the external flow conditions on the condenser pipe (velocity and flow direction). If these external flow conditions are known, the heat transfer coefficient h_{oil} in Eq. (5.65) can be estimated using an appropriate correlation for cross flow over cylinders of ciruclar cross-section, for example, the one proposed by Zhukauskas (1972). However, as was discussed in Chapter 4 (Section 4.1.2), in this work, h_{oil} was determined experimentally for different sink temperatures and stirrer angular velocities.

For each run in the LHP experiments, the thermal and hydrodynamic conditions in the oil bath were essentially constant: Thus, R'_{oil} and $R'_{pipewall}$ in Eq. (5.65) are assumed constant for all N sections. However, the first term in Eq. (5.65), $R'_{2\varphi}$, varies with the fluid properties and the vapor quality: Therefore, it is calculated separately for each segment i.

The heat transfer coefficient $h_{2\varphi}$ depends on the flow regimes that occur in the two-phase region inside the condenser. As was discussed in the last subsection for the vapor-transport line, the two-phase flows in all of the LHP experiments undertaken in this work were in the stratified (smooth or way) regime. Furthermore, it is again assumed that the influence of the U-bends on the rate of heat loss in the condenser is negligible. Therefore, as was done for two-phase flows in the vapor-transport line, the correlation of Dobson and Chato (1998) is used to predict $h_{2\varphi}$: See Eq. (5.28) and related discussions in the last subsection.

In the correlation of Dobson and Chato (1998), the temperature of the inside surface of the pipe convey the two-phase flow, T_{wall}, is required as an input to compute $h_{2\varphi}$. T_{wall} is not known *a priori*. Using the resistance analogy presented in Figure 5.11 for the two-phase region, the following relation can be used to relate T_{wall} to T_{sink}:

$$\frac{T_{sat,cd} - T_{wall}}{R'_{2\varphi}} = \frac{T_{sat,cd} - T_{sink}}{R'_{2\varphi} + R'_{pipewall} + R'_{oil}} \tag{5.64}$$

For each section i, and for given values of $T_{sat,cd,i}$, $\dot{m}$, and T_{sink}, the two unknown values, $h_{2\varphi,i}$ and $T_{wall,i}$ are determined iteratively. Then, using Eqs. (5.63) and (5.64), $(UA'_{2\varphi})_i$ and Δz_i are determined. It should be noted that all fluid properties in these calculations are obtained at the saturation temperature $T_{sat,cd,i}$.

At this stage, the total length of the two-phase region is calculated:

$$L_{cd}^{2\varphi} = \sum_{i=1}^{N} \Delta z_i \tag{5.65}$$

Once $L_c^{2\varphi}$ is determined, it is compared to the total length of the condenser pipe, L_{cd}. As was mentioned previously, three possible cases could exist:

a) $L_{cd}^{2\varphi} = L_{cd}$: The fluid exits the condenser as a saturated liquid state in this case, at the saturation temperature $T_{2\varphi-exit}$. The quality at the exit is $x_{vqual,cdexit} = 0$, and the total rate of heat rejection in the condenser is:

$$q_{cd-reject} = q_{fgc} = \sum_{i=1}^{N} (UA'_{2\varphi})_i \Delta z_i \left(T_{sat-cd,i} - T_{sink}\right) = \Delta x A_{cd} G \sum_{i=1}^{N} i_{fg,c}\Big|_{T_{sat-cd,i}} \tag{5.66}$$

b) $L_{cd}^{2\varphi} > L_{cd}$: This situation occurs when the capability for the rate of heat rejection in the condenser is not enough to condense the vapor completely, and a two-phase (vapor-liquid) flow exits the condenser at the saturation temperature $T_{sat-cd,j}$. Here, j (j<N) denotes the segment at the end of which, collectively, the total length of the segments $0 \le i \le j$ is equal to the total length of the condenser pipe. In this case, the quality of the fluid at the exit would be $0 < x_{vqual,cdexit} < 1$, and the total rate of heat rejection in the condenser is:

$$q_{cd-reject} = \sum_{i=1}^{J} (UA'_{2\varphi})_i \Delta z_i \left(T_{sat-cd,i} - T_{sink}\right) = \Delta x A_{cd} G \sum_{i=1}^{J} i_{fg,c}\Big|_{T_{sat-cd,i}} \tag{5.67}$$

$$q_{cd-reject} = \dot{m}\left(i_{cd-in} - i_{cd-exit}\right)$$

Here, $q_{cd-reject} < q_{fg,c}$, $i_{cd-exit}$ is the fluid specific enthalpy at the exit of the condenser, and i_{cd-in} is the fluid specific enthalpy at the inlet of the condenser. Both $i_{cd-exit}$ and $q_{cd-reject}$ are

determined using Eq. (5.71). Once $i_{cd-exit}$ is calculated, the quality at the exit of the condenser, $x_{cd-exit}$, can be determined using the following equation:

$$i_{cd-exit} = i_g\Big|_{T_{sat-cd,j}} x_{cd-exit} + (1-x_{cd-exit}) i_f\Big|_{T_{sat-cd,j}} \tag{5.68}$$

where i_f and i_g are, respectively, the enthalpy of the saturated liquid and the saturated vapor.

c) $L_{cd}^{2\varphi} < L_{cd}$: In this situation, the ability of the condenser to reject heat is more than that required for complete condensation of the vapor, and the position where this happens ($x = 0$) is located within the condenser pipe. As the rate of heat rejection to the sink continues over the rest of the condenser pipe, the fluid exits in a subcooled state. The total rate of heat rejection in the condenser is calculated as follows:

$$q_{cd-reject} = q_{fgc} + q_{sc} \tag{5.69}$$

In this equation, q_{fgc} is the rate of heat transfer required to fully condense the vapor in the condenser, see Eq. (5.70); and q_{sc} is the rate of heat rejection from the condensed liquid, causing it to exit the condenser in a subcooled state. The rate of heat rejection from the condensed liquid in the condenser is given by the following equation:

$$q_{sc} = \dot{m} c_{p,l} \left(T_{2\varphi-exit} - T_{cd-exit}\right) \tag{5.70}$$

To determine q_{sc} using this equation, $T_{cd-exit}$ is needed. The method for calculating $T_{cd-exit}$ is presented in the next subsection.

As was mentioned earlier, the two-phase pressure drop in the condenser is determined using the same procedures as those employed for this task in the vapor-transport line. For each section *i*, the total pressure drop is given by

$$(\Delta P)_i^{2\varphi} = (\Delta P)_{fric,i}^{2\varphi} + (\Delta P)_{mom,i}^{2\varphi} + (\Delta P)_{grav,i}^{2\varphi} \tag{5.71}$$

The total pressure drop in the two-phase region is

$$\Delta P_{cd-2\varphi} = \sum_{i=1}^{N} (\Delta P)_i^{2\varphi} \tag{5.72}$$

The total mass of fluid in the two-phase region of the condenser is obtained using the following equation:

$$m_{cd-2\varphi} = \sum_{i=1}^{N} [\alpha_i \rho_g + (1-\alpha_i)\rho_l](\pi D_{vl}^2 / 4)\Delta z_i \tag{5.73}$$

Subcooled Region

The subcooled (or single-phase liquid) region exists in the condenser only if $L_{cd}^{sc} = \left(L_{cd} - L_{cd}^{2\varphi}\right) > 0$. If such a subcooled region exists, then, neglecting the viscous dissipation and axial diffusion terms, and assuming thermally fully developed conditions pervail, the solution for the local bulk temperature is the following:

$$\left(T_{bulk-sc} - T_{sink}\right) / \left(T_{2\varphi-exit} - T_{sink}\right) = e^{-\left(\frac{UA'_{sc}}{\dot{m}c_{p,l}}\right)z_{sc}} \tag{5.74}$$

In this equation, $T_{bulk-sc}$ is the liquid bulk temperature, and UA'_{sc} is the total thermal conductance per unit length for heat loss from the subcooled region:

$$UA'_{sc} = \frac{1}{R'_{sc} + R'_{pipewall} + R'_{oil}} \tag{5.75}$$

$$R'_{sc} = \frac{1}{h_{sc}\pi D_{cd}}$$

$$R'_{pipewall} = \frac{\ln\left(\left(D_{cd} + 2t\right) / D_{cd}\right)}{2\pi k_{pipe}} \tag{5.76}$$

$$R'_{oil} = \frac{1}{h_{oil}\pi(D_{cd} + 2t)}$$

where, referring to Figure 5.11, R'_{sc}, $R'_{pipewall}$, and R'_{oil}, respectively, are the thermal resistances (per unit length of the pipe) for the convective heat transfer in the subcooled region, radial heat conduction in the pipe wall, and the convective heat transfer from the outside surface of the condenser pipe to the oil bath. R'_{oil} is essentially constant (for the given constant sink conditions), and it is the same as that for the two-phase region. $R'_{pipewall}$ can also be assumed constant. Assuming fully developed laminar flow and heat transfer in the subcooled region of the condenser, the Nusselt number in this region lies in the range $3.65 \leq Nu_{sc} = h_{sc}D_{cd} / k_l \leq 4.36$: A value in the middle of this range, $Nu_{vl-in} = 4.0$, is used in this work. Therefore, R'_{sc} is also constant. The resulting constant value for UA'_{sc} is calculated using Eq. (5.75).

The length of the subcooled region, if it exists, is calculated as follows:

$$L_{cd}^{sc} = L_{cd} - L_{cd}^{2\varphi} \tag{5.77}$$

and the subcooled liquid temperature at the condenser exit is obtained from

$$T_{cd-exit} = T_{sink} + \left(T_{2\varphi-exit} - T_{sink}\right) e^{\left(-\frac{UA'_{sc} L_{cd}^{sc}}{\dot{m} c_{p,l}}\right)} \tag{5.78}$$

After the calculation of $T_{cd-exit}$, Eq. (5.70) is used to obtain the total rate of heat rejection in the subcooled region of the condenser.

Assuming fully developed flow, the friction pressure drop along the subcooled length of the condenser pipe is calculated using the following equation:

$$(\Delta P_{fric})_{sc} = \frac{\left(f_{sc}\,\mathrm{Re}_{sc}\right)}{2} \frac{\bar{\mu}_{l,sc} L_{sc} \dot{m}}{\bar{\rho}_{l,sc} A_{cd} D_c^2} + \Delta P_{fittings,sc} \tag{5.79}$$

In this equation, $\Delta P_{fittings,sc}$ is used to account for the friction pressure drop in fittings and bends; and $\bar{\mu}_{l,sc}$ and $\bar{\rho}_{l,sc}$ are the average dynamic viscosity and mass density of the subcooled liquid, respectively. In the LHP experiments, for all runs, $(\Delta P_{fric})_{sc}$ was a very small fraction of the overall pressure (as the velocity of the liquid in this region is extremely low). Thus, a rather rudimentary approach was adopted for the estimation of $\Delta P_{fittings,sc}$: It was set equal to a third of the total friction loss in the subcooled region $(\Delta P_{fric})_{sc}$. Furthermore, as the liquid flow is laminar and fully developed, $f_{sc}\,\mathrm{Re}_{sc}$ in Eq. (5.79) is set equal to 64.

The gravity pressure drop in the subcooled region of the condenser, if it exists, is given by

$$\left(\Delta P_{grav}\right)_{sc} = \bar{\rho}_{l,sc} g L_{cd}^{sc} \sin\theta \tag{5.80}$$

In this work, the condenser pipe sloped very slightly (< 1%) downwards with respect to the gravitational acceleration vector: Thus, θ for this section is negative, and so is $\sin\theta$. In Eq. (5.80), $\bar{\rho}_{l,sc}$ is the average density of the subcooled liquid.

There is no momentum pressure drop in the subcooled region of the condenser, as the flow is assumed to be essentially fully developed and there is no phase change.

The overall pressure drop in the subcooled region of the condenser is calculated as follows:

$$\Delta P_{cd-sc} = \left(\Delta P_{fric}\right)_{sc} + \left(\Delta P_{grav}\right)_{sc} \tag{5.81}$$

The total mass of the liquid in the subcooled region is calculated as follows:

$$m_{cd-sc} = \bar{\rho}_{l,sc}(\pi D_{cd}^2 / 4) L_{cd}^{sc} \tag{5.82}$$

5.2.4 Liquid-Transport Line

The fluid charging strategy for the LHP experiments undertaken in this work was designed to ensure the vapor always condensed completely inside the condenser pipe ($L_{cd} > L_{cd}^{2\varphi}$). Thus, it is assumed in this discussion that subcooled liquid exits the condenser. Furthermore, again, the mass flow rate (and Reynolds number) of the liquid flowing in this transport line is very small; thus the effects of the U-bends on the pressure drops and heat transfer in this transport line are negligibly small.

The subcooled liquid exiting the condenser flows through a liquid-transport line and reaches the inlet of the evaporator. This liquid-transport line was made of a horizontal serpentine pipe of circular cross-section (the U-bends are not shown in Figure 5.1). This pipe was insulated in the same manner as the vapor-transport line (see Figure 5.6). An energy balance on the liquid-transport line yields the following equation, which is used to calculate the temperature of the liquid exiting this section (and entering the liquid pool of the evaporator) and also the rate of heat loss to the ambient.

$$q_{loss-ll} = (UA)_{ll}\left(\frac{T_{cd-exit} - T_{ev-in}}{\ln\left(\left(T_{cd-exit} - T_{amb}\right)/\left(T_{ev-in} - T_{amb}\right)\right)}\right) = \dot{m} c_{p,l}\left(T_{cd-exit} - T_{ev-in}\right) \tag{5.83}$$

Here, $(UA)_{ll}$ is the total thermal conductance for the rate of heat loss from the liquid-transport line: It is defined as

$$(UA)_{ll} = \frac{1}{R_{th-ll-in} + R_{th-ll-out}} \tag{5.84}$$

In this equation, $R_{th-ll-in}$ and $R_{th-ll-out}$, respectively, are the thermal resistance for the convective heat transfer in the liquid-transport line and the external thermal resistance (it includes radial heat conduction through the pipe wall + insulating material and also external convection). Both these resistances are based on the internal surface of the pipe and are defined as follows:

$$R_{th-ll-in} = \frac{1}{h_{ll-in}\pi D_{ll} L_{ll}}$$
$$R_{th-ll-out} = \frac{1}{h_{ll-out}\pi D_{ll} L_{ll}} \tag{5.85}$$

Here, h_{ll-in} and h_{ll-out} are heat transfer coefficients and D_{ll} is the internal diameter of the liquid-transport line. For the full range of the mass flow rates encountered in the LHP experiments, the flow in the liquid-transport line is laminar. Therefore, $3.65 \le Nu_{ll} = h_{ll-in} D_{ll} / k_l \le 4.36$: $Nu_{ll} = 4$ is used in this work. As was discussed in Chapter 4, the external thermal resistance, $R_{th-ll-out}$, was obtained experimentally: $R_{th-ll-out}$ = 14.7 K/W. Once $(UA)_{ll}$ is obtained, T_{ev-in} and $q_{loss-ll}$ are calculated using Eq. (5.83).

The pressure drop in this liquid-transport line is calculated using the same approach as that employed for the subcooled region:

$$\Delta P_{ll} = \frac{(f_{ll}\,\mathrm{Re}_{ll})}{2} \frac{\bar{\mu}_{l,ll} L_{ll} \dot{m}}{\bar{\rho}_{l,ll} A_{ll} D_{ll}^2} + \Delta P_{fittings,ll} \tag{5.86}$$

The Reynolds number is calculated:

$$\mathrm{Re}_{ll} = \frac{\dot{m} D_{ll}}{\bar{\mu}_l A_{ll}} \tag{5.87}$$

As was mentioned earlier, the flow is laminar and assumed to be fully developed. Therefore, $f_{ll} Re_{ll}$ is set equal to 64.0, and the momentum pressure drop in the liquid-transport line is zero. Furthermore, as the liquid-transport line is horizontal in the LHP experiments, the gravity pressure drop in this line is also zero.

The mass of the liquid in the liquid-transport line is calculated using an average mass density (arithmetic mean):

$$m_{ll} = \left(\pi D_{ll}^2 / 4\right) L_{ll} \left(\rho_l \big|_{T_{cd-exit}} + \rho_l \big|_{T_{ev-in}} \right) / 2 \tag{5.88}$$

5.2.5 Total Pressure Drop in the Loop Heat Pipe

In the context of the discussions presented in Section 5.2.1 – 5.2.4, the total pressure drop in the LHP, is calculated as follows:

$$\Delta P_{tot} = \Delta P_{wick} + \Delta P_{vl} + \Delta P_{cd-2\varphi} + \Delta P_{cd-sc} + \Delta P_{ll} \tag{5.89}$$

The maximum capillary head available in the wick is given by

$$\Delta P_{cap,\max} = \frac{2\sigma \cos\theta_c}{r_p} \tag{5.90}$$

In this equation, θ_c is the contact angle at the static equilibrium condition (it depends on the wick material and the working fluid), σ is the liquid-vapor surface tension, and r_p is the effective capillary pore radius. The effective capillary pore size, d_p (=2 r_p), was experimentally determined for two different wicks, both sintered powder-metal porous plates, one made of nickel 200 and the other of stainless steel 316: The results are presented in Chapter 3 and also in Atabaki and Baliga (2005a). The wick made of stainless steel 316 was used in the LHP experiments: The characteristics of this wick are presented in Table 4.1.

For the LHP to operate successfully under steady-state conditions, the total pressure drop should be less than the maximum capillary head:

$$\Delta P_{tot} < \Delta P_{cap,\max} \tag{5.91}$$

This condition was met in all of the LHP experiments conducted in this work.

5.3 Model Implementation

The proposed network thermofluid model was incorporated in a computer program written in FORTRAN. This computer program is designed to simulate the LHP described in Chapter 4, with distilled water as the working fluid.

Correlations for the required thermophysical properties of the working substance (water in this case) are incorporated into the computer program, as are all correlations needed to calculate the various single-phase and two-phase friction pressure drops, heat transfer coefficients, and vapor void fraction. The following inputs are provided to the computer program for each run: The geometrical details of the LHP; the total mass of the fluid (charge) inside the LHP, $m_{charged}$; the temperature of the oil bath, T_{sink}; the ambient environment temperature, T_{amb}; and the rate of heat input, q_{app}, applied to the evaporator. At the start of each run, the operating temperature of the loop, T_{sat}, is guessed and also provided as an input. Here, T_{sat} is the saturation temperature of the working substance at the liquid-vapor interface in the wick of the evaporator.

The sequence of the various calculations and checks performed in the overall iterative solution procedure of the proposed network model, as incorporated in this computer program, are presented concisely in the flow chart in Figure 5.12.

The results produced by this computer program include the steady-state mass flow rate, the temperature distribution, and the pressure distribution in the LHP. These and other numerical results are presented and discussed in the next chapter along with the results obtained in the complementary experimental investigation of the LHP.

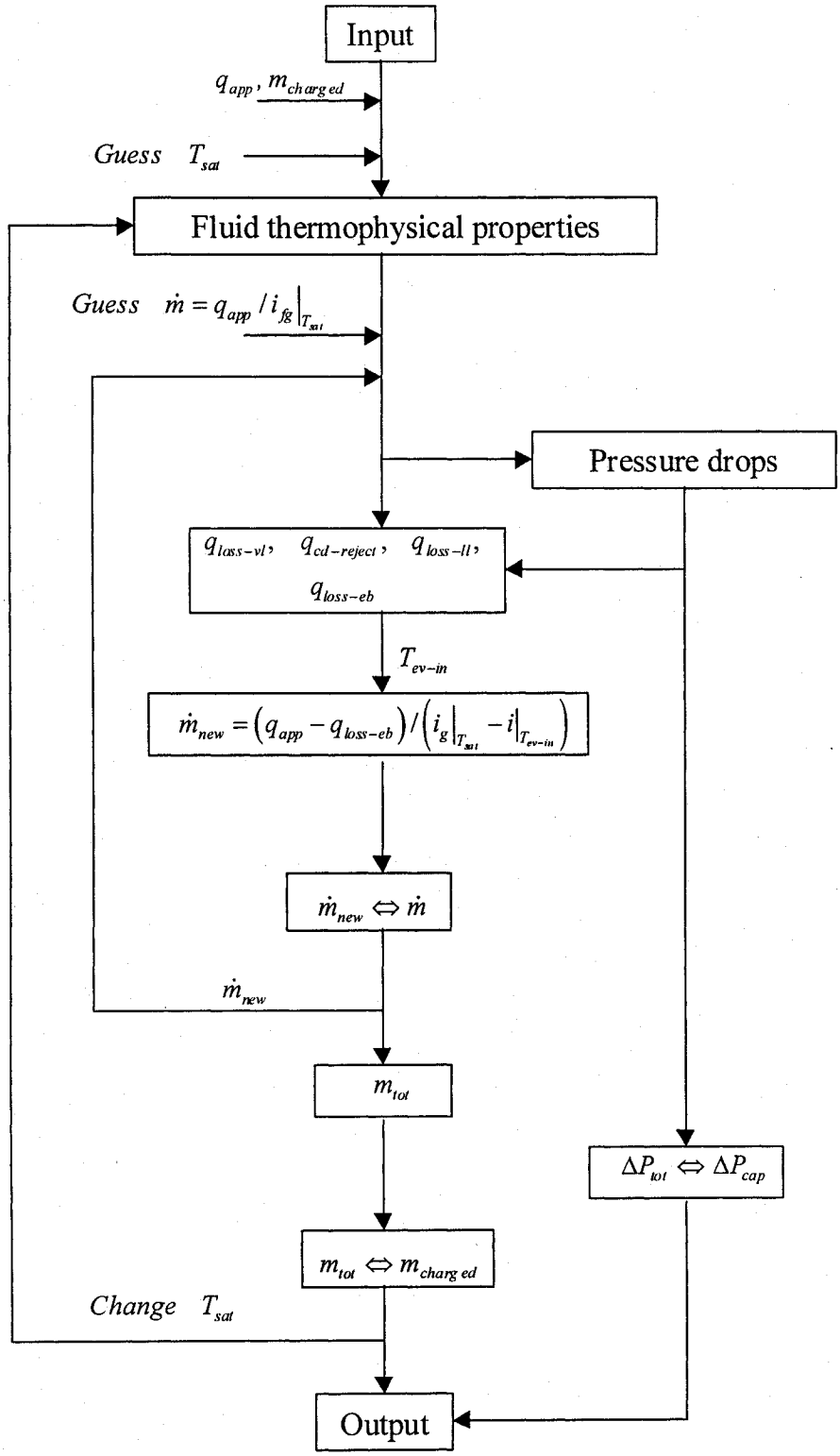

Figure 5.12: Flow chart depicting key elements of the overall iterative solution procedure of the proposed network thermofluid model.

Chapter 6:
Results and Discussions

The results of complementary computational and experimental investigations of the loop heat pipe (LHP) described in Chapter 4 are presented and discussed in this chapter. The network thermofluid model described in Chapter 5 was used to explore the steady-state operation of this LHP in the computational investigation. In the experimental investigation of this LHP, the emphasis was again on its steady-state operation, but its startup phase was also explored.

The LHP considered in this work is schematically illustrated in Figures 4.1 and 5.1. The dimensions and characteristics of its different elements are given in Table 4.1. As was described in Chapter 4, this LHP has a flat (plate-type) evaporator: Details of this evaporator are presented schematically in Figure 4.2, and a schematic of the full evaporator assembly (evaporator; heaters; flux-measuring plate; and supporting plates, bolts, and nuts) is given in Figure 4.3. There is no compensation chamber integrated with this flat evaporator; rather, the LHP is connected to a two-phase reservoir (akin to those used in capillary pumped loops) that is used only during the charging procedure (filling the LHP with the working fluid) and then isolated; thus, once this LHP is charged, it operates with a fixed active mass of the working fluid. In this work, this LHP was run with distilled water as the working fluid and a stainless steel (SS 316) sintered powder-metal porous plate as the wick (porous material # 1 in Table 4.1). Full details of the procedure that was used to charge this LHP are given in Chapter 4, so they are not repeated here.

In this chapter, the operational conditions that were considered in the complementary experimental and computational investigations of the LHP are summarized in the next section. Following that, the transient operation of the LHP during its startup phase is discussed with reference to a representative set of operating conditions. Then, in the next eight sections, the focus is entirely on the steady-state operation of the LHP. In particular, a variety of steady-state experimental results and complementary predictions yielded by

the proposed network thermofluid model (described in Chapter 5) are presented and discussed.

6.1 Summary of Operational Conditions

Complementary computational and experimental investigations of the LHP described in Chapter 4 (and schematically illustrated in Figures 4.1 and 5.1) were conducted for a range of power inputs to the evaporator, q_{app}, and three different combinations of the average temperatures of the sink (oil bath in which the condenser pipe was immersed) and the ambient environment, T_{sink} and T_{amb}, respectively. Specific values of these operational conditions are given below in Table 6.1.

Table 6.1: Operational conditions considered in the complementary computational and experimental investigations.

Range of power input to the evaporator	$150 \text{ W} \leq q_{app} \leq 450 \text{ W}$
Average temperature of the sink (oil bath) and the corresponding average temperature of the ambient environment	$T_{sink} = 42.16\ ^{\circ}\text{C}$ and $T_{amb} = 27.08\ ^{\circ}\text{C}$ $T_{sink} = 52.11\ ^{\circ}\text{C}$ and $T_{amb} = 26.09\ ^{\circ}\text{C}$ $T_{sink} = 61.27\ ^{\circ}\text{C}$ and $T_{amb} = 25.64\ ^{\circ}\text{C}$

As was mentioned earlier, this LHP was run with distilled water as the working fluid and a stainless steel (SS 316) sintered powder-metal porous plate as the wick (porous material # 1 in Table 4.1).

The procedures that were used to charge, start, and run this LHP in the experimental investigation are described in Chapter 4. Once the charging procedure is completed, the active mass of the working fluid inside this LHP is fixed. This mass was measured using the following procedure. After all experimental runs were completed, the evaporator heaters were turned off, and the oil-bath was shut down. The LHP was then left undisturbed and allowed to reach a state of thermal equilibrium with the ambient environment. In this condition, the LHP was filled with a two-phase (vapor-liquid) mixture of distilled water. The temperature of the ambient environment during this

procedure was about 24 °C: Thus, the saturation pressure inside the LHP at the aforementioned thermal equilibrium state was about 0.02985 bars (far below the atmospheric pressure). At this stage, a graduated flask filled with deaerated distilled water and located at an elevation of about 2.0 m above that of the LHP was connected to it using a flexible tube fitted with a plug valve. Once air was purged from this flexible connecting tube, the plug valve was opened, and distilled water was allowed to flow very slowly into the LHP. This filling process was continued until the distilled water could no longer flow into the LHP under the action of gravity. At this stage, the volume of the distilled water that had flowed from the graduated flask into the LHP was read and recorded. This volume was subtracted from the total volume of the LHP (calculated from the known geometry of the loop) to obtain the volume of the liquid water that was inside the LHP before the initiation of this filling process. In this procedure, it is assumed that liquid water is incompressible; and the mass of the saturated vapor inside the LHP before the initiation of the filling process (at 0.02985 bars) is considered negligible compared to that of the saturated liquid water.

Using data measured in the above-mentioned procedure and the mass density of saturated liquid water at 24 °C, the mass of the active working fluid in the LHP during the experimental runs was determined to be 657.5 g (±3%). This value was used as an input to the aforementioned network thermofluid model in the computational investigation of this LHP.

6.2 Startup of the LHP

The startup of the LHP presented in Chapter 4 was studied experimentally for the three average sink temperatures mentioned in Table 6.1 (T_{sink} = 42.16 °C, 52.11 °C, and 61.27 °C). The startups of the LHP for these three sink temperatures were qualitatively similar. Therefore, in the this section, only the startup for T_{sink} = 42.16 °C is discussed.

As was described in Chapter 4, after charging the LHP with a fixed active mass of the working fluid (657.5 g ± 3% for the experiments undertaken in this work), it was isolated from the two-phase reservoir. After that, the elevation of the condenser was adjusted so that the zero-quality point inside it was slightly higher than that of the upper surface of the wick in the evaporator. This ensures that the whole evaporator (and also a part of the

vapor-transport line), a part of the condenser, and the liquid-transport line are completely filled with the liquid phase. Following that, the entire LHP and the oil bath were allowed to come to thermal equilibrium with the ambient environment: The average ambient environment temperature during this startup was T_{amb} = 27.0 °C.

The startup of the LHP was initiated by turning on the constant-temperature oil bath and setting its desired temperature (T_{sink} = 42.16 °C). Then the power supply to the evaporator was turned on and set equal to q_{app} = 200 W. The acquisition and recording of data from all thermocouples, differential pressure transducers, and multimeters (used to measure the voltages and currents supplied to the heaters) were initiated at least two hours before this startup procedure, and continued throughout the experiment.

In Figure 6.1, the evolutions of T_{sink}, T_{sat}, $T_{cd\text{-}in}$, $T_{cd\text{-}out}$, and $T_{ev\text{-}in}$ during the startup are illustrated: A schematic illustration of the locations of the thermocouples used for measuring these temperatures is given in Figure 4.1. The variation with time of the corresponding pressure difference, ΔP_2, measured across the evaporator (pressure difference between points ***A*** and ***B*** in Figure 4.1) is given Figure 6.2: The pressure transducer that was used to measure ΔP_2 was zeroed before initiation of the startup in order to exclude any hydrostatic pressure differences (gravity head).

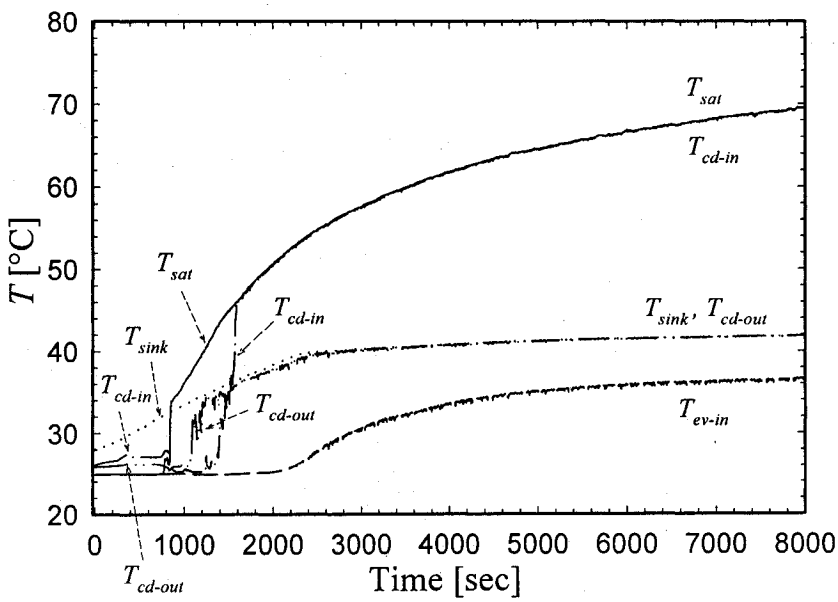

Figure 6.1: Transient thermal behavior of the LHP during startup: T_{sink} = 42.16 °C, T_{amb} = 27.0 °C, and q_{app} = 200 W.

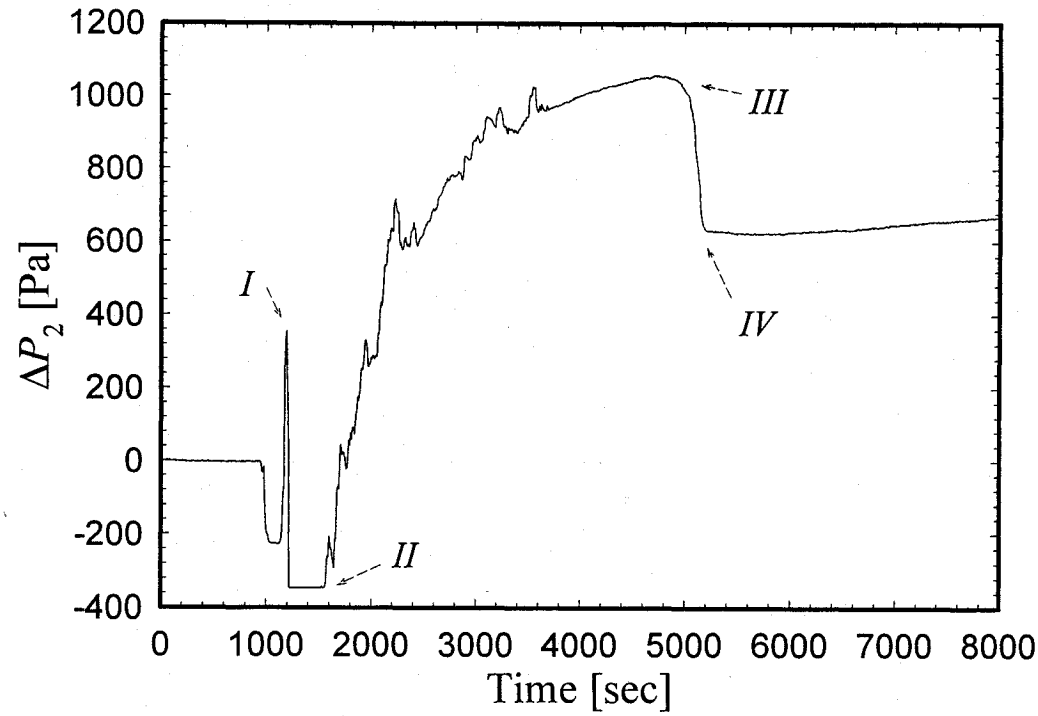

Figure 6.2: Variation with time of the differential pressure measured across the evaporator (ΔP_2) during startup: T_{sink} = 42.16°C, T_{amb} = 27.0 °C, and q_{app} = 200 W.

As shown in Figure 6.1, in the initial stage of the startup, t < 840 s, the sink temperature (shown as a dotted line) rises, however, the temperatures in the rest of the loop do not change much. During this time period (t < 840 s), because the sink temperature is higher than the other temperatures in the LHP, the condenser pipe is almost filled with a two-phase (liquid-vapor) mixture, and the evaporator is fully flooded. Furthermore, during t < 840 s, T_{cd-in} and T_{cd-out} rise slightly above T_{sat} and T_{ev-in} due to contact with the vapor inside the condenser (this vapor temperature is close to the sink temperature during this time period). For the same period of time, Figure 6.2 shows a zero pressure drop across the evaporator, indicating no fluid flow through it: Thus, it may be concluded that all of the power input to the evaporator goes into heating the liquid occupying the vapor grooves, raising its temperature, but not generating any vapor.

At t = 840 s (roughly), the excess temperature of the liquid in the evaporator grooves is enough to initiate nucleate boiling, and vapor bubbles are generated. These vapor bubble grow rapidly and push the liquid out of the evaporator into the vapor-transport line and also into the liquid pool through the wick. Therefore, the fluid temperature at the

exit of the evaporator, T_{sat}, suddenly increases, and $T_{cd\text{-}in}$ decreases: The increase in T_{sat} is due to the exiting hot liquid from the evaporator; and, at the same time, the relatively colder liquid which was initially stocked in the vapor transport line enters the condenser, resulting in a decrease in $T_{cd\text{-}in}$. At this stage, T_{sat} is the highest temperature in the loop, and, therefore, the condenser section starts to behave in accordance to its intended role (condensing the incoming vapor).

As shown in Figure 6.2, the aforementioned emptying of the evaporator grooves is accompanied by an initial decrease in the pressure difference across the evaporator: This is because the liquid is pushed out of the evaporator in both directions, forward towards the vapor-transport line and also backwards through the wick towards the liquid pool and the liquid-transport line; thus, the liquid column in the condenser pipe (that has about a 1% slope downwards from its inlet to its exit) rises, increasing the hydrostatic head in the liquid pool (sudden increase in the pressure at the point ***B*** shown in Figure 4.1) and causing a decrease in the pressure difference measured across the evaporator. However, once the vapor reaches the top surface of the wick and enters it, the liquid-vapor interface (inside the wick) generates a capillary head and the backflow is stopped: At this point, the capillary pumping action in the evaporator is initiated and the pressure of the vapor inside the grooves and in the vapor line is increased; this phenomenon is recorded as a ΔP_2 spike in Figure 6.2 (shown as point *1*).

Roughly coincident with the first ΔP_2 spike (*1*), $T_{cd\text{-}out}$ starts to rise with some oscillations and rapidly reaches a temperature only slightly lower than the sink temperature (see Figure 6.1), indicating flow of liquid out of the condenser. Soon after this pressure spike, ΔP_2 becomes negative and constant for a period of about 200 s, showing absence of the capillary head: This happens because the liquid inside the evaporator grooves and its exit pipe (which is sloped slightly upwards) is not fully pushed out in one shot; rather, the exiting vapor tunnels through in an annular-type flow, and some of the remaining liquid falls back into the evaporator, flooding it, covering the upper surface of the wick, and destroying the capillary head. However, as the heating is continued, the liquid in the evaporator grooves is continuously evaporated, and, as can be seen from the graphs in Figure 6.1, T_{sat} continues to rise. Once the vapor fills the vapor-

transport line and reaches the thermocouple at the condenser inlet, a sudden rise in its reading is observed, and $T_{cd\text{-}in}$ reaches a value very close to T_{sat}.

After some more time, the liquid layer above the wick is entirely evaporated, the capillary head is reestablished, and the fluid inside the LHP starts to flow continuously. This resumption of capillary pumping is marked as point *II* in Figure 6.2. As the startup continues, more of the power input is directed downward into the evaporator, instead of being used to heat up the pipes, fittings, and insulation of the LHP; this causes the rate of evaporation and, consequently, the circulating mass flow rate to increase; and, in turn, ΔP_2 increases. This process is shown in Figure 6.2 as a continuous increase in ΔP_2, with only minor oscillations, from point *II* to point *III*: Coincidentally, as shown in Figure 6.1, $T_{ev\text{-}in}$ increases asymptotically towards it steady-state value, indicating movement of the relatively hot fluid from the condenser to the evaporator entrance. As can be seen in this figure, a difference persists between the temperatures of the liquid at the inlet and outlet of the liquid-transport line, due to heat loss to the ambient environment. However, in spite of heat loss to the ambient from the fluid in the vapor-transport line, no visible temperature drop is observable along this line ($T_{sat} \sim T_{cd\text{-}in}$): This is because the vapor condenses (partially) as it flows through in this line, and the related pressure drop is not high enough (relative to the mean absolute pressure) to change the saturation temperature significantly.

At about t = 2600 s, the sink temperature reaches its preset value in the oil-bath (T_{sink} = 42.16 °C). Consequent, both T_{sink} and T_{cd-out} (which asymptotes to the sink temperature) stay essentially unchanged for t > 2600 sec. However, T_{sat} continues to increase, albeit asymptotically, towards its steady-state value; and, in response, the mass flow rate of the working fluid also continues to increase asymptotically towards its steady-state value.

At point *III* in Figure 6.2, ΔP_2 reaches its maximum value, and then it suddenly decreases significantly to a level marked as point *IV*. This sudden decrease in ΔP_2 can be explained as follows: The vapor-transport line of the LHP used in this study is made of a 4.3 m long pipe with several bends (see Figures 4.1 and 6.8); prior to point *III*, the mass flow rate is not high enough to completely clear this line of all residual liquid (especially

in the bends); thus, the vapor flows through a somewhat restricted open space in this line, requiring a high pressure drop; however, once the mass flow rate becomes adequately large and the absolute pressure in the evaporator becomes high enough (this happens at point *III*), the aforementioned residual amounts of liquid in the vapor-transport line are suddenly purged, this line is opened up more fully for the flow of the vapor, and ΔP_2 is reduced (point *IV* in Figure 6.2).

For t > 5200 sec, as shown in Figures 6.1 and 6.2, the loop operates smoothly, and the temperatures and ΔP_2 continue to asymptote to their steady-state values. As was mentioned in Chapter 4, in this work, when the differences between two consecutive sets of temperature readings (taken at 10 second intervals) were all less than or equal to ±0.05°C over a period of at 30 minutes, it was assumed that the steady-state conditions prevail. For the run illustrated in Figures 6.1 and 6.2, the steady-state condition was reached about five hours (18,000 sec) after the initiation of startup.

6.3 Temperature of Saturated Vapor at the Exit of the Evaporator

Predictions of the steady-state temperature of the saturated vapor at the exit of the evaporator, denoted by T_{sat} in Figure 4.1, were obtained in the computer simulations of the LHP and also measured in the experimental investigation. These results are presented and their implications are discussed in this section.

6.3.1 Comparison of Experimental and Numerical Results

In Figure 6.3, the variation of $(T_{sat} - T_{sink})$ with the power input to the evaporator, q_{app}, is presented for each of the three different combinations of T_{sink} and T_{amb} given in Table 6.1. The experimental results are shown with symbols, and the corresponding numerical results are shown as solid lines. The horizontal error bars in this figure represent the uncertainties in the experimental values of q_{app}. In the experiments, as was discussed in Chapter 4, q_{app} was estimated using the measured temperature difference across a heat-flux measuring plate (of known thermal conductivity) sandwiched between the electrical heaters and the upper piece of the evaporator (Figure 4.3): The uncertainties in q_{app} (represented by the horizontal error bars in Figure 6.3) were calculated following

the procedure described in ASHRAE Standard 41.5-75 (1976). As was discussed in Chapter 4, the uncertainties in the measured temperatures were ±0.05 °C; thus, an uncertainty of ±0.1 °C applies to all experimental values of the temperature difference $(T_{sat} - T_{sink})$ presented in Figure 6.3 (these uncertainties are not shown in this figure in order to avoid cluttering).

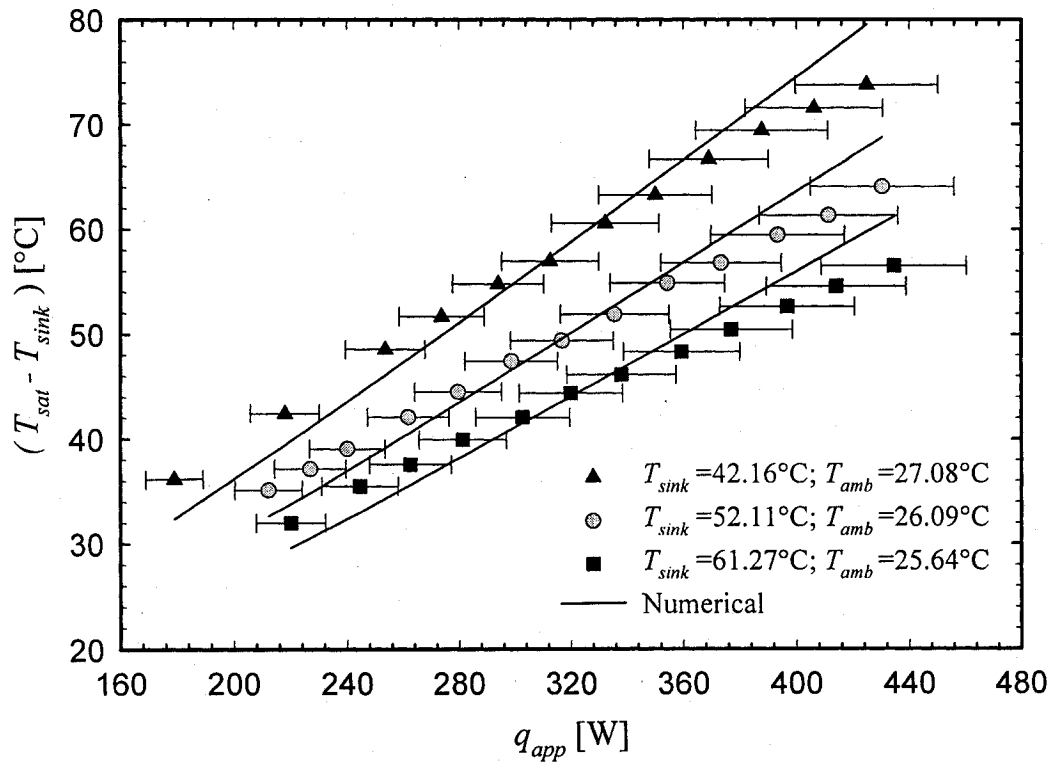

Figure 6.3: Variation of $(T_{sat} - T_{sink})$ with q_{app} : Experimental and numerical results.

There is fairly good agreement between the numerical and experimental results presented in Figure 6.3. To provide a quantitative appreciation of the agreement between these results, the predicted values of $(T_{sat} - T_{sink})$ are plotted against the corresponding experimental values in Figure 6.4. As shown by the results presented in this figure, for the operational conditions considered in this work, the model predictions are all within ±10.0% of the experimental measurements; the mean value of the absolute differences between these results is 4.32%.

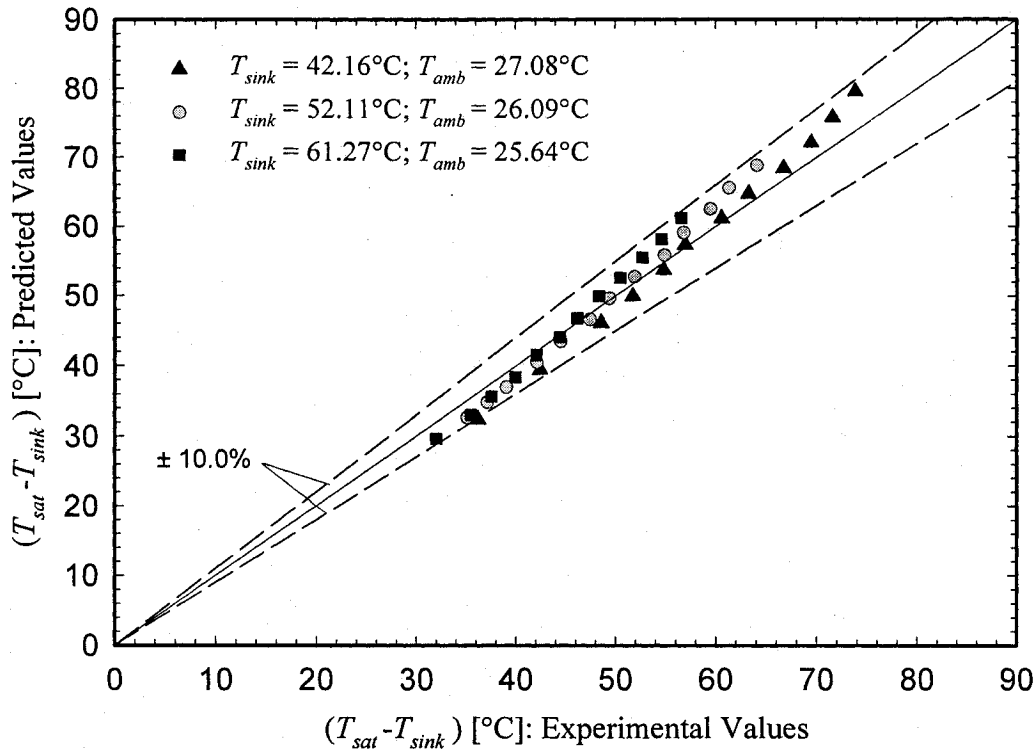

Figure 6.4: Comparison of predicted and experimental values of $(T_{sat} - T_{sink})$.

6.3.2 Effect of Increasing Power Input to the Evaporator, q_{app}

As was stated earlier, the particular LHP investigated here has a fixed mass of active working fluid. Thus, the length of the two-phase region in the condenser pipe is essentially constant (as the variations in the volume of the liquid and the geometry of the LHP with changes in the average temperature are very small for the range of conditions considered here): As a result, the single- and two-phase heat transfer areas in the condenser may be assumed to remain constant.

For each of the three combinations of T_{sink} and T_{amb}, the results presented in Figure 6.3 show that $(T_{sat} - T_{sink})$ increases monotonically and almost linearly with q_{app}. As the value of the sink temperature, T_{sink}, was kept essentially constant for a particular series of runs (at 42.16 °C, 52.11 °C, and 61.27 °C), each of the three curves and sets of data presented in Figure 6.3 indicates a monotonic increase of T_{sat} with q_{app}. This conclusion is explicitly indicated by the results presented in Figure 6.5, where T_{sat} is plotted versus q_{app}.

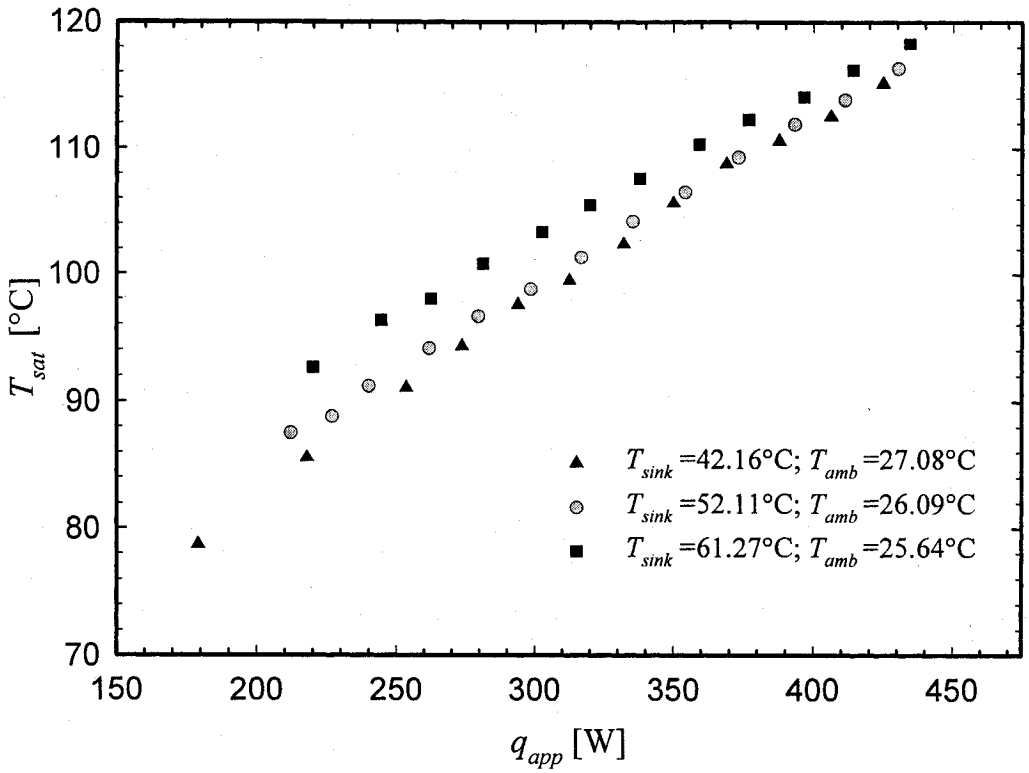

Figure 6.5: Variation of T_{sat} with q_{app} : Experimental results.

For each fixed combination of T_{sink} and T_{amb}, an increase in the value of q_{app} leads to a higher mass flow rate and higher average fluid temperatures inside the LHP: These effects lead to changes in the heat transfer coefficients on the inside surface of the pipe in the two-phase flow regions (in the vapor-transport line and in the condenser), but the overall thermal resistance (from the two-phase fluid flow to the ambient environment or the oil bath) is dominated by the sum of the thermal resistances of the pipe wall (across its thickness) and the insulation or convection (in the oil bath) outside it; furthermore, in the single-phase liquid flow regions (in the subcooled region of the condenser and the liquid-transport line), the flow is laminar, the fully-developed Nusselt number is constant, and the corresponding heat transfer coefficient on the inside surface of the pipe undergoes only slight changes (caused by the increase in the thermal conductivity of the condensed liquid water in response to the small increase in the average temperature in the subcooled region of the condenser). The thermal resistance of the forced convection on the outside surface of the condenser pipe (immersed inside the oil bath) decreases slightly with

increasing q_{app}, as the T_{sat} and, consequently, the temperature of the outside surface of the pipe wall both go up (and the viscosity of the oil goes down substantially and its thermal conductivity goes down only slightly with increasing temperature). Thus, the overall thermal resistances go down slightly with increasing q_{app}, but for all practical purposes, the LHP could be considered to operate in an essentially constant-conductance mode for each fixed combination of T_{sink} and T_{amb}. Therefore, for constant thermal sink conditions, an increase in the rate of heat rejection in the condenser (needed to complement the increase in q_{app} and maintain steady-sate conditions) can be achieved only by an increase in T_{sat}; and this increase in T_{sat} is almost linearly proportional to the increase in q_{app}. These arguments are reflected in the results presented in Figures 6.3 and 6.5. In this discussion, it has been assumed that the variation of the saturation temperature of the fluid inside the condenser with q_{app} is similar to that of T_{sat} (the saturation temperature of the vapor at the exit of the evaporator).

6.3.3 Effect of Increasing the Temperature of the Oil Bath, T_{sink}

For a fixed value of q_{app}, when the temperature of the oil bath, T_{sink}, is increased, the convective heat transfer coefficient on the outer surface of the condenser pipe, h_{oil}, increases (as was reported in Chapter 4, for T_{sink} = 41.9 °C, 51.3 °C, and 62.0 °C, h_{oil} = 290.2 W/m^2-°C, 320.4 W/m^2-°C, and 344.9 W/m^2-°C, respectively); thus, the corresponding thermal resistance per unit length $\{ R'_{oil} = 1/\{h_{oil}\pi(D_{cd} + 2t)\}$ decreases, and the overall thermal conductance of the LHP increases. Therefore, the *slopes* of the $(T_{sat} - T_{sink})$ vs. q_{app} curves in Figure 6.3 decrease with increasing values of T_{sink}; and the *slopes* of the T_{sat} vs. q_{app} curves in Figure 6.5 also decrease with increasing values of T_{sink}. Furthermore, when T_{sink} is increased at a fixed value of q_{app}, T_{sat} increases to a value that is needed to obtain a $(T_{sat} - T_{sink})$ that provides the required rate of heat rejection. However, as described above, when T_{sink} is increased at a fixed value of q_{app},

the overall thermal conductance of the LHP goes up and, therefore, $(T_{sat} - T_{sink})$ decreases (see Figure 6.3).

6.4 Effective Thermal Resistance of the LHP

An effective thermal resistance of the LHP operating at steady-sate conditions is defined as follows:

$$R_{th,ef} = \frac{T_{sat} - T_{sink}}{q_{app}} \tag{6.1}$$

Not all of the power input to the evaporator, q_{app}, is transmitted by the LHP from the evaporator to the heat sink (the oil bath in which the condenser is immersed): A part of it is lost to the ambient environment via rates of heat loss from the outer surfaces of the evaporator body ($q_{loss-eb}$), the vapor-transport line ($q_{loss-vl}$), and the liquid-transport line ($q_{loss-ll}$). Nevertheless, q_{app} is used in the definition of $R_{th,ef}$, Eq. (6.1), as it is readily measured in the experiments, and also because the total rate of heat loss $(q_{loss-eb} + q_{loss-vl} + q_{loss-ll})$ is a relatively small fraction (< 13.5%) of q_{app}: For similar reasons, this definition of $R_{th,ef}$ is also commonly used in the literature [Wirsch and Thomas (1996)].

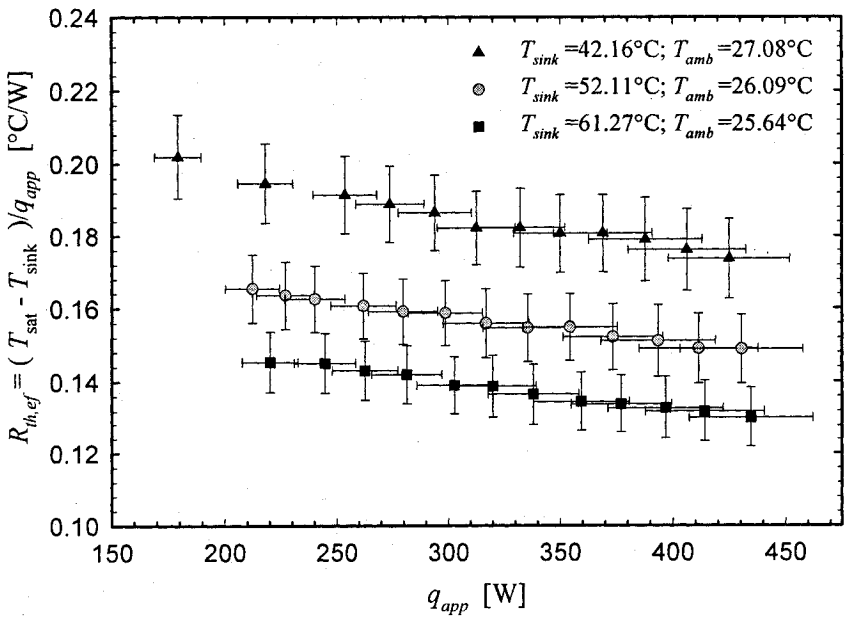

Figure 6.6: Variation of $R_{th,ef}$ with q_{app} for steady-state operation of the LHP.

For steady-state operation of the LHP, graphs of the variation of $R_{th,ef}$ with q_{app} for each of the three different combinations of T_{sink} and T_{amb} considered in the experiments (see Table 6.1) are presented in Figure 6.6: These are experimental results. As was discussed earlier in this chapter and also in Chapter 4, the thermal resistance per unit length for convective heat transfer from the outside surface of the condenser pipe to the oil bath in which it is immersed, R'_{oil}, decreases when T_{sink} increases: Thus, $R_{th,ef}$ also decreases when T_{sink} increases. With respect to the results shown in Figure 6.6, for average sink temperatures of 42.16°C, 52.11°C, and 61.27°C, the *mean* (or *average*) values of the effective thermal resistance of the LHP (over 150 W $\leq q_{app} \leq$ 450 W) are 0.185 °C/W (with variation of ±3.5% about this mean value), 0.157 °C/W (with variation of ±3.0% about this mean value), and 0.138 °C/W (with variation of ±3.2% about this mean value), respectively.

The results presented in Figure 6.6 also show that the $R_{th,ef}$ decreases slightly with increasing q_{app}, for each of the three fixed combinations of T_{sink} and T_{amb} (the reasons for this behavior of $R_{th,ef}$ were presented in the last section).

The horizontal and vertical error bars that represent the uncertainties in the experimental results presented in Figure 6.6 were calculated following the method discussed in ASHRAE Standard 41.5-75 (1976).

6.5 Rates of Heat Transfer in Different Elements of the LHP

Steady-state rates of heat transfer predicted by the proposed network thermofluid model in different elements of the LHP are presented in Figure 6.7 for the combination T_{sink} = 42.16 °C and T_{amb} = 27.08 °C, and three different values of the power input to the evaporator: q_{app} = 200 W (T_{sat} = 78.2 °C), 300 W (T_{sat} = 97.1 °C), and 400 W (T_{sat} = 116.7 °C). In particular, for each of these three values of q_{app}, the following rates of heat transfer normalized with respect to q_{app} are presented in Figure 6.7: Rate of heat leak to the liquid pool in the evaporator (q_{hl}/q_{app}); rate of heat transfer needed for the liquid-vapor phase-change process in the evaporator (q_{fg}/q_{app}); rate of heat loss from the outer

surface of the evaporator body to the ambient environment ($q_{loss-eb}/q_{app}$); rate of heat transfer from working fluid to the oil bath in the two-phase portion of the condenser pipe (q_{fgc}/q_{app}); and rate of heat transfer from working fluid to the oil bath in the subcooled (single-phase liquid) region of the condenser pipe (q_{sc}/q_{app}).

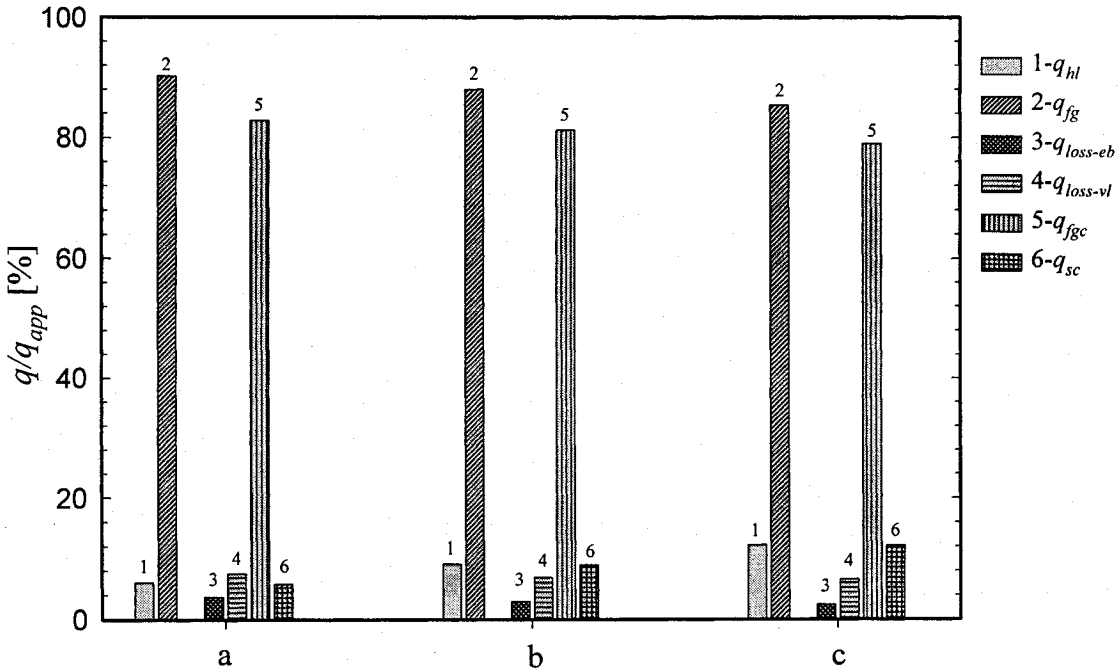

Figure 6.7: Predictions of steady-state rates of heat transfer in different elements of the LHP for T_{sink} = 42.16 °C and T_{amb} = 27.08 °C: (a) q_{app} = 200 W (T_{sat} = 78.2 °C); (b) q_{app} = 300 W (T_{sat} = 97.1 °C); and (c) q_{app} = 400 W (T_{sat} = 116.7 °C).

In Figure 6.7, the results for each value of q_{app} are presented as bar charts that are grouped together (the groups are denoted as *a*, *b*, and *c*). The sum of the first three bars is equal to the rate of heat input to the evaporator q_{app}: $(q_{hl} + q_{fg} + q_{loss-eb})/q_{app} = 1$. The rate of heat loss from the liquid-transport line to the ambient environment, $q_{loss-ll}$, is negligible compared to the other six rates of heat transfer shown in Figure 6.7 for each value of q_{app}; thus, it is not shown in this figure. The sum of the bars 3 to 6 plus $q_{loss-ll}$ is also equal to q_{app}: $(q_{loss-vl} + q_{fgc} + q_{sc} + q_{loss-ll} + q_{loss-eb})/q_{app} = 1$. In Figure 6.8, the variations of q_{hl}, q_{sc}, $q_{loss-vl}$, and $q_{loss-eb}$ (absolute values) with q_{app} for T_{sink} = 42.16 °C and T_{amb} = 27.08 °C (same conditions as those that apply to the results in Figure 6.7) are presented.

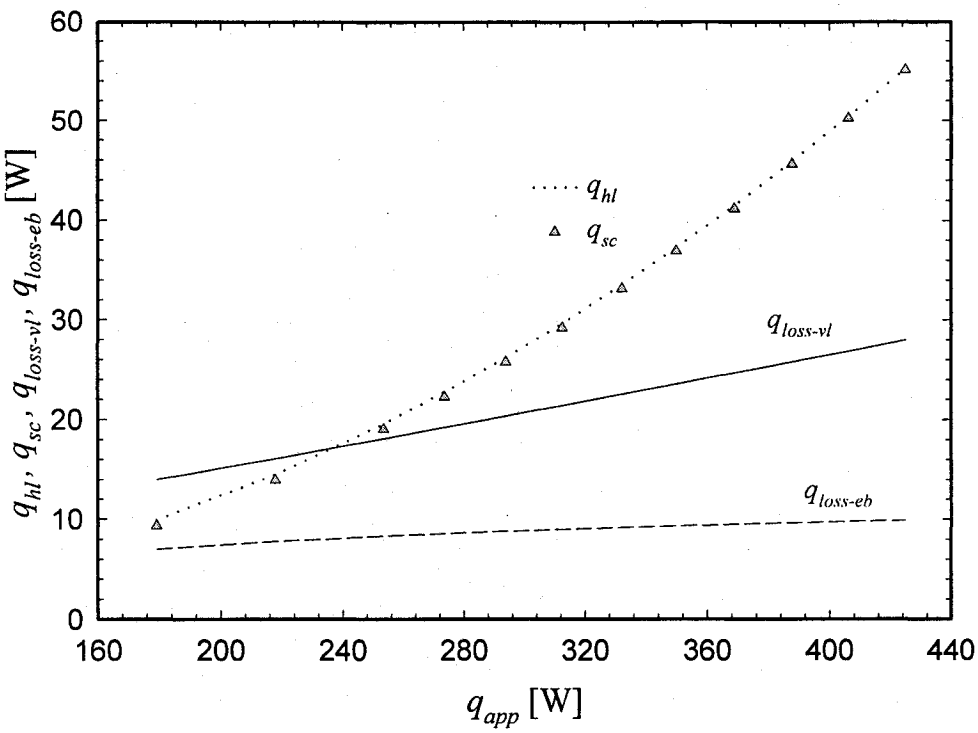

Figure 6.8: Steady-state variation of q_{hl}, q_{sc}, $q_{loss\text{-}vl}$, and $q_{loss\text{-}eb}$ with q_{app} (T_{sink} = 42.16 °C; T_{amb} = 27.08 °C).

The results in Figure 6.7 show that for each value of q_{app} (each group), bars 1 and 6 are almost equal in height: In other words, q_{hl}/q_{app} and q_{sc}/q_{app} are almost equal in each case, showing that the rate of heat leak in the evaporator automatically adjusts to compensate for the rate of heat rejection in the subcooled part of the condenser. The results presented in Figure 6.8 also show that the variations of q_{hl} and q_{sc} with q_{app} are almost identical. For each group of results in Figure 6.7, q_{fg}/q_{app} (bar 2) is a bit higher than q_{fgc}/q_{app} (bar 5), and this finding is also confirmed by the results presented in Figure 6.8: This is an expected finding, as part of q_{fg} is lost to the ambient environment in the vapor-transport line ($q_{loss\text{-}vl}$). However, with increasing q_{app}, both q_{fg}/q_{app} (bar 2) and q_{fgc}/q_{app} (bar 5) decrease slightly: This is because T_{sat} increases with increasing q_{app} and leads to higher values of q_{hl}/q_{app} (bar 1) and q_{sc}/q_{app} (bar 6). As shown by the results in Figure 6.8, the rates of heat loss from the evaporator body, $q_{loss\text{-}eb}$, and from the

vapor-transport line, $q_{loss-vl}$, both increase with q_{app}: This behavior is the result of increasing T_{sat} with increasing q_{app}.

6.6 Temperatures at Different Locations in the LHP

Steady-state temperatures predicted by the proposed network thermofluid model at different locations in the LHP are presented in Figure 6.9 for two different combinations of sink and ambient temperatures (T_{sink} = 42.16 °C and T_{amb} = 27.08 °C ; and T_{sink} = 61.27 °C and T_{amb} = 25.64 °C) and three different power inputs to the evaporator (q_{app} = 200 W, 300 W, and 400 W): The dashed line and filled symbols indicate results corresponding to the sink temperature of 61.27 °C; while the dotted line and open symbols represent results pertaining to the sink temperature of 42.16 °C.

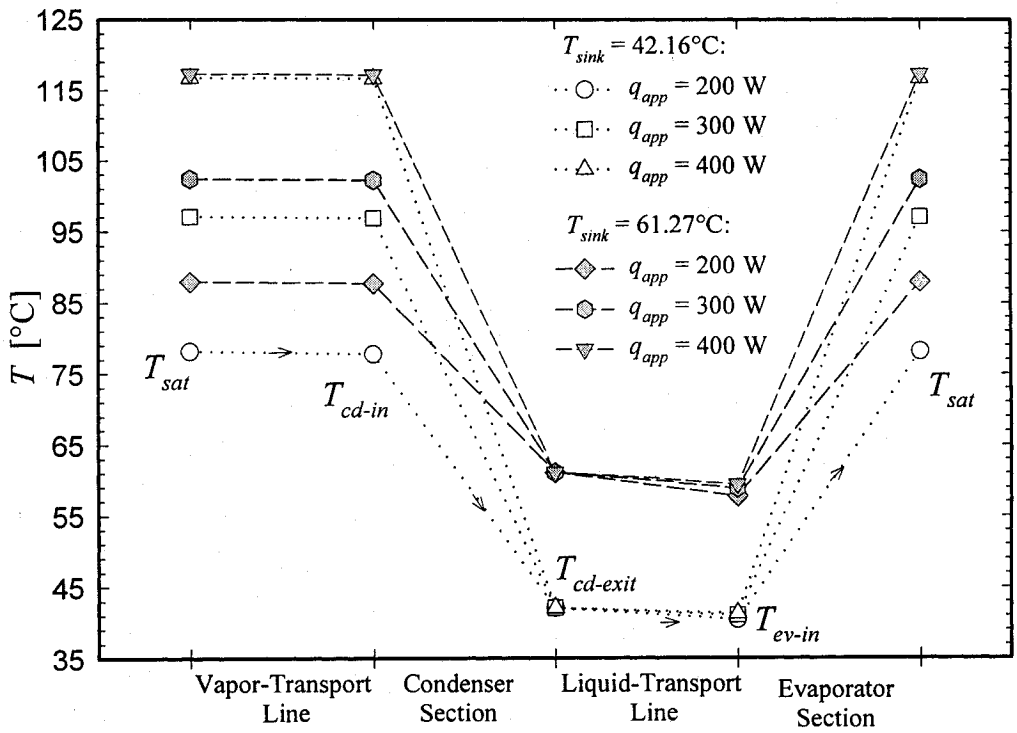

Figure 6.9: Predictions of steady-state temperatures at different locations in the LHP.

Consider the lowest curve in Figure 6.9 (q_{app} = 200 W and T_{sink} = 42.16 °C); the arrows indicate the direction of flow of the working fluid. The saturated vapor exits the

evaporator and enters the vapor-transport line at the maximum fluid temperature, T_{sat}, in the LHP. In the vapor-transport line, due to heat loss to the ambient environment, the vapor condenses partially; the pressure drop is relatively small compared to the absolute pressure; thus the drop in saturation temperature in this line is relatively small; and $T_{cd\text{-}in}$ is almost equal to T_{sat}. The vapor is first completely condensed inside the condenser (this process, in which the saturation temperature drops only slightly due to the relatively small pressure drop, is not explicitly shown in Figure 6.9), and then the condensed liquid is subcooled as it flows towards the exit. As was mentioned earlier, the condenser in this LHP was over designed and very efficient; thus, the liquid exits the condenser at a temperature, $T_{cd\text{-}exit}$, which is very close to the sink temperature, T_{sink}, and considerably lower than $T_{cd\text{-}in}$. The subcooled liquid then enters the liquid-transport line and undergoes heat loss to the ambient environment; thus, the subcooled liquid enters the evaporator at a temperature, $T_{ev\text{-}in}$, that is lower than $T_{cd\text{-}exit}$. Inside the evaporator, the subcooled liquid is heated to the saturation temperature and then evaporated. The saturated vapor exits the evaporator at T_{sat} and the cycle is completed. Similar behavior is also exhibited by all other curves shown in Figure 6.9.

For any given combination of T_{sink} and T_{amb}, when q_{app} is increased, T_{sat} increases, and the fluid temperature also increases at all other locations inside the LHP. However, as can be seen from the results in Figure 6.9, for a fixed sink temperature (for example, see dotted lines corresponding to T_{sink} = 42.16 °C), the temperature of the subcooled liquid exiting the condenser, $T_{cd-exit}$, is almost independent of q_{app}: Again, this result confirms that the subcooled portion of the condenser is long enough to ensure that the condensed liquid cools down to a temperature that is very close to T_{sink} for all conditions explored in this study. However, for any given combination of T_{sink} and T_{amb}, even though $T_{cd-exit} \cong T_{sink}$, when q_{app} is increased, the temperature at the exit of the liquid-transport line, T_{ev-in}, increases (albeit slightly); this is because the mass flow rate increases when q_{app} is increased, but the overall heat loss coefficient in the liquid-transport line remains almost unchanged.

As was expected and as is shown by the results in Figure 6.9, increasing the sink temperature has the effect of boosting up the average fluid temperature over the LHP

(dashed lines are higher in comparison to dotted lines for each value of q_{app}). However, as was discussed earlier, for a fixed value of q_{app}, when T_{sink} is increased, the convective heat transfer coefficient on the outer surface of the condenser pipe, h_{oil}, increases, the corresponding thermal resistance per unit length $\{R'_{oil} = 1/\{h_{oil}\pi(D_{cd} + 2t)\}$ decreases, the overall thermal conductance of the LHP increases, and the *slopes* of the T_{sat} vs. q_{app} curves (see Figure 6.5) decrease with increasing values of T_{sink}. Thus, at q_{app} = 400 W, the values of T_{sat} for the two sink temperatures (T_{sink} = 42.16 °C and 61.27 °C) are almost identical.

6.7 Pressure Drop in the Vapor-Transport Line

Values of the pressure drop associated with the fluid flow in the serpentine portion of vapor-transport line, denoted by ΔP_1 in Figure 6.10, were predicted in the computer simulations of the LHP and also measured in the experimental investigation. These results are presented and their implications are discussed in this section.

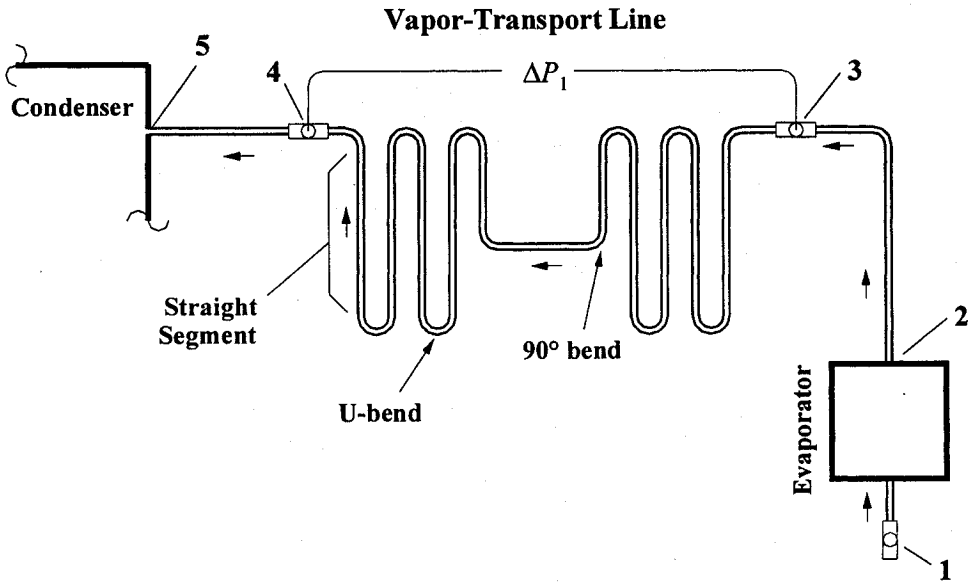

Figure 6.10: Schematic of the vapor-transport line of the LHP and related notation.

It is should be noted here that in most of the models of LHPs in the published literature, single-phase flow is assumed in the vapor-transport line. However, in many

applications of LHPs, the fluid temperature in the vapor-transport line is above that of the ambient environment, as is the case for the LHP investigated here: In such cases, the assumption of single-phase flow in the vapor-transport line is not necessarily correct. Thus, in the present study, the two-phase flow models presented in Chapter 5 were used to predict the pressure drops in the vapor-transport line.

6.7.1 Comparison of Experimental and Numerical Results

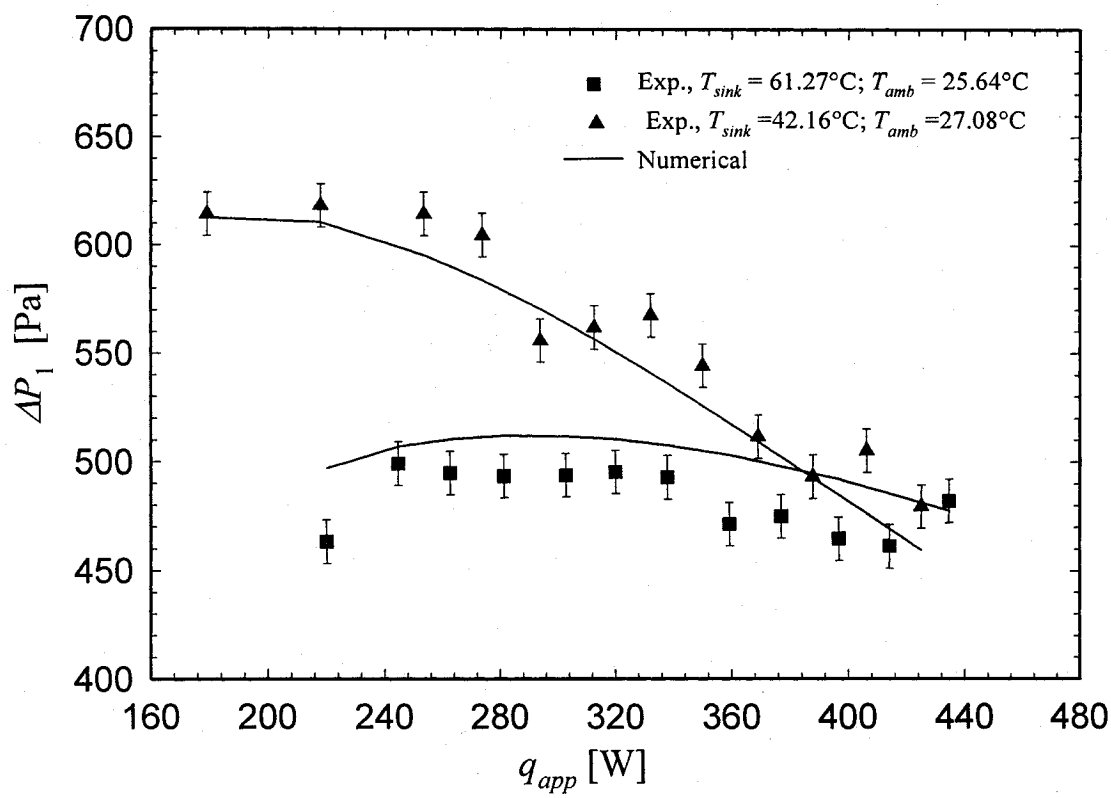

Figure 6.11: Variation of ΔP_1 with q_{app} : Experimental and numerical results.

In Figure 6.11, the variation of ΔP_1 with the power input to the evaporator, q_{app}, is presented for two combinations of the sink and ambient temperatures: T_{sink} = 42.16 °C and T_{amb} = 27.08 °C; and T_{sink} = 61.27 °C and T_{amb} = 25.64 °C. Similar results were also obtained for the intermediate combination of T_{sink} = 52.11 °C and T_{amb} = 26.09 °C, but they are not shown in Figure 6.11 in order to avoid cluttering. The experimental results

are shown with symbols, and corresponding numerical results are shown as solid lines. The vertical error bands shown in this figure are based on the calibration of the pressure transducer that was used to measure these data (Omega® model PX838-40WD10V). The uncertainties in the experimental data for q_{app} are the same as those for the corresponding values shown in Figure 6.3 (they are not reproduced in Figure 6.11 in order to avoid cluttering).

There is fairly good agreement between the numerical and experimental results presented in Figure 6.11. To provide a quantitative appreciation of the agreement between these results, the predicted values of ΔP_1 are plotted against the corresponding experimental values in Figure 6.12. As shown by the results presented in this figure, for the operational conditions considered in this work, the model predictions all within ±10.0% of the experimental measurements.

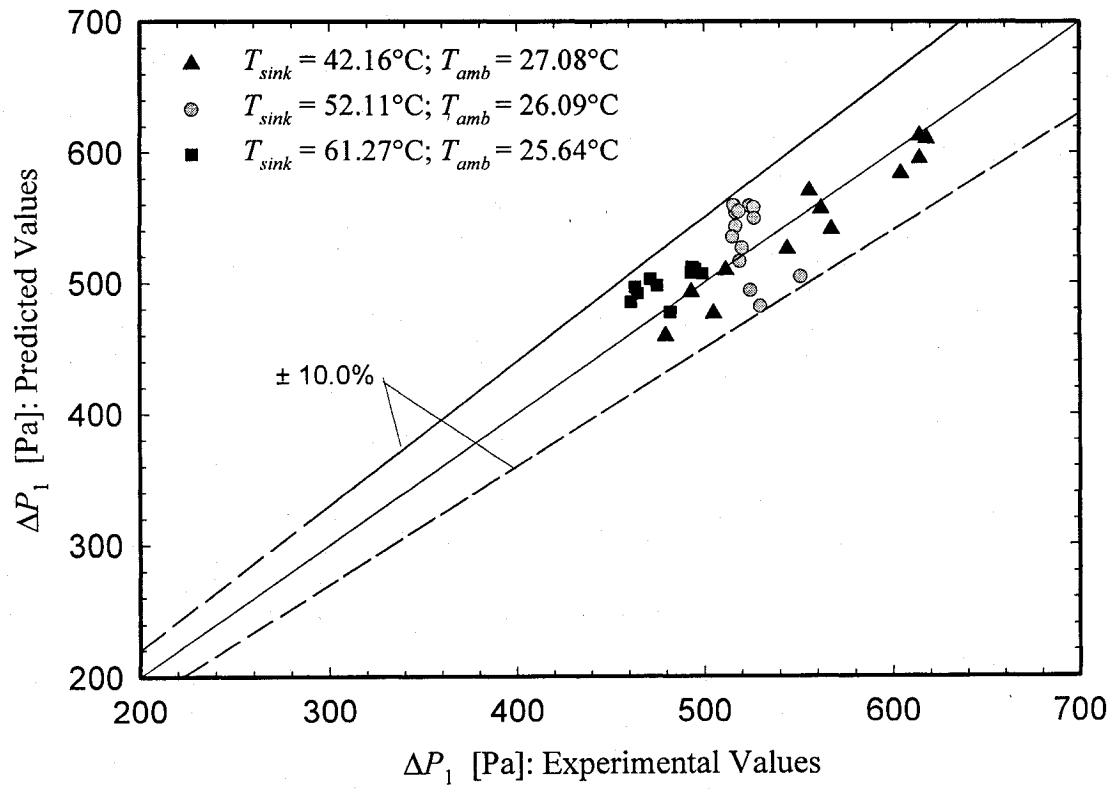

Figure 6.12: Comparison of predicted and experimental values of ΔP_1.

6.7.2 Effect of Increasing Power Input to the Evaporator, q_{app}

As q_{app} is increased for a fixed combination of T_{sink} and T_{amb}, the mass flow rate in the loop is increased and ΔP_1 may also be expected to increase. However, the experimental results presented in Figure 6.11 show that for each combination of T_{sink} and T_{amb}, ΔP_1 initially increases with q_{app} (for q_{app} < 260 W, approximately), but then decreases with increasing q_{app}. This behavior is also reflected in the numerical predictions obtained using the proposed network thermofluid. Thus, it is clear that parameters other than the mass flow rate also influence the variation of ΔP_1 with q_{app}.

In Chapter 5, it was shown that for the conditions considered in this study, the two-phase flow in the horizontal vapor-transport line corresponds to the stratified-flow regime: Thus, the vapor flows axially in the central region of the pipe (core), and the condensed liquid runs down the periphery of the pipe and moves at the bottom of the pipe in the direction of the vapor flow, but with relatively much lower velocity. When q_{app} is increased for a fixed combination of T_{sink} and T_{amb}, the saturation temperature at the exit of the evaporator, T_{sat}, increases: Thus, for the conditions considered in this work, the dynamic viscosity of the condensed liquid in the vapor-transport line decreases and its density also decreases (slightly); on the other hand, for the vapor in this line, the dynamic viscosity increases slightly, but the mass density decreases significantly. To illustrate these points quantitatively, for the combination T_{sink} = 42.16°C and T_{amb} = 27.08 °C, and q_{app} = 200 W and q_{app} = 400 W, the corresponding saturation temperatures and fluid (liquid and vapor) properties are given below in Table 6.2.

Table 6.2: Saturation temperatures and properties of the vapor and the liquid flowing in the vapor-transport line for T_{sink} = 42.16°C and T_{amb} = 27.08 °C , and q_{app} = 200 W and 400 W.

T_{sink}	q_{app}	T_{sat}	T_{sat}	ρ_g	ρ_l	μ_g	μ_l	k_g	k_l
°C	W	°C	K	kg/m^3	kg/m^3	kg/m-s	kg/m-s	W/m-°C	W/m-°C
42.16	200	78.2	351.35	0.27	972.74	1.115E-05	0.000361	0.0231	0.6689
	400	116.7	389.85	1.01	945.41	1.267E-05	0.000242	0.0263	0.6861

For the combination T_{sink} = 42.16°C and T_{amb} = 27.08 °C, when q_{app} is changed from 200 W to 400 W, the properties given in Table 6.2 show that the vapor density increases by a factor of 3.7; for these conditions, the numerical results show that the mass flow rate is increased from 7.8×10^{-5} kg/s to 1.5×10^{-4} kg/s, a factor of only 1.9; so the vapor velocity decreases (by about 50%). All of these changes collectively produce the variation of ΔP_1 with q_{app} exhibited by the results presented in Figure 6.11.

6.7.3 Effect of Increasing the Temperature of the Oil Bath, T_{sink}

As was discussed earlier (in Section 6.3), for a fixed value of q_{app}, when the temperature of the oil bath, T_{sink}, is increased, the convective heat transfer coefficient on the outer surface of the condenser pipe, h_{oil}, increases; the corresponding thermal resistance per unit length $\{R'_{oil} = 1/\{h_{oil}\pi(D_{cd}+2t)\}$ decreases; the overall thermal conductance of the LHP increases; the *slope* of the T_{sat} vs. q_{app} curve (see Figure 6.5) decreases; and $(T_{sat} - T_{sink})$ decreases. The variations of ΔP_1 with T_{sink} for fixed values of q_{app} (see Figure 6.11) reflect these changes in T_{sat} and its influence on the properties of the liquid and vapor phase (as was discussed in the previous subsection).

The variations of the pressure drop in the two-phase region of the condenser of the LHP are expected to be similar to those discussed above for ΔP_1. However, the quality undergoes significant change in the condenser (from about 0.9 to 0.0). Experimental measurements of the variation of the pressure drop in the two-phase region of the condenser with changes in q_{app} and T_{sink} are needed to enhance the published literature on this particular portion of the LHP and provide checks on predictions provided by related mathematical models. Such measurements are suggested as a possible extension of this work.

6.8 PRESSURE DROPS OVER DIFFERENT ELEMENTS OF THE LHP

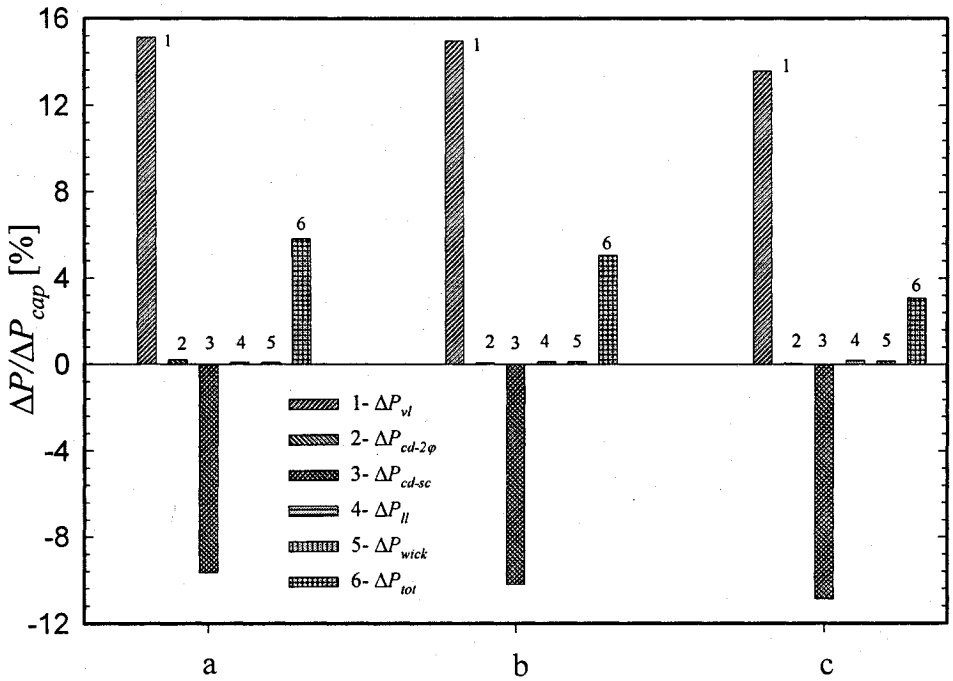

Figure 6.13: Predictions of steady-state pressure drops over different elements of the LHP for T_{sink} = 42.16 °C and T_{amb} = 27.08 °C: (a) q_{app} = 200 W ($\Delta P_{cap,\max}$ = 4618 Pa); (b) q_{app} = 300 W ($\Delta P_{cap,\max}$ = 4360 Pa); and (c) q_{app} = 400 W ($\Delta P_{cap,\max}$ = 4082 Pa).

Steady-state pressure drops predicted by the proposed network thermofluid model over different elements of the LHP are presented in Figure 6.13 for the combination T_{sink} = 42.16 °C and T_{amb} = 27.08 °C, and three different values of the power input to the evaporator: q_{app} = 200 W (T_{sat} = 78.2 °C), 300 W (T_{sat} = 97.1 °C), and 400 W (T_{sat} = 116.7 °C). In particular, for each of these three values of q_{app}, the following pressure drops normalized with respect to the corresponding maximum capillary pressure head, $\Delta P_{cap,\max}$, as defined in Eq. (5.90), are presented in Figure 6.13: Sum of pressure drops in the vapor grooves of the evaporator and the vapor-transport line ($\Delta P_{vl} / \Delta P_{cap,\max}$); pressure drop over the two-phase portion of the condenser pipe ($\Delta P_{cd-2\varphi} / \Delta P_{cap,\max}$); pressure drop over the subcooled (single-phase) portion of the condenser pipe ($\Delta P_{cd-sc} / \Delta P_{cap,\max}$); pressure drop over the liquid-transport line ($\Delta P_{ll} / \Delta P_{cap,\max}$); pressure drop as the liquid

flows through the wick ($\Delta P_{wick} / \Delta P_{cap,\max}$); and total pressure drop in the LHP ($\Delta P_{tot} / \Delta P_{cap,\max}$). The maximum capillary head, $\Delta P_{cap,\max}$, which is used to normalize the pressure drops presented in Figure 6.13, is a function of the liquid-vapor surface tension, the contact angle, and the maximum effective pore size of the wick, as given in Eq. (5.90). Thus, when q_{app} is increased, T_{sat} increases (as was discussed earlier), and $\Delta P_{cap,\max}$ decreases: The specific values of $\Delta P_{cap,\max}$ for each of the three aforementioned values of q_{app} are given in the title of Figure 6.13.

In Figure 6.13, the predictions of the aforementioned pressure drops for each value of q_{app} are presented as bar charts that are grouped together (the groups are denoted as *a*, *b*, and *c*). In each group, bars 1 to 5 represent pressure drops over different elements of the LHP, while the last column represents the total pressure drop (which is the sum of the pressure drops indicated by bars 1 to 5). As can be seen from this figure, the pressure drop in the vapor-transport line (bar 2) is higher than that in all other elements: This is because this line is made of a long pipe with many bends and fitting and it convey a two-phase (vapor-liquid) flow. The pressure drop in the two-phase part of the condenser (bar 2) is negligible in comparison to that in the vapor-transport line: This is because the two-phase mixture condenses in a relatively short length of the condenser pipe (about 10%) adjacent to its inlet, before the start of the bent (serpentine) portion (see Figure 4.1). In the subcooled (single-phase) region of the condenser, for all three groups, the pressure drop (bar 3) is negative: This is because the condenser pipe is sloped slightly downwards (about 1% from the inlet to the exit), the gravitational head dominates the frictional pressure drop, and the flow experiences an *increase* (gain, not drop) in the static pressure. The single-phase pressure drop in the liquid transport line (bar 4) is also negligibly small, for all three groups: This is because liquid flow velocity is very low, and thus, even with the many bends in this line, the pressure drop is almost negligible compared to that in the vapor-transport line. Similarly, in the wick, the liquid flow velocity is very low, and the flow length is also quite small (thickness of the wick is about 6.5 mm), so the pressure drop (bar 5) is negligibly small. It is also clear from the results shown in Figure 6.13 that each of the aforementioned pressure drops, including the total pressure drop, is a small

fraction (less than 16%) of the maximum capillary head. Thus, for all cases considered, this LHP operated well below its capillary limit.

The results in Figure 6.13 also show that when q_{app} is increased (that is, moving from groups *a* to *c* in this figure), the total pressure drop decreases. This is mainly because of significant reductions in the pressure drop in the vapor-transport line with the aforementioned increase in q_{app}, as was already noted in earlier discussions related to Figure 6.11.

6.9 Distribution of Friction Pressure Drop along the Vapor-Transport Line

Predictions of the distribution of friction pressure drop along the length of the vapor-transport line of the LHP (between points 2 and 5 in the schematic shown in Figure 6.10) were obtained using the proposed network thermofluid model. These predictions for the combination T_{sink} = 42.16 °C and T_{amb} = 27.08 °C are presented in Figure 6.14 for two values of the power input to the evaporator: q_{app} = 250 W and 400 W.

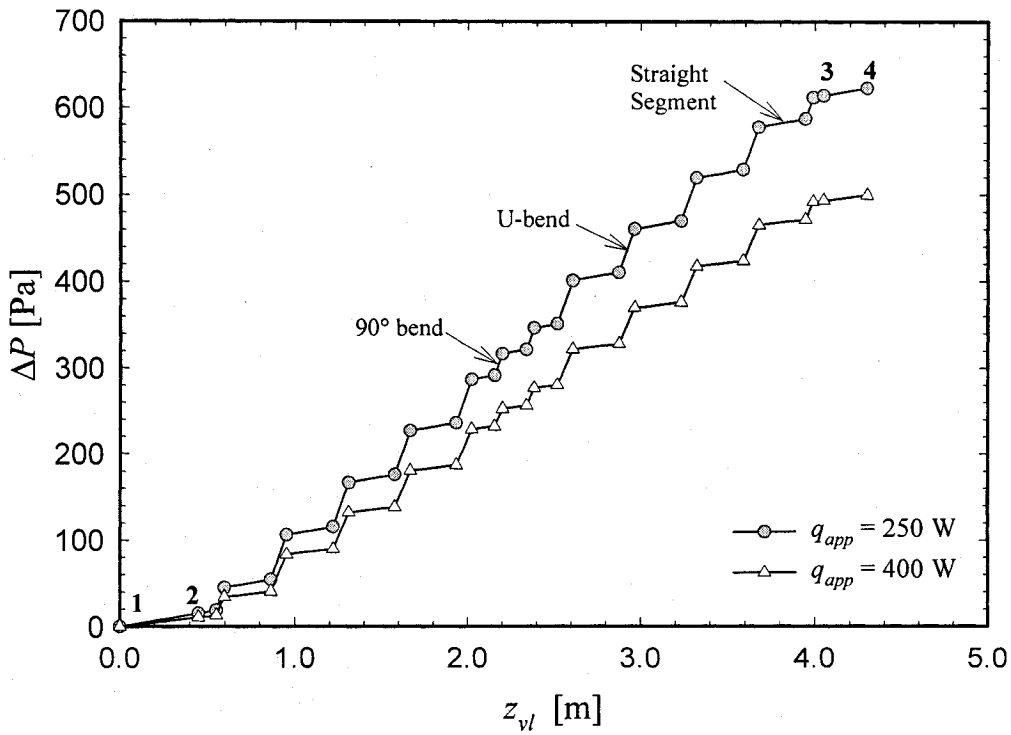

Figure 6.14: Predictions of the steady-state distribution of friction pressure drop along the vapor-transport line (T_{sink} = 42.16 °C and T_{amb} = 27.08 °C).

Each piecewise-linear segment of the curves presented in Figure 6.14 corresponds to a physical segment of vapor-transport line schematically portrayed in Figure 6.10: In both these figures, the first and last segments of the vapor-transport line are shown as 2-3 and 4-5, respectively. Straight-line segments corresponding to friction pressure drops in a 90° bend, a U-bend, and a straight portion of the vapor-transport line are also indicated in Figure 6.14, and the three corresponding physical portions of this line are shown in Figure 6.10.

As was described in Chapter 5, in the proposed network thermofluid model, average values of the streamwise pressure gradient are calculated in each of the bent and the straight segments of the vapor-transport line, and then assumed to prevail over these segments. Thus, the distribution of friction pressure drop is shown as a composite of piecewise-linear segments in Figure 6.14. The segments have a steeper slope in the bent segments than in the straight segments of the vapor-transport line. In reality, the presence of the bends affects the entrance length of the downstream straight segments: For *single-phase* pressure drop in bends, the length affected could be 10 to 30 times the inside diameter of the pipe diameter [Joshi and Shah (1987); Ohadi et al. (1990)]. In the LHP considered in this investigation, the lengths of the straight segments of the vapor-transport line are all lower than 28 times the inside diameter of the pipe. Thus, the distribution of friction pressure drop in a straight segment is affected by an upstream 90° bend or a U-bend, if one exists, and the transition of the pressure drop from the bent to the straight parts would be smooth, rather than piecewise linear as shown in Figure 6.14. However, as the correlations used in the model presented in Chapter 5 were fitted to experimental data for the bent parts, the aforementioned effects are indirectly included via increased contributions attributed to the bent parts. Therefore, even though the piecewise-linear curves in Figure 6.14 do not represent the *shapes* of the actual pressure distributions in the corresponding segments of the vapor-transport line, the friction pressure drop *over* each of these segments is well estimated.

As is shown by the results in Figure 6.14, the overall pressure drop for q_{app} = 250 W is higher than that for q_{app} = 400 W, for the conditions given in the title of this figure. This is in accordance with the experimental data presented in Figure 6.11. The possible reasons for this behavior were discussed in Section 6.7.

6.10 CONDENSATION PROCESSES

In the LHP considered in this study, partial condensation occurs in the vapor-transport line, and full condensation is achieved in the two-phase portion of the condenser pipe. In the vapor-transport line, the fluid looses heat to the ambient environment through the pipe wall and the insulation on its outside surface. In the condenser, the two-phase fluid flow looses heat to the constant-temperature thermal sink (that is, to the oil bath in which it is immersed), through the condenser pipe. Predictions of these condensation processes, obtained using the proposed steady-state network thermofluid model, are presented in this section.

For T_{sink} = 42.16 °C and T_{amb} = 27.08 °C, distributions of the rate of heat transfer loss (normalized with respect to q_{app}) from the entrance of the vapor-transport line (point 2 in Figure 6.10) to the zero-quality (complete condensation) point in the condenser pipe are presented in Figure 6.15 for two values of the power input, q_{app} = 250 W and 400 W.

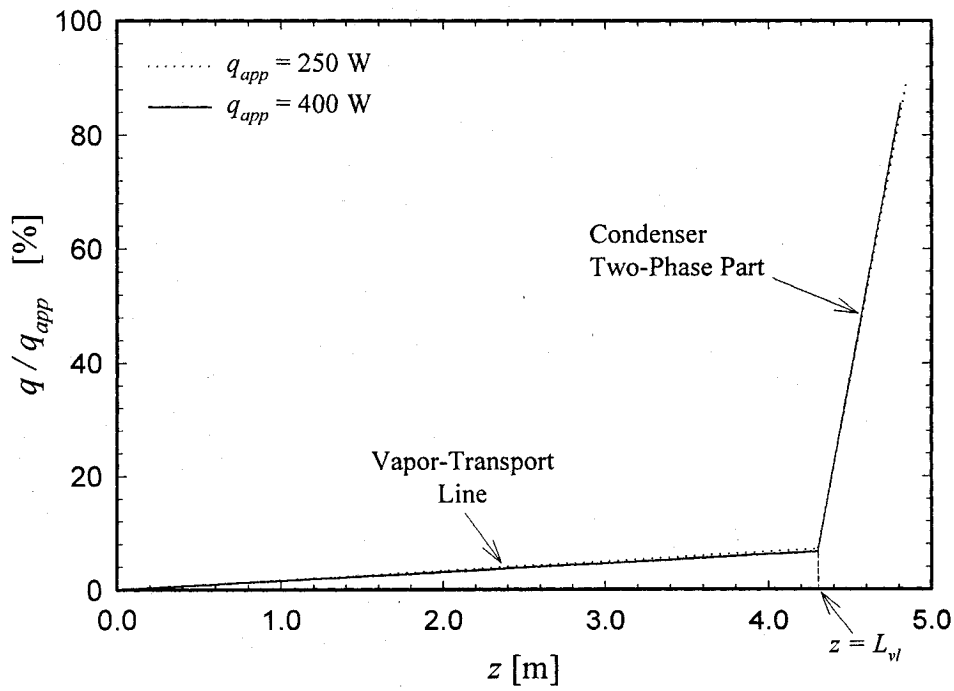

Figure 6.15: Distributions of the variation of the rate of heat loss from the entrance of the vapor-transport line to the zero-quality point in the condenser for T_{sink} = 42.16 °C and T_{amb} = 27.08 °C.

For a given combination of T_{sink}, T_{amb}, and q_{app}, the saturation temperature in the vapor-transport line and also in the two-phase portion of the condenser pipe is almost uniform (as the pressure drops over these portions of the LHP are small compared to the mean absolute pressure): Thus, the driving temperature difference for heat loss in each of these segments of the LHP is constant for all practical purposes. Furthermore, in these two-phase flow regions, the internal condensation heat transfer coefficients are relatively very high: Thus, the internal thermal resistances in these regions are small compared to those of the insulation material outside the vapor-transport line and the forced convection on the outer surface of the condenser pipe immersed in the constant-temperature oil bath. As a result, the overall thermal resistances for each of these two-phase flow segments can be considered constant for all practical purposes. Thus the distributions of q_{loss}/q_{app} in each of these segments of the LHP for both power inputs (q_{app} = 250 W and 400 W) are essentially linear and almost the same, as is seen from the results presented in Figure 6.15. Furthermore, the corresponding distributions of quality for these conditions are also essentially linear and almost identical, as shown by the results presented in Figure 6.16.

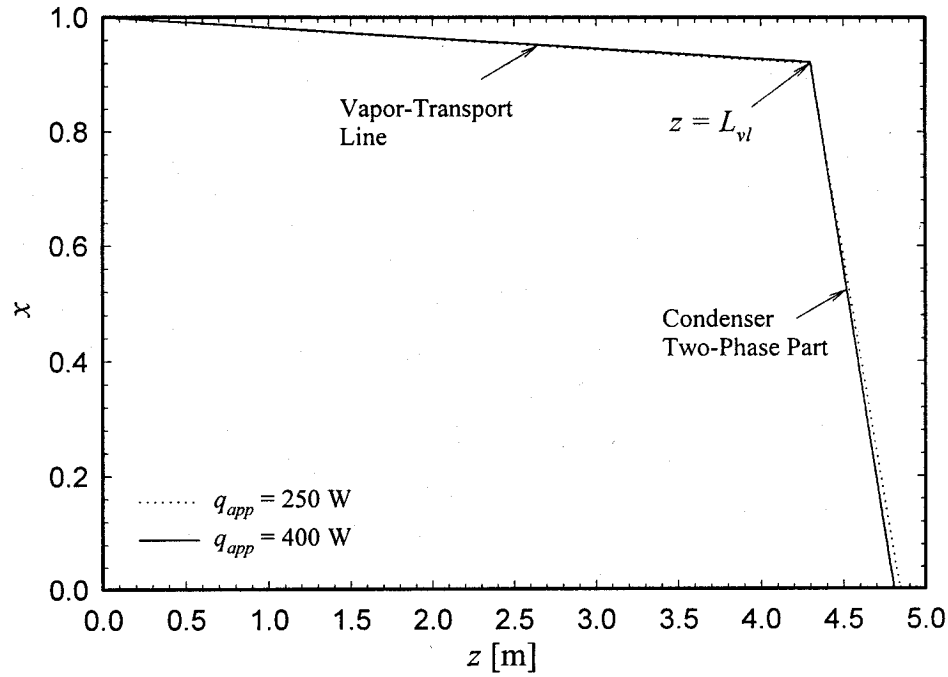

Figure 6.16: Distributions of the quality in the vapor-transport line and in the two-phase portion of the condenser for T_{sink} = 42.16 °C and T_{amb} = 27.08 °C.

Chapter 7:
Conclusion

This final chapter is divided into the following two sections: (1) a review of the thesis and its contributions (highlighted in *italics*); and (2) some suggestions for extensions of this work.

7.1 Review of the Thesis and its Contributions

Complementary computational and experimental investigations of fluid flow and heat transfer aspects of loop heat pipes (LHPs) were presented in the previous chapters of this thesis. The main goal of this work was to formulate and develop cost-effective mathematical models and numerical solution methods for computer simulations of LHPs, and validate these models and methods using the results of complementary experiments.

The motivation and the overall goal of this work, some background information on heat pipes (HPs), loop heat pipes (LHPs), and capillary pumped loops (CPLs), the specific objectives of this thesis, and a review of the pertinent published literature were presented in Chapter 1.

In Chapter 2, *a basic network thermofluid model of conventional LHPs operating under steady-state conditions* was proposed, implemented, tested, and applied. This model is based on relatively rudimentary treatments of the fluid flow and heat transfer phenomena in the vapor- and liquid-transport lines, and also in the two-phase and single-phase portions of the condenser. The aim in this part of the research was to not only illustrate the main steps in the formulation of network thermofluid models of LHPs, but also to formulate a model that is capable of at least qualitatively accurate predictions. The capabilities of this basic model were assessed by applying it to an LHP similar to one investigated experimentally by Kaya and Hoang (1999). A comparison of the predicted results with the experimental results of Kaya and Hoang (1999) confirmed that the proposed model is indeed capable of qualitatively accurate predictions. In this sense, it could serve as a tool in preliminary designs of LHPs. *This proposed basic model is considered as one of the main contributions of this thesis.*

In Chapter 3, descriptions were provided of experimental apparatus and procedures that were designed and implemented for measurements of the following properties of sintered powder-metal porous plates (that are used as wicks in LHPs): Porosity; maximum effective pore size; effective permeability; and effective thermal conductivity when saturated with a liquid (distilled water in this work). These experimental apparatus and procedures were applied to two sintered powder-metal porous plates (nominally 6.35 mm thick), one made of nickel 200 and the other of stainless steel 316, and the results were presented and discussed. A *new apparatus was designed, constructed, used for measurements of the maximum pore size*. This apparatus is an improved version of that designed and used by Alexander (1972): It is simple to construct, easy to use, and reliable. *The pore sizes measured under so-called "rising" and "falling" conditions were discussed, and it was argued that they represent the minimum and maximum effective pore sizes, respectively.* The apparatus that was designed, constructed, and used for measurements of the *effective permeability* had two different test cells: One for cylindrical (disk-shaped) test samples of 22.23 mm diameter (nominal); and the other for 127 mm x 127 mm (nominal) square test samples. The results obtained showed that it is important to account for blockage effects (and the resultant multidimensional flow within the test samples) caused by sealing gaskets used in the test cell: *A novel experimental/numerical method that accounts for these blockage effects was devised and successfully used.* The *apparatus* that was designed, constructed, and used *for measurements of the effective thermal conductivity of water-saturated sintered powder-metal plates* was also somewhat novel, in the sense that it could provide data *in the temperature range 20 °C to 150 °C*. This apparatus was first successfully benchmarked, and then used to obtain measurements of the effective thermal conductivity of the aforementioned sintered powder-metal porous plates saturated with distilled: These experimental measurements were used to fine-tune *a new empirical correlation for the prediction of the effective thermal conductivity of liquid-saturated sintered powder-metal porous materials*. This proposed empirical correlation was formulated by extending the theoretical ideas proposed by Hadley (1986). *All of the aforementioned aspects presented in italics are also considered as part of the main contributions of this thesis.*

The design and construction of *an LHP with a flat (plate-type) evaporator* and fixed active mass of working fluid were described in Chapter 4. This LHP was run with a wick made of a sintered powder-metal stainless steel plate. *Distilled water* was used as the *working fluid.* The *vapor-transport line*, the *condenser pipe*, and the *liquid-transport line* were *all designed with several smooth 90° and 180° (U) bends* (see Figure 4.1), to mimic conditions that could be encountered in practical applications of LHPs. In addition, the *vapor-transport line was well insulated, but still allowed partial condensation of the vapor* for the conditions explored in the experimental investigation: Again, this was done to mimic conditions that may be encountered in practical applications of LHPs. The *LHP* was *instrumented to obtain measurements of* not only the *temperature of the working fluid* at several important points in the flow circuit, but also the *pressure differences across the evaporator* (ΔP_2 in Figure 4.1) and *the serpentine part of the vapor-transport line* (ΔP_1 in Figure 4.1). *Full details of the geometry, materials, effective properties of the water-saturated wick (porosity, maximum effective pores size, effective permeability, and effective thermal conductivity) and operating conditions of this LHP are provided* in Chapters 3, 4, and 6. In the published literature, there is a paucity of data on LHPs that have a flat evaporator and are operated with water as the working fluid; experimental measurements of the aforementioned pressures drops are also scarce; and full details of the geometry, effective properties of the wick, and operating conditions are difficult, if not impossible, to find. In this context, all of the aforementioned aspects presented in italics ensure that the results of this experimental investigation augment the repertoire of published experimental data on LHPs*: Thus, this LHP and the experimental results are considered as part of the main contributions of this thesis.*

In Chapter 5, *an extended* version of the basic *network thermofluid model* (presented in Chapter 2) was described and adapted for simulations *of the LHP* presented in Chapter 4. As was discussed in Chapter 4, in the LHP considered here (see Figures 4.1 and 5.1), after charging (that is, filling it with the working fluid), the external two-phase reservoir is isolated and the active working fluid mass in the loop remains fixed. The proposed enhanced network thermofluid model of this LHP is *specially designed to allow the imposition of* this *requirement* (namely, *conservation of the active fluid mass inside the loop*). *Procedures for calculations of the pressure drop in the two-phase region of the*

condenser and the heat exchange with the ambient environment from (or to) the fluid in the vapor- and liquid-transport lines, which are neglected in most of the network thermofluid models of LHPs in the published literature, *are included* in the new model. Furthermore, *a special procedure is proposed and incorporated for estimating the augmented pressure drops associated with fluid flow (single- and two-phase) through the bent portions of the serpentine vapor-transport line* (see Figure 5.1 and 5.7). This special procedure was essential for obtaining accurate simulations, because a significant portion of the overall pressure drop in the LHP considered in this work occurred in the vapor transport line. The aforementioned two-phase flow and heat transfer procedures and the special procedure for augmenting pressure drops in bent portions of the vapor-transport line could be especially useful in simulations of miniature or micro LHPs, in which heat losses from the vapor-transport line are difficult to curtail, so partial condensation of the vapor is inevitable. *In the light of the above-mentioned enhanced features (presented in italics), the proposed network thermofluid model is considered as another main contribution of this work.*

The *results of both the experimental and computational investigations* of the above-mentioned LHP (see schematic illustrations in Figures 4.1 and 5.1) were presented, compared, and discussed in Chapter 5. The comparisons presented in this chapter show that proposed network thermofluid model provides predictions that are within ±10% of the experimental results. These results *and the related discussions are collectively considered a part of the main contributions of this thesis.*

In summary, the proposed models and numerical solution methods contain several novel features. They are relatively simple but effective (they yield predictions that are quite reliable); thus, they may be considered suitable for use in the design and optimization of LHPs. The experimental apparatus and procedures proposed for measurements of the maximum effective pore size, the effective permeability, and the effective thermal conductivity of water-saturated sintered powder-metal plates also incorporate several novel features. In addition, a new empirical correlation has been proposed for the prediction of the effective thermal conductivity of water-saturated sintered powder-metal plates. Finally, the experimental results pertaining to the LHP

considered in this thesis are a useful augmentation of similar data in the published literature.

7.2 Suggestions for Extensions of this Work

The results of the experimental and computational investigations that were presented in Chapter 6 are encouraging enough (the author believes) to warrant some extensions of this work. A few suggestions in this regard are given in the remainder of this section.

The enhanced thermofluid model proposed in Chapter 5 was used in this work only for simulations of the LHP proposed in Chapter 4: The objective was to assess its capabilities by comparing its predictions to the results of the experimental investigation. This LHP had a flat evaporator (without an integrated compensation chamber) and a fixed active mass of working fluid. It would be worthwhile to amalgamate the enhanced features of this model (namely, the two-phase flow and heat transfer formulations and also the procedure for calculating the enhanced pressure losses in bends) with the key features of the basic network thermofluid model of LHPs proposed in Chapter 2. The result would be a network thermofluid model that could be used to simulate LHPs with either cylindrical or flat evaporators (either with or without an integrated compensation chamber), partial condensation of vapor in the vapor-transport line, and bends in the vapor- and liquid-transport lines and the condenser pipe. Incorporation of procedures to handle condenser designs other than those consider is this work would also enhance the usefulness of the proposed model as a design tool.

It would be worthwhile to extend the proposed steady-state network thermofluid models to allow simulations of LHPs operating in unsteady modes, such as startup, power-down, and power-up. Some guidance for such extensions could be obtained, for example, from the works of Platel et al. (1996), Li and Ochterbeck (1999), Muraoka et al. (1998, 2001), Kaya and Ku (2003), and Furukawa (2006). Hybrid network thermofluid models, that combine quasi-one-dimensional approaches and multidimensional computational fluid dynamics methods, could also prove quite fruitful. Some guidance in this regard could be obtained from the work of Bernier and Baliga (1992b).

In the experimental investigation, the LHP described in Chapter 4 was run with distilled water and only one wick made from a stainless steel sintered powder-metal plate.

It would be useful to obtain additional experimental data with other fluids commonly used in LHPs (such as ammonia, ethanol, and refrigerants) and also other sintered powder-metal stainless steel porous plates.

In the enhanced network thermofluid model presented in Chapter 5, a special procedure was incorporated to calculate the augmentation of pressure drops in bends, in both single- and two-phase flows. However, similar procedures for the calculation of augmented heat transfer rates in bends were not incorporated, as they were not needed: The total rate of heat loss from the fluid to the ambient environment in the vapor-transport line was always less than 10% of the power input to the evaporator; the corresponding overall thermal resistance was dominated by that of the insulation outside this line; and thus, ignoring heat transfer augmentation in the bends did not have any serious consequences. Furthermore, in the condenser, full condensation took place within the initial straight portion of the pipe, so the bends did not affect the corresponding two-phase heat transfer; and in the single-phase (subcooled liquid) region, the liquid velocity was so low that the bends were inconsequential. However, to enhance the applicability of this model, it would be useful to incorporate procedures to account for heat transfer augmentation in bends.

Useful information on procedures for calculating the augmentation of single-phase forced convection in bends is available in work of Ohadi et al. (1990) and in the review article by Joshi and Shah (1987). Information on procedures for calculating the augmentation of two-phase (liquid-vapor) forced convection in bends is relatively scarce: Some rudimentary treatments have been reviewed in the book by Webb and Kim (2005), and work on condensation heat transfer in a microfin tube with a U-bend has been reported by Cho and Tae (2001). In this context, it would be useful to conduct some fundamental experimental work on augmentation of two-phase (liquid-vapor) forced convection in bends. It should also be noted that most of the published experimental works on two-phase (liquid-vapor) flow and heat transfer pertain to applications in heating, ventilating, and air-conditioning (HVAC) systems, and thus the mass fluxes are much higher than those encountered in LHPs: Some published works related to two-phase flow and heat transfer at lower mass fluxes have started appearing [Coleman and Garimella (2003), Wang et al. (2003), Wang et al. (2003a, 2003b), and Chen et al.

(2004a, 2004b, 2005)], but there is an urgent need for some original fundamental experimental investigations of these phenomena.

Experiments aimed at visualization of the fluid flow and heat transfer processes in the passages of LHPs would also be very useful. Guidance for such experiments could be obtained from the works of Bernier and Baliga (1992a), Lagana (1997), and Cimbala et al. (2004). Another improvement to the experimental investigation would be to incorporate instrumentation for measurements of flow rates of the working fluid in the LHP. A review article by Oddie and Pearson (2004) could provide some useful ideas in this regard.

It would also be very interesting and useful to conduct experiments on LHPs with multiple evaporators. The works Ku (1998) and Yun et al. (1999) could be of some interest in this regard.

In closing, the author would like to express his hope that this thesis will aid ongoing efforts to improve LHPs, at least in some small way, and encourage other students and researchers to undertake some of the above-mentioned extensions.

References

Agarwal, S.S., Gregory, G.A., and Govier, G.W. (1973), "An Analysis of Horizontal Stratified Two-Phase Flow in Pipes", *Canadian Journal of Chemical Engineering*, Vol. 51, pp. 280-286.

Alazmi, B. and Vafai, K. (2000), "Analysis of Variants within the Porous Media Transport Models", *ASME Journal of Heat Transfer*, Vol. 122, pp. 303-326.

Alexander, E.J. Jr. (1972), *Structure-Property Relationships in Heat Pipe Wicking Materials,* Ph.D. Thesis, Department of Chemical Engineering, North Carolina State University.

ASHRAE Fundamentals (2005), *Two-Phase Flow*, Chapter 4, American Society of Heating, Refrigerating, and Air-Conditioning Engineers, Inc, pp. 1-17.

ASHRAE Standard 41.5-75 (1976), *Standard Measurement Guide: Engineering Analysis of Experimental*, American Society of Heating, Refrigerating, and Air-Conditioning Engineers, Inc.

Atabaki, N. and Baliga, B.R. (2003), "Steady-State Operation of a Loop Heat Pipe: Network Thermofluid Model and Results", *Proc. ASME International Mechanical Engineering Congress & Exposition*, Paper # IMECE2003-43968, pp. 1-13, Washington, D.C., November 16-21.

Atabaki, N. and Baliga, B.R. (2005a), "Determination of Maximum Effective Pore Size of Sintered Porous Metal Plates", *20th Canadian Congress of Applied Mechanics, CANCAM 2005*, pp.236-237, McGill University, Montreal, Canada, May 30 - June 2.

Atabaki, N. and Baliga, B.R. (2005b), "Measurement of Bulk Temperature in Thermally Developed Laminar Flows in Pipes", *20th Canadian Congress of Applied Mechanics, CANCAM 2005*, pp.205-206, McGill University, Montreal, Canada, May 30 - June 2.

Avallone, E.A. and Baumeister III, T. (1987), *Mark's Standard Handbook for Mechanical Engineers*, Chapter 4, pp. 38-39, McGraw-Hill, New York.

Awwad, A., Xin, R.C., Dong, Z.F., Ebadian, M.A., and Soliman, H.M. (1995), "Measurement and Correlation of the Pressure Drop in Air-Water Two-Phase Flow in Horizontal Helicoidal Pipes", *International Journal of Multiphase Flow,* Vol. 21, pp. 607-619.

Bahrami, M., Yovanovich, M.M., and Culham, J.R. (2004), "Compact Analytical Models for Effective Thermal Conductivity of Rough Spheroid Packed Beds", *Proc. ASME International Mechanical Engineering Congress*, Anaheim, CA, November 13-19.

Baker, O. (1954), "Simultaneous Flow of Oil and Gas", *Oil and Gas Journal*, Vol. 53, pp. 185-195.

Baliga, B.R. (1997), "Control-Volume Finite Element Methods for Fluid Flow and Heat Transfer", in *Advances in Numerical Heat Transfer*, W.J. Minkowycz, and E.M. Sparrow (Editors), Taylor & Francis, Washington, D.C., Vol. 1, Chapter 3, pp. 97-135.

Baliga, B.R. and Atabaki, N. (2006), "Control-Volume-Based Finite Difference and Finite Element Methods", in *Handbook of Numerical Heat Transfer*, 2nd Edition, W.J. Minkowycz, E.M. Sparrow, and J.Y. Murthy (Editors), Chapter 6, John Wiley, New York.

Bankston, C.A. and McEligot, D.M. (1970), "Turbulent and Laminar Heat Transfer to Gases with Varying Properties in the Entry Region of Circular Ducts", *International Journal of Heat and Mass Transfer*, Vol. 13, pp. 319-344.

Barnhart, J. (1992), *An Experimental Investigation of Flow Patterns and Liquid Entrainment in a Horizontal-Tube Evaporator,* Ph.D. Thesis, Department of Mechanical and Industrial Engineering, University of Illinois at Urbana-Champaign.

Bassi, R. and Bansal, P.K. (2003), "In-Tube Condensation of Mixtures of R134a and Oil: Empirical Correlations", *International Journal of Refrigeration*, Vol. 26, pp. 402-409.

Batchelor, G.K. (1967), *An Introduction to Fluid Dynamics*, Cambridge University Press, Cambridge, U.K.

Batchelor, G.K. (1974), "Transport Properties of Two-Phase Materials with Random Structure", *Annual Review of Fluid Mechanics*, Vol. 6, pp. 227-255.

Batchelor, G.K. and O'Brien, R.W. (1977), "Thermal or Electrical Conduction through a Granular Material", *Proceedings of the Royal Society of London*, Vol. A355, pp. 313-333.

Bauer, T.H. (1993), "A General Analytical Approach toward the Thermal Conductivity of Porous Media", *International Journal of Heat and Mass Transfer*, Vol. 36, pp. 4181-4191.

Beavers, G.S. and Sparrow E.M. (1969), "Non-Darcy Flow Through Fibrous Porous Media", *Journal of Applied Mechanics,* pp. 711-714.

Bejan, A. (1995), *Convection Heat Transfer*, 2nd Edition, John Wiley, New York.

Bernier, M.A. and Baliga, B.R. (1992a), "Visualization of Upward Mixed-Convection Flows in Vertical Pipes Using a Thin Semitransparent Gold-Film Heater and Dye Injection", *International Journal of Heat and Fluid Flow*, Vol. 13, pp. 241-249.

Bernier, M.A. and Baliga, B.R. (1992b), "A 1-D/2-D Model and Experimental Results for a Closed-Loop Thermosyphon with Vertical Heat Transfer Sections", *International Journal of Heat and Mass Transfer*, Vol. 35, pp. 2969-2982.

Bienert, W.B. and Wolf, D.A. (1995), "Temperature Control with Loop Heat Pipe: Analytical Model and Test Results", *Proc. 9th International Heat Pipe Conference,* Los Alamos National Laboratory, Albuquerque, New Mexico.

Bird, R.B., Stewart, W.E., and Lightfoot, E.N. (2002), *Transport Phenomena*, 2nd Edition, John Wiley, New York.

Bonnefoy, M., Ochterbeck, J.M., Drolen, B.L., and Nikitkin, M.N. (2004), "Effective Thermal Conductivity of Saturated Sintered Nickel Loop Heat Pipe Wicks", *37th Thermophysics Conference*, AIAA Paper # 2004-2571, pp. 1-10, Portland, Oregon, June 28 – July 1.

Boomsma, K. and Poulikakos, D. (2001), "On the Effective Thermal Conductivity of a Three Dimensionally Structured Fluid-Saturated Metal Foam", *International Journal of Heat and Mass Transfer*, Vol. 44, pp. 827-836.

Bouré, J.A. and Delhaye, J.M. (1982), "General Equations and Two-Phase Flow Modeling", in *Handbook of Multiphase Systems, Section 1.2*, G. Hetsroni (Editor), McGraw-Hill, New York.

Brennen, C.E. (2005), *Fundamentals of Multiphase Flow*, Cambridge University Press, Cambridge, U.K.

Calmidi, V.V. and Mahajan, R.L. (1999), "The Effective Thermal Conductivity of High Porosity Fibrous Metal Foams", *ASME Journal of Heat Transfer*, Vol. 121, pp. 466-471.

Carey, V.P. (1992), *Liquid-Vapor Phase-Change Phenomena: An Introduction to the Thermophysics of Vaporization and Condensation Processes in Heat Transfer equipment*, Taylor & Francis, New York.

Cavallini, A., Censi, G., Del Col, D., Doretti, L., Longo, G.A., Rossetto, L., and Zilio, C. (2003), "Condensation Inside and Outside Smooth and Enhanced Tubes – A Review of Recent Research", *International Journal of Refrigeration*, Vol. 26, pp. 373-392.

Chang, S.W. (1990), "Porosity and Effective Thermal Conductivity of Wire Screens", *ASME Journal of Heat Transfer*, Vol. 112, pp. 5-9.

Chato, J.C. (1962), "Laminar Condensation Inside Horizontal and Inclined Tubes", *ASHRAE Journal*, Vol. 4, pp. 52-60.

Chen, C.K. and Tien, C.-L. (1973), "Conductance of Packed Sphere in Vacuum", *ASME Journal of Heat Transfer*, Vol. 95, pp. 302-308.

Chen, I.Y., Huang, J.C., and Wang, C.C. (2004a), "Single-Phase and Two-Phase Frictional Characteristics of Small U-Type Wavy Tubes", *International Communication in Heat and Mass Transfer*, Vol. 31, pp. 303-314.

Chen, I.Y., Wang, C-C., and Lin, S.Y. (2004b), "Measurements and Correlations of Frictional Single-Phase and Two-Phase Pressure Drops of R-410A Flow in Small U-Type return Bends", *International Journal of Heat and Mass Transfer*, Vol. 47, pp. 2241-2249.

Chen, I.Y., Won, C.C., and Wang, C.C. (2005), "Influence of Oil on R-410A Two-Phase Frictional Pressure Drop in a Small U-Type Wavy Tube", *International Communication in Heat and Mass Transfer*, Vol. 32, pp. 797-808.

Chi, S.W. (1976), *Heat Pipe Theory and Practice: A Sourcebook*, Hemisphere Publishing

Chisholm, D. (1967), "A Theoretical Basis for the Lockhart-Martinelli Correlation for Two-Phase Flow", *International Journal of Heat and Mass Transfer*, Vol. 10, pp. 1767-1778.

Cho, K. and Tae, S-J. (2001), "Condensation Heat Transfer for R-22 and R-407C Refrigerant-Oil Mixtures in a Microfin Tube with U-bend", *International Journal of Heat and Mass Transfer*, Vol. 44, pp. 2043-2051.

Cimbala, J.M., Brenizer, J.S., Chuang, A.P-Y., Hanna, S, Conroy, C.T., El-Ganayni, A.A., and Riley, D.R. (2004), "Study of a Loop Heat Pipe Using Neutron Radiography", *Applied Radiation and Isotopes,* Vol. 61, pp. 701-705.

Colebrook, C.F. (1939), "Turbulent Flow in Pipes, with Particular Reference to the Transition Region between the Smooth and Rough Pipe Laws", *Journal of the Institution of Civil Engineers*, Vol. 11, pp. 133-156.

Coleman, J.W. and Garimella, S. (2003), Two-Phase Flow Regimes in Round, Square, and Rectangular Tubes During Condensation of Refrigerant R134a", *International Journal of Refrigeration*, Vol. 26, pp. 117-128.

Collier, J.G. (1972), *Convection Boiling and Condensation*, McGraw-Hill, London.

Conte, S.D. and de Boor, C. (1972), *Elementary Numerical Analysis*, McGraw-Hill, New York.

Crapiste, G.H., Rotstein, E., and Whitaker, S. (1973), "General Closure Scheme for the Method of Volume Averaging", *Chemical Engineering Science*, Vol. 41, pp. 227-235.

Crowe, C.T. (2006), *Multiphase Flow Handbook*, Taylor & Francis, Boca Raton, Florida.

Cullimore, B.A. (1991), "Start Up Transients in Capillary Pumped Loops", *AIAA Paper No. 91-1374.*

Currie, I.G. (2003), *Fundamental Mechanics of Fluids*, 3rd Edition, McGraw-Hill, New York.

de Gennes, P.G. (1985), "Wetting: Statics and Dynamics", *Review of Modern Physics,* Vol. 57, pp. 827-863.

Dealy, J. and Wissbrun, K.F. (1990), *Melt Rehology and its Role in Plastics Processing*, Kluwer Academic Publishers, Boston.

Dickey, J.T. and Peterson G.P. (1994), "Experimental and Analytical Investigation of a Capillary Pumped Loop", *AIAA Journal of Thermophysics and Heat Transfer*, Vol. 8, pp. 602-607.

Dobson, M.K. (1994), *Heat Transfer and Flow Regimes During Condensation in Horizontal Tubes,* Ph.D. Thesis, Department of Mechanical and Industrial Engineering, University of Illinois at Urbana-Champaign.

Dobson, M.K. and Chato, J.C. (1998), "Condensation in Smooth Horizontal Tubes", *ASME Journal of Heat Transfer*, Vol. 120, pp. 193-213.

Drew, D.A. (1983), "Mathematical Modeling of Two-Phase Flow", *Annual Review of Fluid Mechanics*, Vol. 15, pp. 261-291.

Dul'nev, G.N. (1965), "Heat Transfer Through Solid Disperse Systems", *Journal of Engineering Physics,* Vol. 9, pp. 275-279.

Dullien, F.A.L. (1992), *Porous Media: Fluid Transport and Pore Structure*, 2nd Edition, Academic Press, San Diego.

Dunn, P. and Reay, D.A. (1982), *Heat Pipes*, 3rd Edition, Pergamon Press Ltd, New York.

Eckert, E.R.G. and Drake, R.M. (1971), *Analysis of Heat and Mass Transfer*, McGraw-Hill, New York.

Faghri, A. (1995), *Heat Pipe Science and Technology*, Taylor & Francis, Washington, DC.

Ferziger, J.H. and Peric, M. (1999), *Computational Methods for Fluid Dynamics*, 2nd Edition, Springer, New York.

Fox, R.F. and McDonald, A. (1998), *Introduction to Fluid Mechanics*, 5th Edition, John Wiley, New York.

Friedel, I. (1979), "Improved Friction Pressure Drop Correlations for Horizontal and Vertical Two-Phase Pipe Flow", *European Two-Phase Flow Group Meeting*, Paper E2, June, Ispra, Italy.

Furukawa, M. (2006), "Model-Based Method of Theoretical Design Analysis of a Loop Heat Pipe", *AIAA Journal of Thermophysics and Heat Transfer*, Vol. 20, pp. 111-121.

Garimella, S.V. and Sobhan, C.B. (2001), "Recent Advances in the Modeling and Applications of Nonconventional Heat Pipes", in *Advances in Heat Transfer*, Hartnett, J.P., and Irvine Jr., T.F. (Series Editors), Academic Press, Vol. 35, pp. 249-308.

Gaul, L., Kogl, M., and Wagner, M. (2003), *Boundary Element Methods for Engineers and Scientists*, Springer, Berlin, Germany.

Ghajar, A.J. (2005), "Non-Boiling Heat Transfer in Gas-Liquid Flow in Pipes – A Tutorial", *Journal of the Brazilian Society of Mechanical Sciences and Engineering*, Vol. 27, pp. 46-73.

Gnielinski, V. (1976), "New Equations for Heat and Mass Transfer in Turbulent Pipe and Channel Flow", *International Chemical Engineering*, Vol. 16, pp. 359-367.

Gnielinski, V. (1983), "Forced Convection in Ducts", in *Heat Exchanger Design Handbook*, E.U. Sclünder (Editor), Hemisphere, New York, pp. 2.5.1-2.5.3.

Goncharov, K.A., Golovin, O.A., and Kolesnikov, V.A. (2000), "Multi-Evaporator Loop Heat Pipe", *American Institute of Physics Conference Proceedings 504,* M.S. El-Genk (Editor), American Institute of Physics, New York, pp. 778-784.

Gorring, R.L., and Churchill, S.W. (1961), "Thermal Conductivity of Heterogeneous Materials", *Chemical Engineering Progress*, Vol. 57, pp. 53-59.

Gresho, P.M. and Sani, R.L. (2000), *Incompressible Flow and the Finite Element Method: Volume 2, Isothermal Laminar Flow*, John Wiley, New York.

Griffith, P. (1985), "Two-Phase Flow", in *Handbook of Heat Transfer Fundamentals*, 2nd Edition, W.M. Rohsenow, J.P. Hartnett, and E.N. Ganic (Editors), Chapter 13, pp. 1-41.

Grönnerud, R. (1979), "Investigation of Liquid Hold-Up, Flow-Resistance and Heat Transfer in Circulation Type Evaporators, Part IV: Two-Phase Flow Resistance in Boiling Refrigerants", Annexe 1972-1, *Bull. De l'Inst. Du Froid.*

Grover, G.M., Cotter, T.P., and Erickson, G.F. (1964), "Structures of Very High Thermal Conductance", *Journal of Applied Physics,* Vol. 35, pp. 1990-1991.

Hadley, G.R. (1986), "Thermal Conductivity of Packed Metal Powders", *International Journal of Heat and Mass Transfer,* Vol. 29, pp. 909-920.

Hamming, R.W. (1987), *Numerical Methods for Scientists and Engineers*, 2nd Edition, Dover Publications, New York.

Hinze, J.O. (1975), *Turbulence*, 2nd Edition, McGraw-Hill, New York.

Hoang, T.T. and Ku, J. (1996), "Hydrodynamic Aspects of Capillary Pumped Loops", SAE-96-1435, *Proc. SAE, 26th International Conference on Environmental Systems*, Monterey, CA.

Hsu, C. T. (2000), "Heat Conduction in Porous Media", in *Handbook of Porous Media*, K. Vafai and M. Dekker (Editors), Chapter 4, pp. 171-200.

Hsu, C. T., Cheng, P., and Wong, K.W. (1995), "A Lumped-Parameter Model for Stagnant Thermal Conductivity of Spatially Periodic Porous Media", *ASME Journal of Heat Transfer*, Vol. 117, pp. 264-269.

Incropera, F.P. and DeWitt, D.P. (2002), *Fundamentals of Heat and Mass Transfer*, 5th Edition, John Wiley, New York.

Irvine, T.F. and Hartnett, J.P., (1964 – 2004), *Advances in Heat Transfer*, Vols. 1 – 38, Academic Press, New York.

Jaluria, Y. and Torrance, K.E. (2003), *Computational Heat Transfer*, 2nd Edition, Taylor and Francis, Washington D.C.

Jaster, H. and Kosky, P.G., (1976) "Condensation Heat transfer in a Mixed Flow Regime", *International Journal of Heat and Mass Transfer*, Vol. 19, pp. 95-99.

Jones, O.C. (1976), "An Improvement in the Calculation of Turbulent Friction in Rectangular Ducts", *ASME Journal of Fluids Engineering*, Vol. 98, pp. 173-181.

Joshi, S.D. and Shah, R.K. (1987), "Convective Heat Transfer in Bends and Fittings", *Handbook of Single-Phase Convective Heat Transfer*, Edited by Kakac, S., Shah, R.K., and Aung, W. John Wiley, Chapter 10, pp.1-32, New York.

Kakac, S., Shah, R.K., and Aung, W. (1987), *Handbook of Single-Phase Convective Heat Transfer*, John Wiley, New York.

Karniadakis, G. and Sherwin, S.J. (2005), *Spectral/hp Element Method for Computational Fluid Dynamics*, 2nd Edition, Oxford University Press, Oxford, U.K.

Kaviany, M. (1999), *Principles of Heat Transfer in Porous Media*, 2nd Edition, Springer Verlag, New York.

Kaviany, M. (2001), *Principles of Convective Heat Transfer*, 2nd Edition, Mechanical Engineering Series, Springer-Verlag, New York.

Kaya, T. and Hoang, T.T. (1999), "Mathematical Modeling of Loop Heat Pipes and Experimental Validation", *AIAA Journal of Thermophysics and Heat Transfer,* Vol. 13, pp. 314-320.

Kaya, T. and Ku, J. (2003), "Thermal Operational Characteristics of a Small-Loop Heat Pipe", *AIAA Journal of Thermophysics and Heat Transfer,* Vol. 17, pp. 464-470.

Kays, W.M. and Crawford, M.E. (1993), *Convective Heat and Mass Transfer*, 3rd Edition, McGraw-Hill, New York.

Kays, W.M. and Perkins, H.C. (1973), "Forced Convection, Internal Flow in Ducts", in *Handbook of Heat Transfer*, W.M. Rohsenow, and J.P. Hartnett (Editors), Section 7, pp. 7-1 to 7-193.

Khandlikar, S.G., Shoji, M., and Dhir, V.K. (1999), *Handbook of Phase Change: Boiling and Condensation*, Taylor & Francis, New York.

Kiper, A.M., Feric, G., Anjum, M.I., and Swanson, T.D. (1990), "Transient Analysis of a Capillary Pumped Loop Heat Pipe", AIAA-90-1685, *Proc. AIAA/ASME 5th Joint Thermophysics and Heat Transfer Conf.*, Seattle, Washington.

Kiper, A.M., Swanson, T.D., and Mcintosh, R. (1988), "Exploratory Study of Temperature Oscillation Related to Transient Operation of a Capillary Pumped Loop Heat Pipe", *Proc. ASME National Heat Transfer Conf.*, Houston, Texas, pp. 353-359.

Kiseev, V.M., Belonogov, A.G., and Pogorelov, N.P. (1997), "Development of Two-Phase Loops with Capillary Pumps", SAE-97-2482, *Proc. SAE, 27th International Conference on Environmental Systems*, Lake Tahoe, Nevada.

Kleinstreuer, C. (2003), *Two-Phase Flow: Theory and Applications*, Taylor & Francis, New York.

Kline, S.J. and McClintock, F.A. (1953), "Describing Uncertainties in Single-Sample Experiments", *Mechanical Engineering*, January, pp. 3-8.

Ku, J. (1993), "Overview of Capillary Pumped Loop Technology", HTD-Vol. 236, *Proc. 29th National Heat Transfer Conf.*, Atlanta GA, pp. 1-17.

Ku, J. (1994), "Thermodynamic Aspects of Capillary Pumped Loop Operation", AIAA-94-2059, *Proc. AIAA/ASME 6th Joint Thermophysics and Heat Transfer Conf.*, Colorado Springs, CO.

Ku, J. (1998), "Capillary Pumped Loops with Multiple Parallel Starter Pumps", *Aerospace Engineering*, Vol. 18, pp. 45-50.

Kunii, D. and Smith, J.M. (1960), "Heat Transfer Characteristics of Porous Rock", *AIChE Journal*, Vol. 6, pp. 71-78.

Kunz, H.R., Langston L.S., Hilton B.H., Wyde S.S., and Nashick G.H. (1967), *Vapor-Chamber Fin Studies: Transport Properties and Boiling Characteristics of Wicks*, NASA Contract Report, NASA-CR-812.

LaClair, T.J. and Mudawar, I. (2000), "Thermal Transients in a Capillary Evaporator Prior to the Initiation of Boiling", *International Journal of Heat and Mass Transfer*, Vol. 43, pp. 3937-3952.

Lagana, A. (1997), "Mixed Convection Heat Transfer in Vertical, Horizontal and Inclined Pipes", *M.Eng. Thesis*, McGill University, Montreal.

Landau, L.D. and Lifshitz, E.M. (1987), *Fluid Mechanics*, Translated from the Russian edition by J.B. Sykes and W.H. Reid, Pergamon Press, Oxford, U.K.

Launder, B.E. and Sandham, N.D. (2002), *Closure Strategies for Turbulent and Transitional Flow*, Cambridge University Press, Cambridge, U.K.

Leonard, B.P. (1979), "A stable and Accurate Convective Modelling Procedure Based on Quadratic Upstream Interpolation", *Computational Methods in Applied Mechanics and Engineering*, Vol. 19, pp. 59-98.

Leonard, B.P. (1997), "Bounded Higher-Order Upwind Multidimensional Finite-Volume Convection-Diffusion Algorithms", in *Advances in Numerical Heat Transfer*, W.J. Minkowycz and E.M. Sparrow (Editors), Vol. 1, Chapter 1, pp. 1-57, Taylor & Francis, New York.

Leong, K.C., Liu, C.Y., and Lu, G.Q. (1997), "Characterization of Sintered Copper Wicks Used in Heat Pipes", *Journal of Porous Materials*, Vol. 4, pp. 303-308.

Levy, S. (1999), *Two-Phase Flow in Complex Systems*, John Wiley, New York.

Li, T. and Ochterbeck, J.M. (1999), "Effect of Wick Thermal Conductivity on Startup of a Capillary Pumped Loop Evaporator", AIAA-99-3446, *Proc. AIAA 33rd Thermophysics Conf.*, Norfolk, VA.

Lockhart, R.W. and Martinelli, R.C., (1949), "Proposed Correlation of Data for Isothermal Two-Phase, Two-Component Flow in Pipes", *Chemical Engineering Progress*, Vol. 45, pp. 39-48.

Macosko, C.W. (1994), *Rheology: Principles, Measurements, and Applications*, John Wiley, New York.

Mandhane, J.M., Gregory, G.A., and Aziz, K. (1974), "A Flow Pattern Map for Gas-Liquid Flow in Horizontal Pipes", *International Journal of Multiphase Flow*, Vol. 1, pp. 537-553.

Mandhane, J.M., Gregory, G.A., and Aziz, K. (1977), "Critical Evaluation of Friction Pressure-Drop Prediction Methods for Gas-Liquid Flow in Horizontal Pipelines", *Journal of Petroleum Technology*, Vol. 29, pp. 1348-1358.

Mantel, W.J. and Chang W.S. (1991), "Effective Thermal Conductivity of Sintered Metal Fibers", *AIAA Journal of Thermophysics and Heat Transfer,* Vol. 5, pp. 545-549.

Maxwell, J.C. (1954), *A Treatise on Electricity and Magnetism*, 3rd Edition, Vol. 1, Dover Publications, New York, (reprinted version of original printed by Oxford University Press in 1891).

Maydanik, Y.F. (2005), "Loop Heat Pipes", *Applied Thermal Engineering*, Vol. 25, pp. 635-657.

Maydanik, Y.F., Fershtater, Y.G., and Solodovnik, N.N. (1994), "Design and Investigation of Methods of Regulation of Loop Heat Pipes for Terrestrial and Space Applications", *SAE Paper No. 94-1407.*

Maydanik, Y.F. and Fershtater, Y.G. (1997), "Theoretical Basis and Classification of Loop Heat Pipes and Capillary Pumped Loops", *10th International Heat Pipe Conference,* Stuttgart, Germany, September.

Minkowycz, W.J., Haji-Sheikh, A., and Vafai, K. (1999), "On Departure from Local Equilibrium in Porous Media Due to Rapidly Changing Heat Source: The Sparrow Number", *International Journal of Heat and Mass Transfer*, Vol. 42, pp. 3373-3385.

Minkowycz, W.J. and Sparrow, E.M. (1997), *Advances in Numerical Heat Transfer,* Vol. 1, Taylor and Francis, Washington D.C., pp. 3373-3385.

Minkowycz, W.J. and Sparrow, E.M. (2000), *Advances in Numerical Heat Transfer,* Vol. 2, Taylor & Francis, Washington D.C.

Minkowycz, W.J., Sparrow, E.M., and Murthy, J.Y. (2006), *Handbook of Numerical Heat Transfer*, 2nd Edition, John Wiley, New York.

Mulholland, G., Gerhart, C., Gluck, D., and Stanley, S. (1999), "Comparison Between Analytical Predictions and Experimental Data for a Loop Heat Pipe", *American Institute of Physics Conference Proceedings 458,* M.S. El-Genk (Editor), American Institute of Physics, New York, pp. 805-810.

Müller-Steinhagen, H. and Heck, K. (1986), "A Simple Friction Pressure Drop Correlation for Two-Phase Flow in Pipes", *Chemical Engineering and Processing*, Vol. 20, pp. 297-308.

Muraoka, I., Ramos, F.M., and Vlassov, V.V. (1998) "Experimental and Theoretical Investigation of a Capillary Pumped Loop With a Porous Element in the Condenser", *International Communications in Heat and Mass Transfer*, Vol. 25, pp. 1085-1094.

Muraoka, I., Ramos, F.M., and Vlassov, V.V. (2001) "Analysis of the Operational Characteristics and Limits of a Loop Heat Pipe With Porous Element in the Condenser", *International Journal of Heat and Mass Transfer*, Vol. 44, pp. 2287-2297.

Nield, D.A. and Bejan, A. (2006), *Convection in Porous Media*, 3rd Edition, Springer-Verlag, New York.

Nikitkin, M. and Cullimore, B. (1998), "CPL and LHP Technologies: What Are the Differences, What Are the Similarities?" SAE-98-1587, *Proc. SAE, 28th International Conference on Environmental Systems*, Danvers, MA.

Nikitkin, M., Kotlyarov, E., and Serov, G. (1999), "Basics of Loop Heat Pipe Temperature Control", SAE-99-2012, *Proc. SAE, 29th International Conference on Environmental Systems*, Denver, CO.

Nitheanandan, T. and Soliman, H.M. (1994), "Analysis of the Stratified/Nonstratified Transitional Boundary in Horizontal and Slightly Inclined Condensing Flows", *Canadian Journal of Chemical Engineering*, Vol. 72, pp. 26-34.

Ochterbeck, J.M. and Peterson, G.P. (1997), "Modeling of Heat Transfer in Heat Pipes", in *Modeling of Engineering Heat Transfer Phenomena*, B. Sundén and M. Faghri (Editors), Computational Mechanics Publications, Southampton, UK and Boston, USA, Vol. 2, Chapter 7, pp. 175-212.

Oddie, G. and Pearson, J.R.A. (2004), "Flow-rate Measurement in Two-Phase Flow", *Annual Review of Fluid Mechanics*, Vol. 36, pp. 149-172.

Ofuchi, K. and Kunii, D. (1965), "Heat-Transfer Characteristics of Packed Beds with Stagnant Fluids", *International Journal of Heat and Mass Transfer*, Vol. 8, pp. 749-757.

Ogniewicz, Y. and Yovanovich, M.M. (1978), "Effective Conductivity of Liquid-Saturated Porous Beds of Spheres: Basic Cell Model with Constriction", *Progress in Astronautics and Aeronautics*, Vol. 60, pp. 209-228.

Ohadi, M.M., Sparrow, E.M., Walavalkar, A., and Ansari, A.I. (1990), "Pressure Drop Characteristics for Turbulent Flow in a Straight Circular Tube Situated Downstream of a Bend", *International Journal of Heat and Mass Transfer*, Vol. 33, pp. 583-591.

Oosthuizen, P.H. and Naylor, D. (1999), *An Introduction to Convective Heat Transfer Analysis*, McGraw-Hill, New York.

Ould Didi, M.B., Kattan, N., and Thome, J.R. (2002), "Prediction of Two-Phase Pressure Gradients of Refrigerants in Horizontal Tubes", *International Journal of Refrigeration*, Vol. 25, pp. 935-947.

Parker, M.L. (2000), *Modeling of Loop Heat Pipes with Applications to Spacecraft Thermal Control*, Ph.D. Thesis, Department of Mechanical Engineering, University of Pennsylvania.

Pastukhov, V.G., Maydanik, Y.F., Vershinin, C.V., and Korukov, M.A. (2003), "Miniature Loop Heat Pipes for Electronics Cooling", *Applied Thermal Engineering*, Vol. 23, pp. 1125-1135.

Patankar, S.V. (1980), *Numerical Heat Transfer and Fluid Flow*, Hemisphere Publishing Corp., Washington D.C.

Peric, M., Kessler, R., and Scheuerer, G. (1988), "Comparison of Finite-Volume Numerical Methods with Staggered and Co-Located Grids", *Computers & Fluids*, Vol. 16, pp. 389-403.

Peterson, G.P. (1994), *An Introduction to Heat Pipes. Modeling, Testing, and Applications,* John Wiley, New York.

Peterson, G.P. and Fletcher L.S. (1987), "Effective Thermal Conductivity of Sintered Heat Pipes Wicks", *AIAA Journal of Thermophysics and Heat Transfer,* Vol. 1, pp. 343-347.

Peyret, R. (2002), *Spectral Methods for Incompressible Viscous Flow*, Springer, Berlin, Germany.

Platel, V., Butto, C., Fudym, O., and Laurens, M. (1995), "Boucle fluide diphasique à pompage thermocapillaire: Etude expérimentale du fonctionnement et évaluation des performances", *Revue Générale de Thermique*, tome 34, n° 400-401, pp. 315-324.

Platel, V., Butto, C., Grandpeix, J.Y., and Joly, J.L. (1996), "Modèle d'évaporateur d'une boucle fluide diphasique à pompage capillaire", *Revue Générale de Thermique*, tome 35, pp. 434-449.

Pope, S.B. (2000), *Turbulent flows*, Cambridge University Press, Cambridge, U.K.

Prasad, V., Kladias, N., Bandopadhaya, A., and Tian, Q. (1989), "Evaluation of Correlations for Stagnant Thermal Conductivity of Liquid-Saturated Porous Beds of Spheres", *International Journal of Heat and Mass Transfer*, Vol. 32, pp. 1793-1796.

Press, W.H., Teukolsky, S.A., Vetterling, W.T., and Flannery, B.P. (1992), *Numerical Recipes in FORTRAN*, 2nd Edition, Cambridge University Press, U.K., pp. 678-683.

Reddy, J.N. and Gartling, D.K. (2000), *The Finite Element Method in Heat Transfer and Fluid Dynamics*, 2nd Edition, CRC Press, Boca Raton.

Riehl, R.R. and Dutra T. (2005), "Development of an Experimental Loop Heat Pipe for Application in Future Space Mission", *Applied Thermal Engineering*, Vol. 25, pp. 101-112.

Roache, P.J. (1998) *Fundamental of Computational Fluid Dynamics*, Hermosa Publishers, Albuquerque, New Mexico.

Rohsenow, W.M., (1985), "Condensation- Part 1: Film Condensation", in *Handbook of Heat Transfer Fundamentals*, 2nd Edition, W.M. Rohsenow, J.P. Hartnett, and E.N. Ganic (Editors), Chapter 11, pp. 1-36.

Rohsenow, W.M., Harnett, J.P. and Cho, Y.I. (1998), *Handbook of Heat Transfer*, 3rd Edition, McGraw-Hill, New York.

Rose, J.W. (1998), "Condensation Heat Transfer Fundamentals", *Institution of Chemical Engineers (Trans IChemE)*, Vol. 76, Part A, pp. 143-152.

Sangani, A.S. and Acrivos, A. (1983), "The Effective Conductivity of a Periodic Array of Spheres", *Proceedings of the Royal Society of London*, Vol. A386, pp. 263-275.

Scheidegger, A.E. (1974), *The Physics of Flow Through Porous Media,* 3rd Edition, University of Toronto Press.

Sebben, S. and Baliga, B.R. (1995), "Some Extensions of Tridiagonal and Pentadiagonal Matrix Algorithms", *Numerical Heat Transfer, Part B*, Vol. 28, pp. 323-351.

Shah, R.K. and London, A.L. (1978), "Laminar Flow Forced Convection in Ducts", *Advances in Heat Transfer, Supplement 1*, Academic Press, New York.

Silverstein, C.C. (1992), *Design and Technology of Heat Pipes for Cooling and Heat Exchange,* Hemisphere Publishing Corporation, Taylor & Francis, Washington D.C.

Singh, B.S., Dybbs A., and Lyman F.A. (1973), "Experimental Study of the Effective Thermal Conductivity of Liquid Saturated Sintered Fiber Metal Wicks", *International Journal of Heat and Mass Transfer,* Vol. 16, pp. 145-155.

Slattery, J.C. (1981), *Momentum, Energy and Mass Transfer in Continua*, Krieger, Malabar.

Soliman, H.M. (1982), "On the Annular-to-Wavy Flow Pattern Transition during Condensation Inside Horizontal Tubes", *Canadian Journal of Chemical Engineering*, Vol. 60, pp. 457-481.

Soliman, H.M. (1986), "The Mist-Annular Transition During Condensation and Its Influence on the Heat Transfer Mechanism", *International Journal of Multiphase Flow*, Vol. 12, pp. 277-288.

Soliman, M.M., Graumann, D.W., and Berenson, P.J. (1970), "Effective Thermal Conductivity of Dry and Liquid-Saturated Sintered Fiber Metal Wicks", *ASME Paper 70HT/SpT-40.*

Sparrow, E.M. and Patankar, S.V. (1977), "Relationships Among Boundary Conditions and Nusselt Numbers for Thermally Developed Duct Flows", *ASME Journal of Heat Transfer*, Vol. 99, pp. 483-485.

Special Metals (2002), *Technical Bulletin for Nickel 200.* http://www.specialmetals.com.

Stepanov, V.G., Volyak, L.D., and Tarlakov Y.V. (1977), "Wetting Contact Angles of Certain Systems", *Journal of Engineering Physics and Thermophysics,* Vol. 32, pp. 1000-1003.

Swanson, T.D. and Birur, G.C. (2003), "NASA Thermal Control Technologies for Robotic Spacecraft", *Applied Thermal Engineering*, Vol. 23, pp. 1055-1065.

Taitel, Y. and Dukler, A.E. (1976), "A Model for Predicting Flow Regime Transitions in Horizontal and Near Horizontal Gas-Liquid Flow", *AIChE Journal*, Vol. 22, pp. 47-55.

Tannehill, J.C., Anderson, D.A., and Pletcher, R.H. (1997), *Computational Fluid Mechanics and Heat Transfer*, 2nd Edition, Taylor and Francis, Washington D.C.

Travis, D.P., Rohsenow, W.M., and Baron, A.B. (1973), "Forced Convection Condensation in Tubes: A Heat Transfer Correlation for Condenser Design", *ASHRAE Transactions*, Vol. 79, Part I, pp. 157-165.

Tavman, I.H. (1996), "Effective Thermal Conductivity of Granular Porous Materials", *International Communications in Heat and Mass Transfer*, Vol. 23, pp. 169-176.

Tennekes, H. and Lumley, J.L. (1972), *A First Course in Turbulence*, MIT Press, Cambridge, MA.

Thom, J.R.S. (1964), "Prediction of Pressure Drop During Forced Circulation Boiling of Water", *International Journal of Heat and Mass Transfer*, Vol. 7, pp. 709-724.

Thome, J.R. (2003), "On Recent Advances in Modeling of Two-Phase Flow and Heat Transfer", *Heat Transfer Engineering*, Vol. 24, pp. 46-59.

Tong, L.S. and Tang, Y.S. (1997), *Boiling Heat Transfer and Two-Phase Flow*, Taylor & Francis, Washington D.C.

Touloukian, Y.S., Powell R.W., Ho C.Y., and Klemens P.G. (1970), "Thermal Conductivity, Metallic Elements and Alloys", *Thermophysical Properties of Matter*, Vol. 1, Purdue Research Foundation, Plenum Publishing Corporation, New York, N.Y.

Tribbe, C. (1998), *Gas-Liquid Flow in Cylindrical and Corrugated Channels*, Ph.D. Thesis, Department of Chemical and Process Engineering, University of Surrey, U.K.

Tribbe, C. and Müller-Steinhagen, H. (2000), "An Evaluation of the Performance of Phenomenological Models for Predicting Pressure Gradient during Gas-Liquid Flow in Horizontal Pipelines", *International Journal of Multiphase Flow*, Vol. 26, pp. 1019-1036.

Tritton, D.J. (1988), *Physical Fluid Dynamics*, 2nd Edition, Oxford University Press, Oxford, U.K.

Tsotsas, E. and Martin, H. (1987), "Thermal Conductivity of Packed Beds: A Review", *Chemical Engineering Progress,* Vol. 22, pp. 19-37.

Van Sant, J.H. and Malet, J.R. (1975), "Thermal Conductivity of Some Heat Pipe Wicks", *Letters in Heat and Mass Transfer*, Vol. 2, pp. 199-206.

Van Wylen, G.J., Sonntag R.E., and Borgnakke, C. (1994), *Fundamentals of Classical Thermodynamics*, 4th Edition, SI Version, John Wiley, New York, pp. 711-725.

Vasiliev, L.L. (2005), "Heat Pipes in Modern Heat Exchangers", *Applied Thermal Engineering*, Vol. 25, pp. 1-19.

Wallis, G. (1969), *One-Dimensional Two-Phase Flow*, McGraw-Hill, New York.

Wang, C.C., Chen, I.Y., Yang, Y.W., and Chang, Y.J. (2003), "Two-Phase Flow Pattern in Small Diameter Tubes with the Presence of Horizontal Return Bend", *International Journal of Heat and Mass Transfer*, Vol. 46, pp. 2975-2981.

Wang, H.S. and Honda, H. (2003a), "Condensation of Refrigerants in Horizontal Microfin Tubes: Comparison of Prediction Methods for Heat Transfer", *International Journal of Refrigeration*, Vol. 26, pp. 452-460.

Wang, H.S., Rose, J.W., and Honda, H. (2003b), "Condensation of Refrigerants in Horizontal Microfin Tubes: Comparison of Correlations for Pressure Drop", *International Journal of Refrigeration*, Vol. 26, pp. 461-472.

Wattelet, J.P., Chato, J.C., Chistoffersen, B.R., Gaibel, J.A., Ponchner, M., Allen, D.G., and Hershberger, T.T. (1994), *Heat Transfer Flow Regimes of Refrigerants in a Horizontal-Tube Evaporator,* ACRC Technical Report 55, University of Illinois at Urbana-Champaign.

Webb, R.L. and Kim, N.H. (2005), *Principles of Enhanced Heat Transfer*, 2nd Edition, Taylor & Francis, Washington D.C.

Whalley, P.B. (1996), *Two-Phase Flow and Heat Transfer*, Oxford University Press, Oxford, U.K.

Whitaker, S. (1973), "The Transport Equations for Multi-Phase Systems", *Chemical Engineering Science*, Vol. 29, pp. 139-147.

Whitaker, S. (1999), *The Method of Volume Averaging*, Kluwer Academic Publishers, Dordrecht, The Netherlands.

White, F.M. (1991), *Viscous Fluid Flow*, 2nd Edition, McGraw-Hill, New York.

Wilcox, D. (1993), *Turbulence Modeling for CFD*, 2nd Edition, DCW Industries, La Canada, California.

Wilson, M.J., Newell, T.A., Chato, J.C., and Infante Ferreira, C.A. (2003), "Refrigerant Charge, Pressure Drop, and Condensation Heat Transfer in Flattened Tubes", *International Journal of Refrigeration*, Vol. 26, pp. 442-451.

Wirsch, P.J. and Thomas S.K. (1996), "Performance Characteristics of a Stainless Steel/Ammonia Loop Heat Pipe", *AIAA Journal of Thermophysics and Heat Transfer*, Vol. 10, pp. 326-333.

Yun, S., Wolf, D., and Kroliczek, E. (1999), "Design and Test Results of Multi-Evaporator Loop Heat Pipes", SAE-99-01-2051, *Proc. SAE, ASME, AIAA, et al. 29th International Conference on Environmental Systems*, Denver, Co, July 12-15.

Zhukaukas, A. (1972), "Heat Transfer from Tubes in Cross Flow", in *Advances in Heat Transfer*, J.P. Hartnett and T.F. Irvine, Jr. (Editors), Vol. 8, Academic Press, New York.

Zienkiewicz, O.C. and Taylor, R.L. (2000), *Finite Element Method: Volume 2, Fluid Dynamics*, 5th Edition, Butterworth-Heinemann, Elsevier, New York.

Zivi, S.M. (1964), "Estimation of Steady-State Steam Void-Fraction by Means of the Principle of Minimum Entropy Production", *ASME Journal of Heat Transfer*, Vol. 86, pp. 247-252.

Appendix A:
Thermocouple Calibration

In this appendix, the experimental procedure for thermocouple calibration is described and the results obtained are presented. Seventy chromel-constantan thermocouples (type E; AWG-30, with Teflon insulation) were fabricated (using a spot welder). These thermocouples plus ten additional prefabricated thermocouples (type E; with stainless steel sheath, 152.4 mm long and 1.59 mm diameter) were calibrated in the temperature range 5 °C – 155 °C. A special constant-temperature oil bath was designed and constructed for the calibration of these thermocouples in the temperature range 60 °C – 155 °C. This constant-temperature oil bath was later used as the thermal heat sink for the condenser of the LHP designed, constructed, and used in the experimental investigation (see Chapter 4). For calibration of the thermocouples at temperatures below 60 °C, a constant-temperature water bath (Neslab RTE 220) was used. The uncertainties in temperature readings provided by the calibrated thermocouples were determined to be less than or equal to ±0.05 °C, using the method described in ASHRAE Standard 41.5-75 (1976). In this appendix, the constant-temperature oil bath and its details are explained first, and then the procedure for thermocouple calibration is presented.

A.1 Constant-Temperature Bath

A 0.305 m x 0.610 m x 0.915 m (1′×2′×3′) stainless steel tank was built to contain approximately 140 liters of mineral oil. The mineral oil (flash temperature of 173 °C nominal) was chosen to accommodate the required high bath temperatures (up to 150 °C continuous operating temperatures). The tank was fitted with a total of three electric heaters (900 W, nominal power input), two hooked up to a temperature controller, and a third, functioning as a booster heater, with continuous power input. An insulator casing, made of fiberglass boards, was built and installed on the outside of the stainless steel tank, in order to minimize heat losses to the surroundings. Tap water, controlled by a stainless steel metering valve, is used as a coolant within the bath; it flows through a two-pipe counter flow system. By adjusting the flow rate of this cooling water, it is possible to

fine-tune the value of the stabilized temperature of the bath. A three-blade propeller (152.4 mm diameter) fixed to variable speed agitator (Talboys Stirrer Model 138) was fitted inside the bath to ensure vigorous mixing of the mineral oil: This, in turn, enhanced the essentially isothermal operation of the bath.

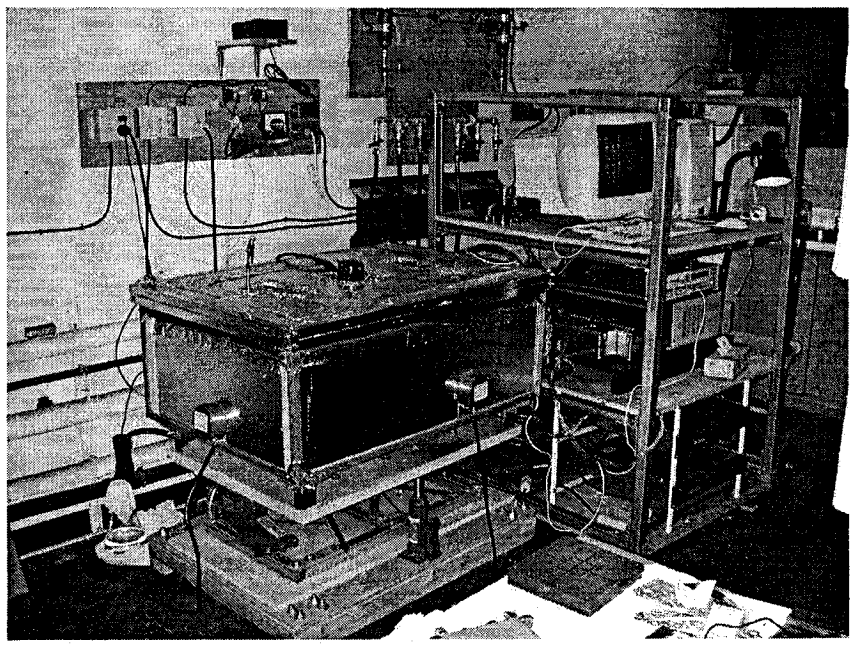

Figure A.1: Photograph of the constant-temperature oil bath, the related instrumentation, the temperature controller, and the data acquisition system.

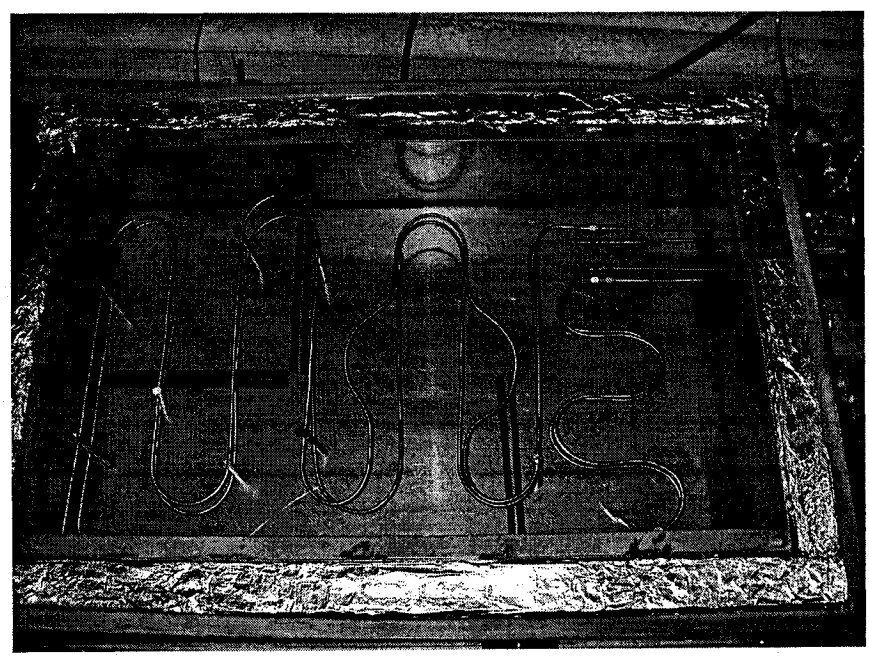

Figure A.2: Photograph of the interior of the constant-temperature oil bath.

In order to allow variation of the height of the bath, the design incorporates an adjustable base. Four car jacks are used in the design of this adjustable-height base of the bath. The adjustable height is necessary to allow adjustments of the gravitational effects in the overall LHP operation. A photograph of the constant-temperature bath, the related instrumentation, the temperature controller, and the data acquisition system is given in Figure A.1. Another photograph, showing the interior of the bath, the two-pipe cooling water arrangement, the heaters, and the mineral oil, is given in Figure A.2.

A.2 THERMOCOUPLE CALIBRATION

As was mentioned earlier, a total of eighty thermocouples were calibrated for use in this study. The readings provided by a quartz thermometer (HP 2804 A) with a quartz probe (HP 18111 A / 2120A; 232 mm long) precisely calibrated (±0.01°C) at the National Research Council Canada (NRC), in Ottawa, were used as reference values for the temperature measurements. The experimental set-up used in the calibration procedure is shown schematically in Figure A.3.

A machined) cylindrical block made of copper (7.5 cm diameter and 6.35 cm long) with one blind hole of 12.7 mm diameter at its center and eighty blind holes of 3.2 mm diameter distributed uniformly (radial distribution around the center) was used to hold thermocouples and the quartz probe together. With this assembly, the thermocouple beads and the quartz probe could be assumed to be essentially at the same temperature. As shown in Figure A.3, once the thermocouple and the quartz probe are installed in the copper block, the ensemble is submerged completely inside the oil. Two DC power supplies (Kepco 1000, 100V/10A) were used to provide electrical power to the two active heaters operating inside the oil bath: These power supplies were necessary to eliminate the effects of the grid voltage fluctuations on the bath thermal stability. The thermocouples were connected to a data acquisition and control unit (HP 3497A), which was used to measure the voltage output of thermocouple. Both the data acquisition unit and the quartz thermometer were connected to a personal computer. To facilitate this calibration, a program was developed in VEE (software application program produced and marketed by Agilent Technologies) and used to control the data acquisition system. This program displays and records all the thermocouple voltage readings and the quartz

thermometer probe temperature readings in real time, and, thus, facilitates quick identification and correction of any erroneous behaviors of the various systems during the calibration process.

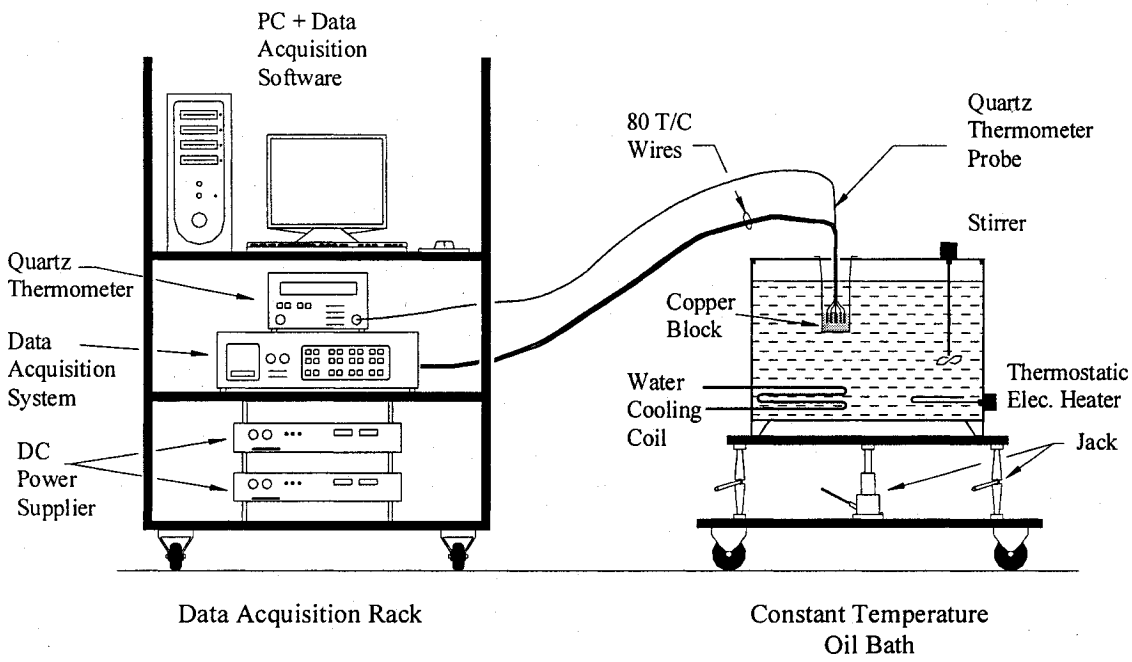

Figure A.3: Experimental set-up used in the thermocouple calibration procedure.

The calibration procedure consists of the following steps:

1. All measurement systems and the PC are turned on for at least two hours before starting the calibration, to allow the electronic circuits to warm up and stabilize;
2. The oil bath temperature is set to 60°C (heaters are activated and the water cooling system is operated);
3. Readings of data are then started, and recorded with a time interval of about 6 sec;
4. Transient responses of the thermocouples and the quartz probe are monitored on the PC screen;
5. Once the difference in two consecutive temperature readings from the quartz probe becomes small enough (±0.03 °C), steady-state conditions are assumed to prevail, and data are acquired and saved on the hard disk of the PC for a period of 10 minute (at least 100 data sets were recorded);

6. For each thermocouple, the voltage readings saved during this last 10-minute period are averaged and compared with the average of the temperature readings provided by the quartz probe during the same period of time;
7. The set temperature of the oil bath temperature is increased by 5 °C (nominal), and steps 3 to 6 are repeated; and this overall procedure is continued until the set temperature reaches 155 °C (nominal);
8. After finishing the collection of data for the temperature range 60 °C to 155 °C, the oil bath is replaced with a constant-temperature water bath (Neslab RTE 220). The ensemble of the copper block, thermocouples, and quartz probe are then transferred to the water bath. The bath set-point temperature is adjusted to 5 °C and the collection of data is continued with the same abovementioned procedures.
9. Again, in steps of 5 °C (nominal), the water-bath temperature is increased, and steps 3 to 6 are repeated until the set-point temperature reaches 55 °C (nominal);
10. For each thermocouple, the averaged voltages obtained during these measurements are plotted versus the corresponding averaged temperature (°C) measured via the quartz probe. As an example, the experimental data obtained for one of the calibrated thermocouples (T_{41}) are presented in Figure A.4;
11. Third-, fourth-, and fifth-order polynomials are then fitted (least-squares procedure) to the experimental voltage-temperature data obtained for each thermocouple to find the best calibration correlation (a total of 3 × 80 correlations are obtained): These correlations have the following form:

$$T_j = \sum_{i=0}^{P} b_{i,j} v_{read,j}^{i} \qquad (P = 3,4, \text{ and } 5) \qquad \text{(A.1)}$$

where $v_{read,j}$ is the voltage read for thermocouple j, T_j is the corresponding temperature (in °C) for thermocouple j, and b_{ij} are the coefficients in the polynomials. Using the three correlations obtained from Eq. (A.1) for each thermocouple, the temperature data are reproduced and compared with the quartz probe readings. The polynomial curve providing the closest predictions is selected and used as the calibration correlation for the corresponding thermocouple. Table A.1 presents the coefficients b_{ij} obtained for each of the thermocouples (j = 1 to 80) for the best polynomial curve.

12. Uncertainty analysis is then performed using the method described in ASHRAE Standard 41.5-75 (1976) to estimate the error bands for the temperature readings (in °C) yielded by each thermocouple. For the temperature range 5 °C – 155 °C, relatively high values of uncertainty were calculated for five thermocouples of T_{11} (±0.078°C), T_{65} (±0.12°C), T_{74} (±0.09°C), T_{75} (±0.12°C), and T_{76} (±0.16°C). For the rest of thermocouples, the maximum overall uncertainty calculated was less than ±0.05 °C. Therefore, the five above-mentioned thermocouples were rejected: The uncertainties in temperature readings provided by the selected calibrated thermocouples are all less than or equal to ±0.05 °C.

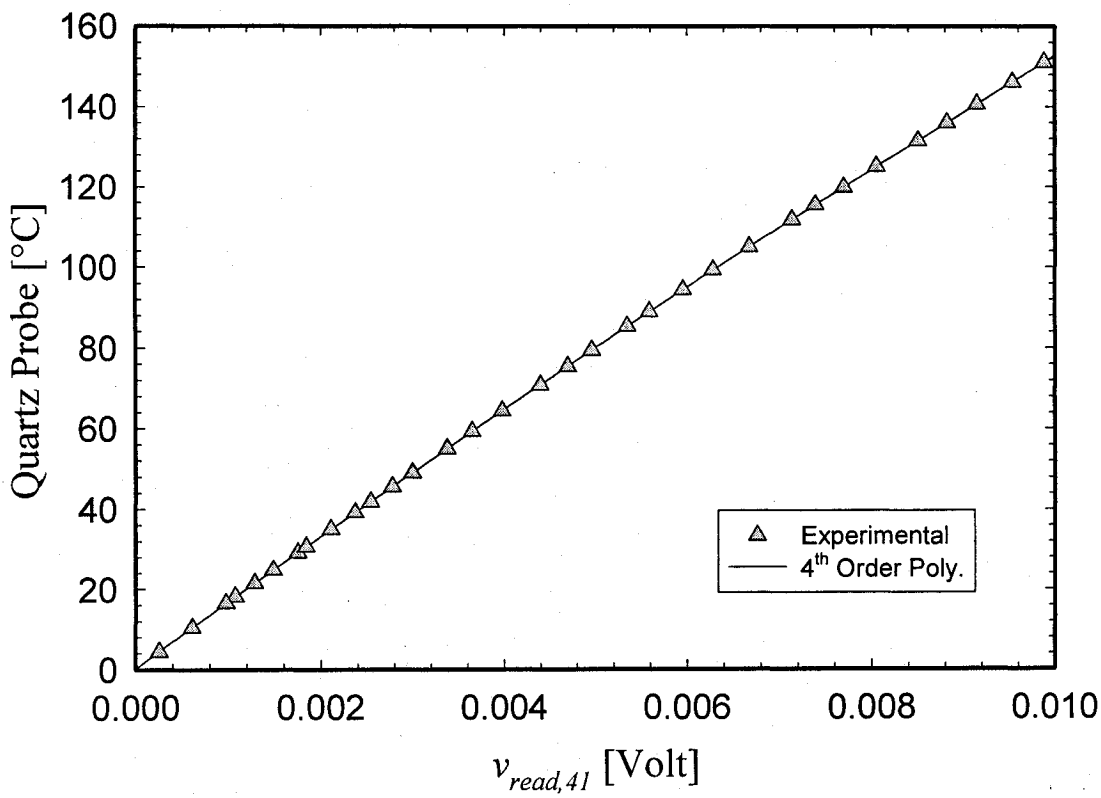

Figure A.4: Experimental results: Temperature-voltage relation for thermocouple 41.

Table A.1: Coefficients in the temperature-voltage calibration correlations

	b_0	b_1	b_2	b_3	b_4	b_5
T_1	0.576825	16976.31	-242975.52	9107465.34	-214127300.80	0
T_2	0.406612	17041.23	-224499.08	5231571.15	0	0
T_3	0.579138	16916.48	-213720.98	4679626.55	0	0
T_4	0.564985	16964.09	-238921.85	9011214.47	-227861458.10	0
T_5	0.592189	16914.47	-213305.36	4673433.97	0	0
T_6	0.574372	16941.92	-226545.71	6894773.81	-118114487.60	0
T_7	0.595051	16901.14	-208959.17	4371503.32	0	0
T_8	0.576785	16926.04	-216174.97	4834705.23	0	0
T_9	0.575387	16920.34	-212122.33	4581896.45	0	0
T_{10}	0.589379	16904.08	-211008.67	4532050.88	0	0
T_{11}	0.596878	16896.61	-208999.12	4387992.95	0	0
T_{12}	0.565938	16921.83	-213538.43	4653009.76	0	0
T_{13}	0.556678	16922.42	-213794.07	4679474.22	0	0
T_{14}	0.549682	16935.15	-217033.35	4890965.91	0	0
T_{15}	0.538166	16945.69	-228601.42	7099541.38	-121986410.20	0
T_{16}	0.513906	16951.05	-228846.94	7278280.17	-137127281.50	0
T_{17}	0.503790	16956.18	-230261.72	7311257.95	-132062104.20	0
T_{18}	0.510149	16952.15	-230293.21	7245112.94	-123538359.80	0
T_{19}	0.491895	16942.37	-224737.71	6626030.47	-103025319.70	0
T_{20}	0.498308	16943.00	-227017.51	7076755.50	-127389580.80	0
T_{21}	0.144264	16991.34	-240016.11	8720726.14	-202727742.60	0
T_{22}	0.139819	16986.40	-238918.88	8565039.24	-193779679.70	0
T_{23}	0.164189	16951.31	-218396.49	4942107.85	0	0
T_{24}	0.134655	17010.61	-245139.31	9358072.29	-231303926.30	0
T_{25}	0.145085	17025.07	-257404.55	11661051.91	-358867658.20	0
T_{26}	0.148468	17003.87	-243570.01	8954430.07	-204978647.30	0
T_{27}	0.164257	17000.14	-243251.19	8896782.02	-201849584.20	0
T_{28}	0.183344	16934.66	-214211.24	4691228.84	0	0
T_{29}	0.149637	16998.82	-239204.97	8228125.82	-168692669.90	0
T_{30}	0.160806	17003.18	-246107.46	9452379.77	-230280933.20	0
T_{31}	0.137837	16991.81	-238993.35	8240883.35	-167771170.90	0
T_{32}	0.130115	16984.86	-234883.96	7521650.45	-129825339.80	0
T_{33}	0.113089	17007.85	-245101.71	9142389.88	-212206395.40	0
T_{34}	0.126827	16984.73	-237245.44	7949208.67	-151712776.60	0
T_{35}	0.108882	16989.25	-237415.76	7898994.66	-146585442.90	0
T_{36}	0.092575	17005.92	-243706.91	8563363.06	-168786054.00	0
T_{37}	0.095783	16987.99	-239427.70	8448195.04	-181996512.90	0
T_{38}	0.093388	16984.42	-235892.66	7652718.11	-134846512.40	0
T_{39}	0.082027	16993.35	-240140.69	8337401.48	-167918392.60	0
T_{40}	0.092492	16969.52	-231362.64	7090748.71	-107215767.80	0

Table A.1 (cont.): Coefficients in the temperature-voltage calibration correlations

	b_0	b_1	B_2	b_3	b_4	b_5
T_{41}	0.114363	17011.91	-248225.34	9603944.70	-231233911.60	0
T_{42}	0.122206	16984.37	-235957.50	8001396.57	-165018661.50	0
T_{43}	0.114695	17024.28	-251236.05	9894494.81	-242713060.80	0
T_{44}	0.107864	17037.96	-254502.66	10167225.33	-250026095.20	0
T_{45}	0.111328	17025.56	-250763.56	9803540.77	-238430365.30	0
T_{46}	0.102533	17058.72	-264859.59	12258302.75	-369861367.90	0
T_{47}	0.113935	17026.37	-251169.86	9909790.53	-245533224.70	0
T_{48}	0.081070	17074.45	-266551.84	11874632.21	-329973806.00	0
T_{49}	0.124105	17015.52	-247378.65	9384167.61	-220553695.60	0
T_{50}	0.121171	17038.61	-257593.88	10919780.82	-295226531.70	0
T_{51}	0.108970	17024.52	-249497.31	9513359.42	-220587554.90	0
T_{52}	0.112419	17012.88	-244617.27	8804548.29	-185826756.30	0
T_{53}	0.097795	17015.59	-247090.62	9251856.85	-209578213.60	0
T_{54}	0.121171	17038.61	-257593.88	10919780.82	-295226531.70	0
T_{55}	0.103574	17003.58	-242349.89	8554912.08	-176324249.20	0
T_{56}	0.084063	17000.30	-238807.84	7839976.42	-134731688.70	0
T_{57}	0.070918	17022.07	-249622.74	9659679.22	-231141438.00	0
T_{58}	0.057178	17009.45	-243333.73	8698471.38	-183971921.70	0
T_{59}	0.079803	16984.71	-227483.37	5539000.31	0	0
T_{60}	0.077715	16956.67	-222824.56	5534258.24	-21770002.90	0
T_{61}	0.195429	17046.79	-263132.09	11897136.04	-350342444.90	0
T_{62}	0.192374	17017.67	-247095.97	9398289.61	-221402225.10	0
T_{63}	0.240626	16973.84	-237894.67	8405895.70	-185440699.10	0
T_{64}	0.228655	16982.80	-238735.40	8469300.42	-189363711.30	0
T_{65}	0.201430	17050.86	-269259.51	13267535.33	-431972096.40	0
T_{66}	0.196608	17024.12	-249434.45	9669479.31	-233486307.70	0
T_{67}	0.196638	17015.36	-244393.43	8702286.81	-180709847.70	0
T_{68}	0.177697	17072.40	-269171.17	12644330.31	-386520329.90	0
T_{69}	0.194432	16969.98	-226414.58	6278888.63	-75335660.44	0
T_{70}	0.203158	17007.14	-245717.57	9277841.70	-221526944.70	0
T_{71}	0.238441	16988.17	-237260.33	5915502.66	0	0
T_{72}	0.272631	16940.84	-227451.35	5387491.06	0	0
T_{73}	0.217643	17044.20	-283857.47	15639537.44	-551491674.60	0
T_{74}	0.181566	17095.67	-309890.90	20529055.26	-825157664.20	0
T_{75}	0.184839	17084.81	-310117.73	21356776.48	-894468192.80	0
T_{76}	0.352695	16781.14	-171377.61	2.53	11122284.82	1.362E+10
T_{77}	0.232718	16932.75	-241613.60	9985803.47	-303100859.40	0
T_{78}	0.220360	16944.60	-244833.74	9722839.89	-262319927.90	0
T_{79}	0.215016	16907.74	-218526.16	4820390.87	0	0
T_{80}	0.248452	16840.84	-184553.22	0.73	12006549.03	1.942E+10

Appendix B

Vapor-Transport Line: Single-Phase Pressure Drop

In this appendix, the experimental procedure used for measurements of the single-phase pressure drop in the vapor-transport line of the loop heat pipe (LHP) and the results obtained are presented and discussed. As was presented and discussed in Chapters 4 and 5, the vapor-transport line was made of a long pipe with several smooth bends, which gives it a serpentine shape (see Figure 5.7). This particular shape of the vapor-transport line, with its U-bends, 90° bends, and fittings (Tees), necessitates a direct measurement of the single-phase pressure drop for a range of Reynolds number that covers the conditions encountered in the steady-state operation of the LHP. The objective here is to obtain correlations that relate the single-phase (dimensionless) pressure drop in the vapor-transport line to the Reynolds number. These correlations are required as inputs in the network thermofluid model proposed in Chapter 5.

In the following sections, the experimental setup and procedures are described first; and then the experimental results and correlations are presented. At the end of this appendix, calibration curves and correlations for the two differential pressure transducers used in the experimental investigation of the LHP and also in these tests are provided.

B.1 Experimental Setup

The experimental setup used in these tests is schematically illustrated in Figure B.1. Pure nitrogen (99.9%) was used as the working fluid in these tests. As can be seen from this figure, the nitrogen is supplied from a compressed-gas cylinder fitted with a pressure reducer and a pressure regulator rated for 204 bars to 27 bars (3000 psi to 400 psi). The nitrogen supply pressure was set to 6 bars in these tests. This nitrogen is passed through a flow-measurement unit (see Figure B.1) that consists of five rotameters (each suited for a different range of flow rate) installed in a parallel configuration: The flow-rate ranges for these rotameters are given in Table B.1. As is shown by the specifications given in this table, the accuracy of each rotameter is 2% of full scale (as reported by the manufacturer): Therefore, it was necessary to use different rotameters for different ranges of flow rate, in order to obtain good accuracy in the measurements. Each rotameter was

equipped at its entrance with a fine metering valve (denoted as M.V. in Figure B.1). At the exit of each rotameter, one shut-off valve was installed, to enable easy isolation or selection of the desired rotameter for each desired range of flow rate.

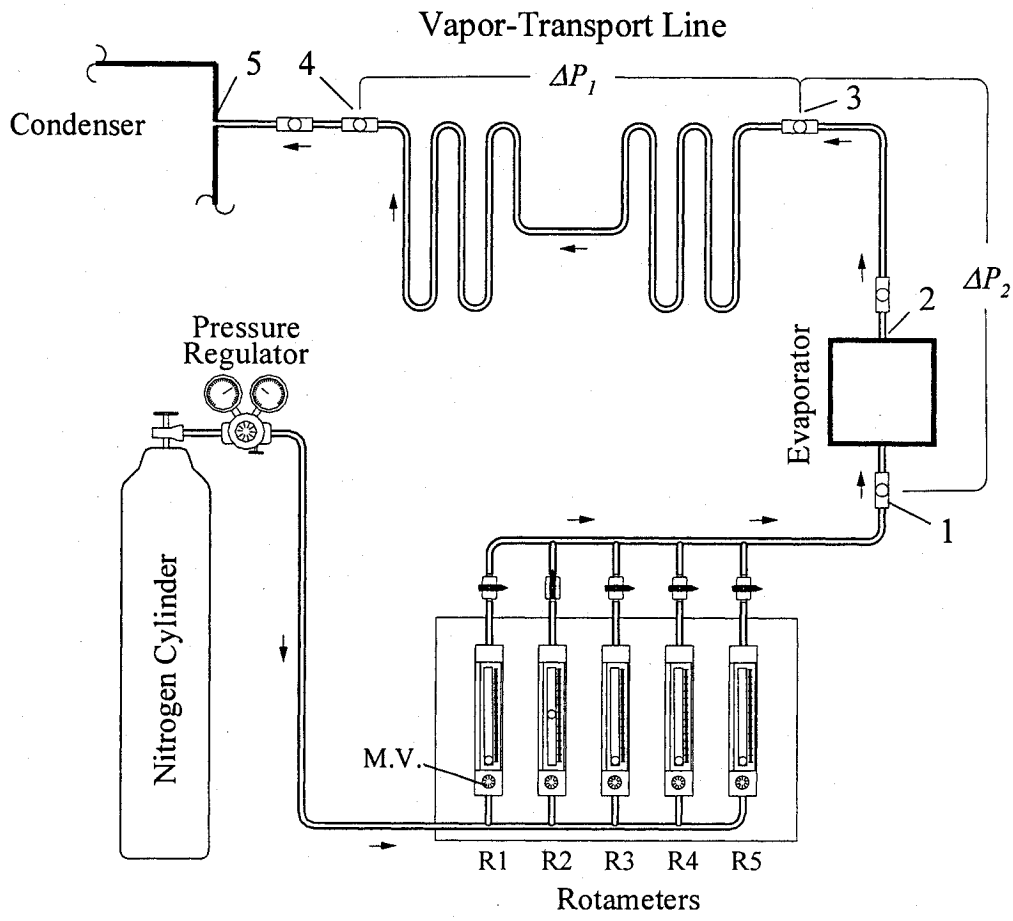

Figure B.1: Schematic presentation of the experimental setup used for measurements of the pressure drop in the vapor-transport line.

Table B.1: Rotameters details.

Rotameter #	Manufacturer / Model	Nitrogen Flow Rate (at 21.1°C)	Accuracy
R_1	Omega® / FL-3663C	0 to 60,618 ml/min	2% FS
R_2	Omega® / FL-3617ST	0 to 25,311 ml/min	2% FS
R_3	Omega® / FL-3796ST	0 to 12,200 ml/min	2% FS
R_4	Omega® / FL-3688C	0 to 5,928 ml/min	2% FS
R_5	Omega® / FL-3665G	0 to 2,624 ml/min	2% FS

As is shown in Figure B.1, after passing through the flow-rate measurement unit, the nitrogen enters the evaporator at point 1. Then it flows through the empty (wickless) evaporator and exits at point 2. The nitrogen then enters the vapor-transport line and exits at the other end of this line (point 5). These tests were run in an open cycle mode: Thus, at the exit of the vapor-transport line (point 5), the nitrogen flows through some connectors (not shown in the figure) and then discharges to atmosphere.

The pressure drop measurements are performed in two steps. First, the pressure drop between points 3 to 4 in Figure B.1 (denoted as ΔP_1) is measured for a wide range of flow rates. In the second step, for the same range of flow rates, the pressure drop between points 1 to 3 in Figure B.1 (presented as ΔP_2) is measured. Two precise differential pressure transducers were used in parallel for these measurements. One of these differential pressure transducers (PT_1), Omega® model PX938-0.4WD10V, was rated for 0 to 1000 Pa (0-4 in of H_2O); the other differential pressure transducer (PT_2), Omega® model PX838-40WD10V, was rated for 0 to 10000 Pa (0-40 in of H_2O). Using an Askania manometer (capable of measuring a maximum differential pressure of 152.4 mm H_2O), the two pressure transducers were calibrated for pressure differences in the range 0 to 1500 Pa. When the second pressure transducer, PT_2, was used to measure pressure differences exceeding 1500 Pa, a calibration curve provided by the manufacturer was used. The overall uncertainty for the pressure drop measured using pressure transducer PT_1 was determined to be less than ±0.15% FS; and for PT_2 it is ±0.25% FS (however, below 1500 Pa, using the calibration data, this uncertainty is ±7.2 Pa). The calibration results for theses pressure transducers are presented at the end of this appendix.

The voltage outputs of the two pressure transducers are measured separately using a data acquisition and control unit (HP 3497A). This data acquisition unit was connected to a personal computer (PC). A program was developed in VEE (software application program produced and marketed by Agilent Technologies) and used to control the data acquisition unit. The voltage vs. pressure difference (in Pa) calibration curves for the two pressure transducers were also deployed in this program. This enabled direct reading of the pressure differences from each of the pressure transducers, and, thus, facilitated quick identification and correction of any erroneous behavior of the various systems during these tests.

B.2 EXPERIMENTAL PROCEDURE

The experimental procedure used in these test consists of the following steps:

1. All measurement systems and the PC are turned on at least two hours before starting the measurements, to allow the electronic circuits to warm up and stabilize;
2. The two differential pressure transducers are installed in parallel in the piping system between points 3 to 4 in Figure B.1 (denoted as ΔP_1);
3. Readings of data from the pressure transducers are started, and then recorded at uniform time intervals of about 6 sec. Readings from a thermocouple installed in the line are also recorded to track the temperature of the nitrogen flowing inside the pipes;
4. The nitrogen supply is turned on, a range of flow rates is selected (starting with highest range), the corresponding rotameter is brought on line, and the four others rotameters are isolated by shutting off the related valves (see Figure (B.1);
5. Using the fine metering valve on the selected rotameter, the volumetric flow rate is adjusted and recorded for later use;
6. The pressure drop data are then monitored on the screen of the PC; once steady-state conditions are achieved, the data is acquired and saved on the hard disk of the PC, and this process is continued for one minute (ten data sets are saved);
7. Then the data are averaged over the total sampling time period, and the averaged value is taken as the pressure drop over the section of interest for the chosen flow rate.
8. For pressure drops up to 1500 Pa, the data obtained from the low-range pressure transducer, PT_1, are used. However, for pressure drops greater than 1500 Pa, data from the high-range pressure transducer, PT_2, are considered;
9. The flow rate is adjusted to a new value and steps 6 to 8 are repeated;
10. Once the range of flow rates measurable with the selected rotameter is covered, it is isolated, and a new rotameter is brought on line. Then, steps 5 to 10 are repeated until the range of flow rates measurable by this rotameter is also fully covered; and this process is continued until all of the desired flow rates are covered;

11. The nitrogen supply is then shut off. The two differential pressure transducers are installed in parallel in the piping system between points 1 to 3 in Figure B.1 (denoted as ΔP_2). Then, steps 3 to 10 were repeated.

Once the above-mentioned tests were completed, analyses of the data were undertaken. Using the known geometry of the vapor-transport line and the thermophysical properties of the nitrogen (for the particular mean pressure and temperature), for each flow rate measured, the pressure drop was normalized by $\rho\bar{V}^2$ ($\bar{V}$ is the average axial velocity in pipe) and plotted versus the corresponding Reynolds number. These experimental results are presented in the next section.

B.3 Experimental Results

For each of the two sections 3-4 and 1-3 (see Figure B.1), the corresponding dimensionless pressure drops, $C_{f,1} = \Delta P_1 / (\rho \bar{V}^2)$ and $C_{f,2} = \Delta P_2 / (\rho \bar{V}^2)$, are plotted against the Reynolds number ($Re = \rho \bar{V} D_{vl} / \mu$) in Figures B.2 and B.3, respectively, on a log-log scale. The symbols in these figures represent the experimental data points. The corresponding horizontal and vertical error bars are also included.

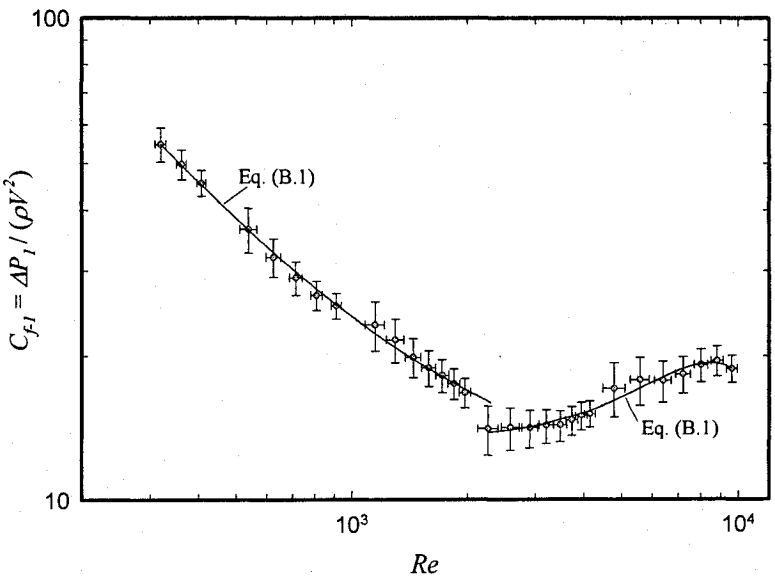

Figure B.2: Dimensionless pressure drop vs. Reynolds number for section 3-4.

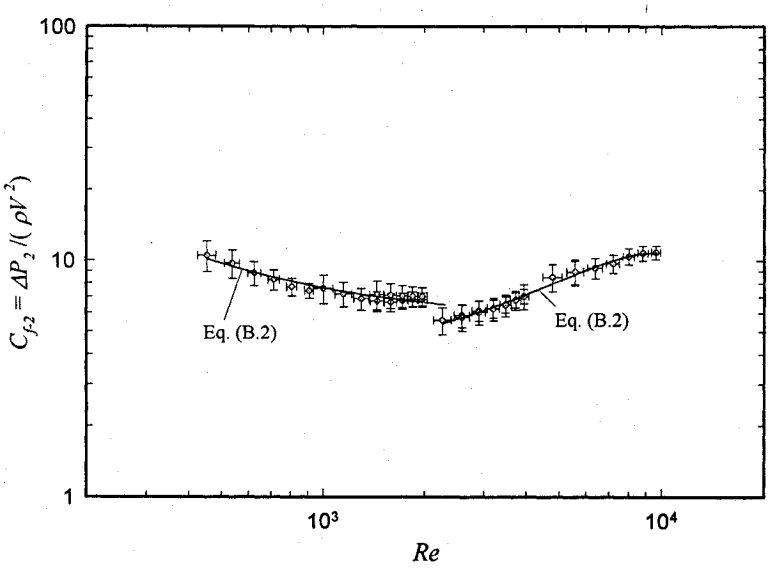

Figure B.3: Dimensionless pressure drop vs. Reynolds number for section 1-3.

As can be seen from these figures, there is a sudden change in the distribution of dimensionless pressure drop at a Reynolds number slightly larger than 2000. This is an expected result, as the laminar-to-turbulent transition regime for flows in pipes starts at about this value of Reynolds number. To obtain the best correlations for the pressure drop in the vapor-transport line, it was decided to curve fit the data in Figures B.2 and B.3 for two different ranges of Reynolds number: $\mathrm{Re} \leq 2300$, for which the flow is assumed to be laminar; and $2300 < \mathrm{Re} < 10000$, for which the flow is either in the transition or turbulent regimes. In each of Figures B.2 and B.3, these two curve fits to the experimental data are presented as lines. The correlations obtained for the two sections 3-4 and 1-3 are presented below in Eqs. (B.1) and (B.2), respectively.

$$C_{f-1} = \frac{\Delta P_1}{\rho \bar{V}^2} = \frac{14{,}360}{\mathrm{Re}} + 9.77 \qquad (\mathrm{Re} \leq 2{,}300)$$

$$C_{f-1} = 14.7 - 1.42\times10^{-3}\,\mathrm{Re} + 5.27\times10^{-7}\,\mathrm{Re}^2 - 3.49\times10^{-11}\,\mathrm{Re}^3 \qquad (2{,}300 < \mathrm{Re} \leq 10{,}000) \qquad \text{(B.1)}$$

$$C_{f-2} = \frac{\Delta P_2}{\rho \bar{V}^2} = \frac{2{,}047}{\mathrm{Re}} + 5.62 \qquad (\mathrm{Re} \leq 2{,}300)$$

$$C_{f-2} = 3.45 + 6.82\times10^{-4}\,\mathrm{Re} + 1.03\times10^{-7}\,\mathrm{Re}^2 - 9.86\times10^{-12}\,\mathrm{Re}^3 \qquad (2{,}300 < \mathrm{Re} \leq 10{,}000) \qquad \text{(B.2)}$$

The overall uncertainties in the dimensionless pressure drops predicted by the correlations were determined using the method described in ASHRAE Standard 41.5-75 (1976), and they are given below:

For Eq. (B.1):	$Re \leq 2{,}300$	±11.75%;
	$2{,}300 < Re < 10{,}000$	±13.12%
For Eq. (B.2):	$Re \leq 2{,}300$	±14.90%;
	$2{,}300 < Re < 10{,}000$	±13.14%

B.4 Pressure Transducer Calibration Curves

Figures B.4 and B.5 present the calibration curves obtained for the two differential pressure transducers (PT_1 and PT_2) used in this study. The corresponding calibration equations for PT_1 and PT_2 are given in Eqs. (B.3) and (B.4), respectively

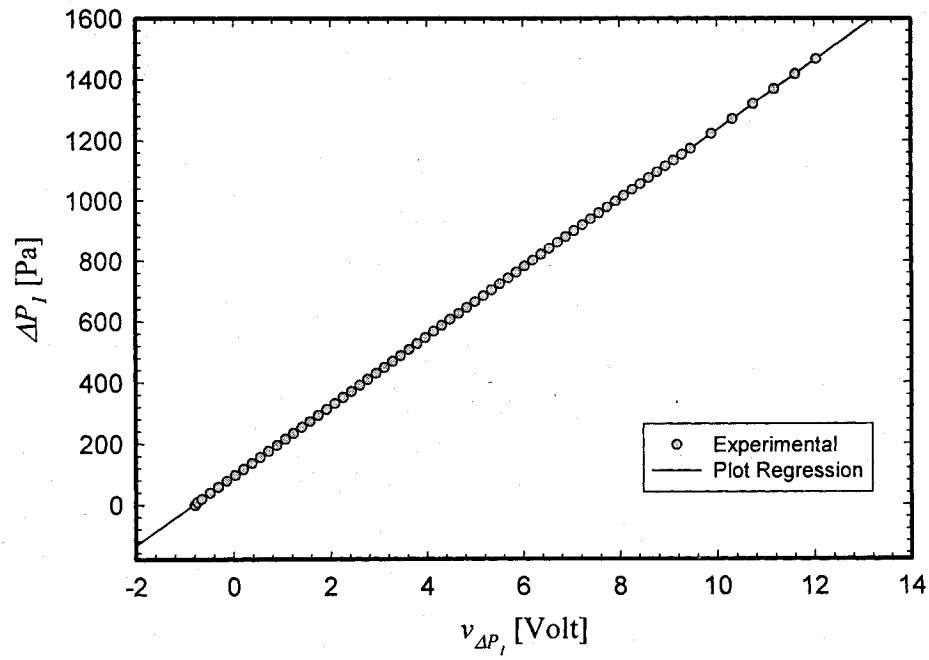

Figure B.4: Calibration curve for pressure transducer PT_1 (Omega® model PX938-0.4WD10V).

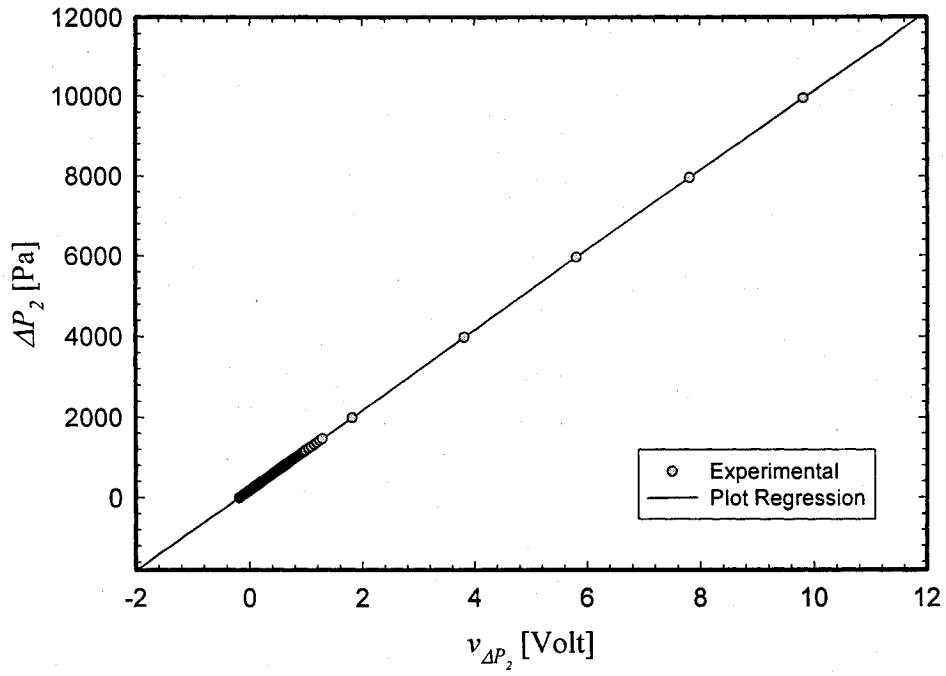

Figure B.5: Calibration curve for pressure transducer PT_2 (Omega® model PX838-40WD10V).

$$PT_1: \quad \Delta P \ [Pa] = 94.31 + 114.07 \times v_{\Delta P} \ [Volt] \qquad (B.3)$$

$$PT_2: \quad \Delta P \ [Pa] = 180.59 + 995.52 \times v_{\Delta P} \ [Volt] \qquad (B.4)$$

Appendix C

Geometrical Details of the Tubes of the Loop Heat Pipe used in the Experimental Investigation

As was mentioned in Chapter 4, a loop heat pipe (LHP) with a flat evaporator and a fixed active mass of the working fluid was designed, constructed, and used in the experimental investigation. Several bends were incorporated in the tubes that were used to construct the vapor-transport line, the condenser, and the liquid-transport line of this LHP. The geometrical details of the bends and also the straight portions of these tubes are provided in Figure C.1 and Table C.1.

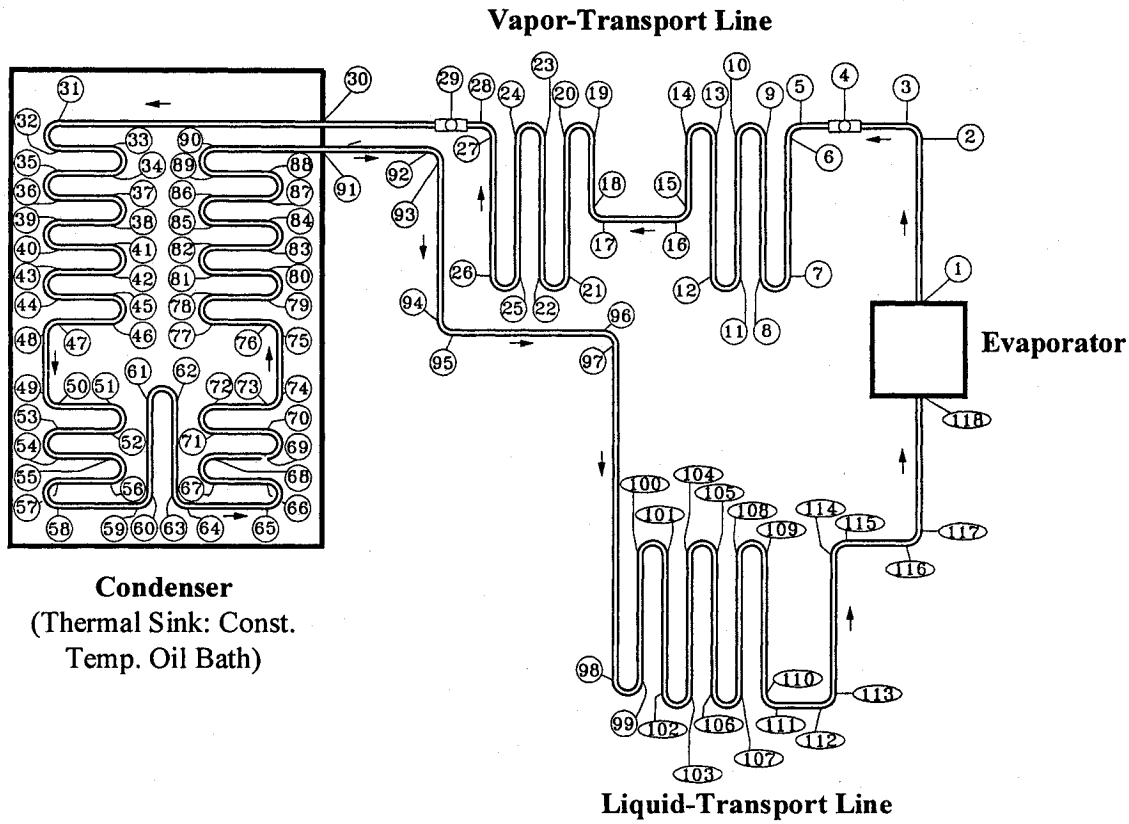

Figure C.1: Schematic illustration of the bends and the straight portions of the tubes of the LHP (not to scale) and the corresponding numbering system.

Table C.1: Details of the bends and the straight portions of the tubes of the LHP (the corresponding numbering system is schematically illustrated in Figure C.1).

Vapor-Transport Line				Condenser								Liquid-Transport Line			
Segment	Description	Segment Length [m]	Total Length [m]	Segment	Description	Segment Length [m]	Total Length [m]	Segment	Description	Segment Length [m]	Total Length [m]	Segment	Description	Segment Length [m]	Total Length [m]
1 - 2	Straight pipe	0.2920	0.2920	30 - 31	Straight pipe	0.5048	0.5048	61 - 62	U-bend	0.0898	3.4706	91 - 92	Straight pipe	0.2032	0.2032
2 - 3	90° bend	0.0449	0.3369	31 - 32	U-bend	0.0898	0.5946	62 - 63	Straight pipe	0.1778	3.6484	92 - 93	90° bend	0.0449	0.2481
3 - 4	Straight pipe	0.1130	0.4499	32 - 33	Straight pipe	0.1016	0.6962	63 - 64	90° bend	0.0449	3.6933	93 - 94	Straight pipe	0.3048	0.5529
4 - 5	Straight pipe	0.1020	0.5519	33 - 34	U-bend	0.0898	0.7860	64 - 65	Straight pipe	0.1524	3.8457	94 - 95	90° bend	0.0449	0.5978
5 - 6	90° bend	0.0449	0.5968	34 - 35	Straight pipe	0.1016	0.8876	65 - 66	U-bend	0.0898	3.9355	95 - 96	Straight pipe	0.2921	0.8899
6 - 7	Straight pipe	0.2670	0.8638	35 - 36	U-bend	0.0898	0.9774	66 - 67	Straight pipe	0.1016	4.0371	96 - 97	90° bend	0.0449	0.9348
7 - 8	U-bend	0.0898	0.9536	36 - 37	Straight pipe	0.1016	1.0790	67 - 68	U-bend	0.0898	4.1269	97 - 98	Straight pipe	0.6452	1.5800
8 - 9	Straight pipe	0.2670	1.2206	37 - 38	U-bend	0.0898	1.1688	68 - 69	Straight pipe	0.1016	4.2285	98 - 99	U-bend	0.0898	1.6698
9 - 10	U-bend	0.0898	1.3104	38 - 39	Straight pipe	0.1016	1.2704	69 - 70	U-bend	0.0898	4.3183	99 - 100	Straight pipe	0.2413	1.9111
10 - 11	Straight pipe	0.2670	1.5774	39 - 40	U-bend	0.0898	1.3602	70 - 71	Straight pipe	0.1016	4.4199	100 - 101	U-bend	0.0898	2.0009
11 - 12	U-bend	0.0898	1.6672	40 - 41	Straight pipe	0.1016	1.4618	71 - 72	U-bend	0.0898	4.5097	101 - 102	Straight pipe	0.2667	2.2676
12 - 13	Straight pipe	0.2670	1.9342	41 - 42	U-bend	0.0898	1.5516	72 - 73	Straight pipe	0.1016	4.6113	102 - 103	U-bend	0.0898	2.3574
13 - 14	U-bend	0.0898	2.0240	42 - 43	Straight pipe	0.1016	1.6532	73 - 74	90° bend	0.0449	4.6562	103 - 104	Straight pipe	0.2667	2.6241
14 - 15	Straight pipe	0.1330	2.1570	43 - 44	U-bend	0.0898	1.7430	74 - 75	Straight pipe	0.1143	4.7705	104 - 105	U-bend	0.0898	2.7139
15 - 16	90° bend	0.0449	2.2019	44 - 45	Straight pipe	0.1016	1.8446	75 - 76	90° bend	0.0449	4.8154	105 - 106	Straight pipe	0.2667	2.9806
16 - 17	Straight pipe	0.1391	2.3410	45 - 46	U-bend	0.0898	1.9344	76 - 77	Straight pipe	0.1016	4.9170	106 - 107	U-bend	0.0898	3.0704
17 - 18	90° bend	0.0449	2.3859	46 - 47	Straight pipe	0.1016	2.0360	77 - 78	U-bend	0.0898	5.0068	107 - 108	Straight pipe	0.2667	3.3371
18 - 19	Straight pipe	0.1330	2.5189	47 - 48	90° bend	0.0449	2.0809	78 - 79	Straight pipe	0.1016	5.1084	108 - 109	U-bend	0.0898	3.4269
19 - 20	U-bend	0.0898	2.6087	48 - 49	Straight pipe	0.1143	2.1952	79 - 80	U-bend	0.0898	5.1982	109 - 110	Straight pipe	0.2667	3.6936
20 - 21	Straight pipe	0.2670	2.8757	49 - 50	90° bend	0.0449	2.2401	80 - 81	Straight pipe	0.1016	5.2998	110 - 111	90° bend	0.0449	3.7385
21 - 22	U-bend	0.0898	2.9655	50 - 51	Straight pipe	0.1016	2.3417	81 - 82	U-bend	0.0898	5.3896	111 - 112	Straight pipe	0.0889	3.8274
22 - 23	Straight pipe	0.2670	3.2325	51 - 52	U-bend	0.0898	2.4315	82 - 83	Straight pipe	0.1016	5.4912	112 - 113	90° bend	0.0449	3.8723
23 - 24	U-bend	0.0898	3.3223	52 - 53	Straight pipe	0.1016	2.5331	83 - 84	U-bend	0.0898	5.5810	113 - 114	Straight pipe	0.2667	4.1390
24 - 25	Straight pipe	0.2670	3.5893	53 - 54	U-bend	0.0898	2.6229	84 - 85	Straight pipe	0.1016	5.6826	114 - 115	90° bend	0.0449	4.1839
25 - 26	U-bend	0.0898	3.6791	54 - 55	Straight pipe	0.1016	2.7245	85 - 86	U-bend	0.0898	5.7724	115 - 116	Straight pipe	0.1143	4.2982
26 - 27	Straight pipe	0.2670	3.9461	55 - 56	U-bend	0.0898	2.8143	86 - 87	Straight pipe	0.1016	5.8740	116 - 117	90° bend	0.0449	4.3431
27 - 28	90° bend	0.0449	3.9910	56 - 57	Straight pipe	0.1016	2.9159	87 - 88	U-bend	0.0898	5.9638	117 - 118	Straight pipe	0.2570	4.6001
28 - 29	Straight pipe	0.0600	4.0510	57 - 58	U-bend	0.0898	3.0057	88 - 89	Straight pipe	0.1016	6.0654				
29 - 30	Straight pipe	0.2540	4.3050	58 - 59	Straight pipe	0.1524	3.1581	89 - 90	U-bend	0.0898	6.1552				
				59 - 60	90° bend	0.0449	3.2030	90 - 91	Straight pipe	0.2064	6.3616				
				60 - 61	Straight pipe	0.1778	3.3808								